City Research Online

City St George's, University of London

Citation: Perera, M. D. A. E. S. (1976). Wind-tunnel modelling of wind-excited lateral and in-line vibrations of tall structures. (Unpublished Doctoral thesis, The City University)

This is the accepted version of the paper.

This version of the publication may differ from the final published version. To cite this item please consult the publisher's version.

Permanent repository link: https://openaccess.city.ac.uk/id/eprint/37938/

Copyright and Reuse: Copyright and Moral Rights remain with the author(s) and/or copyright holders. Copies of full items can be used for personal research or study, educational, or not-for-profit purposes without prior permission or charge, unless otherwise indicated, provided that the authors, title and full bibliographic details are credited, a hyperlink and/or URL is given for the original metadata page and the content is not changed in any way. For full details of reuse please refer to City Research Online policy.

City Research Online: http://openaccess.city.ac.uk/ publications@citystgeorges.ac.uk

Wind-tunnel modelling of wind-excited lateral and in-line vibrations of tall structures

by

Mahahettige Don Anton Earle Stephen Perera

A thesis submitted for the
Degree of Doctor of Philosophy

Department of Aeronautical Engineering
The City University, London

October 1976

CONTENTS

		Page No.
List of figures		1
List of tables		2
Acknowledgements		3
Declaration		4
Abstract		5
Notation		6
I. INTRODUCTION		10
I.1.	General	10
I.2.	Formulation of the Problem	11
I.3.	Structural Response to Wind Effects	13
I.4.	Review	21
II. ANALOGUE DATA AND ITS ANALYSES		25
II.1.	Acquisition and Recording of Experimental Data	26
II.2.	Description of Random Data	29
II.3.	Analogue Analysis of Signals	38
III. DIGITAL ANALYSIS		43
III.1.	Recording and Storage of Analogue Data	44
III.2.	Data Preparation	45
III.3.	Analysis of Digitised Data	56
IV. SIMULATION OF THE ATMOSPHERIC BOUNDARY LAYER IN THE WIND-TUNNEL		67
IV.1.	Description of the ABL	68
IV.2.	Experimental Apparatus Used for Generation of a Simulated ABL	82
V. DESIGN AND CONSTRUCTION OF EXPERIMENTAL APPARATUS		89
V.1.	Design and Construction of Models	89
V.2.	Design and Construction of Vibration Rig	97
V.3.	Damping and Housing Rig	106

CONTENTS

		Page No.
VI.	GENERATED TURBULENT FLOW	111
VI.1.	Results from Analogue Analysis	112
VI.2.	Results from Digital Analysis	117
Vi.3.	Discussion	120
VII.	VIBRATION MEASUREMENTS OF MODELS	129
VII.1.	Measurements	130
VII.2.	Results	135
VII.3.	Discussion of Results	141
VIII.	DISCUSSION AND FINAL CONCLUSIONS	167
VIII.1.	Aims and Requirements of Research	167
VIII.2.	Review	168
VIII.3.	Proposals for Future Work	172
FIGURES		174
TABLES		272
APPENDICES		
2.A.	Calibration of Hot-wire Anemometers	281
3.A.	Analogue to Digital Conversion Program	283
3.B.	Summary of Procedure for Analogue to Digital Conversion of Signals	293
4.A.	Design of Cowdrey's Velocity-profile Simulation Grids	299
5.A.	Calculations for Modelling Inertia Values	302
5.B.	Design Calculations for Torsion Bars	303
5.C.	Strain-guage	305
5.D.	Electro-magnet Damping	306
6.A.	Mean Wind Characteristics from Velocity Profiles	308
7.A.	Determining Damping Parameters	309
A.	Equipment Used	314
B.	Digital Computer Program	316
REFERENCES		336

FIGURES

1.1. Aerodynamic stability diagram for a two-dimensional square-section prism (Scruton [24])

1.2. Comparison of dynamic response in smooth and turbulent flow for square model [30]

2.1. Traverse mechanism

2.2. Pitot rake

2.3. Analogue equipment

3.1.a. Patching required for ramp test-generator

3.1.b. Analog patching required for each data channel

3.1.c. Logic patching required for multi-channel A/D conversion

4.1. Van der Hoven's spectrum of horizontal wind speed near the ground (at 100m. height)

4.2. Parameters of wind profile for different surfaces

4.3.a. Castellated barrier

4.3.b. Vortex generator

4.4. Mounting of vortex generators on board: a bi-planar screen is shown at the back

4.5. Positioning of turbulent-shear-flow generators in wind-tunnel and origin of co-ordinate system

5.1. The World Trade Centre

5.2. Models used in the experiments

5.3. Gimbal sustem

5.3.a. Centre block of gimbal system

5.3.b. Intermediate ring of gimbal system

5.3.c. Support ring of gimbal system

5.4. Attachment linkage

5.4.a. Spacer link

5.4.b. Spacer

£.4.c.i. Square plug

5.4.c.ii. Circular plug

FIGURES

5.5. Model mounted on the experimental rig

5.6. Tube and collar of the damping system

5.6.a. Copper plate

5.6.b. Collar

5.7. Mounting of electro-magnets

5.8. Support plate

5.9. Schematic showing clearing between wind-tunnel floor and model mounted on vibration rig

6.1.a. Velocity profile: Generated flow with Cowdrey grid only

6.1.b. Velocity profile: Generated flow with vortex generator system only

6.1.c. Velocity profile: Generated flow with vortex generator system and Cowdrey grid but without roughness elements

6.1.d. Velocity profile: Generated flow (T_s)

6.1.e. Velocity profile: Generated flow ($T_s + 1$)

6.1.f. Velocity profile: Generated flow ($T_s + 2$)

6.1.g. Velocity profile plot to obtain possible zero-plane displacement

6.2.a. Turbulent intensity profile: Generated flow without roughness

6.2.b. Turbulent intensity profile: Generated flow with roughness

6.3. Comparison of turbulence spectra by digital and analogue methods

6.4. Example of auto-correlation using analogue analysers

6.5.a. Probability density distribution for the longitudinal wind velocity at $z/\delta = 0.75$

FIGURES

6.5.b. Probability density distribution for the longitudinal wind velocity at $z/\delta = 0.50$

6.6.a. Auto-spectrum: Generated flow (T)

6.6.b. Auto-spectrum: Generated flow (T_s) — low speed

6.6.b.i. Auto-spectrum: Generated flow (T_s) — $\ln \{G_u(n)/\sigma u^2\}$ vs $\ln \{n\}$

6.6.c. Auto-spectrum: Generated flow (T_s) — high speed

6.6.d. Auto-spectrum: Generated flow ($T_s + 1$)

6.6.e. Composite spectra of generated turbulence (digital analysis)

6.6.d. Fitting of Harris and Von Karman equations to the longitudinal fluctuating wind velocity spectrum

6.7. Coherence between hot-wire anemometers A ($z/\delta = 0.75$) and B ($z/\delta = 0.50$)

6.8.a. Auto-correlation: Generated flow (T_s) — low speed

6.8.b. Auto-correlation: Generated flow (T_s) — high speed

6.8.c. Auto-correlation: Generated flow ($T_s + 1$)

7.1.a. Natural decay trace in still-wind conditions (from UV trace)

7.1.b. Natural decay trace in still-wind conditions (from UV trace)

7.1.c. Natural decay trace in still-wind conditions (from UV trace)

7.2. External structural damping induced by the electro-magnets

7.3. Calibration of strain-guage system

7.4.a. In-line static deflection: Square model with various damping/flow configurations

7.4.b. Fluctuating deflection: Square model in turbulent flow

FIGURES

7.4.c. Fluctuating deflection: Square model in smooth flow

7.4.d. Fluctuating deflection: Square model in turbulent shear flow

7.5.a. In-line static deflection: Circular model with various flow configurations

7.5.b. Fluctuating deflection: Circular model in smooth flow

7.5.c. Fluctuating deflection: Circular model in turbulent and turbulent shear flow

7.6.a. In-line static deflection: Wedge model with various flow configurations

7.6.b. Fluctuating deflection: Wedge model in smooth flow

7.6.c. Fluctuating deflection: Wedge model in turbulent flow

7.6.d. Fluctuating deflection: Wedge model in turbulent shear flow

7.7.a. Probability density distribution of the in-line motion of the square model in turbulent shear flow

7.7.b. Probability density distribution of the lateral motion of the square model in turbulent shear flow

7.8.a. Probability density distribution of the lateral motion of the circular model in turbulent shear flow

7.8.b. Probability density distribution of the in-line motion of the circular model in turbulent shear flow

7.9. Cumulative probability distribution

7.10. Cumulative probability distribution

7.11. Locus of oscillations

7.12. Envelope of fluctuations

7.13.a. Auto-spectrum: Square model in smooth flow without applied damping

7.13.b. Auto-spectrum: Square model in smooth flow with maximum applied damping

FIGURES

7.13.c. Auto-spectrum: Square model in turbulent shear flow without applied damping

7.13.d. Auto-spectrum (linear plot): Square model in turbulent shear flow with and without applied damping

7.13.e. Auto-spectrum: Square model in turbulent shear flow (screen 2) without applied damping

7.14.a. Auto-spectrum: Circular model in smooth flow without applied damping

7.14.b. Auto-spectrum: Circular model in turbulent shear flow without applied damping

7.15. Auto-spectrum: Wedge model in turbulent shear flow without applied damping

7.16.a. Auto-correlation: Square model in smooth flow without applied damping

7.16.b. Auto-correlation: Square model in turbulent flow without applied damping

7.16.c. Auto-correlation: Square model in turbulent shear flow without applied damping

7.16.d. Auto-correlation: Square model in turbulent shear flow (screen 2) without applied damping

7.16.e. Auto-correlation: Square model in turbulent shear flow with maximum applied damping

7.16.f. Comparison between 2 DOF and 1 DOF motion: Maxima and minima points of the respective auto-correlations

7.17.a. Auto-correlation: Circular model in smooth flow without applied damping

7.17.b. Auto-correlation: Circular model in turbulent shear flow without applied damping

FIGURES

7.17.c. Auto-correlation: Circular model in turbulent shear flow with maximum applied damping

7.18.a. Auto-correlation: Wedge model in turbulent shear flow without applied damping

7.18.b. Auto-correlation: Wedge model in turbulent shear flow with maximum applied damping

7.19. Strain-guage signals

7.20.a. Coherence: Square model for various damping/flow configurations

7.20.b. Coherence: Circular model in turbulent shear and smooth flow

7.20.c. Coherence: Wedge model in turbulent shear flow

7.21.a. Wake spectra behind square model in smooth flow

7.21.b. Wake spectra behind wedge model in smooth flow

7.21.c. Wake spectrum behind square model in turbulent shear flow

TABLES

4.1. Bi-planar screens

6.1. Characteristics of generated velocity profiles obtained from Fig. 6.1

6.2. Amplitude-domain characteristics of turbulent generated flows -- sample of the digitised runs

6.3. Length scales of turbulence of some cases of the generated flows, calculated using various methods

7.1 Amplitude domain characteristics of model vibrations -- a sample of digitised runs

7.2. Cumulative probability distributions for the lateral vibrations of thesquare model in turbulent shear flow

7.3.a. Joint probability distribution for square model oscillating in turbulent shear flow

7.3.b. Joint probability distribution for square model oscillating in turbulent shear flow

7.4. Sample of damping values evaluated by various methods

ACKNOWLEDGEMENTS

I should like to express my deep gratitude for the continuous and constant supervision, guidance and encouragement given to me throughout this research by my supervisor, Mr D.M.Sykes M.Sc., C.Eng., AFRAeS, Senior Lecturer of the Department of Aeronautics.

I should also like to thank Professor [redacted], former Head and now Emiritus Professor of the Department of Aeronautics, for his encouragement and for making available the necessary facilities for carrying out the research.

Thanks are also due to the members of the technical staff of the Department of Aeronautics, especially to Mr J [redacted], who constructed most of the apparatus and helped in many other ways.

The help of Mr P Saward, formerly of the Department of Computing, in writing the analogue to digital conversion programme is gratefully acknowledged.

I should also like to thank my dear wife [redacted] for her constant help, patience and support throughout the period of this research

Finally, it is with great pleasure that I thank my mother for the encouragement and guidance she always gives me.

The research project was carried out under a City University Research Studentship grant.

DECLARATION

I hereby grant powers of discretion to the University Librarian to allow this thesis to be copied in whole or in part without further reference to me. This permission covers only single copies made for study purposes, subject to normal conditions of acknowledgement.

M.D.A.E.S. Perera

ABSTRACT

The research described in this thesis showed that, under certain conditions, coupling can take place between the lateral and in-line motion of a structure vibrating in a turbulent wind. This has important consequences both for full-scale and for model-scale tests.

Previous researchers have usually confined their investigations to models with only one degree of freedom (lateral), assuming that the in-line motion is of no consequence to the final results. It has been shown here, however, that this assumption can lead to erroneous results. It was found that for a lightly damped structure there is a significant transfer of energy between the two motions of oscillations. With the motion restricted to only one degree of freedom, no such energy transfer takes place. Consequently, compared to a two degree of freedom model, a much lower value for the structural damping for the model is obtained.

The above conclusion was reached as a result of tests made on models placed in a generated atmospheric boundary layer (GABL). The models were mounted on a novel gimbal system, designed and constructed to permit motion with either one or two degrees of freedom. Emphasis was placed on digital techniques as opposed to analogue, for analysing the vibrations of the models and the turbulence structure of the GABL. For this purpose, a digital and an analogue computer were used together for off-line analyses of the various signals.

NOTATION:

Symbol	Suffix	Description	Chapter
a	1,2,..	Constants in various equations	1,2
A		'wetted' area	
A(t)		non-random function	3
AR		aspect ratio (=h/D)	1
b	1,2,..	constants in various equations	1
b		width of bar in bi-planar screens	4
b		breadth of the flat in torsion bar	5
B		signal bandwidth	2
B	e	filter bandwidth of analyser	2
c′		damping per unit length	1
c	a,s	non-dimensional damping coefficient	1
c		constant in coherence equation	4
C	D_o	surface drag coefficient	4
C	F	force coefficient	1
C(n)		co-incident spectral density function	2
d		zero-plane displacement	4
d		distance downstream from bi-planar screen	4
D		length parameter of structure, usually width of face	1
E		Hot-wire anemometer out-put voltage	2
f	D,H,K	non-dimensional frequency parameter of Davenport, Harris & Kaimal	4
f	S	analogue to digital sampling rate	3
f	N	Nyquist frequency	3
f(t)		fluctuating component of force	1
f(η)		relative horizontal displacement of structure at height η (=z/h)	5
F(t)		aerodynamic force per unit length	1
G(n)		single-sided power spectral density	2
h		height of structure	5
h(τ)		transfer function	2
H(n)		Fourier transform of h(τ)	2
i		counter	3
I		mass moment of inertia	5
I		turbulence intensity	4
j		$\sqrt{-1}$	

Symbol	Suffix	Description	Chapter
k		von Karman's constant ($\simeq 0.4$)	4
k'		stiffness per unit length	1
k	a,s	non-dimensional stiffness coefficient	1
K		kurtosis	3
l		no. of points for frequency averaging	3
l	D	Davenport's length scale of turbulence	4
	H	Harris's length scale of turbulence	4
L	x	integral length scale of turbulence	4
m		modal mass per unit length	1,5
n		frequency (Hz)	
n	0	natural frequency of structure	1
n	*	cut-off upper frequency of tape recorder	3
n	c	carrier frequency of tape recorder	3
n	max	anticipated maximum frequency of the signal	3
n	L	low-pass filter frequency point	3
n	i	intercept frequency point on Kaimal spectrum	4
$\tilde{n}$		reduced frequency, $nD/\bar{U}_{REF}$	1
N		number of digitised values in a frame of data	3
p		exponent in H.W.A. calibration	2
p(x)		probability density function of x	2
P(x)		probability density distribution of x	2
q		number of frames for ensemble averaging	3
Q(n)		quadrature spectral density function	2
r		ratio of speed variation ($= R_p / R_r$)	3
R(τ)		correlation coefficient at time lag τ	2
R	p	play back speed of tape recorder	3
R	r	recording speed of tape recorder	3
S(n)		double-sided power spectral density	2
S		skewness	3
t		time	
t		thickness of the flat in torsion bar	5
T		absolute temperature	4
T		observation time (or record length)	
T	x	integral time scale of turbulence	4

Symbol	Suffix	Description	Chapter
u,v,w		fluctuations of the wind velocity in the x,y,z direction	
u	*	friction velocity ($=\sqrt{\tau_0/\rho}$)	4
u	G	gradient wind speed	4
U	i	instantaneous wind velocity	
U	r	reduced wind velocity ($= \bar{U} / nD$)	1
$\bar{U}$		mean wind velocity ($= U_i - u$)	4
U(z)		horizontal wind velocity at height z	4
W	x	data width for probability distributions	3
x,y,z		Cartesian co-ordinates	
x		static component of x-data	2
x(t)		fluctuating component	2
X(t)		time varying data	2
X n)		Fourier coefficient of x(t)	3
z		height above the ground	4
z	G	gradient height	4
z	x	normalised value of x(t) with zero mean and unit variance	2
z	0	roughness length	4

Greek symbols:

α		exponent in velocity profile; angle of incidence	
δ	a,s	logarithmic decrement (log. dec.) of damping	
δt		digital sampling interval	3
δn		resolution bandwidth	3
δ_n	Q	half-power bandwidth	
ϵ		measurement error	2
ψ^2		mean square value	2
γ		lapse rate	4
$\gamma^2(n)$		coherence function	2
λ	u	micro-scale of turbulence	4
ν		dynamic viscosity of air	4
η	x	deflection / diameter ratio (= x/D)	1
η		normalised height (= z/h)	5
ρ	a,s	density, air and structural	1
$\rho(\tau)$		correlation coefficient at time lag τ	2

Symbol	Suffix	Description	Chapter
σ		standard deviation	1
σ^2		variance	1
τ		lag time	2
τ	0	shear stress at surface	4
$\theta(n)$		phase angle	2
ω		radial frequency ($= 2\pi n$)	1
$\chi(n)$	a,m	admittance	1
ξ		critical damping ratio	1

Suffices:

r.m.s.	root-mean-square
d.c.	direct current
full	full-scale
model	model-scale
a	aerodynamic
s	structural
m	mechanical

I. INTRODUCTION

I.1 General

Until the beginning of this century the mechanisms of destruction of structures (eg, buildings and bridges) by the action of wind were not understood. Destruction was attributed to the will of a deity and, as such, was presumed to be beyond the understanding of mortals. During this period, there were some very dramatic, wind-induced collapses of structures, notably the destruction of a chain pier at Brighton in 1836, the collapse of Telford's original suspension bridge over the Menai Straits in 1839 and the Tay Bridge disaster in 1879. It was in 1940, after the collapse of the Tacoma Narrows Bridge as a result of oscillations caused by a wind of 19 m/sec, that serious attention was given to wind-loading.

The failure to understand wind-induced phenomena can be partly attributed to the lack of instruments capable of measuring the dynamic or fluctuating effects, although static wind-effect measurements had been made. For example, Baker [1] in 1884 and Stanton [2] in 1925 measured static wind-loads on the Forth and Tower bridges, respectively.

A significant development, before the Tacoma Bridge disaster, was the construction of the Empire State Building. When it was realised that wind-forces might be important, an attempt was made to determine these effects [3]. These tests, and a subsequent investigation by Rathburn [4], produced the important conclusion that 'natural wind movements are not at all like those in a wind tunnel'.

Modern methods of design and fabrication of tall structures tend towards lighter weights and more lightly damped structures. Buildings are also higher and therefore exposed to stronger winds, resulting in an increase in the likelihood of destruction or unacceptable vibrations during adverse conditions of wind. One example is the collapse of three

cooling towers at Ferrybridge power station in November 1969 [5]. The emergence of congested urban areas has also led to an increase in large-scale destruction by wind. During gales in November 1962, nearly two-thirds of the 161,000 houses in Sheffield were damaged [6]. Rare wind conditions, also cause urban areas considerable loss of life and property, for example, the damaged caused by Hurrican Tracy over Darwin [7].

To combat such damage, various codes have been written for designers. Osipovich [8] has shown, however, that even though many structures are designed according to specified codes of practice, failures still occur.

In a survey of press-cuttings, Menzies [9] has shown that for the period 1962-1969, an average of 100 000 buildings a year are damaged by wind in Britain, costing £7 million in repairs and replacements.

It is therefore necessary to revise these codes continuously, and to make this revision possible, research into wind and structure interactions must be done.

I.2 Formulations of the Problem

In examining the effect of wind on structures, the 'correct' understanding of such effects can be obtained only through full-scale tests. Though many researchers do make full-scale measurements [10], it is not always feasible to do so. The main problem occurs during the design stage, when a good estimate of the performance characteristics of the prototype is required.

Model-testing, however, gives a more flexible approach to the final design. Changes can be made during the design stage so that an

titiotimum design decision can be taken. The confidence placed in the model tests
lllllll depend on the extent to which similarity requirements between model and
l-sıull-scale tests are satisfied. Since not all requirements can be met simultaneously
-scsonfidence in the tests will depend on the choice of scaling parameters known to
fidvave significant influence on the performance of the prototype.

n thn the present work, the dynamic response of a square cross-sectional prism of
d-tıspect ratio (R) 8 to a generated boundary-layer wind was investigated in the
-t dwind-tunnel. The square prism was modelled on an existing prototype. Since
onmsome data on the vibration characteristics of the prototype were available,
nitinitial checks on the modelling procedure were possible so that some confidence
Nɔccould be placed in correlating model response with that of the prototype.

ɛyliFor the purposes of comparison, tests were also made on a circular, thin-walled
ylı cylinder having the same R , mass moment of inertia and stiffness as the
ɛquı square cylinder.

st Most workers, engaged in similar research, have not allowed their models to vibrate in the along-wind (ie in-line) direction but have given them freedom only in the cross-wind (ie lateral)direction. Neglect of the in-line vibration is justified on the premise that the in-line fluctuating component is much smaller than the corresponding lateral component [76]. An investigation by Lee[11]on the wind-induced vibration of a pair of model stacks showing that, in certain conditions, coupling between the two components can take place. A major object of the present investigation therefore, was to determine whether the behaviour of a model, constrained to one degree of freedom (DOF) ie lateral vibration only, showed vibration characteristics different from those obtained with two DOF when both in-line and lateral vibration was allowed.

o thTo this end, a system of gimbals and supports was designed and constructed.
rieoModels mounted on the gimbals were able to vibrate in two mutually perpendicular
ireodirections. It was also possible to suppress motion in any one direction.
irrThis allowed comparisons to be made between models vibrating with one DOF and
regitwo DOF. The gimbal consisted of a system of torsion-bass, strain-gauged to
rwo give a measure of the dynamic and static deflections in the two directions
ive considered.

In order to achieve a good representation of full-scale conditions, a simplified
In model of the natural wind was generated, as accurately as possible, in a
del wind-tunnel using a combination of flow-mixing devices.

Signals obtained from the various transducers monitoring the fluctuations of wind and vibrations of models required random signal analyses. At the beginning of this investigation, only very limited facilities were available to analyse the data obtained. A considerable amount of time therefore had to be spent in setting up a system capable of acquiring, reducing and analysing random signals. A complete description of the initial requirements and final design, implementation and running of this data-analysis sytem is given.

I.3 Structural Response to Wind Effects

Wind effects on structures can be considered under the following headings [12]:

(a) Time-averaged mean loads.

(b) Response to the fluctuating forces caused by the turbulence of winds, i.e. the direct forcing of an elastic structure by wind flunctuations.

(c) Oscillating and divergent instabilities caused by wind.

For buildings and structures where the design considerations may concern over-turning instability or, more probably, wind pressure on the cladding, knowledge

of (a) is often inadequate and (b) and (c) become more important for slender, lightly-damped structures.

The problem of steady wind-loading is well documented [13] and will not be considered further here. Dynamic wind-loading will be discussed next.

3.i. The Direct Forcing of a Structure by Turbulent Wind

The direct forcing of a structure can be caused by the turbulence of the wind or because it is buffeted by the wake flow of another structure, as in the Tacoma Narrows Bridge disaster [14]. The random excitation of a structure cannot be analysed deterministically. Statistical concepts must be used. Davenport [15] extended the work of Liepmann [16] on the application of statistical concepts to buffeting. An outline of Davenport's procedure [17] is as follows:

Three assumptions were made to simplify the problem:

(a) The structure is elastic and its response $x(t)$ to fluctuating forces $f(t)$ can be expressed by a familiar linear differential equation.

(b) Mean aerodynamic force is the same in fluctuating flow as in a steady flow having the same mean velocity.

(c) Fluctuations in aerodynamic forces are linked to the fluctuations in velocity through a linear process, where velocity fluctuations are not large compared to the mean flow.

Having made these assumptions, the relation between the statistical properties of the response and these other properties of the structure are explored:

(a) Mean response

(b) Probability distribution of the response amplitudes

(c) The spectrum of the response

The first consequence of the linear relationship between velocity, force and response, coupled with the Ganssian distribution of fluctuating velocity, is that the probability distribution of both force and response are also Gaussian. To define this particular type of distribution, all that is required is knowledge of the standard deviation, σ. This can be found from the spectrum, the area under which is equal to the variance, σ^2.

The second consequence is that the spectra of the response and force can be found from the velocity spectrum using the 'admittance functions', ie, the 'aerodynamic and mechanical admittances'. These functions express the mean square amplitude of the output of a process having a sinusoidal input of unit mean square amptitude, as a function of the input frequency. Mechanical admittance can be written:

$$\left|\chi_m(n)\right|^2 = \frac{1}{\left(1 - \frac{n^2}{n_0^2}\right)^2 + 4\xi^2 \frac{n^2}{n_0^2}}$$

(where n_0 is the natural frequency of the system and ξ is the critical damping ratio, $c/2\sqrt{km}$).

The aerodynamic admittance, showing the fluctuation in aerodynamic force associated with unit fluctuation in velocity at a point, is less familiar and more indeterminate. It is expressed as [17]

$$\left|\chi_a(\tilde{n})\right|^2 = C_F^2(\tilde{n}) / C_F^2(0)$$

where $C_F = \bar{F} / \frac{1}{2} \rho_a A \bar{V}_{ref}^2$ is the steady flow aerodynamic coefficient and where $\tilde{n}$ is the reduced frequency, $nD / \bar{U}_{ref}$).

The normalised spectrum of the response can be written:

$$\frac{n \cdot G_x(n)}{\sigma_x^2} = 4 \left|\chi_a(n)\right|^2 \left|\chi_m(n)\right|^2 \cdot \frac{n \cdot G_u(n)}{\sigma_u^2}$$

In lightly damped systems, in which the resonance peak is very pronounced,

$$\frac{\sigma_x^2}{\bar{x}^2} = \frac{\pi}{\beta} \left|\chi_a(n_o)\right|^2 \frac{n_o \cdot G_u(n_o)}{\sigma_u^2}$$

since it is generally found that the bulk of the variance consists of fluctuations at or near the natural frequency n_o [17].

3.ii. Mechanisms of Wind-induced Oscillations (Mainly 'Lateral') of Structures

There are a number of mechanisms by which a flexible structure can extract the energy from the wind-stream to set up and maintain oscillations, mainly in the the 'lateral' direction. Some of the most important forms of wind-induced oscillations are due to

(a) ovalling

(b) galloping

(c) vortex-excitation

(a) Ovalling is a form of vortex excitation (discussed below) which induces elastic deformatior of such structures as thin-walled circular stacks [18]. Here, elastic distortions of the sectional shape can be induced in a range of modes. The wind speed at which ovalling occurs are related to the frequency of shedding of discrete vortices from the cylinder, rather than to the frequency of shedding of pairs of opposite-handed vortices as for the transverse bending oscillations of cylindrical structures. This form of instability occurs only rarely and, since the present research was not concerned with 'ovalling' oscillation, it is discussed here only for the sake of completeness.

(b) Galloping is a self-excited oscillation of an elastic cylinder in a uniform transverse flow, in which the shape of the cylinder cross-section and its attitude to the incident stream cause flow separation and the formation of a broad wake. The resulting fluid forces and/or moments on the cylinder produce instability to small lateral or torsional displacements [19,20,21]. Oscillation occurs in a direction transverse ('lateral') to the wind but, unlike the vortex excitation (described below), there is generally no upper limit at which the oscillation dies out. The typical wind-speed for the onset of galloping depends on the structural damping but, for all practical values of damping, speeds are well above those for vortex shedding.

(c) Vortex excitation is the form most often encountered and can occur on a wide rage of bluff structural shapes from circular to square. Most oscillations on full-scale structures can be attributed to this.

Vortex-excited oscillations are generated by the periodic discharge of alternating vortices into the wake. The vortices, shed alternately from each side, are of equal strength but of opposite circulation. They give rise to an alternating 'lift' or cross-wind force tending to move the structure in a direction transverse to the wind-stream.

A simple idealised explanation for this oscillatory behaviour [22] is that, as an individual vortex is shed, a circulation is induced around the cylinder in the opposite direction to that of the shed vortex. This temporarily increases the velocity on part of the surface of the cylinder and decreases it on the other, both by the same amount. A difference in the surface pressure on the cylinder is therefore produced acting in a direction approximately across that of the flow. As the vortex passes downstream, its influence on the cylinder is reduced and the force decreases until another vortex is shed from the opposite side.

A force is then produced in a direction opposite to the previously induced force. The cross-flow fluctuation is therefore of the same fundamental frequency as that of the shedding of pairs of vortices. The fluctuating force is the cross-wind aerodynamic force.
Though the assumed one-to-one relationship between bending oscillations and vortex-shedding is common, it should be noted that there is a possible alternative [23], in which there is a three-to-one relationship. This would result in a lower critical wind speed.

The vortices shed from each side of the cylinder produce fluctuations of drag force in the 'in-line' direction. These have a predominant frequency equal to that of the shedding of individual vortices, and is equal to twice the frequency of the cross-flow force fluctuations[22].

If the structure is flexible and free to oscillate with a natural frequency, n_o then it would be expected that the tendency to oscillate would be most marked when the frequency of shedding of the complementary pairs of vortices, n_s, coincides with a natural frequency of oscillation. In general this is so, but it has been noted [24] that the representations of the cross-wind aerodynamic force as a sinusoidal forcing function cannot be reconciled with observation of the oscillatory phenomena because, for cetain speeds, and amplitude ranges, it is found that the motion of the cylinder controls the frequency of vortex-shedding.

One of the most important effects that structural movement has on vortex-shedding is to induce it to 'lock-on' [22]. As the flow speed past a lightly damped, flexible structure is increased from rest, the shedding frequency increases correspondingly. When the shedding frequency is close to, but below, the natural frequency of the structure, the amplitude can increase considerably (if the mass and damping are sufficiently low) as the

shedding locks on to the structure. A further limited increase in the flow speed has no effect on the shedding frequency, which remains equal to that of the structure.

As wind-speed increase through the 'capture' interval, the amplitude of oscillation rises to a peak before declining, when, in the case of a stationery cylinder, the shedding frequency at the same wind-speed is well above the structural frequency. The most important way in which 'locking-on' manifests itself is to increase the wind-speed range over which apprciable oscillations take place.

The phenomenon of capture of the vortex-shedding frequency by the cylinder vibrating frequency during oscillation is described by Ferguson and Parkinson [25] and Parkinson and Modi [26].

A simple mathematical model to explain how a structure oscillates in a wind stream with a linear displacement, η_y, (= y/D) normal to the direction of the wind-stream and to the spanwise axis of the body, has been proposed by Scruton and Flint [27].

When oscillations are sinusoidal

$$\eta_y = \eta_{o.y} \sin \omega_o t$$

where $\omega_o = 2\pi n_o$ is the natural frequency of the structure

The aerodynamic force per unit length of the body, written to include components in phase and out of phase of motion is

$$F(t) = \rho_a . U^2 D (a_1 \sin \omega_o t + a_2 . \cos \omega_o t)$$

$$= k'_a . y + c'_a . \dot{y}$$

i.e. $k'_a = \rho_a . U^2 . a_1$ and $c'_a = \rho_a U^2 a_2 / \omega_o$

or in a non-dimensional form

$$k_a = \frac{k'_a}{\rho_a . D^2 . n_o^2} = U_r^2 . a_1 \quad \text{and} \quad c_a = \frac{c'_a}{\rho_a . D^2 . n_o} = U_r^2 . \frac{a_2}{2\pi}$$

where k_a is the non-dimensional stiffness coefficient, c_a is the non-dimensional damping coefficient and $U_r \left(= U/n_o D\right)$ is the reduced velocity.

c_a is called the non-dimensional damping coefficient because it can be shown [27] that

$$c_a' = 2 m n_o \delta_a$$

where the body of mass, m, per unit length has a logarithmic decrement of damping (log. dec.), δ_a.

Hence $$c_a = 2m.\delta_a/(\rho_a.D^2)$$

Similarly, it was shown that

$$k_a = \frac{4\pi^2 m}{\rho_a D^2}\left(1 - \frac{n_o'^2}{n_o^2}\right)$$

where the suffix ''' denotes <u>in-vacuo</u> conditions.

For a simple spring-mass damping system in an air-stream, the equation of motion is

$$m\ddot{y} + (c_s' + c_a')\dot{y} + (k_s' + k_a')y = 0$$

where the suffices 'a' and 's' denote aerodynamic and structural values, respectively.

During instability in single degree-of-freedom motion, for

(i) $c_a' = c_s'$, oscillations will be maintained.

(ii) $c_a' + c_s' > 0$, response will be random-amplitude, constant frequency motion [12].

and (iii) $-c_a' > c_s'$, (ie, aerodynamic excitation), oscillations will grow in amplitude until structure fails or equilibrium is obtained because of non-linearities in the system or in the aerodynamic force.

The frequency of motion is

$$n_o = \frac{1}{2\pi}\sqrt{\frac{k_a' + k_s'}{m}}$$

For most structures, it has been found [24] that,

(i) oscillations usually take place at a frequency close to a natural frequency, indicating that k'_a is small compared to k'_s.

(ii) therefore wind has little effect on the frequency of oscillation, thus giving $n_o = n'_o$.

I.4. Review

4.i. General

Nearly all building shapes are classified as bluff bodies and they have pressure distributions distinctly different from streamlined bodies [28]. The distinguishing property is the broad wake of separated flow surrounding the rear part of the body. The flow approaching the body is deflected by the front-facing surfaces but separates from the surface completely at a sharp edge. Because of shear along the edge of the wake, a return flow towards the body is induced in the centre of the wake.

Due to this separation, sharp-edged structures give rise to vortex shedding. Therefore, polygonal sections, immersed in a fluid, may be subject to vortex excitation or galloping.

Scruton [24], analysing the vibrational characteristics for regular polygonal sections, found that vortex excitation was always present but varied in degree with the number of sides and the inclination of the wind. From tests on sections with 4, 6, 8 and 12 sides, he found that the strongest vortex excitation was experienced by the square section with the wind normal to a force ($\alpha = 0^\circ$) while the weakest was experienced by the hexagonal section, again with $\alpha = 0^\circ$. The galloping excitation occurred for a limited range of wind inclination and disappeared entirely when tests were made on a circular section.

he ahe ability of a sharp-edged bluff body to exhibit both vortex excitation and
quigalloping excitation is shown in the stability diagram, Fig. 1.1 for a
tqqsquare-section prism in smooth flow [24]. A region of instability caused
by vby vortex-shedding begins at a reduced wind speed, $V_r = 6$, for a variety of
uctstructural damping values. This instability persists over a range of wind
ppespeeds but this range decreases with increased structural damping. For wind
spoespeeds above this range, stability is maintained until the critical wind
oes; speed for the onset of galloping instability is reached.

The The vibrational characteristics of sharp-edged bluff bodies under aerodynamic
The excitation depend on many factors, but mainly on the structure of the fluid flow. We shall now review some of these effects. For corresponding static effects on stationary cylinders, the reader is referred to an excellent review article by Bearman [29].

4.ii. Effect of Various Parameters on the Vibrational Characteristics of Square-section Prisms

(a) Reynolds Number

Smith [21] has investigated the effect of Reynolds number on the lateral response of a square-sectional prism, placed in a smooth wind-stream and free to oscillate in a cross-wind direction. According to Smith, there is a significant variation of the lateral force coefficient with Reynolds number for the Reynolds number range ($2.2 \longrightarrow 6.6 \times 10^4$) considered. Examination of his results does not, however, show any of these 'significant' deviations.

(b) Turbulence

Significant differences in model response have been obtained for tests conducted in smooth, uniform velocity and turbulent boundary layer flows [30].

Fig. 1.2 given by Davenport and Isyumov [30] shows a comparison
etwebetween the dynamic response of a lightly damped (δ_s = 0.063) square,
twe;prismatic building shape model (h/D = 7) in a uniform-velocity flow and in
risma turbulent boundary layer is to reduce, or completely eliminate, the
vor vortex-shedding peak found in the lateral response in a smooth uniform flow.
lte The resulting lateral response increases monotonically with amplitude
ope proportional to a power of velocity slightly greater than 2.

The dynamic response in the logitudinal direction, normally quiescent in smooth uniform flow, is also found to increase monotonically with velocity in a turbulent boundary-layer flow.

Results obtained by Whitbread and Scruton [31] also confirm this difference between the shape of the response curve in smooth flow and in turbulent flow. In smooth flow the curve is peaked, typical of a discrete or narrow-band excitation whereas in turbulent flow there is a steady increase in amplitude with wind speed, indicative of random-forcing over a wide frequency spectrum.

A further effect is the reattachment of separated boundary layers in turbulent flow [32], a phenomenon which would not normally occur in smooth-flow conditions. This can have the effect of reducing any wake-induced instability by reducing the width of the wake [33].

(c) Damping

The effect of damping on the vibration characteristics can be seen by referring to the stability diagram of Fig. 1.1.

From the results obtained from a series of wind-tunnel tests to determine the response of a square-section tower to both turbulent shear flow and smooth uniform flow, Whitbread [33] notes that:

> 'there is a dependence of the peak amplitude on the inverse ratio of structural damping which, again, characteristic of smooth-flow response data, is not apparent in the turbulent flow results. In fact, considerably more structural damping is required with turbulent flow to achieve the same relative reduction in amplitude than in smooth flow.'

II - ANALOGUE DATA AND ITS ANALYSES

Most of the information had to be obtained in the form of raw analogue signals from various transducers. These signals, without exception, were random in nature, although some had strong periodic characteristics.

The first section of this chapter describes the measurements made, the transducers used to acquire the analogue signals, and the devices used to record some of these signals for subsequent off-line analysis.

Section 2 reviews and describes the concepts needed for analysis of random signals so that reference can be made to them in later chapters. Descriptions will be brief as the concepts are standard tools of the trade, and are discussed exhaustively in the references which are cited.

The third section deals with the analogue instruments used to analyse the signals and the limits imposed on the analysis by these instruments.

II.1. Acquisition and Recording of Experimental Data

The signals, produced in the experiments, fall into two distinct catagories, narrow-band random or wide-band random.

The narrow-band random signals were generated by strain-guage transducers (Section V.2.ii.b), monitoring the mainly resonant responses from the oscillating models in the generated boundary layer. The dominant frequencies of these signals were all near 10 Hz.

Hot-wire anemometers measured the structures of the generated boundary-layer flow and also the wake behind the models. Signals obtained from the anemometers showed (Section VI.3.iv) characteristics similar to wide-band random noise [34]. Analysis of these signals were made in the frequency range DC to 1 kHz. The upper frequency limit was choosen for two reasons (a) the energy contained by the eddies in the flow-field was minimal (Section VI.2.) above the 1 kHz upper limit and (b) it was decided that, in the generated boundary layer, simulating the low-frequency energy content of the atmospheric boundary layer was more important. A two-directional mechanical traverse (Fig. 2.1) was built to mount the hot-wire anemometers for wake measurements.

1.i. Data Acquisition

(a) Strain-gauge Output for Cylinder Oscillations

The cylinders under test were mounted on a system of gimbals designed so that the models were free to vibrate in any two orthogonal directions. The directions that were choosen were lateral to (cross-wind) and in-line with (along-wind) the incident wind.

The supports for the gimbals were strain-gauged. The resistive elements of the strain-gauges were then connected to circuit elements in the

in the amplifier and demodulator units of an SE-Laboratories carrier-amplifier system (Appendix A) to form bridge networks. Any movement of the cylinders caused the resistances of the strain-gauges to change and put the bridge network into an out-of-balance state. Because of this, the amplifier units produced a voltage proportional to the movement of the models.

(b) Measurement of Fluctuating Wind Velocities

The turbulent structure of the air-flow incident on the model and the wake behind the models was determined by using constant-temperature hot-wire anemometers. These transducers were choosen for their very desirable characteristics in measuring turbulent air-flows, notably [35],

(a) their smallness (thus interfering only minimally with the air flow),

(b) the good frequency response of the sensing element, making it possible to measure turbulence characteristics up to the required upper frequency limit of 1 kHz.

Hot-wire anemometers manufactured by DISA Electronik (Appendix A) were used. For measurements, straight hot-wire anemometer probes DISA 55F31 were used.

All of these probes were calibrated on a low intensity of turbulence, (< 1%), DISA calibration rig, 55 D42 (Appendix A) and in the range of the mean velocities used in the experiments.

During calibration (Appendix 2.A), it was shown that the output voltage, E, of the hot-wire anemometer was related to a mean wind velocity so that a second order equation

$$E^2 = a_1 + a_2 \cdot U^p + a_3 \cdot U^{2p}$$

gave a better fit to the calibration data than the more conventional.

$$E^2 = a_4 + a_5 \cdot U^p$$

All the hot-wire anemometer data was reduced using the second-order equation.

(c) Reference Velocity Measurement

A reference mean-velocity of the generated boundary-layer wind was measured with a pitot-static probe at a point (480, 230, 480mm). The origin of this co-ordinate system was positioned at the centre of the station where the models were placed (Fig. 4.5.).

The pitot-static probe was connected to a Furness Electronic Manometer (Appendix A) with plastic tubing. The electronic manometer was calibrated previously against a Casella manometer. The dynamic pressure of the incident wind, given in mm of water pressure, was then read directly from a built-in scale (or taken out as a voltage proportional to the scale reading). The dynamic pressure reading was then corrected for ambient temperature and pressure at the time of measurement to give the true wind speed.

(d) Mean-velocity Profile Measurements

The mean-velocity profiles of the generated boundary layers were determined with the use of a pitot-rake (Fig. 2.2), connected with plastic tubing

to a multi-tube manometer. Using as a reference the static pressure at the top of the generated boundary-layer, dynamic pressures at each measuring point were obtained, and the profiles then plotted.

1.ii. Data Recording

The acquired analogue data were recorded in different ways. The reference velocity measurements (Section (c) above) and mean velocity profile measurements (Section (d) above) were usually quite steady, and their values were recorded manually.

The hot-wire anemometer and the strain-gauge signals had some of their basic properties (eg mean and rms) evaluated on-line using analogue devices. For more complex data analysis (Section II.2), off-line analysis was necessary and the signals had to be recorded.

The anemometer and strain-gauge signals were recorded on a Sangamo-Western 3500 Magnetic Tape recorder (Appendix A). Six out of 14 channels were available for simultaneous record/replay. More details of the tape recorder is given in Section III.1.

An ultra-violet (UV) trace recorder (Appendix A) was also used to record the damped oscillations of the models when initially displaced and then allowed to oscillate freely in still-air conditions.

This was the procedure used to measure the damping characteristics of the models from their trace readings (Section VII.1.i).

II.2. Description of Random Data

Time varying data fall into either of the two classes, deterministic or random.

Deterministic data can be represented by an explicit mathematical term. Random data, on the other hand, has no explicit mathematical relationships but may be dealt with on a statistical basis. A random process may be either stationary or a non-stationary process, the definition of stationarity being that all statistical properties are invariant with time. A sub-set of stationary data, ergodic data, occurs when time-averages of individual records from the same process are the same for all records.

Three basic catagories of functions are generally available for analysing random data, though it is not necessary to use all of them at any one time. These three are, amplitude, time and frequency. Frequency domain and time domain information are interchangeable but each can highlight a particular facet of random signals.

2.i. Amplitude Domain

(a) Basic Properties

Physical data, X (t), can be thought of as a combination of a 'static' or time-invariant component, $\bar{x}$, and a'dynamic' or fluctuating component, x (t).

Assuming that a random process x (t) is stationary, the static component may be described by a time-average, ie a mean value $\bar{x}$ given by,

$$\bar{x} = \lim_{T\to\infty} \frac{1}{2T} \int_{-T}^{T} X(t).\,dt \qquad (2.1.a)$$

If only a finite portion of the record for $t_1 \le t \le t_2$ is available then

$$\bar{x} = \frac{1}{t_2 - t_1} \int_{t_1}^{t_2} x(t).\,dt \qquad (2.1.b)$$

The intensity of random data can be described by the mean-square value

$$\psi_x^2 = \lim_{T\to\infty} \frac{1}{2T}\int_{-T}^{T} x^2(t).dt \qquad (2.2.a)$$

or for finite records

$$\psi_x^2 = \frac{1}{t_2 - t_1}\int_{t_1}^{t_2} x^2(t).dt \qquad (2.2.b)$$

The dynamic component may be described by the variance

$$\sigma_x^2 = \lim_{T\to\infty} \frac{1}{2T}\int_{-T}^{T} \left[x(t) - \bar{x}\right]^2 .dt \qquad (2.3)$$

or for finite records by

$$\sigma_x^2 = \frac{1}{t_2 - t_1}\int_{t_1}^{t_2} \left[x(t) - \bar{x}\right]^2 dt \qquad (2.4)$$

$$= \frac{1}{t_2 - t_1}\int_{t_1}^{t_2} \left[x(t)\right]^2 dt$$

Expanding Eqn 2.4 shows that,

$$\sigma_x^2 = \psi_x^2 - \bar{x}^2 \qquad (2.5)$$

(b) Probability Density Functions (PDF)

Considering a sample time-history record x (t), the probability that x (t) assumes a value within the range between x and (x+ δx) may be obtained by taking the ratio of T_x/T, where T_x is the total amount of time that x (t) falls inside the range (x, x+δx) during the observation time T.

For small δX, a probability density function, p (x), can be defined as,

$$p(x) = \lim_{\delta x\to 0} \frac{1}{\delta x}\left[\lim_{T\to\infty}\left(\frac{T_x}{T}\right)\right] \qquad (2.6)$$

The probability distribution function P(X) is then defined as,

$$P(x) = \int_0^x p(x) \cdot dx \qquad (2.7)$$

(c) Moments of a Probability-Density Distribution

In general, the r^{th} moment about the origin for a random signal is given by,

$$\psi_r(t) = \lim_{T \to \infty} \frac{1}{2T} \int_{-T}^{T} \left[X(t) \right]^r \cdot dt \qquad (2.8)$$

or for a finite record,

$$\psi_r(t) = \frac{1}{t_2 - t_1} \int_{t_1}^{t_2} \left[X(t) \right]^r \cdot dt \qquad (2.9)$$

When r = 1 and 2, the mean value and the mean square value of the signal respectively are produced and are referred to as the first and second moments of x(t). These two moments form a larger set of moments ($r \geqslant 1$), the first-order statistics of x(t).

(d) Gaussian (Normal) Distribution

Random data, x(t), usually has an amplitude probability density distribution of the form

$$p(x) = \frac{1}{\sqrt{2\pi} \cdot \sigma_x} \cdot \exp \left\{ \frac{- \left[x(t) - \bar{x} \right]^2}{2\sigma_x^2} \right\} \qquad (2.10)$$

which is called the Gaussian (or Normal) distribution.

Standardising Eqn 2.10 with zero mean and unit variance gives

$$p(\zeta_x) = \frac{1}{\sqrt{2\pi}} \cdot \exp \left(-\zeta_x^2 / 2 \right) \qquad (2.11)$$

where

$$\zeta_x = \frac{X(t) - \bar{x}}{\sigma_x} = \frac{x(t)}{\sigma_x}$$

If moments of $x(t)$ are considered about the mean such that

$$\mu_r = \frac{1}{t_2 - t_1} \int_{t_1}^{t_2} \left[x(t) \right]^r dt$$

and if μ_r is normalised by σ_x^r such that, $\alpha_r = \mu_r / \sigma_x^r$

then the first moment, $\alpha_1 = 0$

and second moment $\alpha_2 = 1$

For a Gaussian (or Normal) distribution, the 3rd moment, the 'skewness' factor can be shown [37] to be equal to zero. Thus, according to whether $\alpha_3 \gtrless 0$, the distribution is left or right-skewed. The 4th moment, the 'kurtosis' factor, can be shown [37] to have a value 3.0 for a Gaussian distribution. If $\alpha_4 \gtrless 3$, the distribution curves are more peaked or are relatively flat with respect to the distribution, $\alpha_4 = 3$.

(e) Probability Theory for Two Random Variables

The joint probability density function of two random sample records, $x(t)$ and $y(t)$, describes the probability that both sample records will simultaneously assume values within some defined pair of ranges, $X < x(t) < X + \delta X$, $Y < y(t) < Y + \delta Y$ at any instant. The principal application of this measurement is to establish a probabilistic description of an event which is associated with two sets of random data.

If $T_{x,y}$ is the total amount of time that the signals fall within these ranges during an observation period T, then the joint probability density function is defined by

$$p(X,Y) = \lim_{\delta X \to 0} \lim_{\delta Y \to 0} \frac{1}{\delta x \cdot \delta y} \left[\lim_{T \to \infty} \frac{T_{xy}}{T} \right] \qquad (2.12)$$

If both $x(t)$ and $y(t)$ are normally distributed, then it can be shown [37] that the joint density function of each is

$$p(x,y) = \frac{\exp.\left\{-\frac{1}{2}\left(z_x^2 - 2.\rho_{xy} z_x . z_y + z_y^2\right)\right\}}{2\pi . \sigma_x . \sigma_y \sqrt{1-\rho_{xy}^2}} \qquad (2.13)$$

where ρ_{xy} is the correlation coefficient relating $x(t)$ and $y(t)$ and is defined as

$$\rho_{xy} = \frac{\sigma_{xy}}{\sigma_x . \sigma_y} \qquad (2.14)$$

and satisfies the condition, $-1 \leq \rho_{xy} \leq 1$

σ_{xy} is the co-variance of $x(t)$ and $y(t)$ and is a measure of the way $x(t)$ and $y(t)$ vary together. It is defined as,

$$\sigma_{xy} = \frac{1}{t_2 - t_1} \int_{t_1}^{t_2} x(t) . y(t) . dt \qquad (2.15)$$

For a bi-variate normal distribution, two variables are independent only if $\rho_{xy} = 0$ [37].

If $z_x(t)$ and $z_y(t)$ are normally distributed, ie,

$$p(z_x) = \frac{1}{\sqrt{2\pi}} \exp\left(-z_x^2/2\right) \qquad (2.16)$$

and

$$p(z_y) = \frac{1}{\sqrt{2\pi}} . \exp\left(-z_y^2/2\right) \qquad (2.17)$$

and are also uncorrelated to one another, then Eqn 2.13 reduces to the form

$$p(z_x, z_y) = p(z_x) . p(z_y) \qquad (2.18)$$

$$= \frac{1}{2\pi} . \exp\left[-\left(z_x^2 + z_y^2\right)/2\right] \qquad (2.19)$$

This is the bi-variate normal distribution expressed in its simplest terms. It is 'bell-shaped' and solid, formed by the revolution of the normal distribution about the y axis. A contour plot in the x-y plane is a series of concentric circles with the origin as centre.
When the variates are correlated, the above equation no longer holds. The joint probability distribution will then not have its principal axes parallel with the co-ordinate axes.

2.ii. Time Domain

(a) Auto-correlation

The auto-correlation function of random data describes the general dependence of the values of the data at one time on the values at another time. If the observation time $T \to \infty$, then an exact value for the auto-correlation function, $R_{xx}(\tau)$, will be approached, where $R_{xx}(\tau)$ is defined

$$R_{xx}(\tau) = \lim_{T\to\infty} \frac{1}{T} \int_0^T x(t) \cdot x(t+\tau) \cdot dt \qquad (2.20)$$

The normalised form of the auto-correlation is the auto-covariance or the auto-correlation coefficient $\rho_x(\tau)$ given by

$$\rho_x(\tau) = \frac{R_{xx}(\tau)}{\sigma_x^2}$$

(b) Cross-correlation

Eqn 2.20 can be extended to obtain the cross-correlation function $R_{xy}(\tau)$ of two sets of random data to describe the general dependence of the values of one set of data on the other.

$R_{xy}(\tau)$ is then defined as

$$R_{xy}(\tau) = \lim_{T\to\infty} \frac{1}{T} \int_0^T x(t) \cdot y(t+\tau) \cdot dt \qquad (2.21)$$

and the cross-correlation coefficient is

$$\rho_{xy}(\tau) = R_{xy}(\tau) / \sigma_x \cdot \sigma_y .$$

2.iii Frequency Domain

(a) Power Spectral Density Function

The power spectral density function of random data describes the general frequency composition of the data in terms of the spectral density of its mean square value. The power spectral density function $S_x(n)$ of a time-record $x(t)$ is then defined as,

$$S_x(n) = \lim_{\delta n \to 0} \frac{1}{\delta n} \left[\lim_{T \to \infty} \frac{1}{2T} \int_{-T}^{T} x^2(t, n+\delta n)\, dt \right] \quad (2.22)$$

where δn is a bandwidth centred at a frequency, n.

If $x(t)$ is non-periodic, it can often be represented by the Fourier integral,

$$x(t) = \int_{-\infty}^{\infty} X(n) \cdot \exp(j 2\pi n t)\, dn \quad (2.23)$$

It has been shown [ ] that the power spectral density can be expressed in terms of the Fourier transform, $X(n)$, of the signal $x(t)$ as:

$$S_x(n) = |X(n)|^2 / 2T \quad (2.25)$$

by the use of Eqn 2.22 and Parseval's Theorem,

$$\int_{-\infty}^{\infty} x^2(t)\, dt = \int_{-\infty}^{\infty} |X(n)|^2\, dn \quad (2.24)$$

Since the double-sided function $S_x(n)$ is even and non-negative, the integration in Eqn 2.22 could be carried out from 0 to ∞, in which case the function under the integral becomes the single-sided function $G_x(n)$, so that

$$G_x(n) = 2 \cdot S_x(n) \quad (2.25)$$

While in practical systems, analogue equipment measures $G_x(n)$ the use

of $S_x(n)$ defined over $(-\infty,\infty)$ often simplifies the analysis during mathematical calculations.

An important property of the power spectral density function ties in its relationship with the auto-correlation function. This relationship, known as the 'Wiener-Khintchine' relation, shows [34] that the two functions are related by a Fourier transform of the form,

$$S_x(n) = \int_{-\infty}^{\infty} R_x(\tau) \cdot \exp\left[-j \cdot 2\pi n\tau\right] d\tau \qquad (2.26)$$

with $$R_x(\tau) = \int_{-\infty}^{\infty} S_x(n) \cdot \exp\left(+j \cdot 2\pi n\tau\right) \cdot dn$$

(b) Cross-spectral Density Function

The cross-spectral density function, $S_{xy}(n)$, can be expressed as the Fourier transform of the cross-correlation function, so that,

$$S_{xy}(n) = \int_{-\infty}^{\infty} R_{xy}(\tau) \cdot \exp\left(-j \cdot 2\pi n\tau\right) \cdot d\tau \qquad (2.27)$$

Because the cross-correlation is not an even function, the cross-spectral density function is generally complex number such that,

$$S_{xy}(n) = \left|S_{xy}(n)\right| \cdot \exp\left[-j \cdot \theta_{xy}(n)\right] \qquad (2.28.a)$$

$$= C_{xy}(n) - j \cdot Q_{xy}(n) \qquad (2.28.b)$$

Where the real part, $C_{xy}(n)$, is the co-incident spectral density function and the imaginary part, $Q_{xy}(n)$, is called the quadrature spectral density function.

Clearly, the magnitude, $$\left|S_{xy}(n)\right| = \sqrt{C^2_{xy}(n) + Q^2_{xy}(n)} \qquad (2.29.a)$$

and phase angle $$\theta_{xy}(n) = \tan^{-1}\left[\frac{Q_{xy}(n)}{C_{xy}(n)}\right] \qquad (2.29.b)$$

The physically realistic single-sided spectral density function corresponding to Eqn 2.25 is defined for $0 \leq n \leq \infty$ as

$$G_{xy}(n) = 2 \cdot S_{xy}(n) \qquad (2.30)$$

(c) Coherence Functions

The coherence function between the signals $x(t)$ and $y(t)$ is a real-valued quantity defined by,

$$\gamma^2_{xy}(n) = \frac{|S_{xy}(n)|^2}{S_x(n) \cdot S_y(n)} \qquad (2.31)$$

If $\gamma^2_{xy}(n) = 0$, the two signals are said to be completely incoherent at that particular frequency. If $\gamma^2_{xy}(n) = 1$, the two signals are fully coherent.

(d) Transfer Function

If $x(t)$ and $y(t)$ are the input and output signals of a linear system, then the frequency transfer function is defined by

$$H(n) = S_{xy}(n) / S_x(n) \qquad (2.32)$$

where $H(n)$ is the Fourier transform of $h(\tau)$, and $h(\tau)$ is defined by the relationship.

$$y(t) = \int_0^\infty h(\tau) \cdot x(t-\tau)\, d\tau \qquad (2.33)$$

II.3. Analogue Analysis of Signals

This section concerns the analogue methods by which the signals were measured to determine their various characteristics. The limits imposed by analogue-measuring system is discussed. The analogue analysing equipment is shown in Fig. 2.3.

3.i. Amplitude Characteristics

The mean DC level of the signal given by Eqn 2.1 should have been evaluated by using a true integrating digital volt-meter (DVM) which would have sampled the signal for a specific time interval. Though true integrators were on the market, only a RC (resistance-capacitance) type DVM, the DISA 55 D30 (Appendix A) was available for our work. In such an instrument, the signal is Resistance-Capacitive (RC) averaged as opposed to the true-averaging of the integrator. RC averaging is obtained by passing the signal through a low pass filter (RC-filter) and smoothing the signal.

Depending on the nature of the signal, various time-constants for smoothing the signal were available on the DVM. To obtain valid results the averaging time was usually at least three time-constants long.

The variance σ_x^2 given in Eqn 2.4 was evaluated using RC-averaging, rather than true averaging. For this purpose a DISA 55 D35 RMS voltmeter was used. Variable time constants were again available in order to damp fluctuations in the squared signal.

Bendat and Piersol [34] show that for the case of bandwidth-limited Gaussian white-noise, the statistical error of a mean value measurement obtained by true-averaging is given in terms of the normalised rms error ϵ by

$$\epsilon \simeq \frac{\text{s.d.}\left[\hat{\bar{x}}\right]}{\bar{x}} \simeq \frac{1}{\sqrt{2BT}}\left(\frac{\sigma_x}{\bar{x}}\right) \qquad (2.37)$$

where T is the record length, B is the bandwidth and $[\,\hat{}\,]$ denotes estimated value.

For mean square value measurements where $\bar{x} = 0$

$$\epsilon = \text{s.d.}\left[\hat{\psi}_x^2\right] / \psi_x^2 \simeq 1/\sqrt{BT} \qquad (2.38.a)$$

If the rms values are read (for $\bar{x}=0$) then

$$\epsilon \sim \text{S.d.}\left[\hat{\psi}_x\right]/\psi_x \simeq 1/\left(2\sqrt{BT}\right) \qquad (2.38.b)$$

In the case of true averaging, Bendat and Piersol have shown that ϵ can be minimised by using an averaging time which is equal to the length of the available sample record.

On the other hand, RC-averaging for a steady-state periodic signal produces an accurate measurement after a time interval equal to about three time constants. For stationary random signals, the measurements continues to fluctuate after the original rise. These fluctuations indicate the statistical error of the measurements at any instant of time. According to theory [34], the minimum error is achieved by using an infinite time-constant, which is impractical. Bendat and Piersol [34] have shown, however, that very little is to be gained by using an RC- averaging time constant longer than one sample record length (ie, the same as for true averaging).

Analogue analysis of the amplitude probability density functions of the signals was not attempted since no suitable instrument was available.

3.ii. Time Characteristics

From a sample time history record $x(t)$ of a stationary random signal, the auto-correlation function, $R_{xx}(\tau)$, of the signal is estimated from Eqn 2.20 to give

$$\hat{R}_x(\tau) = \frac{1}{T}\int_0^T x(t).\, x\,(t+\tau)\, dt \qquad (2.39)$$

for a record length T.

$R(\tau)$ was measured by using a DISA Time Correlation Analysis (TCA) system. The two signals to be correlated (the same signal for auto-correlation, two separate signals for cross-correlation) were fed to a DISA type 55D75 time delay unit (TDU) where they were prefiltered according to the delay range, τ secs. Time delay value could be set within five ranges from 0 $\rightarrow$ 0.1 msec to 0 $\rightarrow$ 100 msec. From the TDU, the signals were fed through pre-amplifiers in the DISA type 55D70 analogue correlator, where they were amplified or attenuated to a suitable level. From there, they were fed back into the TDU where one signal was delayed by time τ with respect to the other. Finally, these signals were fed to the analogue correlator for computation of the correlation function, $\hat{R}_x(\tau)$, or the correlation coefficient $\hat{\rho}_x(\tau)$. The time delay range in the TDU was set by a DC-voltage which controlled the delay clock. This voltage was generated externally by a DISA type 55B01 sweeps drive unit, capable of sweeping through the required range of voltage at a controlled rate. By driving the TDU and a Bryans XY plotter in this way, auto and cross-correlation functions were automatically plotted. Slowing of the time scale by a factor of 8:1 with the tape-recorder (Section III.2.ii.a) increased the range of time delays with a corresponding increase in the lower-frequency analysis time.

An advantage of the DISA analogue-correlator was that it contained circuits which compensated for changes in the statistical properties of the input signals during analysis. A ± 10% deviation in the rms value of one of the input signals causes, according to the manufacturers (Appendix A), a relative error of only ± 0.5% in the normalised correlation coefficient.

3.iii. Frequency Characteristics

In analogue measurements, it is the single-sided power spectral density that is required, and is estimated from Eqn 2.23 by

$$G_x(n) = \frac{1}{B_e . T} \int_0^T x^2(t) . dt$$

where B_e is the filter bandwidth used to estimate the energy content of the signal within this band.

To estimate the power spectral density of the analogue signals, a Bruel and Kjaer (B and K) type 16/2, 1/3 and 1/10 octave band-pass filter set was used in conjunction with a B and K type 2603 microphone amplifier. The filter-set was tunable over the range 20 Hz to 20 kHz and with the 8:1 speed change of the magnetic tape recorders, analysis down to 2.5 Hz was possible.

The variance of the filtered signal was required for the power spectral density estimate. The damping of the internal meter was found to be inadequate at the lower frequencies leading to significant variations in the values obtained at these frequencies. This was very noticeable during analysis of the turbulent wind-velocity spectra.

III DIGITAL ANALYSIS

As the equipment and techniques for measurement of random signals were being evaluated, it became clear that there would be many deficiencies in the analysis if only analogue techniques were used. There are a number of problems inherent in analogue analysis:

(i) Long periods of observation are required when RC-smoothing equipment is used.

(ii) It is difficult to obtain the characteristics of the low-frequency components of the signals.

(iii) The lack of a general-purpose apparatus makes difficult the measuring of the higher-order moments of amplitude distributions, probability density functions (single and joint), cross-power spectral density and coherence and transfer functions.

It was therefore decided that digital analysis would be preferable because it would make possible manipulation of data into the required form. Analogue measurements could be used subsequently to verify the results of the analogue analysis.

When the project began, there were no facilities at the City University for digital analysis of analogue signals. A considerable amount of time was therefore spent in developing a system which would perform this function. Computer time was available on the ICL 1905E digital computer and the EAI 690 hybrid computer system, both of which were housed some distance from the aerodynamics laboratory. The processing of the signals was therefore an off-line operation and some method of signal storage was required. The analogue signals were

recorded and stored on magnetic tape and a system was developed for the conversion of the recorded data from analogue to a digital form [36]. The digital data was then reduced using digital software programmes.

III.1. Recording and Storage of Analogue Data

The frequency-sensitive characteristics of 'direct-recording' places a low limit on the minimum frequency that can be satisfactorily recovered from a magnetic tape containing recorded analogue signals. This precludes the use of direct-recording tape-recorders when signal contain a DC component, and a frequency-modulating (FM) carrier system tape-recorder was therefore used.

A Sangamo-West 3500 FM magnetic tape-recorder (Appendix A) with the ability to record and reproduce 14 channels simultaneously was used. Only six were available during the experiments, but this was quite adequate. The Sangamo-West has six record speeds (47.6, 95.2, 190.5, 381.0, 762.0 and 1524.0 mm/sec), which permitted signals to be recorded from DC to an upper cut-off frequency n^* Hz, given by

$$n^* \sim \frac{n_c}{5} \cdot R_r$$

where n_c is the carrier frequency (= 70.87 Hz/mm.sec^{-1}) and R_r is the recording speed.

Two playback speeds, R_P, of 95.2 mm/sec and 762.0 mm/sec were available. By recording analogue signals at one speed and reproducing at another, a change in signal time-base was possible, which was very useful in the analysis of low-frequency signals. The importance of this is shown in Section III.2.ii.a.

MEMOREX tapes were used which were 355.6 mm in diameter, 25.4 mm wide and 2500 m long.

III.2. Data Preparation

To make possible a digital analysis of the analogue data produced during the experiments, it was necessary to devise a system for the conversion of analogue signals into a form acceptable to a digital computer. The Department of Aeronautics provided no system for analysing analogue data other than through analogue machines, and an extensive programme for conversion of the data was therefore required. This programme, referred to as digitization, is called an analogue to digital conversion (ADC) system.

The benefits derived from using the existing ADC units in the EAI 690 to digitise analogue records and from using the ICL 1905 to process the results were as follows:

(a) There was no capital outlay.

(b) The method of setting up an analogue to digital data analysis system which was derived will provide guidelines for subsequent users needing to adapt general systems for the analysis of random data.

(c) The computing power of large machines like the ICL 1905 is greater than that of the more purpose-built machines like the PDP or Honeywell processor.

2.i. Digitising Theory

Digitising comprises two separate and distinct operations: sampling and quantising. Sampling is the process of observing the values of

a signal at defined instants over a period of time. Quantising is the conversion of data values at the sampling points into numerical form [34].

(a) Sampling

Digital data collected during a test may be thought of as related to a hypothetical continuous function, x(t), defined for all 't' by the equation

$$x_i = x(t_0 + i.\delta t) \qquad (3.1)$$

where t_0 is the time sampling begins, and δt is the sampling interval.

When deciding on the sampling rate, $f_s (= 1/\delta t)$, care should be taken that the sampling is fast enough to avoid the problem of aliasing [34] which could constitute a source of error. At the same time, the sampling should not be so fast that it results in the production of useless information.

In aliasing, if a sinusoid of frequency higher than $1/(2.\delta t)$ Hertz is sampled at a rate of $1/\delta t$ samples per second, then the sinusoid will appear as a lower frequency. The frequency

$$f_N = \frac{1}{2.\delta t} = \frac{f_s}{2} \qquad (3.2)$$

is called the folding or 'Nyquist' frequency. For example, suppose that

$$x(t) = \cos 2\pi n t$$

and that

$$t = 1/(2.f_N)$$

then

$$\cos 2\pi n t = \cos 2\pi \left(2i f_N \pm n\right).\frac{1}{2f_N} = \cos\left(\frac{\pi n}{f_N}\right)$$

All the data at frequencies $2if_N \pm n$, therefore, will have the same cosine function as data at frequency n when sampled at points at intervals of $1/(2f_N)$. Frequencies in the data above $1/(2\delta t)$ will be folded back into the frequency 0 to $1/(2\delta t)$ and will be confused with the data in this lower range.

There are two practical methods of handling the aliasing problem [34]:

(i) Choose δt sufficiently small so that it is physically unreasonable for data to exist above the associated cut-off frequency, $f_N (= 1/2\delta t)$. If the maximum anticipated frequency is n_{max}, then

$$f_N \geq n_{max} \tag{3.3}$$

Enochson and Otnes [38] describe as a 'folk tale' the belief in the engineering profession that a sampling rate of five times the highest frequency to be observed is necessary for good, unbiased results. They suggest that this criterion is pessimistic and wasteful for most applications and say that a 2.5 sample per cycle gives excellent results. Thus

$$f_s = 2.5 \cdot n_{max} \tag{3.4}$$

so that

$$f_N = f_s/2 = 1.25 \cdot n_{max} \tag{3.5}$$

(ii) Filter data above the maximum frequency of interest so that the minimum value of f_N will be set by Eqn 3.2 as

$$f_N = n_{max} \tag{3.6}$$

The second method saves computing time and cost, but it is not physically possible to filter out all data above the maximum required frequency, f_N. For data such as wide-band random noise, therefore,

it is necessary to set a low-pass filter at n_{max} with maximum cut-off rate and then to sample the filtered signal at a sampling frequency given by Eqn 3.4.

(b) Quantising

ADC systems quantify analogue signals by looking at them through finite width windows or levels. The signal is then approximated to a value as it falls within a certain window. The accuracy of these approximations depends on how wide the windows are. For greater accuracy there must be a large number of these levels. Typical ADC systems produce 6 to 16 bits which correspond to a range of 64 (2^6) to 65,536 (2^{16}) levels. In the EAI 640 digital computer, used in this research, 13 bits are produced. The full range of signal is quantified at 8192 (2^{13}) scale units. Since the r.m.s. value of the quantification error (which may be considered as an r.m.s. noise on the desired signal) is [34]

$$\sigma_x \simeq 0.29 \text{ scale units}$$

the peak signal to r.m.s. noise was

$$\frac{8192}{0.29} \simeq 2.83 \times 10^4 \text{, ie } 90 \text{ dB}$$

The quantising error, as shown, is relatively unimportant, but care was taken to ensure that the signal the ADC receives covers the full quantising region so that resolution was good and errors insignificant.

2.ii. Analogue to Digital Conversion (ADC)

This section discusses the analogue to digital conversion of a voltage signal, first briefly and then in detail. The signal to be digitised were taken from the playback amplifier channels to signal conditioners

using screened output cables with BNC sockets. The signal conditioners then amplified and filtered the input signals and produced them in a form suitable for the analogue to digital conversion process. These modified signals were fed into an EAI 680 analogue computer using a patching panel. Control of the EAI 680 was directed through manual control of its console or indirectly through the EAI 640 digital computer. The EAI 680 and EAI 640 together formed the EAI 690 hybrid system, providing greater versatility, and enabled a software program processed in the EAI 640 to control the EAI 680 analogue system.

The EAI 640 and the ICL 1905, were linked by a British Standard Interface (BSI) [39]. The main object of the link was to give the EAI 640 greater computing power when it was being used as an integral part of the EAI 690 hybrid system.

The 640 computer consisted of a central processor, an 8K memory, a teletype controller, a high-speed reader and punch, and a BSI. The 1905 consists of a central processor, a 32K memory, a teletype controller, two high speed readers, a high-speed punch, a BSI, two exchangeable disc stores, two line printers, two card readers, and four magnetic tape units.

Each computer considered the central processor of the other as another peripheral, and any peripheral of one could be used by the other.

The hybrid system enabled a program stored in the EAI 640 to digitise the continuous signals supplied to the EAI 680. The link then sent the data over in a recognisable format to be stored as output on one

of the peripheral systems of the ICL 1905. This process is discussed in greater detail below.

(a) Transfer of the Signal Stored in the Magnetic Tape to the EAI 680 Analogue Computer

The data recorded at a speed R_r could be played back at a speed R_p (R_r and R_p are given in Section III.1). The ratio of the speed variation, r, given by

$$r = R_p / R_r \qquad (3.7)$$

is called time base compression when $r<1$, and time base expansion when $r>1$.

Expansion of the time base ($r>1$) enabled the frequency range of the data to be expanded so that low frequencies could be looked at in more detail. Similarly, when $r<1$, high frequency signals reappeared at a lower frequency and therefore high frequencies could be analysed more easily. Thus a sinusoid of frequency n in real time, on replay at a speed ratio r, appeared as a sinusoid of frequency n' given by

$$n' = r \cdot n \qquad (3.8)$$

When computing the power spectral density analysis, the resulting output needed to be multiplied by the speed variation, r. This is because the speed variation had itself increased ($r<1$) or reduced ($r>1$) the density of the data before the normalising process of dividing by band width.

Time-base compression or expansion can also be used as a technique for varying the effective resolution bandwidth, δn, of an analysis. If, for example, a resolution bandwidth of $\delta n = 1$ Hz is needed to

analyse a given sample record of data with an acceptable bias error λ and, if the narrowest filter incorporated in the available spectrum analyser or in the digitising program is 5 Hz, then the desired resolution can be achieved by simply analysing the data at r = 5 real-time speed.

The signals, whether speeded up, slowed down or kept the same, were passed through DISA 55D26 signal conditioners. The signals were then amplified so that their maximum peak-to-peak voltage lay within the range, $\pm$ 10v. This is the maximum range that the EAI 680 analogue computer could take.

The amplified signals were also filtered to remove unwanted low and/or high frequencies. Low-pass filtering is usually necessary in the ADC conversion process to deal with the problem of unwanted data above the Nyquist folding frequency given by Eqn 3.2 . Thus a low-pass filter at frequency n_L was set with a maximum cut-off rate so that

$$n_L = n_{max}$$

where n_{max} defined the limit of the maximum frequency of interest to us. If there was a change in playback to record speed of the tape-recorder by a factor, $r(\gtrless 1)$, then the low-pass filter was set at

$$n_L' = r \cdot n_L \qquad (3.9)$$

Similarly, high-pass filtering is necessary when only the fluctuating or AC component is required and the mean (or DC) component removed, or when analysing certain classes of non-stationary data. To be more specific, consider a non-stationary random process of the form

$$x(t) = A(t) + y(t) \qquad (3.10)$$

where A(t) is a non-random function and y(t) is a random process with

a stationary mean value of zero. Then, assuming that the variations of y(t) are very slow in comparison with the lowest frequency in A(t), A(t) can be separated from y(t) by high-pass filtering.

(b) ADC-Operation on the EAI 690 Hybrid System

Each data channel to be digitized was patched through a track/store amplifier and inverted to an ADC channel in the EAI 680. The ADC channels had to be patched sequentially and the logic patching is shown in Fig. 3.1.

Timing patches (ie wiring on the patch panel of the analogue computer) to determine the sampling rate, f_s, were obtained from the Binary Coded Decimal (BCD) counters on the EAI 680. These were cascaded and patched as down counters, ie they counted down to zero from the value set on the thumb-wheels situated in the EAI 680 console. A timing pulse was issued whenever both counters were zero, and the patching is as shown in Fig. 3.1. The sense switch, 0, on the EAI 680 was used to start and stop the BCD counters which counted pulses at the rate of 10^4 per second so that sampling pulses were obtained at rates which were 'integer fractions' in the range 1 to 10^4 per second according to the thumb-wheel setting. The upper limit of 10^4 could be increased by a relatively small repatching.

It was possible to avoid the inter-channel time-base error, which occurred when each channel was sampled and digitised individually, by sampling the various channels simultaneously and digitising them separately. This was achieved by using the sample-hold circuits in the ADC equipment. This allowed all required channels to be sampled simultaneously and then held until an ADC multiplexing switch passed on the various signals so that they could be digitised.

The sampling rate, f_s, was determined by Eqn 3.4. As before, the actual sampling rate, f_s', was determined by the playback-to-record-speed ration $r(= \rho_p/\rho_r)$ so that

$$f_s' = r \cdot f_s \qquad (3.11)$$

when the output of the BCD counter became high, each track/store unit was put into store mode, so that its output retained the value it had at that instant, and the EAI 640 was interrupted. After acknowledging the interrupting signal, the program was directed to an interruption service routine (see Appendix 3.A) which was either held on permanent file in the ICL 1905 digital computer or loaded through the EAI 640 with the routine written on paper tape as input.

To ensure that the system was working properly, a ramp voltage was generated from a patching routine (see Fig. 3.1), the ramp going from - 1.0V to + 1.0V. This could be activated manually when setting up the EAI 680. Later, when necessary, a TEST routine (Appendix 3.A) was used to generate the ramp on the display oscilloscope of the EAI 680.

The signals controlling the track/store period and the time pulses were displayed on the monitor scopes, Y1 and Y2, of the EAI 680 oscilloscope. Monostables 00 and 10 controlled the display time on the oscilloscope and was set to the smallest possible interval to give a clear display.

On the Y1 display, the high part of the signal indicated the store period and the low part the track period. The track/store was put back into track mode as soon as the A/D conversion was complete. On the Y2 display a sampling pulse appeared as a blip. When setting

the sampling rate, f_s, sufficient time was allowed for the track/store units to regain the track made before the next timing pulse was issued.

The interruption service routine at this point,

(a) Selected and converted the first ADC channel according to specified parameters, such as sampling frequency, number of samples per channel, etc (see Appendix 3.B. for details).

(b) Read the ADC output register and stored the values in a data buffer.

(c) Repeated this process for the next ADC channel until all the channels requiring simultaneous conversion had been read.

Data for each channel was stored sequentially in the data buffer as it was read, so that if conversion was being done on P channels, data for the Pth channel was stored in every Pth word in the buffer.

To enable the fastest possible sampling rate to be used, there had to be one interruption service routine for each group of channels that required simultaneous conversion. The appropriate routine was selected during the setting up of the initial program (see Appendix 3.B).

As stated before, there was also a routine written which put the program in a TEST mode. In this case no check was made on the number of conversions done on each channel so that the program went on sampling indefinitely, and for P channels, data was stored only in the first

P words of the data buffer. This ensured that the sampling rate had been set up correctly since it could be checked from the timing pulses and track/store interval displayed on the monitor scope. In the TEST mode, the analogue signals fed into the EAI 680 were also shown on the display scope.

The program had three service routines and would convert on 1, 2 or 3 channels. Extra routines had to be supplied to convert on any more than three up to a maximum of 24 channels. The form of a routine could be obtained from examination of the attached flow diagram (Appendix 3.A).

When all channels had been converted, the track/store units were returned to track mode and the program awaited the next interruption.

Converted data could be transferred to any of the peripherals associated with the ICL 1905 digital computer. For subsequent analysis, the data could be stored on disc, listed on the line-puncher, punched on cards by the card-puncher or punched on paper tape by the EAI 640 high-speed punch. Each number was converted to four decimal places in the range -0.9999 to +0.9999, corresponding to a voltage range of -9.999v to + 9.999v (one machine unit on the EAI 680 corresponds to 10 volts. Each output record consisted of eight numbers, each in a field width of 10 characters (Fortran format 8 F 10.4). On output, the data for each channel was preceded by a title record, thus

CHANNEL nnn, RUN mmm

where nnn and mmm are decimal numbers for the data channel and current run. The run number was also typed on the teletype console after each

run so that the console log could be matched against results. The run number was not reset unless the program was reloaded or re-entered manually.

Before each title record, 'empty leaders' were introduced to facilitate later separation of the output according to channels. In the case of paper tape, data for each channel was preceded by 78 frames of leader.

The complete step-by-step procedure for using the hybrid system is given in Appendix 3.B.

III.3. Analysis of Digitised Data

3.i. Amplitude Characteristics

(a) From a sampled record, the digitised values of x_i for i = 0, 1, 2, ..., N - 1 gives a mean-value

$$\bar{x} = \frac{1}{N} \sum_{i=0}^{N-1} x_i \qquad (3.11)$$

corresponding to Eqn 2.1.

(b) Similarly, the variance σ_x^2 of the data is given by,

$$\sigma_x^2 = \frac{1}{N-1} \sum_{i=0}^{N-1} (x_i - \bar{x})^2 \qquad (3.12)$$

where the denominator is (N - 1) rather than N, in order that an unbiased estimate may be obtained [34].

The positive square root of Eqn 3.12 gives the standard deviation.

(c) In the case of a single time history, the probability density function p(x) defined by Eqn 2.6 was estimated by using the following equation on the digitised data

ie $$p(X_1) = \frac{1}{W_{X_1}} \left(\frac{N_{X_1}}{N} \right) \qquad (3.13)$$

where $p(X_1)$ is the probability density function of data centered about a value X_1 and having a width of W_{X_1}. N_{X_1} is the number of points falling within this band.

(d) The skewness, S, and the kurtosis, K, of the data were estimated using Eqns 2.4 and 2.9 by

$$S = \frac{1}{\sigma_x^3} \left[\frac{1}{N} \sum_{i=0}^{N-1} (x_i - \bar{x})^3 \right] \qquad (3.14)$$

and $$K = \frac{1}{\sigma_x^4} \left[\frac{1}{N} \sum_{i=0}^{N-1} (x_i - \bar{x})^4 \right] \qquad (3.15)$$

(e) The joint probability density theory for two analogue signals discussed in Section II.2.i.e, can be extended to two digitised records, x_i and y_i (i = 0, 1, 2, ..., N - 1).

The joint probability density function (Eqn 2.12) then becomes

$$p(X_1, Y_1) = \frac{1}{W_{X_1} W_{Y_1}} \left(\frac{N_{X_1, Y_1}}{N} \right) \qquad (3.16)$$

where $p(X_1, Y_1)$ is the probability density function of data centred about a value (X_1, Y_1) and having widths of (W_{X_1}, W_{Y_1}). N_{X,Y_1} is the number of points falling within this band.

3.ii. Frequency Characteristics

(a) Power Spectral Density Function

For a discrete time series, the power spectral density is estimated from Eqn 2.22 as

$$\hat{G}_k(n_k) = 2.\frac{\delta t}{N} \left| X_k \right|^2 \qquad (3.17)$$

where

$$X_k = \sum_{i=0}^{N-1} x_i \exp\left(\frac{-j.2\pi ki}{N}\right) \qquad (3.18)$$

at the usual discrete frequency values $n_k = k/T = k/(N.\delta t)$ for k = 0, 1, 2, ..., N - 1. X_k is a complex number representing the Fourier coefficient of $x_i(t)$ at N data points.

In practice, the auto-power spectrum is produced by a self-conjugate multiplication (ie, squared magnitude) of the complex Fourier coefficients X_k, of the time history. The result is the positive side only of a mathematically correct two-sided spectrum (Section II.2.iii).

The sum of the harmonic coefficients are thus one half of the rms power of the sinusoidal components of the input. The other half resides in the uncalculated symmetrical negative-frequency side, except for the shared zero frequency (DC) component which carries its full value.

To obtain a power spectral density, each value (except the zero-frequency point) of the positive-frequency auto-power spectrum must

be multiplied by two and then all values are normalised by dividing with the bandwidth, δn $(= f_s/N)$.

(b) Cross Power Spectral Density Function

It is shown [34] that cross-spectra can be obtained from the relationship

$$\hat{G}_{xy}(n_k) = 2 \cdot \frac{\delta t}{N} \left(X_k^* \cdot Y_k \right) \qquad (3.19)$$

where * indicates the complex conjugate.

The cross-spectral density function contains as its real part the coincident spectral density function, $C_{xy}(n)$, while the imaginary part is the quadrature spectral density function, $Q_{xy}(n)$ (Section II.2.iii).

Hence magnitude, $$\left| \hat{G}_{xy}(n_k) \right| = 2 \cdot \frac{\delta t}{N} \left| X_k^* \cdot Y_k \right| = \sqrt{C_{xy}^2(n_k) + Q_{xy}^2(n_k)} \qquad (3.20)$$

and phase $$\hat{\theta}_{xy}(n) = \tan^{-1} \left[\frac{Q_{xy}(n)}{C_{xy}(n)} \right] \qquad (3.21)$$

(c) Transfer and Coherence Functions

The power spectral density functions $\hat{G}_x$, $\hat{G}_y$ and $\hat{G}_{xy}$ of the two signals, and x and y were used to calculate the transfer and coherence function from x to y. Signal x was assumed to be the input to a single-input linear system while signal y was taken as the output from the system.

The transfer function, $\hat{H}(n)$, is a complex function representing the amplitude response (gain) and phase response of the linear system. It is defined (Section II.2.iii) as the ratio of the complex linear spectrum (ie discrete Fourier Transform) of the output to the complex linear spectrum (ie discrete Fourier Transform) of the input $\hat{S}_x$, or

$$H(n) = \frac{\hat{S}_y(n)}{\hat{S}_x(n)} \qquad (3.22)$$

To avoid complex division, the ratio was actually calculated by dividing the input-output cross power spectral density by the auto power spectral density of the input. These quantities simply represent the result of multiplying both numerator and denominator by the complex conjugate of the input auto-spectrum, $\hat{S}_x$, ie

$$\hat{H}(n) = \frac{\hat{S}_y}{\hat{S}_x} = \frac{S_y \cdot S_x^*}{S_x \cdot S_x^*} = \frac{\hat{G}_{xy}}{G_{xx}} \qquad (3.23)$$

The coherence function, $\gamma^2_{xy}(n)$, is a measure of the efficiency of the transfer of energy from one time history to another, ie

$$\hat{\gamma}^2_{xy}(n) = \frac{|\hat{G}_{xy}(n)|^2}{\hat{G}_x(n) \cdot \hat{G}_y(n)} \qquad (3.24)$$

$\hat{\gamma}^2_{xy}(n)$ is bounded between 0 and 1. A coherence value of one means that energy is transmitted from one time history through a linear system to a second, without any corruption by noise.

(d) Leakage

Leakage is caused by the presence of frequencies other than those at the discrete frequencies, $n_k = k \cdot f_s/N$ $(k = 0, 1, 2, \ldots, N-1)$. These in-between frequencies modify the coefficients over the adjacent frequencies, giving false results in the form of side-lobes of unwanted power [40].

The large side-lobes obtained from 'raw' estimates can be greatly reduced by using 'data-windows'. Of the many available [38] one of the most simple and effective is the so-called 'Hanning' filter and can be generally written as a three-sample smoothing routine,

$$x'_k = 0.25\, x_{k-1} + 0.5\, x_k + 0.25\, x_{k+1} \qquad (3.25)$$

where $'$ denotes 'Hanned' data.

Anderson and Nettleton [41] have shown that the use of this filter is similar to doubling the number of records when the total number of sampled data points is fixed. This is very useful for purposes of statistical accuracy (see para (e) below).

(e) Averaging for Statistical Accuracy

In addition to Hanning filtering, there are two further methods which can be used to obtain statistically accurate results from the raw spectral estimates: frequency smoothing and ensemble averaging.

In the first method, the raw spectral estimates of 'l' frequency components $n_k, n_{k+1}, \ldots, n_{k+l-1}$ as representing the mid-point of the frequency interval from n_k to n_{k+l-1}. Bendat and Piersol [34] have shown that the normalised standard error of the estimate is then given by

$$\epsilon_r = \sqrt{1/l} \qquad (3.26)$$

By increasing the bandwidth, frequency-smoothing effectively conceals the spectral energy estimates from the original frequency components. In cases where the energy is contained within the low-frequency range, this loss in resolution is not desirable.

To preserve the fine resolution required in the low-frequency end of the spectrum, while at the same time increasing the bandwidths at the

upper range (where little energy was found) a program THOC (Appendix 8) was written. This program effectively smoothed the energy contained by frequency components within a third-octave band with successive centre frequencies placed at intervals of a third-octave.

The program could also be easily modified to evaluate p^{th} octave ($p = 1, 1/2, 1/3, \ldots\ldots$) band frequency-smoothing with centre frequencies p - octave apart.

In ensemble-averaging, the total time record is broken into q time slices (groups). The final smooth spectral estimate is given by

$$\hat{G}_k = \frac{1}{q}\left[\hat{G}_{k,1} + \hat{G}_{k,2} + \ldots\ldots + \hat{G}_{k,q} \right] \qquad (3.27)$$

where $\hat{G}_{k,q}$ is the raw estimate at frequency n_k of the q^{th} time slice.

Hence by ensemble averaging, Bendat and Piersol [34] have shown that

$$\epsilon_r = \sqrt{1/q} \qquad (3.28)$$

During analysis, the length of tape on which the analogue signals were recorded restricted the number of groups (ie frames) over which spectra were averaged. For hot-wire analysis (Section VI.2), $q = 100$ giving $\epsilon_r = 10\%$. For vibration analysis (Section VII. $q = 25$ giving $\epsilon_r = 20\%$.

It has been shown [34] that combined averaging using both frequency smoothing and segment averaging gives a normalised statistical error of

$$\epsilon_r = \sqrt{1/l\,q} \qquad (3.29)$$

(f) The Fast Fourier Transform (FFT) Technique

The FFT is a numerical technique for rapidly and efficiently calculating the discrete Fourier transform coefficients, as in Eqn 3.18. This technique was first described in a form suitable for machine calculation by Cooley and Tukey [42].

It can be shown [43] that this method is most efficient when the number of data points is a factor of three ($N=3^m$). For practical reasons in calculations, N composed of factors of two is used, and such factoring can nearly always be arranged by adding zeros to the data.

With $N=2^m$ data points, it can be shown [34] that computing Fourier coefficients require N^2 arithmetic operatives while with the FFT, the number of operations is reduced to about $2N \log_2 N$.

Eqn 3.18 can be re-written as

$$X(k) = \sum_{n=0}^{N-1} x(n) \cdot W(kn) \quad , \quad k = 0,1,2,\ldots,N-1 \tag{3.30}$$

where $x(n)=x_n$, $X(k)=X_k$ and

$$W(u) = \exp\left(-j \cdot 2\pi u / N\right) \tag{3.31}$$

The basis of the FFT in calculating the above coefficients is that a large number of $W(kn)$ terms are equal, or the negative of each other, so that if the data points which are multiplied by the same term are brought together first, for a vast saving in arithmetic results.

No further explanations of this technique are given here since excellent and comprehensive descriptions of the FFT technique and the programming of this algorithm are given by many authors [44,45].

During analysis, the Fourier coefficients of the digitised data were calculated using an FFT programme, PROGRAM EARL (Appendix B). This was a modified version of a program written by Anderson and Nettleton [40] who, in turn, made use of various sub-routines written by Villasenor [45].

3.iii. Time Characteristics

(a) Auto-correlation

The estimated auto-correlation function at the displacement $k.\delta t$ is defined by

$$\hat{R}_k = \hat{R}_x(k,\delta t) = \frac{1}{N-k}\sum_{n=1}^{N-k} x_n . x_{n+k} \quad , \quad k=0,1,2,\ldots,m \tag{3.32}$$

where k is the lag number, m is the maximum lag number. This is the direct method of estimating the true value, R .

An indirect method of calculating auto-correlation function estimates is first to compute by FFT techniques the power spectral density (Eqn 3.19) and then to compute the inverse Fourier transforms of the result [34]. This is possible because of the 'Weiner-Khintchine' relationship (Eqn 2.26). Bendat and Piersol [34] have shown that this indirect method can make the total operation to compute both the spectral density and correlation function more efficient than direct procedures, depending upon the maximum lag values required.

The auto-correlation values can be normalised by $\hat{R}_x(o)$ to give the auto-correlation coefficient, $\hat{\rho}_x(\tau)$

ie
$$\hat{\rho}_x(\tau) = \hat{R}_x(\tau) / \hat{R}_x(o) \tag{3.33}$$

(b) Circular Correlation

When two finite Fourier transforms are multiplied together, the finite length of the record, T, has an effect, such that the elements which

have been time-shifted past the period T, reappear at the beginning again [43]. Therefore, the correlation that is obtained is not true but is a 'circular' correlation, $R_x^c(\tau_k)$, such that

$$R_x^c(\tau_k) = R_x(\tau_k) + R_x(\tau_{N-k}) \qquad (3.34)$$

at the discrete time lags $\tau_k = k.\delta t$ for k = 0, 1, 2, ..., N - 1.

Bendat and Piersol [34] say that this is not of concern for correlation functions which damp-out rapidly if $k < N/5$. Circular correlation can, however, be avoided by augmenting the original data by N zeros, computing the direct FFT and then the inverse FFT as in paragraph (a) , and then discarding the last half of the computed correlation estimates. This method effectively separates the two portions (Eqn 3.34) of the circular correlation estimates and thus gives us the first 'true' half of the estimated correlation function.

(c) Linear Bias

An accurate representation of the estimated correlation function (Eqn 3.32) is

$$\hat{R}_{xy}(\tau_k) = \frac{1}{N-k} \sum_{i=1}^{N-k} x_i \cdot y_{i+k} \quad \text{for } k = 0, 1, 2, \ldots, m \qquad (3.35)$$

Calculation of $\hat{R}_{xy}(\tau_k)$ from the inverse of the PSD gives an effective $\hat{R}'_{xy}(\tau_k)$ such that

$$\hat{R}'_{xy}(\tau_k) = \frac{1}{N} \sum_{i=1}^{N-k} x_i \cdot y_{i+k} \qquad (3.36)$$

The 'indirect' FFT procedure thus imposes a bias error, increasing linearly with delay time on the correlogram. Hence the correlation values obtained from the indirect method must be multiplied by the scale factor

$$W_k = N/(N-k) \qquad (3.37)$$

so that a 'true' estimate may be obtained.

(d) Cross-correlation Function

The cross-correlation function for two digitised records can be evaluated 'indirectly' from the cross-power spectral density estimates. The method of evaluating is similar to the methods described in the preceding three paragraphs.

IV SIMULATION OF THE ATMOSPHERIC BOUNDARY LAYER IN THE WIND-TUNNEL

Jensen [ ] has shown that models should be tested in a simulated atmospheric boundary layer (ABL) so that both the static and dynamic response of the full-scale structure to natural wind can be modelled correctly. This is because models tested in smooth flow show characteristics that differ markedly from those obtained in generated turbulent boundary-layer flow (Section I.4.ii.b).

The turbulent boundary layer is generated in the wind tunnel by using a variety of flow-mixing devices (Section IV.2.ii). Simulating the ABL requires similarity, not only in the velocity distributions, but also of its turbulent characteristics.

Complete model simulation of the ABL is beyond present capabilities because of the complexity of the problems involved. By careful examination, however, it is possible to simulate those characteristics of the flow which are important in influencing the response of a tall structure. For adequate description of the flow, knowledge of the following parameters [69] is required:

(a) Mean velocity distribution as a function of altitude.

(b) Intensity of each component of turbulence as a function of altitude.

(c) Integral scales of turbulence.

(d) Spectra of turbulence.

This chapter begins with a general description of the ABL and its properties. Characteristics of the ABL which require modelling in the generated flow are also discussed (Section IV.1). In Section IV.2, a

description of the devices used to produce the generated, turbulent flow is given.

IV.1. Description of the ABL

The flow of air over the surface of the Earth is affected by the 'Coriolis' force and also by atmospheric pressure gradients. These gradients are caused by variations in the amount of heat received from the sun at heights above the surface of the Earth where surface friction can be ignored. These two factors produce a steady air-flow that follows the lines of constant barometric pressure (ie the isobars). This air-flow is the gradient wind with velocity, $\bar{U}_G$. The height at which the wind velocity is equal to the gradient velocity is known as the gradient height, z_G.

The gradient wind does not conform to the no-slip conditions at the surface, indicating the existence of a boundary layer [47]. This is called the planetary boundary layer and is, on average, about one kilometre thick. Within this layer the wind velocity shows continual rapid fluctuation, the amplitude of which varies throughout the day.

Most structural wind-loading problems are concerned with high-wind conditions. In high winds, surface friction causes so much mechanical stirring of the atmosphere that the thermal gradients giving rise to convection processes are destroyed. The lapse rate

$$\gamma = \frac{dT}{dz}$$

(where T is the absolute air temperature at height z) is therefore always approximately adiabatic and the stability of any rising air is neutral, it is in thermal equilibrium with its surroundings. The

following discussion is concerned with the special case of strong-wind, neutral stability conditions.

Strong-wind, neutral stability wind conditions imply that the ABL is in highly turbulent motion. To understand properly the properties of the ABL wind, a statistical approach is used. From a spectrum obtained by Van der Hoven [48], of the horizontal wind speed near the ground, Davenport [49] was able to show that there were two very different time scales in the random variation in wind speeds. On this low-frequency side, the macro-meteorological region is associated with changes in the large scale patterns of air flow. These changes usually occur as depressions and anti-cyclones, with energy periods of four days. The high-frequency micro-meteorological region is associated with the small-scale fluctuations. These are generated by wind shears induced by surface friction, and the spectrum has corresponding energy peaks at one-minute periods (gusts). In between these two regions there is a meso-meteorological section affected by the diurnal variations of heating (Fig. 4.1).

An interesting feature of this spectrum is the pronounced gap centred at a period of about half an hour. In this gap, the energy of the spectrum is at a minimum. This area, the spectral gap, lies mainly within the range of 1 to 10 cycles/hour, ie near the low-frequency side of the micro-meteorological region. It should be noted, however, that its frequency, location and definition may vary [50].

The main significance of the spectral gap is that it is then possible to describe the wind conveniently in terms of (a) a mean velocity reflecting only the synoptic variations in wind-speed and (b) the superimposed gusts.

Using the above arguement, Davenport [50] suggests that a good averaging period for defining a mean velocity is approximately 10 to 20 minutes. This is because:

(a) This period lies near the centre of the spectral gap, ensuring that, in general, trends will not be strong.
(b) The period is short enough to reflect sharp, sudden storms, usually lasting about 5 to 10 minutes.
(c) The period is adequate for the development of steady-state oscillations since the natural frequencies of most structures are in the range of 0.1 Hz and higher.
(d) Although standard averaging periods vary throughout the world (Britain uses a one-hour period), we can assume that the consequences of using different averaging periods are not very significant, provided that they are within the spectral gap.

As indicated above, it is important to remember that wind-flow is turbulent. The mean and fluctuating properties of wind are of particular interest in structural design. These properties are discussed below.

1.i. Mean Velocity Profile

The ABL can be divided into two sub-layers: (a) the surface boundary layer in which the shearing stress is approximately constant, and (b) a transitional region in which the shearing stress decreases to practically zero in the free atmosphere.

In the surface boundary layer, it has been shown [51] for strong-wind, neutral-stability conditions that the wind velocity profiles can be

defined by the Prandtl logarithmic law,

$$\bar{U}(z) = \frac{u_*}{k} \cdot \ln\left(\frac{z+z_0}{z_0}\right) \qquad (4.1)$$

where $\bar{U}(z)$ is the mean velocity at height z; the friction velocity is u_* ($u_* = \sqrt{\tau_0/\rho_a}$ where τ_0 is the shearing stress at the surface and ρ_a is the air density); z_0 is a constant of integration known as the roughness length related to the roughness of the surface and k is Von Karmans constant $\simeq$ 0.4.

Although this profile is theoretically valid down to z = o, it should be noted that this cannot be true when there is any uncertainty about the ground plane. In practice, rougher surfaces (larger z_0) are associated with larger obstructions on the ground. A difficulty therefore arises concerning the origin of z and it is customary to introduce a zero-plane displacement, d, to provide a datum level above which active turbulent interchange begins. A modified logarithmic profile

$$\bar{U} = \frac{u_*}{k} \ln\left(\frac{z-d}{z_0}\right) \qquad (4.2)$$

is thus expected to hold.

The surface drag coefficient, C_{D_0}, is related to the friction velocity [51] so that,

$$C_{D_0} = \tau_0/\left(\tfrac{1}{2}\rho_a \bar{U}^2\right) = \tau\left(u_*/\bar{U}\right)^2 \qquad (4.3)$$

Sutton [51] cites the work of Calder [52] who found the values of the constant in Eqn 4.2 by choosing values of d and z_0 independently to give the best fit. With a mean wind-speed of 5 m. sec^{-1}

at a height of 2 m above the ground, Calder found that for (a) short grass (1–3 cms), $U_* = 33$ cm sec^{-1}, $z_0 = 0.5$ cm, $d = 0$ and for (b) long grass (60–70 cms); $u_* = 50$ cm sec^{-1}, $z_0 = 3$ cms and $d = 30$ cms.

It has been shown [51] that, if protuberances on a surface are sufficiently similar in shape for a mean height ϵ to be defined, then

$$z_0 \sim \epsilon / 30 \qquad (4.4)$$

Making use of this relation, Sutton [51] has modified Nikuradse's criteria [53] to give

$$\begin{aligned} u_* z_0 / \nu &< 0.17 \\ &> 2.3 \end{aligned} \qquad (4.5)$$

for smooth and rough surfaces respectively.

Using Nikuradse's criterion for fully-rough flow, it is then possible to conclude that natural surfaces are aerodynamically rough.

Above the surface-layer, the effect of the Coriolis force increases, the effect of the surface roughness decreases and the profile departs significantly from the logarithmic form [54]. An empirical law for the mean-wind velocity profile through the deeper boundary layer is

$$\frac{\bar{U}_z}{\bar{U}_{ref}} = \left(\frac{z}{z_{ref}} \right)^{\alpha} \qquad (4.6)$$

in which $\bar{U}_{ref}$ is a reference velocity at a height z_{ref}, and α is a constant.

In practice, it is useful to standardise the relationship by using either the gradient height, z_G, or a standard height of 10 m as reference.

Davenport [54], analysing mean wind-speeds profiles measured by investigators working in different countries and different terrains, showed that the index of the power law varied with the nature of the terrain. This variation is shown in Fig. 4.2. together with the variation in gradient height.

In modelling, it is assumed that the variation with height could be represented by a power law (Eqn 4.6). If appropriate velocity and length scaling are employed in the wind-tunnel (Section V.1.iii) then the velocity profile should be represented in the wind-tunnel by,

$$\left[\frac{\bar{U}(z)}{\bar{U}_{ref}}\right]_{model} = \left(\frac{z}{z_{ref}}\right)^{\alpha}_{model} \qquad (4.7)$$

where $\bar{U}_{ref}$ is a representative wind-speed at a height z_{ref}. The value of α, appropriate to the terrain over which the boundary layer is to be simulated, is obtained from Fig. 4.2.

The absence of a profile of mean wind-speed, however, is not considered to have a significant influence on the dynamic response of very tall, slender buildings and structures [33].

A further parameter that needs modelling is the roughness parameter, z_0. This is because z_0 is a measure of the roughness of the surface concerned, and, at the same time of the turbulence in the turbulent boundary layer over the surface. This implies that a more

turbulent layer corresponds to a surface of greater roughness z_o is derived from Prandtl's logarithmic law (Eqn 4.1).

The condition of obtaining similarity between the phenomena observed in the wind-tunnel and that in the atmosphere, is [46]

$$\left(\frac{z_o}{d}\right)_{model} = \left(\frac{z_o}{d}\right)_{full\text{-}scale} \qquad (4.8)$$

where d is some characteristic length.

In addition, the model must be immersed entirely in the generated, turbulent boundary layer. Otherwise, erroneous results may occur [55].

1.ii. Turbulence Properties of the Wind.

One of the most recognisable features of the wind is its randomness, ie its turbulent nature. This property is best understood by using a statistical approach. Some of the basic turbulent characteristics of the ABL are examined below.

(a) Probability Distribution

According to Davenport [56], the probability distribution of wind velocity, sampled over an approximate short time period, has been shown to agree well with the familiar normal or Gaussian distribution, and is given by,

$$p(V_i - \bar{U}) = \frac{1}{\sqrt{2\pi}} \cdot \frac{1}{\sigma_u} \cdot \exp\left[-\frac{1}{2}\left(\frac{V_i - \bar{U}}{\sigma_u}\right)^2\right] \qquad (4.9)$$

where V_i = instantaneous wind velocity ($= \bar{U} + u'$)

$\bar{U}$ = mean wind velocity component

u' = fluctuating wind velocity component

and σ_u = standard deviation of the fluctuating wind velocity component

In practice, however, the turbulent motion in the lower atmosphere is considerably more complicated, and the Gaussian distribution, valid for homogeneous, isotropic turbulents (HIT) conditions, does not truly represent wind flow. Therefore, Eqn 4.9 must be regarded only as an approximation of the general model of the ABL.

(b) Wind Energy Spectrum

When considering the effect of wind on the structure, the most important parameter is probably the longitudinal wind-velocity spectrum, $G_u(n)$. This is because the fluctuations in the drag component of the motion of the structure are mainly influenced by $G_u(n)$.

Davenport [49] analysed the micro-meteorological range of frequencies of the wind during high wind conditions at a variety of measuring sites. He then suggested an empirical expression

$$n \cdot G_{uu}(n) = 4 k \cdot \bar{U}_{ref}^2 \cdot \frac{f_D^2}{(1+f_D^2)^{4/3}} \qquad (4.10)$$

to represent the longitudinal wind velocity spectra. In this expression, $f_D = n \cdot l_D / \bar{U}_{ref}$ where l_D is a 'scale' length.

Integrating Eqn 4.10, the total variance, σ_u^2, of the wind velocity fluctuations at a height z is obtained.

ie $$\sigma_u^2 = \int_0^\infty G_u(n)\, dn = 6.0\, k \bar{U}_{ref}^2 \qquad (4.11)$$

This shows σ_u^2 to be invariant with height.

Since σ_u^2 is easier to obtain than $u_*^2 \left(= k \bar{U}_{ref}^2\right)$, Eqn 4.10 can be modified to,

$$\frac{n \cdot G_u(n)}{\sigma_u^2} = \alpha_D \cdot \frac{f_D^2}{(1+f_D^2)^{4/3}} \qquad (4.12)$$

With $\bar{U}_{ref} = \bar{U}_{10}$ (a mean wind speed in m /sec at a height of 10 m), Davenport reports values of 0.67 and 1200 m for α_D and ℓ_D respectively.

At the high frequency region of the spectrum, the above form indicates that the eddies appear to belong to the inertial sub-range of frequencies in which $G_u(n)$ varies as $n^{-5/3}$. This decrease in spectral density with increasing frequency corresponds to Kolmogroff's similarity theory [57].

Care must be taken in interpreting the $-5/3$ index. Pasquill [58] has reviewed available published data and found that there were appreciable departures from the $-5/3$ index. He concludes that such departures may be a consequence of some input or extraction of turbulent energy in the range of frequencies considered. This is assumed not to occur in the 'similarity theory'.

A length scale, L_x, known as the longitudinal integral scale of turbulence describes the energy-containing eddies of the longitudinal wind fluctuations. It is related to the energy contained in a narrow band ($\delta n \to 0$) near zero frequency, and is given by,

$$L_x = \frac{\bar{U}_{ref}}{4\sigma_u^2} \left[\lim_{\delta n \to 0} G_u(n)_{n=0} \right] \qquad (4.13)$$

The two scales, L_y and L_z, can be obtained similarly from the lateral and vertical spectra.

A disadvantage of Davenport's relationship, Eqn 4.12 is that $n \cdot G_u(n)/\sigma_u^2$ does not vary as f^2 but as f for small f. Hence Eqn 4.12 does not yield a finite value for the power spectral density near zero frequency.

To overcome this theoretical objection, Harris [59] has suggested an alternative form,

$$\frac{n \cdot G_u(n)}{\sigma_u^2} = \alpha_H \cdot \frac{f_H}{(2 + f_H^2)^{5/6}} \qquad (4.14)$$

where α_H ($\simeq$ 0.6) is another empirical constant. A change in the value of the length scale, l_D, from 1200 m to 1800 m was also proposed.

Both Davenport's and Harris's representation of the longitudinal gust spectrum suffer from the difficulty of finding a suitable length scale, $l_{D,H}$. According to Armitt [60], 'fitting curves to spectra in order to deduce length scales imposes the experimenter's ideas on the data. Even if the curves are correct in functional form, there is still a requirement that the data analysis should be sufficiently accurate to allow a good curve fit. Even here, the requirements are not easily satisfied'.

Kaimal et al [61] have overcome the uncertainty of using l_D by replacing l_D in the non-dimensional frequency parameter, f, by z (ie $f_K = n z / \bar{U}_{ref}$ where z is the observation height).

They used a modified frequency scale f/f_i where f_i is the intercept of the extrapolated inertial subrange spectrum with the $n \cdot G_u(n)/\sigma_u^2 = 1$ line. This brings all spectra into coincidence on a -2/3 line in the

inertial subrange. When all stable longitudinal gust spectra are plotted in this manner, they display a universal shape, approximated empirically by the form,

$$\frac{n \cdot G_u(n)}{\sigma_u^2} = \frac{0.16\,(f_k/f_i)}{1 + 0.16\,(f_k/f_i)^{5/3}} \qquad (4.15)$$

Using Eqns 4.13 and 4.15, the variation of l_x with altitude is seen to be

$$L_x = \frac{0.04\,\bar{U}}{n_i} \qquad (4.16)$$

Flows with the correct turbulence, similar to the ABL can be generated in the wind-tunnel, but they yield scales of turbulence much too small when compared with the linear scale of turbulence. Only the higher range of frequencies encountered in the ABL can therefore be properly simulated if scales of turbulence are to be modelled.

The loss of simulation in the low-frequency region however, is not restrictive. Whitbread [33] says, 'If it is assumed that the response of a lightly - damped structure is proportional to the (wind) spectral density at a particular value of wind speed, and there is some experimental evidence to support such as assumption, then it should be reasonable to reduce, the requirements for similarity of scale and intensity of turbulence simulation to one of spectral density only over the wave number, $nD/\bar{U}_{ref}$, range of interest'.

Using a grid, Cook [62] obtained a similar part simulation, but only with the acceptance of an incorrect intensity of turbulence.

It is relevant at this point to include an observation made by Whitbread and Scruton [31]. On a test of the dynamic response of a tall building model, marked similarity was found between tests conducted in uniform turbulent flow and in turbulent shear flow. They took this observation as being qualitative evidence that precise reproduction of the turbulent characteristics of wind flow is not essential.

(c) Turbulence Intensity

The rms gust speed can be defined as

$$\sigma^2 = \sigma_u^2 + \sigma_v^2 + \sigma_w^2 \qquad (4.17)$$

Harris [63] says that $\sigma_v \sim \sigma_u/3$ with σ_w being still smaller.

$\therefore$ Eqn 4.17 becomes

$$\sigma \simeq \sigma_u \qquad (4.18)$$

Using Eqns 4.14 and 4.18, the turbulence intensity, I, is given as

$$I = \sigma / \bar{v}_z$$

$$= 2.58\, k^{1/2} \left(\bar{v}_{10} / \bar{v}_z \right) \qquad (4.19)$$

Section I.4 shows that the intensity of turbulence contributes significantly to the dynamic response of a structure. Therefore, the turbulent structure of the ABL (Eqn 4.19) should be closely modelled.

(d) Scales of Turbulence and Equivalence in Space and Time.

Taylor [57] has stated that space and time spectra and correlation functions are equivalent, provided that the turbulence intensity is low.

This assumption becomes useful when the spatial integral scale of turbulence, L_x, is evaluated from the time scale of turbulence, T_x, and Taylor's hypothesis.

The time integral scale is obtained from the auto-correlation curve,

$$T_x = \int_0^\infty R_{uu}(\tau) \cdot d\tau \qquad (4.20)$$

The spatial integral scale of turbulence,

$$\begin{aligned} L_x &= \int_0^\infty R_{uu}(x) \cdot dx \\ &= \bar{U} \int_0^\infty R_{uu}(\tau) \cdot d\tau \\ &= \bar{U} \cdot T_x \end{aligned} \qquad (4.21)$$

can then be obtained.

Panofsky et al [64] tested Taylor's hypothesis in a natural wind with high turbulence intensities ($I \sim 16$–30%). They found Taylor's hypothesis to be still approximately valid.

Care must be taken in using Taylor's hypothesis in the wind-tunnel since departures from this hypothesis have been observed [62].

Interpretations of the time scales obtained by using Eqn 4.20 must be made with care because mean values are removed by filtering the data before evaluating T_x. Formally, this gives zero time scales.

According to Armitt [60], finite time scales of reasonable validity can be obtained if

$$T_A >> T_{max} >> T_\lambda$$
$$T_F >> T_{max}$$

where T_A = averaging time

T_{max} = maximum time delay considered

T_F = time constant of filter used to remove mean.

A scale length, λ_u, known as the micro-scale and corresponding to the high frequency eddies can be defined [57] as

$$\frac{2}{\lambda_u^2} = -\frac{1}{\bar{U}_{ref}}\left[\frac{\partial^2 R_{uu}(\tau)}{\partial \tau^2}\right]_{\tau=0} \qquad (4.22)$$

In experiments, λ_u, denotes the part of the abscissa between the origin and the point of intersection with the osculation parabola fitted at the vertex of the correlation curve.

(e) Coherence

When considering the wind-loading on a tall structure, it is clearly important to have some measure of the spatial distribution of gusts. This can be measured by the correlation coefficient between two velocity measurements partially separated by a spatial interval, δ_z.

For lateral and vertical correlations, the current trend is to present the space-correlations data in terms of the coherence function, γ^2, (Eqn 2.31), such that

$$\gamma^2(n) = \frac{|G_{12}(n)|^2}{G_1(n) \cdot G_2(n)} \qquad (4.23)$$

where $G_1(n)$ = power spectral density measured at point 1

$G_2(n)$ = power spectral density measured at point 2

$G_{12}(n)$ = cross power spectral density between points 1 and 2

Davenport [49] found that the coherence for both lateral and vertical separation apparently shows a universal relationship of the form

$$|\gamma| = \exp\left[-(c \cdot \delta z \cdot n)/\bar{U}_{mt}\right] \quad (4.24)$$

The value of C has not been determined with certainty since it varies greatly with meteorological conditions. He has suggested that an unstable, high wind conditions, it lies in the range, $6 < c < 8$. He also noticed that $|\gamma|$ approaches zero for the first time when $n.\delta z/\bar{U} \sim 0.5$, indicating that there is negligible correlation when the height separation is about half the wave-length. The eddies are therfore, on average, about as long as they are high.

IV.2. Experimental Apparatus Used for Generation of a Simulated ABL

In this section, the design and construction of the apparatus used in the generation of the simulated ABL is discussed.

All experiments were made on an National Physical Laboratory (NPL) type, open-return wind tunnel designated TI. (Fig. 4.5). The working section was rectangular, 76 cms wide and 61 cms high. The upstream fetch, from the wind-tunnel inlet to the working section used for the development of the air flow, was about 250 cms long.

The wind-tunnel fan was powered by a 6 horse-power DC motor. With a honeycomb flow-straightner placed at the inlet, a tunnel wind-speed range of 8 - 16 m/sec was obtained.

The relatively short working length of the wind tunnel made it necessary to accelerate the natural growth of the boundary layer. This was done using a turbulence generating system, comprising a castellated barrier, quarter-elliptical-shaped vortex generators and distributed roughness elements. A similar system was first used by Counihan [65] to adequately represent the turbulence characteristics of the ABL in a wind-tunnel.

An initial velocity profile was impressed at the entrance (ie the bell-mouth) to the wind-tunnel. A grid of horizontal bars with graded separations between their centre-line axes was used for this purpose. The grid was designed by slightly modifying a theoretical analysis by Cowdrey [66].

Coarse, square-meshed screens were also designed to reduce the minimum wind speed of the tunnel.

2.i. Simulation of Mean Wind Velocity Profile

Many methods [67,68] have been suggested for the generation of mean velocity profiles inside a wind-tunnel. When simulating the ABL however, these methods are unable to model the very high shear found close to the surface of the earth. To overcome this problem, Cowdrey [66] has proposed an analytical approach to the design of velocity-profile generators. This technique uses rods that span the tunnel horizontally and are separated from each other by graded distances.

Experimental results obtained using this system compared very favourably with his theoretical predictions.

For the experiments described here, Cowdrey's analysis was slightly modified to take into account as an extra parameter, the height of the required boundary layer. The use of this parameter was essential because the amount of immersion of the model structure in the boundary layer was an important factor

A grid with circular, mild-steel bars of diameter 127 mm and length 762 mm was placed across the mouth of the wind tunnel (Fig. 4.5). The separation between the centre-line of these rods (Appendix 4.A) was designed for a power exponent of 0.4 and BL height of 610 mm. These values were chosen to represent an urban BL wind profile (Fig. 4.2) with a gradient wind-height, z_g, of 520 metres.

The detailed design of a grid which would produce a boundary layer of height δ and having a power index α is given in Appendix 4.A.

2.ii. Generating in the Wind Tunnel, a Turbulent Boundary Layer to Represent the ABL

Most ways of producing a simulated ABL require a long upstream fetch. Wind tunnels lacking this characteristic require some form of obstruction to trip and accelerate the growth of the BL.

One of the most successful trip-methods is a system of obstructions devised by Counihan [65]. It contains three components: a barrier, the height of which is a function of the velocity profile required, a row of vorticity generators, and surface roughness, the

form of which is also dependent on the required velocity. After exhaustive tests, Counihan concluded that adequate representation of a neutral ABL, regarding both general characteristics and flow structure, could be obtained in a wind tunnel using this method.

Counihan's system was therefore used, and a turbulent structure, similar to the ABL, was imposed on the air-flow which already had a mean velocity profile (Section IV.2.i).

The dimensions of these obstacles and their relative positions, in the wind tunnel were obtained by scaling the dimensions given by Counihan [69].

(a) Barrier

The barrier (Fig. 4.3a), essential to the simulation system, was castellated. The barrier takes some of the required momentum from the flow and produces vorticity with a spanwise axis. The castellations prevented the formation of a two-dimensional flow pattern. According to Counihan [65] they also induce earlier spanwise uniformity of the flow downstream of the generators.

The barrier made from 6.35 mm thick plywood was positioned 152 mm from the contraction in the TI wind tunnel (Fig.4.5) the height of the barrier was 74 mm and the castellation increased this to 95 mm.

(b) Vorticity Generators

The vorticity generators had a side-view profile of a quarter-ellipse, the major axis of which was twice its minor axis. In plan view, the sections were wedge shaped, with a constant semi-wedge angle of 6°.

The apex of the wedges faced directly into the wind and therefore no assymmetry was introduced into the flow.

The rationale for the design of these vorticity generators was the need to obtain a distributed turbulence in the wake of the generators.

The distribution had to have a maximum value near the ground, decreasing to zero at the top of the BL. The low wedge angle was thought to encourage the production of a vertical distribution of vorticity rather than a vortex in the wake.

Using design plans supplied by Counihan, three vorticity generators were constructed, each 508 mm high with a constant semi-wedge angle of 6°. The generators were made with a brass outer skin covering graded triangular plywood stiffeners. These were fixed at suitable heights to a profiled plywood back-plate and the brass skin was then formed around it (Fig. 4.3b).

The generators with the castellated barrier were mounted on a 3 mm thick plywood board to facilitate insertion and removal of the complete system from the wind tunnel. The generators were spaced across the tunnel with their centre-lines 250 mm apart. The leading edges of the generators were 320 mm from the castellated barrier (Fig. 4.4).

(c) Roughness Elements

Roughness was introduced into the wind tunnel by covering with small blocks of wood the floor area from the back of the vortex generators

to the model-testing station. These elements were each 7.5 mm high having a square cross-section with 17.5 mm sides. To facilitate insertion and removal, all elements were fixed to a hardboard sheet, 2030 mm long and 760 mm wide. The elements were distributed in parallel, but staggered rows, so that each element in one row lay midway between the elements in the previous row. The centre-line spacings of the elements were 32.5 mm in line with the tunnel length and 45.0 mm lateral. This gave a covered ratio of about 8%.

(d) Bi-planer Screens

In normal use, the minimum wind speed obtained in the tunnel was about 8 m/sec. For some of the tests however, it was necessary to reduce this speed by placing additional blockage, in the form of coarse, square mesh screens at the entrance to the bell-mouth of the tunnel. The construction of the wind tunnel made it impossible to insert these screens behind the working section.

According to Lawson [70], the difficulty in using screens to produce natural wind velocity profiles is that the profiles decay with downstream distance. This characteristic was used to advantage. It was assumed that since these screens were placed at a sufficient distance from the working-section, they would not alter radically the characteristics of the flow generated by the other obstructions.

The mesh dimensions of the screens for differing blockage ratios were obtained by using empirical formulae relating integral scales and intensities of turbulence to mesh dimensions and downstream distance.

For intensity of turbulence, Baines and Peterson [71] suggest

the expression:

$$\frac{\sigma}{U} = 1.12\left(\frac{d}{b}\right)^{-0.75} \qquad (4.25)$$

where d is downstream distance from the screen and b is the screen-bar width.

Whitbread [33] modified some results from Barnes and Peterson to express a longitudinal integral scale of turbulence,

$$\frac{L_x}{b} = 0.0706\left(\frac{d}{b}\right)^{0.775} \qquad (4.26)$$

In the experiments described here, screens with blockage ratios of 71, 50 and 45% were made. Using Eqns 4.25 and 4.26, a turbulence intensity of about 5% and a longitudinal scale of turbulence of 75 mm were predicted. This length scale was chosen to be of the same order of magnitude as the depth of the model.

The three screens were made from 6.4 mm thick plywood. Their dimensions are given in Table 4.1. A representative photograph of a bi-planar grid is shown in Fig. 4.4.

V. DESIGN AND CONSTRUCTION OF EXPERIMENTAL APPARATUS

The aim of the research was to investigate the response of a scaled model of a prototype building to smooth and turbulent shear flows and the effect of restricting its movement from two to one degree of freedom (Section I.2). The design and construction of the models (Section V.1), the unique gimbal system on which the models were mounted (Section V.2), and the damping rig and a rig to house and support the models and gimbal system (Section V.3) are discussed in this chapter.

V.1. Design and Construction of Models

Two models were tested in the simulated ABL, a square-sction prism representing one of the towers of the World Trade Centre in New York, and a circular-section prism with similar characteristics (ie height, wall thickness and width of the face normal to the flow). The modelling technique is discussed in Section V.1.i, choice of models in Section V.1.ii, design in Section V.1.iii, and construction in Section V.1.iv.

1.i. Modelling Techniques

Laws relating the results of model experiments to the behaviour of full scale structures can be determined by dimensional analysis. Whitbread [72] obtained eight non-dimensional scaling parameters by considering eight physical quantities defining the physical characteristics of a structure, and three quantities that of the airstream in which the structure is placed. These were used to obtain similarity in response between a full-scale prototype and a model with a similar aerodynamic shape placed in a turbulent, shear airstream.

In practice it is rarely possible to satisfy all non-dimensional parameters needed for model simulation, and it is therefore necessary to relax the similarity requirements. This can be done by choosing a model which will give the information which is specifically required.

The family of models which can be used to represent full-scale structures can be divided into two groups - rigid or aero-elastic. Static, rigid models having minimal scaling requirements, can be used for flow studies and for determining surface pressures and the overall steady forces and moments experienced by a structure.

The measurement of response requires a more thorough evaluation of the scaling requirements. The dynamic behaviour of a structure in wind is most accurately represented by a 'full model' (ie an aero-elastic model of the complete structure), but this is impracticable for many structures and a linear-mode or sectional model has to be used. Description of scaling requirements and types of models used to investigate specific characteristics can be found in the literature [73,74].

For the research described in this thesis, a linear-mode model of the prototype was considered to be adequate. Linear-mode models are geometric, but rigid, copies of prototypes. They are free to pivot about the base so that an approximation to the fundamental displacement mode

$$f(\eta') = \eta' \qquad (5.1)$$

of a cantilevered structure is obtained. Here, $f(\eta')$ is the relative horizontal displacement of a point in the structure at the normalised height, $\eta' = z/h$, where z is the height of the point from the base and h is the height of the model.

One advantage of the simpler linear-mode model is that it can be more easily provided with variable structural damping. Extensions of the model below the floor of the wind-tunnel make possible the attachment of stiffness and controlled variable damping systems (Section V.3.).

Eight parameters define structural similarity between model and full scale prototype (see above). From a consideration of the importance of each of these terms to the vibrational characteristics of a thin-shelled structure, Whitbread [75] concluded that adequate structural similarity is possible if three of the non-dimensional parameters are simulated:

(a) structural damping, δ_s,

(b) reduced velocity parameter, v_r $(= \bar{v}/n_o D)$,

and (c) inertial ratio $m/\rho_a D^2$ or $I/\rho_a D^4$,

where I is the mass moment of inertia of the structure.

1.ii. Choice of Models

A square-section model was constructed to represent one of the tallest buildings erected and a circular-section model with similar geometrical characteristics was also designed.

(a) Square-section Models

Because of the difficulty in obtaining Reynolds number similarity between full-scale and model tests, a model had to be selected which would be insensitive to Reynolds number effects. Structures with sharp separating edges show this independence (Section I.4.i), and therefore a square-section model was designed and built to represent one of the two idential tower blocks at the World Trade Centre in New York. The two blocks, with constant square cross-sections, are erected on a plaza 21.6 metres high. The overall dimensions of the towers and their relation to the building complex in which they are situated are shown in Fig. 5.1.

The choice of one of these tower blocks as prototype was made because:

(i) It had a suitable height-to-breadth ratio ($\simeq$ 6), sharp corners and a simple external shape.

(ii) Its structural parameters, which were required for modelling, were known.

(iii) Tests had already been made by Whitbread and Scruton [31] making possible a comparison of results.

Whitbread and Scruton give the characteristics of the prototype as follows:

Cross-sectional dimension (D) = 63.4 x 63.4 m.

Height of tower = 387.6 m

Mass moment of inertia about the axis (in-line to wind), I, = 1.542×10 kg. m.

Height of tower above ground level = 409.2 m.

Natural frequency of tower in the direction of the wind flow $(n_o)_x$ = 8.55×10^{-2} Hz

Natural frequency of the tower in direction lateral to the wind flow, $(n_o)_y$ = 9.62×10^{-2} Hz

(b) Circular Cross-Section Model

A model with a circular cross-section was constructed to provide a comparison with the vibrational characteristics of a model with a well defined separating edge. It was similar to the square-section model in its dimensions with the same height, h, and wall thickness, t. The diameter, D, of the circular-section model was made equal to the length of one side of the square-section model, giving similar aspect ratios, R ($= h/D$).

1.iii. Design of Models

In the following discussion, the models are referred to as square or circular cylinders.

The models were mounted in turn on a gimbal system (Section V.2.i). This allowed the models to pivot about the base in two mutually orthogonal directions, the deflections corresponding to the fundamental linear bending

modes, Eqn 5.1.

The scaling laws used to obtain similarity between model and full-scale prototypes are as follows:

(a) Length scale

The total height (δ = 0.61m) of the working section of the wind-tunnel was used as the boundary layer height of the generated turbulent flow. The geostrophic height z_{g_a} of the A B L above an urban area was taken as 520 m (Fig. 4.2).

For equal immersion of model and full-scale prototype in their respective b.l's, the relationship

$$\frac{D_m}{D_F} = \frac{\delta}{z_{g_a}} \simeq 853 \qquad (5.2)$$

had to be satisfied. In this expression, D is a characteristic length of the structure and subscrips 'm' and 'f' denote model and full-scale respectively:

A 1:850 linear scale gave the following dimensions for the square models;

height, h = 456 mm.

cross-sectional dimension, D = 74.6 x 74.6 mm.

When the model was placed inside the wind tunnel, an area blockage ratio of approximately 7-8% was obtained. This ratio was considered to be just tolerable.

(b) Speed Scale

A wind-speed scale of

$$\frac{V_m}{V_F} = \frac{1}{8} \qquad (5.3)$$

was adopted. Acording to Whitbread and Scuton [31], separation is necessary to avoid uncertainties arising from possible flexural vibration of the model. Separation is therefore possible between the model body frequencies and those of the model oscillating as a rigid body on its gimbal mounting.

(c) Frequency Scale

Using both the linear and speed scale factors in scaling parameters, Eqns 5.2 and 5.3, a frequency scale

$$\frac{n_m}{n_F} = \frac{V_m}{V_F} \cdot \frac{D_F}{D_M} \qquad (5.4)$$

$$= 106.25$$

was established.

From the data quoted earlier (Section V.1.ii) for the full-scale tower, the following natural frequencies for modelling were obtained.

Natural frequency of model in the direction of wind flow, $(n_o)_x = 9.084$ Hz.

Natural frequency of model lateral to the wind flow, $(n_o)_y = 10.221$ Hz.

From Eqn 5.4, a time-scale between wind-tunnel and full-scale measurements was obtained.

ie $$\frac{T_m}{T_F} = \frac{n_F}{n_M} \qquad (5.5)$$

(d) Inertia Scale

Inertia scaling was similarly derived from scaling parameters, eqn 5.3 so that

$$\frac{I_M}{I_F} = \left(\frac{D_m}{D_F}\right)^5$$

$$= 2.254 \times 10^{-15} \qquad (5.6)$$

Using the full-scale data given in Section V.1.ii, a desired model

inertia of

$$I_m = 1.542 \times 10^{13} \times 2.254 \times 10^{-15} \text{ kg m}^2$$
$$= 3.475 \times 10^{-2} \text{ kg m}^2$$

was obtained.

I.iii. Construction of Models

(a) Square Cylinder

Initial calculations indicated that a model constructed from commercially available alumunium tubing would fulfil length and inertia-scale requirements. The use of a tube, rather than a metal skin wrapped around stiffeners as suggested by Whitbread and Scruton [31] was thought to result in a more rigid model, giving only the fundamental linear-mode of deflection. This was possible because the model pivoted about the base which was fixed to the two-degree-of-freedom gimbal system (Section V. 2.i).

The square cylinder (Fig. 5.2) was made from a length of square cross-section aluminium tubing with 74.7 x 74. 7mm sides, 45.7 mm length and with a 3.25 mm (10 swg) wall thickness.

(b) Length and Inertia Modelling

Using a procedure outlined in Appendix 5.A, it was found that, for a model mass moment of inertia of $I = 3.514 \times 10^{-2}$ kg.m^2, the following tube dimensions apply:

Length h of tube = 457 mm,

Outside dimension D = 72.5 mm,

Wall thickness, t = 1.4 mm,

where the value D is sufficiently close to the value required.

A change in the wall thickness by $\pm$ 0.1 mm changed I by $\pm$ 7%, and the natural frequency of the model, n_o , by $\pm$ 2%. Therefore, since there was no significant effect on n_o for a change of 0.1 mm in t, for ease in

machining, the wall thickness was allowed to lie between 1.3 and 1.5 mm. Using a milling machine, the excess material was skimmed from the sides of the square tube to give an average t of 1.4 mm.

(c) Modelling the Natural Frequencies

The natural frequency of the model is given by

$$n_o = \frac{1}{2\pi}\left(\frac{k}{I}\right)^{1/2} \qquad (5.7)$$

where k is the stiffness of the model

Model natural frequencies of 9.084 Hz and 10.221 Hz respectively in the in-line and lateral directions (Section V.1.iii.c) had to be reproduced correctly. Given a mass moment of inertia (Section V.1.iv.b),

$$I_{xx} = 3.514 \times 10^{-2} \text{ kg m}^2$$

The stiffnesses that required modelling are given as

$$k_x = 1.145 \times 10^2$$
$$k_y = 1.45 \times 10^2$$

in the in-line and cross-wind directions, respectively.

The stiffnesses were provided, not by the model, but with two pairs of torsion bars incorporated into the two-degree-of-freedom gimbal system. Details of design and construction of the torsion bars are given in Section V.2.ii.a.

(d) Circular Cylinder

The circular model (Fig. 5.2) was made from an aluminium tube, of length 457 mm with an outer diameter of 76 mm. The wall thickness was 1.6 mm. Using Appendix 5.A, the moment of inertia, I, was calculated to be 3.39×10^{-2} kg m^2. This value is very close to that quoted for the square cylinder above.

V. 2 Design and Construction of Vibration Rig

A rig to which the models could be attached was designed and constructed to satisfy three conditions:

(i) The models had to be able to vibrate freely with two degrees of freedom in two mutually orthogonal directions. It also had to be possible to suppress one degree of freedom so that comparisons could be made.

(ii) The natural frequencies had to be modelled by introducing stiffeners from a source external to the model. This gave a certain amount of freedom, as only length and inertia-scaling requirements then had to be satisfied in constructing the models.

(iii) The effective structural damping of the model and support system had to be varied from an external source, allowing tests to be made over a wide range of damping.

The movement of the models in two mutually orthogonal directions was made possible by a unique gimbal (Section V.2.i). By incorporating torsion bars as an integral part of the gimbal, the required stiffness characteristics of the models were obtained (Section V.2.ii).

Models were attached to the gimbal by various plugs and fixing plates (Section V.2.iii).

An electro-magnetic system (Section V.3.i) was used to vary the effective structural damping of the models. The damper consisted essentially of a copper plate oscillating in an induced electro-magnetic field. The motions of the copper plate were coupled to the vibrations of the models so that damping of the motions of the plate induced damping on the vibrations of the model.

2.i. Gimbal System

A gimbal system to which models could be attached was constructed so that the models could vibrate in a vertical plane along any two mutually orthogonal directions.

Gimbal systems permitting one-degree-of-freedom motion are known. One system often used [76] consists of a centre-block connected to an enclosing support ring, both lying in the same plane. They are connected by a pair of torsion bars opposite to each other but with their longitudinal axes in the same line. When a model is attached to the centre-block, with the outer ring rigidly held, the model is then free to oscillate about an axis passing through the longitudinal axis of the torsion bars.

To extend the motion of the model to a second axis, orthogonal to the first but in the same horizontal plane, an intermediate ring and a second pair of torsion bars were added. The centre-block supporting the model was connected to the intermediate ring by the first pair of torsion bars. The ring was connected to the outer support ring by the second pair of torsion bars which lay in the same plane as the first pair but with the centre-line longitudinal axes normal to each other.

The motion of the models could be considered as being resolved into two rotational movements about two mutally orthogonal axes, both axes lying in the same horizontal plane. Vibrational movement of the models with two degrees of freedom was then possible, provided that the two axes of rotation correspond to the axes formed by the two pairs of torsion bars (Fig. 5.3).

The first pair of torsion bars, connecting the centre-block to the intermediate ring, were placed with their axis of the bars placed cross-wind to the mean wind direction. This allowed all motion of the model in the along-wind (in-line) direction. The second pair of torsion bars, connecting the intermediate ring to the fi xed support ring thus had their longitudinal axes in the in-line direction. The intermediate ring, which was free to rotate about an in-line axis, therefore allowed all motion of the model in-line axis, therefore allowed all motion of the model in the cross-wind (lateral) direction. This design made possible the model-simulation of structures vibrating in a linear mode with two degrees of freedom.

The three elements of the gimbal (Fig. 5.3) - centre-block, intermediate ring and outer support ring - were machined from a slab of duraluminum plate, 19.5 mm thick. Duraluminum was chosen because of its high stiffness, low density and ease of machining.

(a) Centre-Block

The centre-block (Fig. 5.3) was the carrier of the models. The block was rectangular in shape. In plan-view its dimensions of 89 x 76 mm were slightly greater than those of the models. The rectangular shape was choosen for two design reasons. The shape allowed the gimbal to be made as compact as possible while, at the same time, allowing adequate clearance for the torsion-bars bridging the centre block and the intermediate ring. Various holes were drilled and threaded in the block so that the attachment linkage (Section V.2.iii.) and the tube of the damping system (Section V.3.i.b) could be fixed to it. Two holes, opposite to each other, were carefully drilled into two vertical sides of the centre-block. These housed the first pair of torsion-bars. Great care was taken in aligning the two 'housing' holes.

This arrangement allowed the aligning longitudinal axes of the two torsion bars to lie along one line normal to the vertical faces of the block, When the gimbal was completed and placed in a horizontal plane, the torsion bars also lay in an horizontal plane. To fix the torsion bars to the centre-block, securely but not permanently, two holes for dowell pins (Section V.2.ii.a) were drilled on the top of the block.

(b) Intermediate Ring

The intermediate ring (Fig. 5.3) was rectangular with outer dimensions of 178 x 114 mm^2 and inner dimensions, 153 x 89 mm^2. Four holes, of 12.7 mm diameter were drilled through the ring at the midpoint of each vertical face. Opposite holes had their longitudinal axes coinciding. The two pairs of 'housing' holes were machined accurately so that the two pairs of torsion bars could lie in the same horizontal plane but normal to each other. Immediately above each hole, a small 4 mm diameter hole was drilled to accept dowell pins needed to secure the torsion-bars.

(c) Support Ring

The shape and dimensions of the support-ring are shown in Fig. 5.3.c. Two bore-holes were drilled in the suport ring to house the second pair of torsion-bars thus providing the link with the intermediate ring. Two holes for dowell pins were drilled in the support ring immediately above the two 'housing' holes.

Six holes were drilled along the perimeter of the support-ring so that the gimbal could be fixed firmly to the distance-ring (Section V.3.ii.a).

2.ii. Providing Stiffness to the Models

(a) Torsion Bars

Torsion bars, incorporated into the gimbal (Section V.2. i), provided the necessary model stiffness. Two different pairs of torsion-bars, each pair containing identical bars, were machined from a 12.7 mm diameter duraluminum rod. The torsion bars were each of overall length 50.8 mm. A central 25.4 mm portion of each bars was machined equally from opposite sides to form a flat, central slab. The appearance of the bars (Appendix 5.B).

The thickness, t, and breadth, b, of the central 'flat' portions were calculated using a procedure outlined in Appendix 5.B. The values of t and b that were obtained were as follows:

Pair of torsion-bars	1st	2nd
Connecting elements	Central block intermediate ring	Intermediate to support
Direction of longitudinal axes	In-line	
Direction of model deflection	Lateral	In-line
Required natural frequency of model (Hz)	10.22	9.08
Breadth, b, (mm) of each bar	12.7	12.7
Thickness, t, (mm) of each bar	4.04	3.73

The bars were held firmly in their housing by the 4 mm diameter dowel pins. Dowell pins chosen because, while providing excellent firmness in holding the torsion bars, they could be removed easily when required. This allowed different pairs of torsion bars to be substituted to give different external stiffnesses to the models.

(b) Strain-Gauges

From each pair of torsion-bars one bar was strain-gauged with a Tinsley torque-gauge, Type TK9/50/P/c, (Appendix A). A double pair of these torque-gauges was used in each bar so that

(i) temperature-compensation was obtained

(ii) a full-bridge network, as opposed to a half-bridge was used. This enabled the output sensitivity from the strain-gauge bridge to be doubled (Appendix 5.C).

The two chosen torsion-bars had the gauges bonded to one flat side. Sheathed wires were soldered to the four junctions of each strain-gauge pair for connections for the input and output of current.

The strain-gauges were connected to circuit-elements in the amplifier and demodulator units of a S E Laboratories Type 429 Carrier System (Appendix A) to form a bridge-network. The wiring diagram is shown in Appendix 5.C. The theoretical analysis of the relationship between torque exerted on the strain-gauges by the bars undergoing torsion and the resulting output from the strain-gauge full-bridge network is given in Appendix 5.C.

The mode of operation of the carrier-system was to feeing the bridge net-work from a low-frequency carrier of 3 kHz. The bridge was adjusted for balance so that, as long as the strain-gauges were unstressed, no output signal was produced. The application of torque on the strain-gauge changed its resistance (Appendix 5.C) and unbalanced the bridge so that the latter produced a proportional amplitude-modulation on the carrier signal. This was then suitably amplified and demodulated. The output was recorded either digitally with a D V. M or as an analogue signal on a magnetic tape recorder. The signal was also displayed on an oscilloscope.

2.iii. Attachment Linkage

The model was attached to the gimbal with a lining-system. This contained.

(i) two plugs, one for the square cylinder and the other for the circular. The plugs fitted into the base of their appropriate models,

(ii) the spacer, by which the models were raised to the required heights above the floor of the wind tunnel, and

(iii) the spacer-link, connecting the spacer to the gimbals.

(a) Spacer

The spacer (Fig. 5.4.b) was designed

(i) to securely link any one of the two models to the centre-block of the gimbal,

(ii) to raise the models to their correct height above the floor of the tunnel, modelling the plaza in the full-scale building (Section V.1.ii.a).

The spacer was machined from duraluminum to the dimensions given in Fig.

After the spacer was made, two further requirements became apparent; these were:

(iii) that provision should be made so that the square model could be tested at various flow incidences while the axes of vibration (governed by the orientation of the gimbal) remained the same,

(iv) that the gimbal should not be housed in a recess cut in the lower surface of the wind-tunnel, which would have meant the wind tunnel losing some of its structural strength.

Much time had been spent in constructing the spacer. It was therefore decided not to build another incorporating these further requirements but to make a few simple modifications.

Requirement (iii) was satisfied by making two different plugs, for insertion into the square and circular models.

To satisfy requirement (iv), a 'spacer-link' was built. It connected firmly the spacer to the central block of the gimbal. The plug, spacer and spacer-link, when in use, formed a 'thick' sandwich between the model and gimbal.

(b) Plugs

A square plug, 69.5 x 69.5 mm^2 was machined from a 15 mm thick duraluminum slab (Fig. 5.4.c). One horizontal face of the plug was machined to give a raised circular area, 2 mm high and 69.5 mm in diameter. The remaining depth of 13 mm of the square plug was inserted into the bottom of the square model. The plug was secured to the model with four grub-screws, one on each of its vertical sides.

The models had to be tested at varying angles of incidence with reference to a fixed system of axes (Fig. 4.5). The axes of vibrations of the models were governed by the arrangement of torsion bars with respect to the wind-axes (Section V.2.i). Incidence effects therefore had to be examined by rotating the model relative to the gimbal.

This was achieved by milling-out four grooves, in the form of a circular arc of radius 22 mm, subtended an angle of 60° to the centre. The machining required two separate operations. First, the grooves were sunk to a depth of 8 mm using a 7 mm diameter drill. Than a 5 mm drill extended the grooves right through the plugs.

The plug was fixed to the upper surface of the spacer element by inserting

a grub-screw, through each groove, and screwing it to 'fixing' holes in the spacer. If the screws were loose, the plug (and indirectly the model) could be revolved relative to the spacer. The lip, made by the two separate milling operations, was used to catch the head of the grub-screws. This enabled the plug to be securely fixed to the spacer.

The circular plug (Fig. 5.4.c) 72 mm in diameter and 8 mm thick, was machined from duraluminum. Holes were drilled and threaded in it. The plug could therfore be secured to both the circular model and the spacer element.

(c) Spacer-link

The spacer-link (Fig. 5.4.a) increased the separation between the spacer and the gimbal. This allowed the top surface of the gimbal to lie slightly below the bottom surface of the wind-tunnel floor. In housing the spacer-link, care was taken in cutting the hole through the tunnel floor, and the clearance between the spacer link and the edges of the hole was kept to a minimum.

The spacer-link, machined from duraluminum, was a disc 15 mm thick and 95 mm in diameter. The lower 3 mm of the disc thickness had its outside diameter reduced to 84 mm to give a slight clearance between itself and the intermediate ring, when the model was vibrating.

The spacer and the spacer-link were fixed to the centre-block of the gimbal with four grub-screws, each 32 mm long. Each screw passed through coincident holes 8 mm in diameter in the spacer-link and the spacer, and was then screwed into a threaded hole in the centre-block of the gimbal.

V.3 Damping and Housing Rig

3.i. Damping System

Damping was provided by electro-magnets generating eddy currents in a copper-plate, connected indirectly to the vibrating models, (Appendix 5.D). This method of damping has been shown [76] to generate a satisfactory representation of required structural-damping for models. It also has other applications [77].

One end of a thin-walled aluminium tube (Section V.3.i.a) was attached to the centre-block of the two degree-of-freedom gimbal. A circular copper-plate was fixed with a collar (Fig. 5.6.a) to a position along the longitudinal axis of the tube. With the tube hanging vertically from the centre-block of the gimbal, the copper plate lay in a horizontal plane. The plate passed between the poles of a pair of electro-magnets (Section V.3.i.c) The complete assembly of the damping-system is shown in Fig. 5.5.

(a) Tube and Collar

The aluminium tube of outer diameter 254 mm and 3.2 mm wall thickness was 457mm long (Fig. 5.6.a).

Each collar (Fig. 5.6.b) machined from a duraluminum bar, was attached to the tube by two grub-screws, tightened directly against the outside surface of the tube.

A collar was attached to one end of the tube, and screwed to the lower surface of the centre-block of the gimbal. The other collar fixed the copper-plate to the tube. This collar could be fixed at any station along the tube, allowing the position of the copper plate to be varied, if required.

(b) Copper-plate

The circular copper-plate (Fig. 5.6.a) was cut from a 1 mm thick plate.

Its diameter of 254 mm was wide enough to let the disc pass through the pole-faces of two electro-magnets. Two segments of the copper plate, lying near the periphery of the plate but at opposite ends of a diameter completely cut the magnetic field produced by the two electro-magnets.

(c) Electro-magnets and Power-Supply

Two electro-magnets, Type C, made by Newport Instruments Ltd were used. Their technical specifications are given in Appendix A.

The electro-magnets were mounted inside the case and fixed with bolts. They were placed on opposite sides of the case but with their corresponding pole-faces in the same horizontal plane. They were mounted so that they were skewed at 45° to the mean wind-axis (Fig. 4.5). This is shown in Fig. 5.7. Given the use of only two electro-magnets, this configuration was taken to distribute as evenly as possible the damping influencing the cylinder motion in the in-line and lateral directions.

The gaps between the pole faces were 7.5 mm, large enough to allow the motion of the copper-plate between them, but small enough to allow strong magnetic fields be set-up between each pair of poles.

Power was supplied to the electro-magnets from a Newport VR 3 DC supply power-pack (Appendix A). Variable damping was induced on the motion of the copper plate by varying the input supply to the electro-magnets, thus changing the magnetic flux between the poles.

The electro-magnets were cooled by pumping water around the electrical coils. The water, contained in a tank was re-circulated

through the coils using a 12 V dc water pump. A manifold system, made from PVC tubing, carried the water and distributed it evenly between the two electro-magnets.

3.ii. Support Rig

The model protruded through a hole cut in the floor of the wind-tunnel (Fig. 5.9). To minimise air-leaks, the hole had an all-round clearance of only 6 mm with respect to the spacer-link (Section V.2.iii.c).

The gimbal with the model mounted on it was placed on a supporting rig placed outside the wind-tunnel but immediately below the hole in the tunnel-floor. The rig (Fig. 5.5) consisted of a distance ring, a support plate, a cast-aluminium ase and a welded support table.

(a) Distance-Ring

The distance-ring was machined from a redundant pulley. The cast-iron pulley was in the form of two circular discs connected by a smaller diameter core. The discs were 310 mm in diameter and 6.4mm thick. The core was 12.7 mm long and 175 mm in diamter. A hole, of 150mm diameter was bored along the longitudinal axis of the pulley. This allowed the duraluminum tube of the damping system (Section V.3.i.a) to be connected to the centre-block of the gimbal (Section V.2.i.a).

Metal packing was inserted between the outer support-ring of the gimbal and the top surface of the distance ring to give clearance of approximately 8 mm. This allowed the centre-block and the intermediate ring of the gimbal to move freely without touching the distance-ring. The distance ring was not bolted to the support-plate (Section V.3.ii.b) but only held securely in place with

four ⌜ clamps (Fig. 5.11) to allow the gimbal system to rotate with respect to the co-ordinate system of the air-flow (Fig. 4.5).

(b) Support-plate

The support-plate was machined from a mild-steel plate. It had dimensions of 355.6 x 304.8 x 12.7 mm^3 (Fig. 5.8) and was fixed to the cast-aluminium case (Section V.3.ii.b) by four bolts.

The upper surface of the plate had a circular recess 2 mm deep. The recess thus helped to rotate the distance-ring (Section V.3.ii.a) and hence the gimbal. This allowed the axes of vibration of the models to be linedup with the wind-axes.

To measure the orientation of the axes of motion of the models w.r.t the wind-axes, two coincident scales were marked on the distance-ring and the support plate. The ring was securely fixed to the support plate with the ⌜ clamps.

(c) Cast-aluminium Case

While housing the damping-system (Section V.3.i) the cast-aluminium case (Fig. 5.7) also held the support plate and its contents (ie model, gimbal). The support-plate was bolted firmly to the case.

As the case was too low to cover the distance between the tunnel floor and laboratory floor, it was placed on a support-table (Section V.3.ii.d) and clamped with four G - clamps.

(d) Support Table

The support table was a welded construction of a thick mild steel plate 510 x 510 x 12.7 mm^3 supported by three splayed-out legs. At the end of each leg thre was a screw-adjuster to allow the table

to be raised, lowered and levelled. The legs were placed on rubber absorption pads to reduce the transmission of external vibrations to the gimbal and models.

VI GENERATED TURBULENT FLOW

This chapter is concerned with the analogue and digital analyses of the structure of the generated turbulence (Chapter IV). The first section deals with the results obtained and the second with their interpretation.

For the sake of convenience, the different generated flows are denoted as:

(a) Smooth (S) - ie with honeycomb flow straightener at wind-tunnel entry.

(b) Turbulent (T) - ie flow generated with the elliptical vortex generators, castellated.

(c) Turbulent with impressed profile (T_s) ie as in (b) but with the addition of the Cowdrey grid.

Superimposition of the bi-planar screens (Section IV.2.ii.d) on flows S, T and T_s are denoted by the addition of the identity number of the screen. For example, screen 1 with turbulent flow T is indicated by T + (1).

VI.1 Results from Analogue Analysis

1.i. Velocity Profiles

Analogue measurements were made of the velocity profiles using the total head rake (Section II.1.ii.d).

From the velocity profiles obtained in the working section, many parameters defining the nature of the various generated flows were deduced. These parameters, taken from profile measurements, were the power exponent, α. the surface drag coefficient, C_D, the roughness length, z_0, and the macro-visconsity, N. The method of obtaining these from the velocity profile plots is given in Appendix 6.A. Using the values of these parameters as a guide, the mixing devices (vortex-generators, grids, floor roughness and screws) were changed during preliminary experiments to achieve the best possible ABL flow simulation.

The results obtained in this way are discussed below in the order in which the preliminary experiments were made.

(a) Cowdrey's Grid

A grid designed to give a power exponent of 0.143 to the velocity profile was placed across the mounth of the wind-tunnel. For convenience, the simulated flow within the wind-tunnel is called the generated boundary layer (GBL). The velocity profile obtained in this way is shown in Fig. 6.1.a. There are two distinct profiles which blend together to give the full profile. The lower velocity profile, which extends up to

approximately 0.3 of the working-section height, has properties (Table 6.1) suggesting a power exponent near the theoretical, but it has very low surface shear properties. In fact, using Sutton's criterion for roughness, Eqn 4.5, the macro-viscosity, N, indicated a smooth-surface flow.

The upper 0.7 of the GBL has an exponent of 0.22, similar to a value given by Shellard [78] for metropolitan London. Shellard, however, obtained this exponent using the so-called effective heights defined by him as, 'the height at which the anemometer would register a speed equal to that actually observed if there were no obstructions in the vicinity'. It seems more appropriate to use Davenport's [54] value of 0.40. The surface-drag coefficient is much lower than that given by Davenport [54] for an urban terrain, but the full-scale surface roughness,

$$\left(z_0\right)_F = 3{\cdot}75\ \text{m.}$$

is much nearer the value quoted by Davenport (Fig. 4.2). The full-scale value is derived from the model scale value by using Jensen's criterion for modelling (Eqn 4.8) and the length scale factor, given in Eqn 5.2.

(b) Vortex-generator System

Using the vortex-generator system (elliptical vortex-generators and castellated barriers), the profiles (Fig. 6.1.b) and the velocity profile characteristics (Table 6.1) were quite similar to those obtained from the grid. No marked improvement was, therefore, obtained.

(c) Vortex-generator System and Grid

The Cowdrey grod was re-designed for a power exponent of 0.4 (Appendix 4.A). Using the vortex-generator system as well as the grid, improved profiles (Fig. 6.1.c) were obtained. These profiles, however, did not show the merging of two distinct profiles, even though the velocity-profile characteristics (Table 6.1) were much closer to the values hoped for (Section IV.1.i).

(c) Vortex-generator System, Grid and Surface Roughness

In order to eliminate the lower profile which covered about 0.3 of the GBL and to make the upper profile continue down to the tunnel floor surface, it was decided to introduce roughness (Section IV.3.iii) to provide the high shear stress required at the surface. This was done using evenly-distributed roughness elements which eliminated the lower profile and made the upper profile continuous (Fig. 6.1d). The flow parameters obtained by this method (Table 6.1) show good agreement with the values of α and C_{D_o} hoped for. It should be noted, however, that a much larger value for the roughness length, z_o, was obtained. It is assumed that this is the result of the large scatter of values near the surface. Since, according to Sutton's criterion, the flow is rough and the power exponent of the mean velocity profile is in agreement with that found over an urban environment, no further refinement in mean-velocity flow simulation was considered necessary.

(e) Vortex-generator System, Grid, Surface Roughness and Bi-planar Screens

As the intention was to examine the effects of turbulence characteristics of flow on the models, the bi-planar screens that were to be used (Section IV.3.iii) were tested in conjunction with the above system. The introduction of the screens at the mouth of the tunnel produced no marked change in either profile or mean velocity flow characteristics (Figs 6.1e and 6.1f). The only effect on the mean properties of the flow was to reduce the operating velocity range of the wind-tunnel.

1.ii. Turbulence Intensity Profiles

Turbulence intensity profiles of the incident-wind were measured at the model station using a straight hot-wire probe, DISA 55F31. The probe was clamped to a retort stand with the probe axis along the downwind x-axis while the wire axis was normal to the mean wind (ie the axis lay along the z-axis). Turbulent intensity profiles were determined by traversing the clamp along the vertical retort stand.

The hot-wire signals, corresponding to the velocity of the turbulent wind, was processed using the DISA equipment (Section IV.1). The hot wires were linearised to give a voltage output of 1.0 V for a mean wind speed of 10 m/sec.

DC and RMS components of the output voltage signal corresponding to mean and fluctuating components of the wind velocity were read on DISA 55D31 and 55D35 Voltmeters, respectively. The time-constant of the instrument was set, so that, after about three time-constants, fairly steady readings could be obtained. Because of the high turbulent intensities (20%) sometimes encountered, the time-constant used in both meters was $\sim$ 30 seconds.

Although it was not easy to take steady readings, because of the high turbulence of the flow, approximate profiles were obtained. Fig. 6.2a shows the change in intensity when the honeycomb was replaced by the EVG system and later when Cowdrey grids were added. For comparison, a theoretical curve is given using Eqn 4.13 and Davenport's values of α and C_{D_o} for an urban environment (Fig. 4.2) as well as those obtained from the mean-velocity profile plots (Fig. 6.1).

Fig. 6.2.b. shows the profile produced when the roughness elements (Section IV.2.ii.c) were introduced into the system comprising the EVGs and Cowdrey's grid. Theoretical curves are again given for comparison.

1.iii.Frequency Domain

Frequency domain analysis of the output from the hot-wire anemometers were made with the use of the Brüel and Kjaer (B and K) Type 1612, 1/3rd octave analyser (Section II.3.iii). For freqencies from 20 Hz to 2 kHz, the analysis was on-line. To analyse frequencies below this, the signals were recorded at 95.25 mm/sec. and then played back at a speed of 762.0 mm/sec.

With this speed change, analysis of the energy content of frequencies down to 2.5 Hz was possible.

Many analysis were made this way, although each took up to 45 minutes. Even then, the scatter in the low-frequency region was so large, that it was doubtful whether any useful information could be obtained. This scatter was due to two factors; the highly turbulent nature of the generated flows and the low damping of the internal meter of the spectrum analyser.

An example of a spectrum so obtained is shown in Fig. 6.3.

Fig. 6.3 shows that the points obtained with analogue analyses generally fell near the results obtained by digital means.

Digital analyses of auto-power spectral densities indicated (Section VI.2) the following:

(a) Reproduction of the spectra obtained by digital means means were excellent.

(b) The time taken to make the analyses was cut down dramatically, sometimes by a factor of 10.

(c) Analyses of the energy content of very low frequencies, (to 0.25 Hz) was possible.

Analogue analyses of power spectral density estimates were therefore replaced by digital analyses.

1.iv. Time Domain

The hot-wire anemometer signals were analysed using the DISA Time Correlation Analysis (TCA) system (Section II.3.ii). Fig. 6.4 shows an example of an auto-correlation plot.

Like power spectral density analysis, auto-correlation analogue analysis also took a long time. In the case considered (Fig. 6.4.), the maximum time delay was 100 msec. To prevent sudden turbulent bursts from overloading the pre-amplifiers of the TCA system a long intergrating time of 30 seconds was used. The total time taken for analysis was 10 minutes.

A comparison between plots was made with the auto-correlation plot obtained by digital means. Since good agreement was found it was decided that digital analyses should replace analogue analyses for time-domain measurements.

VI.2. Results from Digital Analyses

In order to determine the structure of the turbulence in the generated boundary layer, two DISA 55F31 straight hot-wire probes were used. The axes of the probes lay along the mean wind direction, with the wire-axes vertical The probes were placed at the model station, with the models removed, at heights of 450 mm (wire A) and 300 mm (wire B) from the wind-tunnel floor. It was considered necessary to monitor only these two points as the character of turbulence measured ($z/\delta \simeq$ 0.75 and 0.50) would give a representative picture of the generated flow.

The signals were conditioned before recording them on magnetic tape using the Sangamo-West tape recorder (Section III.1).
Using two DISA 55 D01 signal conditioners (Appendix A), the hot-wire signals had most of their DC component backed off. The resulting signals were then amplified and filtered using the low-pass filter set at 1 kHz with the roll-off set at 18 dB/octave. This cut-off frequency and rate was considered adequate because analogue analysis (Section IV.1.iii) of the signals using a Brüel and Kjaer 1/3 octave analyser, indicated very little energy content above 1 kHz. Also, as the signals were recorded through FM, the tape recorder acted as a low-pass filter by filtering components above 1 kHz when recording

at the usual speed of 95.25 mm/sec.

To obtain digitised data values for analyses, simultaneous analogue-to-digital conversions were made (Section III.2.ii.b) with the magnetic tapes played back at a speed of 95.25 mm/sec, Depending on whether the interest was in the high-frequency or low frequency regions of fluctuations, signals were pre-filtered at 1 kHz or 200 Hz respectively using the DISA signal conditioner as a low-past filter.

To satisfy the Nyquist criterion and to avoid aliasing (Section III.2) the sampling rate was set at either 2500 samples/sec or 500 samples/sec respectively. In all cases, the signals were amplified to cover the $\pm$ 10 V quantising range of the EAI 680 analogue computer in order to minimise quantising errors (Section III.3.i.b).

Many flows with different combinations of turbulence generating devices were tested, for conciseness in presentation, but because of lack of space, only a few representative cases are given here (Table 6.2).

2.i. Amplitude Domain

For amplitude domain runs, a sample of 4096 points per signal was used. The sampling rate was 2500 samples/second.

Using sub-routine PROB (Appendix B) the probability distributions of these signals were then made. In addition, PROB also calculated skewness and kurtosis of the digitised data (Section III.3.i).

The probability distribution curves so obtained are shown in Fig. 6.5. The plots also show the amount of skew and kurtosis of the signals.

Table 6.2 gives values of the mean (nearly equal to the magnitude of the backed-off DC value), the runs, skewness and kurtosis.

2.ii. Frequency Domain

The spectra were calculated using the Fast-Fourier Technique implemented in programme EARL (Section IV.3.i.d) and was Hanning filtered. The available bandwidth was covered in two stages. The higher range (1 Hz to 1 kHz) was obtained by dividing each record into 100 consecutive blocks of 2048 data points. The sampling frequency was 2500 samples/sec. The signal was low-pass filtered at 1 kHz with a filter having an 18 dB/ octave roll-off.

For the lower range (0.2 Hz → 200 Hz), the signal was re-sampled at 500 samples/sec. Each record was divided into 36 frames of 2048 samples. In all cases, the sampled values were stored in disc for subsequent analysis.

According to Eqn 3.30, a spectra computed from 100 frames indicates a statistical error of 10% while it is 17% for 36 frames. The spectra computed for the lower range had inherently more scatter than the composite spectrum. However, the agreement between the two in the two decades where they overlapped was shown to be very good. The higher range was, therefore, treated as the basic spectrum with estimates from the lower range used only to extend its bandwidth to 0.2 Hz.

The auto-spectra of the turbulence signals were plotted in the form of non-dimensional energy, $\log n \cdot G_u(n)/\sigma_u^2$ against logarithmic frequency, $\log n$. This form gave weighting to the high-frequency range of turbulence, where the energy was relatively low. Examples of such spectra are shown in Fig. 6.6.

An example of the coherence between the two hot-wires, A and B, is shown in Fig. 6.7.

2.iii. Time Domain

The auto-correlations of the turbulence signals were obtained by performing an inverse FFT on a Spectra. To avoid circular correlations (Section III.3.iii) before the spectra were computed, each frame was only half filled with real data values, the rest being all zeros. The first half of the resulting auto-correlation curves are shown in Fig. 6.8.

VI.3. Discussion

This section discusses the significance of the results obtained in the previous two sections.

3.i. Velocity Profiles

The velocity distributions obtained without any surface roughness on the tunell floor but with flow-mixing devices in combination or alone, showed that two distinct profiles existed through the GBL (Fig. 6.1.a). The over-all velocity distribution therefore had, in effect, an upper and lower profile. The transition in profile was not continuous but abrupt and occured at about 0.3 of the tunnel height when measured from the wind-tunnel floor.

On examining the values of the mean flow parameters (Table 6.1), the lower profile appeared as a smooth-flow regime when Suttons criterion of macroviscosity (Section IV.1.i) was applied. This was also confirmed by the low values of the power exponents, the surface drag coefficients etc. The upper profile, however, was more representative of a rough region. The value of the macro-viscosity indicated a rough flow, and the surface roughness length when scaled up (Section VI.2.i) satisfied Davenport's criterion for flow over an urban

terrain. The profile exponent, α, on the other hand, though satisfying Shellard's criterion (Section VI.1.i.a) did not satisfy Davenport's (Fig. 4.2). Similarly, according to Davenport, the extrapolated surface drag coefficient was much too low.

It seems probable that the reason for a rough-flow upper region and a smooth-flow lower region might be that the flow-mixing devices imparted a momentum deficiency to the top 0.7 of the GBL. The flow near the bottom 0.3 of the GBL, on the other hand, did not have any devices near the floor of the tunnel in order to destroy some momentum from the fluid flow after it had re-attached some distance down stream behind the castellated barrier.

The addition of surface roughness produced a remarkable improvement by removing the two distinct profiles in any one of the earlier wind-velocity distributions thus giving an over-all smooth profile (Figs 6.4d, e, f). The power-law exponents obtained from these profiles (Table 6.1) corresponded closely to those values quoted by Davenport (Fig. 4.2). In addition, Sutton's criterion of macroviscosity indicated a definite rough flow. The surface drag coefficients were also of the right order (Fig. 4.2) and the only deviation from mean flow properties seemed to be the surface roughness lengths. This was probably because it was impossible to monitor the wind-flow distributions closer to the tunnel floor and because it was necessary to extrapolate from measurements made at points relatively further away from the tunnel floor. As stated earlier, this did not make it possible to satisfy totally Jensen's criterion for modelling (Eqn 4.8), but it was felt that the main requirements for mean flow exponent and surface drag coefficients were quite satisfactory.

3.ii. Turbulent Intensity Profiles

With EVGs or EVGs and a Cowdrey grid placed in the flow, the longitudinal intensity profile had a uniform value of about 10% from about a quarter of the tunnel's height (Fig. 6.2.a).

Davenport's theoretical curve suggests intensities of about 15–20%. In the lower quarter an even greater difference appeared with the theoretical curve predicting intensities much higher than 20% then the experimental curves lay between 10 and 20%.

Addition of roughness elements made the turbulent intensity profile in the lower quarter much nearer to the predicted theoretical values but the smooth upper profile obtained previously was distorted, indicating low turbulent intensity (10%) in the half-way region of the profile. In the lower quarter, however, there was good correspondence with the theoretical curve based on Davenport's values for α and C_{D_o}.

3.iii. Amplitude Domain

Within the limits of accuracy in which full-scale measurements are termed Gaussian, inspection of the normalised probability density function plots (Fig. 6.5) of the logitudinal fluctuating velocity in SBL are also Gaussian. These and other amplitude probability density plots for velocity fluctuations give negligible skewness values, though they deviate slightly from a theoretical normal distribution in being somewhat flatter (kurtosis $\simeq$ 2.7).

3.iv. Frequency Domain

Harris's proposed theoretical form for the spectra of the atmospheric velocity fluctuations in the longitudinal direction (Section IV.1.ii.b) were evaluated according to the method given in Appendix 6.8. These theoretical curves were superimposed on the spectra obtained experimentally (Fig. 6.6.

If integral length scales of turbulence was used, there was no close correspondence between the theoretical curves and the experimental curves, they agreed in form. This result was not unexpected, since the semi-empirical theoretical forms diverge even from full-scale atmospheric results.

On the other hand, Kaimal's empirical form for the longitudinal velocity spectra (Section IV.1.ii.b) show a good fit. By using the modified frequency point n_i where n_i is the intercept of the extrapolated inertial sub-range spectrum with the $n.G_u(n)/\sigma_u^2 = 1$ line, all the spectra were brought into coincidence on the -2/3 line. Table 6.3 shows the variation of n_i for the various flow conditions tested.

All spectra showed two distinct regions. The first, where the spectral energy varied as n^{-1}, is shown on the $n.G(n)/\sigma_u^2$ curve as a plateau region. Within this region, strong production of turbulence energy takes place [57].

The second region, where $n.G(n)/\sigma_u^2$ varied as $n^{-2/3}$, is the inertial sub-range in which ν is unimportant and ϵ is the determining physical parameter [57]. For the purpose of illustration, lines with an index of - 2/3 have been superimposed on auto-spectra curves (Fig. 6.6. It can be seen that, although there is close agreement with the

dimensionally correct - 2/3 index, where indices are specifically determined, slight departures from - 2/3 can be found. These departures may be merely a statistical uncertainty in the determinations, or they may be a consequence of some input or extraction of turbulent energy in the range of frequencies considered, a circumstance which, in similarity theory, is assumed not to occur.

Various length scales of turbulence may be defined. Bearing in mind the difficulty in interpreting these values (Section IV.1.ii.d), the scales can give a qualitative feel to the turbulence structure.

Using Eqn 4.16, an integral scale length, L_x, is found to be $L_x = 0.04\ \bar{U}_{ref}/n$. These values are given in Table 6.3.

Caution must be exercised when using the first point in supposedly stable spectra to determine scale length. Fig. 6.6.b.i. shows that such a definition would give wrong results as the spectral energy, after passing the plateau, started to increase again.

A further scale, L_{max}, may be defined by

$$L_{max} = \bar{U} / n_{max}$$

where n_{max} is the peak-energy frequency point.

From a theoretical analysis of Eqn 4.15, it is shown that

$$n_{max} = 4 \cdot n_i$$

This result was verified experimentally.

In conclusion, it was decided that an adequate representation had been made of the spectrum of the longitudinal velocity fluctuations with the ABL within the simulated boundary-layer in the wind-tunnel.

3.v. Time Domain

Figs 6.8 show the exponential decay of the auto-correlation curves, characteristic of turbulence signals. Ideally, the curves should initially drop off steeply and then decay towards zero as the time-lag τ becomes larger.

These auto-correlation curves, however, did not behave this way. Even though there was an initial steep decay, the curves went below the horizontal time-axis, attaining negative correlation values.

This implies that the signal record was not long enough. The maximum time-lag τ_{max}, considered here was only 500 msec. This means that a longer record was necessary for an auto-correlation curve which finally decayed to zero. This could have been achieved by reducing the number of groups into which the digital record was divided, giving more correlation points. This procedure, however, would have resulted in less statistically accurate estimates, since the auto-correlation function was calculated from the spectra via inverse FFT.

It is useful to note that the original analogue DC back-off and the subsequent digital removal of any residual mean DC level successfully resulted in $R(\tau)$ not having a positive bias for large τ.

Calculating the exact integral time-scale of turbulence from these curves was difficult, but a time-scale of turbulence could be estimated from these curves. This was achieved by shifting the origin of the time-axis (ie, horizontal axis) to the point where $R(\tau) = R'$ for large values of τ Re-scaling the correlation values so that $R(0) = 1$ with respect to the new-origin and estimating the area under the auto-correlation curve and the new axis gave the new time-scale. Table 6.3 gave such estimated values and comparison could be made with values obtained from the corresponding auto-spectra (Section VI.3.iv).

Care had to be taken in interpreting these scales bearing in mind the reservations given in Section IV.1.ii.d.

3. vi. Comparison with ESDU Parameters.

The 'correctness' in modelling the generated boundary layer was evaluated by comparing it with the general description of the atmospheric boundary layer.given by Engineering Science Data Unit (ESDU), London. All the generated flows were compared with ESDU data. The generated flows that were finally used showed adequate correspondance. For example, the flow generated by the vortex-generator system with the Cowdrey grid,in the absence of any bi-planar screens (i.e. T_s flow) was compared with ESDU parameters with the following results.

(a) Velocity Profile Exponent (α)

The power law exponent of the GBL, T_s, was 0.39 (Table 6.2). This compared favourably with the value of 0.35 quoted by ESDU Item No. 72026 for centres of large towns and cities with concentrations of very tall building blocks.

(b) Surface Roughness Length (z_o)

ESDU 72026 quotes a value of $(z_o)_F = 1.5$ m. The simulated value $(z_o)_M$ of 1.253×10^{-2} m. (Table 6.1), is therefore too high if the length scaling of 1:850 (Section V.1.iii.) is used. To determine whether the high value of $(z_o)_M$ was because the zero-plane displacement, d , was neglected, a curve of U/U_{ref} vs. z/δ was plotted (Fig. 6.1.g). d/δ can be seen to lie between 0.0 and 0.05. Assuming that d/δ took the maximum value of 0.05, the profile data was re-fitted to the logarithmic law (Eqn 4.2) over the expected logarithmic region .. From this plot, the estimate of $(z_o)_M = 0.37 \times 10^{-2}$ m. was obtained. indicating $(z_o)_F = 3.1$ m., much higher than the quoted value of 1.5 m. This value of 3.1 m., however, was near to the value of 2.7 m. obtained by Counihan in his simulation [69].

(c) Turbulent Intensity Profile.

Using ESDU 74031, an expected full-scale profile was drawn (Fig. 6.2.6). The experimental curve corresponded to the full-scale profile in the lower region of the generated boundary layer. In the middle region, however, the experimental profile was less (by I = 5%) than the full-scale, but it was slightly higher in the upper regions.

(d) Probability Density Distribution

According to ESDU 74031, atmospheric turbulence can generally be considered 'normal' or 'Gaussian'. Deviations from this distribution sometimes occur, however, when theeturbulence contains 'patches' of a significantly non-Gaussian nature. Fig. 6.5 for T_5 shows that the probabilty density distribution was, in general, Gaussian, though with a slight skew and kurtosis (Table 6.2).

(e) Frequency Domain

ESDU 74031 suggests a Von Karman spectral equation of the form

$$\frac{n \cdot G_u(n)}{\sigma_u^2} = \frac{4\tilde{n}}{(1+70.8\,\tilde{n}^2)^{5/6}}$$

wher $\tilde{n} = n \cdot L_x / \bar{U}$ sufficiently represents the full-scale spectrum of the longitudinal velocity of atmospheric turbulence under strong-wind, neutral conditions.

The above equation was fitted to all the experimental spectra so that there was a good overall fit to the spectrum points. Fig.6.6. for T_5, shows that the experimental spectra followed the above spectral form very closely.

(f) Length Scales of Turbulence

From the above equation, it can be shown that

$$L_x = 0.1456\,\bar{U}/n_{max}$$

Once the Von Karman equation was fitted to the experimental points, the value of n_{max} at which the curve had its peak value was determined. Thus the length scale L_x was calculated. These values are recorded in Table 6.3 .

These values show good correspondence with the length scales obtained by other methods.

Comparison with design full-scale values, obtained from ESDU Item 74031 indicated that the length scales of turbulence obtained in the wind-tunnel were about four times smaller than those found in the atmosphere.

VII VIBRATION MEASUREMENTS OF MODELS

This chapter describes the measurement (Section VII.1) of the model vibrations, the results obtained (Section VII.2) and their analyses (Section VII.3). The apparatus and procedures have been dealt with fully in previous sections. Reference will be made to the relevant sections, when necessary.

Section VII.1 describes the method of estimating the induced structural damping. Descriptions of various combinations of models tested in generated flows with different characteristics are also given. This section also describes the calibration of the strain-gauges for subsequent analogue analyses.

Section VII.2 gives a selection of the results obtained. Only amplitude domain results are given for analyses using analogue techniques because of the difficulty experienced in analysing the other two domains. To overcome this, digital analysis is shown to be a powerful method of analysing the narrow-band random signal responses obtained from the model vibrations. All three domains, amplitude, frequency and time, are analysed using digital techniques.

Section VII.3 gives a discussion of the results obtained in Section VII.2 and uses both analogue and digital results to describe the various response characteristics of the different models excited by differently generated flows. Additional data on the wake structures are introduced to explain certain phenomena more fully. Part of this section deals with the difference in response of the models with only one degree of freedom of movement (ie lateral only) compared with two degrees of motion.

VII.1 Measurements

1.i Structural Damping

External damping was introduced into the vibrating model system by using the electro-magnetic damping system described in Section V.3.i.

The amount of damping, proportional to the magnetic field strength of the electromagnets, was controlled by adjusting the strength of the input current fed into the electro-magnets.

At constant current inputs, the models were displaced in still wind conditions. Decay in the amplitude of the vibrations picked up through the strain-gauge system (Section V.2.ii.6) were amplified and recorded using an ultra-violet (UV) trace recorder (Appendix A). Examples of such traces for vibrations of the models in both the in-line and lateral displacement directions are shown in Fig. 7.1.

Using traces such as these, the logarithmic decrement (log dec) of damping, δ_s, for various input currents, i amps, were obtained for the square and circular models. δ_s were calculated from the traces using the methods described in Appendix 7.A. The 'area' method described in Appendix 7.A was used as the standard method with the other methods used as checks. The variation of δ_s versus i for the square model is shown in Fig. 7.2.

1.ii. Calibration of Strain-gauge Output

The models were attached in turn to the gimbal system. The strain-gauge responses were calibrated by applying horizontal loads through a pulley system to the top of the cylinders. The horizontal loads, applied at the top of the models, were either in the lateral or in-line

directions and the corresponding voltage values from the strain-gauge system were noted. The tip displacements were measured with a Wayne-Kerr deflection meter (Appendix A). The meter worked on a principle of capacitive measurements with the capacitance proportional to the gap between the test surface and a flat-faced probe.

A calibration curve of tip deflection versus strain-gauge output voltage is shown for the square cylinder in Fig.7.3.

1.iii. Testing Configuration

Tests were made on the square (Sq) and circular (C) cross-sectional models. The rotation of the square model by 45^{o} with respect to the incident mean-wind flow enabled the testing of a 'wedge' (W) model configuration.

The models were free to vibrate in two mutually perpendicular directions. The gimbal was set so that a model mounted on it could vibrate either in-line with or lateral to the mean wind direction. For convenience, vibrations in these two mutually perpendicular directions were called 'in-line' or 'lateral' vibrations. Models free to vibrate in the two mutually orthoginal directions were referred to as two-degrees-of-freedom (2 DOF) models and models with one direction of vibration suppressed as(1 DOF) models. For the results shown in this chapter, the 1 DOF is free to vibrate in the lateral directions with the in-line vibration suppressed (Section V.2.i.d).

Vibration tests were made in three basically different flow conditions described in Chapter VI.

1.iv. Analogue Measurements of Vibrational Characteristics

From the large amount of data gathered, only those test runs which indicate important characteristics are shown and discussed in this chapter.

The mean and fluctuating output voltages obtained from the amplified strain-gauge signals were monitored on DISA DC and RMS meters (with time constants of 30 secs). They represented the static and fluctuating components of the amplitude of vibration of the various models. Because of the tendency to fluctuate with a random periodicity, each amplitude reading was obtained by monitoring the signal for a period of about 120 seconds and noting a consistent maximum value.

As expected, mean DC value of the in-line vibration signals were two orders of magnitude greater than the corresponding lateral oscillations. Therefore, mean DC values for lateral oscillation were neglected.

1.v. Digital Analysis of Vibrational Characteristics

Because of the inadequacies of the available analogue techniques (Section II.3), frequency and time domain analyses were made digitally.

The signals, representing the vibrations, were recorded on magnetic tape at a recording speed of 95.25 mm/sec for subsequent digitisation and analysis. The signals, before recording, were amplified and low-

pass filtered at 25 H_z (with a roll-off of 18dB/octave) using DISA 55D26 signal conditioners (Appendix A).

From analyses of the decayed amplitude traces (Section VII.1.i) the minimum and maximum structural damping values (Fig.7.2) for the square model were found to be

$$\xi_{min} = 1.52 \times 10^{-2}$$

and $$\xi_{max} = 5.67 \times 10^{-2}$$

since $\delta_s \simeq 2\pi\xi$ (Appendix 5.D.)

This gives Q-values (Appendix 7.A) of

$$Q_{min} = 33$$

and $$Q_{max} = 9$$

using the natural frequency of oscillation of 9.6 Hz for the square cylinder (Section VII.3.ii.b).

Using the definition of Q-values given in Appendix 7.A, half-power band-widths, δn_Q, were obtained for low- and high-damping cases.

Therefore $(\delta n_Q)_{min} = 0.29$ Hz

and $(\delta n_Q)_{max} = 1.09$ Hz

In the case of digital estimates of narrow band response spectra, in addition to the standard error (Eqn 3.30), an additional bias error, ϵ_B [34], was introduced.

It was decided to analyse the signals so that an 'effective' resolution band-width of

$$\delta n \simeq 0.125 \text{ Hz}$$

was obtained.

From a graph of $\delta n_a/\delta n$ versus ϵ_s [34], the bias errors were estimated to be less than 4% and 1% for the low- and high-damping cases. Thus, the resolution of digitisation was considered adequate.

Because of the length of record available, only 36 frames were averaged for each spectrum. This gave a theoretical standard error of $\epsilon_s = 17\%$. Therefore the errors involved in spectral estimation for the cases of low and high damping were 21% and 18% respectively.

To speed up analyses, the tapes were played back at a speed of R_p = 762 mm/sec, giving a speed-up factor r ($= R_p/R_r$) of 8.

Pre-analysis showed that the signals did not contain any significant energy above 25 Hz. Because of the speed up, the DISA 55D26 low-pass filter was set at 200 Hz (8 x 25 Hz) with a cut-off rate of 18 dB/octave.

The speeded-up signals were digitised at a sampling rate of f_s = 500 samples/sec. For each frame of data, 512 samples were obtained.

Because of the speed-up factor, all frequencies were multiplied up by a factor of 8. Hence the true resolution band-width was

$$= \frac{1}{r} \cdot \frac{f_s}{N} \qquad = \frac{1}{8} \times \frac{500}{512}$$

$$= 0.122 \text{ Hz}$$

Table 7.1 describes the various model/flow configurations which are a representative sample of the many test runs that were digitally analysed. The results obtained from this sample are discussed in Section VII.3.

VII.2. Results

2.i. Damping

From the values of structural damping, δ_s, obtained (Section VII.1.i) the non-dimensional damping coefficient, c_s, ($= 2m\delta_s / \rho_a D^2$) could be evaluated, since, for the

square model, $2m/(\rho_a D^2) = 5.483 \times 10^2$

circular " , " $= 1.938 \times 10^2$

wedge " , " $= 2.742 \times 10^2$

where m is the modal mass per unit length and D is the width of model face.

2.ii. Analogue Measurements

The mean and fluctuating values of the strain-gauge signals obtained from various model and flow combinations were converted from voltages to tip displacements using calibration curves such as Fig. 7.3. The values were then normalised by D, the width of face normal to the

mean wind direction, to give non-dimensional displacements,

The various curves of mean and fluctuating amplitudes of vibration of the models are shown in Fig.7.4 for the square model, Fig. 7.5 for the circular model and Fig. 7.6 for the wedge model.

2.iii. Digital Analysis

For each signal, 36 frames of data, each containing 512 numbers, were obtained. The data was acquired by simultaneously sampling the two channels containing the lateral and in-line vibration signals for each test configuration. Amplitude, frequency and time domain analyses were then made for each signal by using the digital analyses computer programme (Appendix B) discussed in Chapter III.

For joint probability density analyses a frame of 4096 samples per signal was taken. The number of samples was limited by the amount of core space available in the ICL 1905E computer during subsequent analysis.

In addition to the auto- and joint-probability density distribution (Section II.2.i.e), two further distributions, the cumulative probability density distributions and the distribution for the envelope of fluctuations (both described below), were evaluated for the vibration data.

(a) Amplitude Domain - Results for Individual Records.

From digital analysis in the amplitude domain, Table 7.1 was constructed giving mean, variance, skew and kurtosis values for both in-line and lateral oscillations of the various cylinders in the many cylinder/flow/damping configurations that were tested.

The normalised probability density distributions of lateral and in-line amplitudes of vibration for the square and circular cylinder are shown in Figs 7.7 and 7.8 respectively.

(b) Amplitude Domain - Cumulative Probability Distributions

The amplitude response obtained from the square-section model, oscillating with 2 DOF in the turbulent shear flow, T_s, was analysed for three different cases;

(i) low structural damping, δ_s and high reduced velocity, U_r;

(ii) high δ_s and high U_r; and

(iii) low δ_s and low U_r.

Using the subroutine PRØB (Appendix B), the mean components were removed from each signal, leaving the fluctuating in-line, $x'(t)$, and lateral, $y'(t)$, components. These in turn were normalised by their standard deviations, σ_x and σ_y, to give fluctuations,

$$Z_x = x'/\sigma_x$$

and

$$Z_y = y'/\sigma_y$$

having zero means and unit variances.

Excitations caused by the response of structures to a forcing turbulent wind, in both the in-line and lateral directions are usually assumed to be independent. This is because the excitation mechanisms in both these directions are different. The amplitude probability density distributions of these individual deflections, can also be shown to be Gaussian (Figs 7.7 and 7.8).

According to Melbourne [79], the majority of cases of structures oscillating under wind action deal with a lightly-damped system

oscillating at one fundamental frequency. It is therefore more relevant to express the probability distribution in terms of up-crossings rather than on a time basis.

The number of up-crossings per unit time of a stationary random process, Z_+ is given by [79].

$$P(>z) = \exp\ (- z^2/2)$$

where z has zero mean and unit variance.

The above distribution, which is Rayleigh, belongs to a class of distributions called Weibull [50]. The Weibull distributions are represented by,

$$P(>z) = \exp\ (- z/c)^k\ )$$

For a normally-distributed process, $k = 2$ and $c = \sqrt{2}$.

Expanding the above equation gives

$$\ln \{ - \ln\ P(>z)\} = k \ln z - k \ln c.$$

For a pure sine wave, $k \to \infty$ while for a highly intermittent signal, $k < 2$ [80].

The cumulative probability distributions of up-crossings for the displacements Z_x and Z_y of the models were evaluated using SUBROUTINE WEIBULL (Appendix A).

Representative cases of the cumulative distributions for the lateral vibrations are given in Table 7.2 which contains values for the square model in turbulent with shear flow for three combinations of

wind speed/damping described at the beginning of this section.

Fig. 7.9 is a graph with the values in Table 7.2 plotted to indicate the influence of speed and damping on the lateral vibrations of the square model.

Fig. 7.10 gives cumulative probability distribution graphs for the lateral vibration of the circular and wedge models in turbulent with shear flow with low damping and a mean wind speed of 9.5 m/sec.

(c) Joint Probability Distributions

The joint probability distribution between the two signals, lateral (z_x) and in-line (z_y) were calculated from 4096 pairs of simultaneously-sampled data values according to Section II 2. i.e.

Table 7.3 shows the joint probability distribution $P(z_x, z_y)$ obtained from the digitised data using SUBROUTINE JTPROD (Appendix B).

For purposes of comparison, bi-variate normal distribution values, obtained from Bendat and Piersol [34] are included (shown in brackets) in Table 7.3.a.

(d) Envelope of Fluctuation

While information on the probability distributions of x and y are suitable for wind-tunnel modelling, architects find it more convenient to deal with the total vector fluctuations (r, θ) where

$$r(t) = \left[x^2(t) + y^2(t)\right]^{1/2}$$

and

$$\theta(t) = \tan^{-1}\left[x(t)/y(t)\right]$$

Suppose that the joint probability density distribution $p(x,y)$, is known

Then $$p(x,y)\cdot dx\cdot dy = p(r\sin\theta, r\cos\theta)\, J\cdot dr\cdot d\theta$$

where the Jacobian, $$J = \left|\frac{\partial(x,y)}{\partial(r,\theta)}\right|$$

$$\therefore p'(r,\theta)\, dr\cdot d\theta = p(x,y)\cdot dx\cdot dy$$
$$= \frac{1}{2\pi}\cdot\exp\left\{-\frac{1}{2}(x^2+y^2)\right\} r\, dr\cdot d\theta$$
$$= \frac{r}{2\pi}\exp\left(-\frac{r^2}{2}\right) d\theta$$

assuming normal and uncorrelated distributions.

Hence the probability of obtaining a displacement between r and $r+\delta r$ is,

$$p'(r)\, dr = \int_0^{2\pi} p'(r,\theta)\, dr\cdot d\theta = r\cdot\exp\left(-r^2/2\right) dr$$

Considering r to be positive,

$$P(r) = \int_0^{\infty} p'(r)\cdot dr = \exp\left(-r^2/2\right)$$

The above Rayleigh distribution is similar to a particular form of the Weibull distribution with $k=2$, $c=\sqrt{2}$.

From the two simultaneously-sampled records, of 4096 numbers each, (z_x, z_θ) values have been calculated from (z_x, z_y) values using the SUBROUTINE VECTOR (Appendix B). Using SUBROUTINE WEIBULL, $P(r)$ has been plotted in Fig. 7.12. for the representative case of the square model oscillating in a turbulent shear wind flow.

(e) Frequency Domain.

The digitised data of the in-line and lateral vibration signals of the models in various flow configurations were analysed using the FFT

programme (MASTER EARL, Appendix B) to obtain frequency domain information.

The auto-spectra were plotted in the form of non-dimensionalised energy $G(n)/\sigma^2$ against frequency, n Hz. The data were also re-plotted in the form of,

$$\log_{10}\{G(n)/\sigma^2\} \quad \text{v.s} \quad n$$

so that any 'echoes' as well as the dominant natural frequency could be seen.

These spectra are shown in Figs 7.13-7.15.

(f) Time Domain

Inverse Fonrier transforms were performed on the above spectra according to the methods described in Section III.3.iii. These correlation curves were put out on a graph-plotter controlled by the ICL 1905E. The auto-correlation curve can be seen in Figs 7.16 – 7.18.

VII.3. Discussion of Results

3.i. Analogue Measurements

In this sub-section, results obtained from analogue analyses of the mean and fluctuating components of the lateral and in-line oscillations are discussed. It must be remembered that all signal levels have been converted to tip displacements and normalised by the width of face normal to the mean flow. The value of the width for the wedge was taken to be the same as for the square.

(a) Mean Component

It was found that the mean component, if any, of the lateral component in all cases was two orders of magnitude less than the in-line component. Hence, lateral mean levels were neglected and the analysis is confined to the in-line component.

a.1. Effect of Wind Speed

For all models in different flows, an increase in wind speed produced a corresponding increase in tip deflection.

a.2. Effect of Damping

The effect of increasing the damping was to reduce slightly the mean tip deflection, irrespective of the model or the nature of the generated wind.

a.3. Model

In similar flow/damping configurations, the square and wedge models gave a strain-gauge signal with nearly equal means. The circular cylinder signals, however, were much lower.

The normalised tip deflections were such that

$$\eta_{(\text{square})} \simeq \eta_{(\text{wedge})} > \eta_{(\text{circular})}$$

a.4. Nature of the Flow

It can be seen that for all models, the nature of the generated flow in which it was situated influenced considerably its in-line mean response. The response was greatest in the turbulent with shear flow

and least in smooth flow. It is therefore very necessary in modelling mean in-line response that the flow simulated should not only be turbulent, but that it should also have a shear profile.

(b) Fluctuating Component

Inspecting Figs 7.4 – 7.6 and Table 7.1 it is possible to generalise to some extent on the influence of various parameters (ie nature of generated flow, damping, degrees of freedom etc) on the fluctuating forces experienced by the various models.

b.1. Direction of Oscillation

It was shown that the r m s component for lateral vibrations was usually much greater than for the in-line vibrations. The increase for low-damping tests was usually between 5 and 10 times greater. This ratio decreased to between 5 and 2 times as the damping was increased.

b.2. Model Shape

From Fig. 7.4–7.6 it was seen that the normalised lateral vibrations of square models were such that

$$\eta_{sq} \simeq \eta_w > \eta_c$$

This pattern is shown for both smooth and turbulent flows. The square model results were compared with those given by Whitbread and Scruton [31] While showing similar trends, the values obtained were about half those given by Whitbread.

The in-line vibrations followed a pattern similar to the lateral but the differences in amplitudes were not so marked in smooth-flow conditions.

b.3. Nature of Flow

Changing the generated flow from smooth to turbulent drastically altered the fluctuating response of all models. Both the lateral and in-line r m s values increased.

But what is more important is that the response was greater in turbulent wind with shear profile than in uniform turbulent flow. This increase was greater in the in-line direction (20-40%) than in the lateral direction (5-30%). Modelling in turbulent wind gave consistently higher values for both fluctuating and mean deflections, $\eta_{r.m.s.}$ and $\eta_{D.C.}$ if the flow had a shear profile impressed. Caution should be exercised, however, as the T_s flow had a turbulent intensity profile slightly higher than the T flow.

b.iv. Damping

The effect of damping was to reduce considerably the fluctuating amplitudes of vibrations in both lateral and in-line directions.

6.v. Degrees of Freedom

Figs 7.4-7.6 show the effect of restricting the movement of the models to the lateral direction of vibrations. An interesting feature was seen in smooth-flow conditions when the rms values of lateral vibrations with two DOF exceeded the values obtained with one DOF. In some cases, the variation was 100%.

3.ii. Digital Analysis

This section discusses the results obtained in Section VII.2.ii for the amplitude, frequency and time domains of the model vibration records.

a. Amplitude Domain

From Table 7.1, various characteristics of the lateral and in-line vibrations were deduced. The mean and rms values were not normalised and thus are given as voltages. It must be emphasised that the amplitudes of oscillation had a tendency to fluctuate with a random periodicity (Fig 7.19) and this tendency increased with the more turbulent flows.

In direct analogue measurement, the procedure adopted was to monitor the amplitudes over a long period of time with meters having a considerable time-constant value (Section II.3). In digital analyses, however, it was assumed that the fluctuations in amplitude were smoothed by re-playing at high speed (r = 8) and sampling at a fast rate.

a.1. Mean DC Component

(i) For all cylinder/flow combinations the in-line values were approximately two orders of magnitude (10^2) greater than the corresponding lateral values, confirming analogue measurements (Section VII.3.i). This was to be expected since the mean-wind direction in all cases corresponded to the in-line direction of motion of the cylinders. Consequently, the models registered the effect of the mean-wind speed as a steady (DC) force only in the in-line direction. The discussion on mean DC values therefore concerns only the in-line DC component.

(ii) Runs (2) and (3) showed that an increase in damping decreased the mean values, a result confirmed by analogue measurements.

(iii) In T_S flows, ie where the turbulence had a shear profile impressed by the use of a Cowdrey grid, values were about 20% higher than for the turbulent, T, case. This feature can be seen by comparing runs (2) and (5) for the square, runs (6) and (7) for the wedge, and runs (8) and (9) for the circular models.

(iv) In similar flow conditions and equal damping δ_s , the square and wedge cylinders gave signals indicating equal mean tip deflections, while the circular model had a value about 50 % lower.

a.2. rms Component

(i) In all cases, the fluctuating (rms) component for lateral vibrations was two to three times greater than for the in-line vibration thus confirming analogue measurements.

(ii) An increase in structural damping decreased the intensity of vibrations in both lateral and in-line directions. This is confirmed by direct analogue measurements.

(iii) In turbulent with impressed shear flow (τ_s), the fluctuation of the models was greater than in turbulent (τ) flow. This variation was greater in the in-line direction (20–40%) than in the lateral direction (2–30%).

(iv) Under equivalent flow conditions, the square model had greater fluctuation (rms) in tip deflection amplitudes than the circular model which in turn had larger values than the wedge model.

(v) With the in-line freedom of motion suppressed (ie 1 DOF only), the lateral rms values of vibration were 20–40% greater than in the 2 DOF case for all models tested in similar generated-

flow conditions. This can be seen by comparing runs (2) and (15) for the square, runs (7) and (16) for the wedge and runs (9) and (17) for the circular model.

a.3. Auto-Probability Distributions

(i) Although the amplitudes of vibrations of both the lateral and in-line oscillations of all models in different flows did not indicate significant deviations from normal probability density distributions (Fig.7.7–7.8), it was possible to detect a slight negative skewness. Table 7.1 shows that this negative skewness was more marked with the in-line oscillations than with the lateral.

(ii) Kurtosis

There are slight deviations from the normal distribution for both the lateral and in-line oscillation amplitude probability density distributions (Figs 7.7). Results (Table 7.1) show that the distributions are flatter (kurtosis < 3.0) for the lateral while being steeper (kurtosis > 3.0) for the in-line oscillations. This is quantitative confirmation of the spiky signals seen in the traces of in-line oscillations (Fig. 7.19).

a.4. Cumulative Probability Distributions (CPD)

Fig. 7.9. shows the effect of varying structural damping and incident wind speed on the CPD of the lateral vibrations of the square model. The distributions could be represented over various $z_y (= y'/\sigma_y)$

regions by straight-line segments. The discontinuity occurred at about $z_y \simeq 2.7$. In all cases, the value of the exponent k of the Weibull distribution was less than 2.0, indicating the intermittent nature of the vibration signals (Figs 7.19). This was because the amplitudes had a tendency to fluctuate with a random periodicity. Fig. 7.9 shows that this tendency was more dominant in the less structurally-damped cases. The influence of wind speed on the CPD was negligible.

The wedge and circular models showed a similar intermittent nature of their signals (Fig. 7.10).

a.5. Joint Probability Distribution (JPD)

The JPD of the normalised lateral (y) and in-line (x) oscillation of the square model in turbulent with shear flow, given in Table 7.3 were for various mean wind speed/damping configurations.

Table 7.3b shows that when the model had high structural damping there were no significant departures from the theoretical bi-variate normal distribution (Table 7.3.a). As the damping was reduced, departures from the theoretical distribution occurred, whatever the wind speed. They also show that the fluctuations dominated more in the 2nd and 4th quadrants (ie $y < 0$, $x < 0$ and $y < 0$, $x > 0$ ranges) thus indicating some correlation between the two exciting motions. Since the individual lateral and in-line motions had amplitude probability densities which were near Gaussian (Section VII.3.ii), the cause for the assymetry in their joint probability densities seems to have resulted from a correlation between the two motions. This observation, for low structurally-damped model motion was in marked contrast to the

assumptions usually associated with the vibrations of lightly-damped structures.

Fig.7.11 shows a photograph of an oscilliscope trace of the motion of the square cylinder with low damping, and with the abscissa representing the lateral oscillation and the ordinate, the in-line motion. The marked preference for the 2nd and 4th quadrants can be clearly seen.

a.6. Envelope of Fluctuations

From each simultaneously-digitised record for the lateral and in-line vibrations, each pair of deflections (x,y) were converted to polar (r,θ) co-ordinates using the programme VECTOR (Appendix B). The number of up-crossings for r and θ have been calculated using the programme WEIBULL (Appendix B).

Fig. 7.12. shows that, with high damping, the excitation given by the absolute magnitude vector r was near a Rayleigh distribution with the constants $k \simeq 2.0$, $C \simeq 2.0$. When the damping was low, whatever the wind speed, departures from a Rayleigh distribution were indicated.

This confirms that, for the square model with high damping, the assumption of independence between the in-line and lateral motion is justified. However, for the low-damped square model, the two motions are shown to be correlated.

Unlike the square model with low damping, both the circular and wedge models gave envelopes of amplitude fluctuations which were quite clearly Rayleigh distributed (Fig.7.12).

b. Frequency Domain

In this and subsequent sections all frequencies quoted have been converted to refer to the model-scale values. These were obtained from the analysis frequencies by dividing with the playback ratio, r. To obtain full-scale project values, the frequency scaling, given in Section had to be used.

General shapes of vibration spectra for the same tests showed differences between the lateral and in-line oscillations. These were:

(i) The lateral spectra indicated a very narrow-band excitation response. The Q-values obtained from these spectra (Appendix 7.A) gave damping parameter values ξ very near to those taken as the reference (Section VII.1.i). Table 7.4 gives a comparison between the values of ξ deduced from spectra and those obtained by other methods.

The in-line spectra, on the other hand, showed a much broader band excitation response. The normalised peak value, $G(n_0)/\sigma^2$ was about half that for the corresponding peak value of the lateral spectrum. The in-line spectra were broader because the energy appeared to have diffused into a frequency range below that of the resonant (Fig. 7.13 and 7.15). Whitbread [81] also has noticed this characteristic.

(ii) The in-line spectra also indicated a possible coupled mode. While the Q-value (and hence ξ) calculated from the peak at the resonant frequency, matched well the estimated 'true' ξ (Table 7.4), the ξ computed from the coupled mode did not. The Q-value was

lower for the coupled mode (estimated by extrapolating the form of the 'crinkle' found at the coupled mode frequency). Hence ξ (= 1/2Q) for this 'extra-vibrating system [88] was much higher (Table 7.4). In estimating the damping parameter, ξ, from Q-values, therefore, care must be taken in selecting the Q-value associated with the resonant frequency.

The lateral and in-line oscillation spectra shown in Figs 7.13-7.15 are discussed in detail below, in particular, the effects on the spectra due to various changes in the test parameters. Sub-section b.1 examines the lateral and b.2 examines the in-line spectra.

b.1 Lateral Spectra

(i) Models

Figs 7.13.c, 7.14.b and 7.15 show the oscillation spectra for the square, circular and wedge models, vibrating in a turbulent with shear (T_s) profile under minimum damping conditions. All spectra show similar discrete peaks and these peaks were taken as the natural frequencies of the various models. These were,

$(n_o)_{sq}$ = 9.63 Hz

$(n_o)_c$ = 11.5 Hz

$(n_o)_w$ = 9.75 Hz

for the lateral direction.

Integrating the area under the $G(n)$ versus frequency, n, curve, the variances of the amplitude of the vibrations in the lateral direction were found and are given in Table 7.1 for

comparison with analogue-measured values. These values are given as raw voltages and have not been converted to tip-displacement.

Similarly, the ξ values calculated for the models using the half-power bandwidths, δn_a (Appendix 7.A) show good correspondence to the reference values. (Table 7.4).

(ii) Flow

Figs 7.13 show the spectra for the in-line oscillation of the lightly-damped square cylinder in turbulent with shear, turbulent and smooth flows respectively. The reference wind speed in all cases was the same.

Similarly Figs 7.14 and 7.15 show the spectra of lateral vibrations in turbulent with shear and smooth flows for the circular and wedge models respectively.

Spectra of the square model vibrations in turbulent with shear and turbulent flows were similar, although the intensity of oscillation was greater in the former case (Table 7.1) This is in line with analogue measurements.

The spectra for oscillations of all three models in smooth flow conditions showed peaks at the resonant frequency, more sharply defined than the corresponding spectra in turbulent flow. The intensities of oscillation, however, were much less. All spectra obtained in smooth flow showed a peak at an analysis frequency of

50 Hz. This is not a true model frequency of 6.25 Hz (= 50/8 Hz). This peak was not caused by vortex shedding since a spectrum of the wake structure (Section VII.4) did not show any significant contribution at a model frequency of 6.25 Hz for any model considered. This was verified by high-pass filtering the speeded-up signal at 60 Hz (with a cut-off of 18 dB/octave) before sampling. This filtering did not alter the peak value of the 50 Hz signal. It can be assumed therefore that the 6.25 Hz model frequency peak was a 50 H mains pick-up. This did not significantly interfere with the spectrum as its power was 22 dB down on the peak resonant value.

Frequencies below the resonant contained more energy in smooth than in turbulent flow. This can be seen by looking at Fig. 7.13 for the lateral spectra of the square model.

(iii) Wind Speed

The spectra for the square model with 2 DOF and with low damping is given for two reference wind speeds of 9.32 m/sec (Fig.7.13.c) and 5.66 m/sec (Fig.7.13.e) showing that the latter spectra is much more well defined. To account for this, the wake spectra were examined. For the 9.3 m/sec wind, while n_o = 9.63 Hz, the shedding frequency n_s = 14.63 Hz (Fig.7.21). For the 5.7 m/sec wind, however, n_o = 9.63 Hz and n_s = 9.63 Hz (Fig.7.21). Using the Strouhal number obtained from n_s for the 9.3 m/sec wind, n_s for the 5.7 m/sec should have been 9.47 Hz. The analysis bandwidth should have resolved the 9.47 from the 9.63 Hz. The lack of a peak at 9.47 Hz on the wake spectra (Fig.7.21) indicated that the vortex shedding had been captured by the natural resonant

oscillations of the model. This, therefore, might account for the very sharply defined peak in the vibration spectra in the 5.7 m/sec wind.

(iv) Damping

For zero external electro-magnetic damping, $\xi_{ref} = 1.5 \times 10^{-2}$.

If the indicated natural frequency is and the true frequency is n , then, from Appendix 7.A.

$$n_i = n_o \sqrt{1 - \xi^2}$$

For the square model

$$n_i = 9.63 \text{ Hz} \quad \text{(Section VII.3.ii.6.1)},$$

$$\delta n_o = n_o - n_i = 0.001 \text{ Hz}$$

is not resolvable from the digital analysis. Hence

$$n_o = n_i$$

is taken as the natural frequency.

Figs 7.13.d show lateral response spectra for the square model in turbulent with shear flow and with an applied damping of $\xi_{ref} = 5.674 \times 10^{-2}$

An increase in ξ decreased Q and thus increased the half-power bandwidth, δn_2 (Appendix 7.A). This effect can be seen quite clearly by comparing Figs 7.13.d. The narrow band response of the minimum damping case is broadened and the peak value lowered. Because of this spread, it was difficult, though not impossible, to distinguish the resonant frequency from the cluster of peaks present. The ξ obtained from the lateral spectra however showed good correspondence to the 'reference' value (Table 7.4).

(v) Degrees of Freedom

The spectra of the square with only 1 DOF (Fig.7.13) is a much narrower band response than the 2 DOF spectrum . ξ calculated from the 1 DOF spectrum, however, was within 10% of the reference value (Table 7.4). It should also be noted from Table 7.1 that the mean square intensity (obtained by integrating the area under the spectrum) of the 1 DOF of oscillation was greater than that for the 2 DOF oscillations. The ξ calculated here differs from those obtained from auto-correlation curves (Fig.7.16). This shows the difficulty involved in estimating ξ from response spectra for low damping.

6.2 In-line Spectra

(i) Models

The response spectra of the in-line vibration of the three models in turbulent with shear flow having the same reference speed of 9.4 m/sec is shown in Figs 7.13. -7.15.

All spectra showed two peaks, the natural and a possible coupled mode.

ie square:- n_o = 9.63 Hz, coupled mode, n = 9.00 Hz

circular:- n_o = 11.5 Hz, " " n = 10.63 Hz

wedge:- n_o = 9.25 Hz, " " n = 9.63 Hz

The response from the square model was more discrete than from the circular or wedge models. The mean square fluctuations (non-normalised) followed the same pattern as for the lateral with the strongest fluctuations occurring with the square and the weakest with the wedge model (Table 7.1).

ξ calculated from the Q-values at the resonant peak point, showed very good correspondence to the reference value (Table 7.4): Values of ξ calculated at the coupled mode

frequencies, however, showed significant departures from the 'true' damping by having high values.

(ii) Flow

By examining Figs 7·13 it is easy to see that in-line normalised spectra did not differ appreciably in their shape for turbulent with shear and turbulent flow. Spectra obtained in smooth flow conditions, however, showed the corruption of the spectra by noise, caused by the low intensity of the strain-gauge signals.

(iii) Speed

By examining Figs .7·13 it can be seen that higher wind speeds showed the natural and coupled mode frequencies very distinctly. As the speed was reduced, the coupled mode frequency gave way to a clump of peaks, centred at the coupled mode frequency.

(iv) Damping

As the damping increased, the difference in the energy content of the two peaks became smaller (Fig.7·13). It was therefore very difficult to decide which was the natural frequency of the model. As mentioned in the previous sub-section, the ξ values, calculated from the Q-value associated with the natural frequency peak was the estimate closest to the true value (Table 7·4).

c. Time Domain

As in the previous section, all values of time, and frequencies, quoted have been converted to refer to the true model-scale values. True times have been obtained by multiplying the analysis time with the playback ratio, r (= 8). To obtain full-scale values, scaling, given in Section V.1.i should be used.

The auto-correlation curves for the lateral and in-line oscillations for various model/flow configurations are shown in Figs 7.16 – 7.18. Brief descriptions of the test conditions are given in Table 7.1.

The resonant frequencies of oscillations of the models in both lateral and in-line modes of vibration could be obtained from the auto-correlation plots. They showed excellent agreement with these values obtained from the auto spectrum plots.

All correlation curves showed a 'ripple' modulation in that while some peaks of the correlation curve were well defined, others were truncated. This can be seen quite clearly in Fig. 7.16.f. In addition, the correlation curves also showed a heavy co-sinusoidal modulation. Both these effects were a result of the digital analysis technique.

The co-sinusoidal modulation is quite distinct from the linear decay produced in the auto-correlation curves when biased, estimators for $R(\tau)$ are used. Since all auto-correlation plots have been produced using unbiased estimators (Section III.3.iii.), there is no linear decay in the curves.

This co-sinusoidal modulation is the result of the FFT procedure. According to Mercer [82], the co-sinusoidal modulation occurs when the centre frequency of the signal does not coincide with an 'analysis' frequency (an 'analysis' frequency is defined as an integer multiple of $1/\delta t$ where δt is the time between successive samples). The resultant spectrum then appears to have at least two frequency components, n_1 & n_2, both bounding the 'centre frequency', n_c. Since the two frequency components are separated by at least the sampling bandwidth, δn, $(= n_2 - n_1)$, a 'beat' represented as a co-

sinusoidal modulation of frequency $\delta n/2$ is shown.

The same arguments apply for tests made under maximum damping conditions. Section VII.3.ii.b showed that heavy damping removes the discrete resonant peak and replaces it with a cluster of peaks, centred around the resonant frequency, giving rise to heavily modulated auto-correlation curves. This modulation is illustrated in Fig. 7.16.e , obtained from the signal whose auto-spectrum curve (Fig. 7.13d) showed the ill-defined cluster of peaks.

The damping factor, ξ , was obtained from the auto-correlation plots as described in Appendix 7.A. Care had to be taken in this analysis because of the undue influence of various parameters on the resonant behaviour of the various models (see below).

Sub-section c.1 discusses in detail the lateral auto-correlation curves and c.2 discusses the in-line curves. Unless otherwise stated, all results are for the 2 DOF oscillations.

c.1 Auto-correlation of Lateral Oscillations

The effects of various model/flow configuration are discussed below.

(i) Models

Compare the auto-correlation plots, Figs 7.16, 7.17 and 7.18 for the square, circular and wedge model, without any externally applied electromagnetic damping, oscillating in a turbulent shear (τ_s) profile flow.

The damping parameter, ξ , was calculated from the auto-correlation plots. Because of the co-sinusoidal modulation, it was decided to use only the initial parts of the curve. Correcting for the 'ripple' modulation by extrapolating to a point the truncated peaks, and not using the 1st point since it contained a noise component, the following estimates for were obtained.

$$\xi_{sq} = 1.343 \times 10^{-2}$$
$$\xi_{c} = 1.353 \times 10^{-2}$$
$$\xi_{w} = 1.260 \times 10^{-2}$$

These values compare quite favourably with the reference damping value of $\xi_{ref} = 1.518 \times 10^{-2}$.

All spectra showed the co-sinusoidal and the ripple modulations even though their respective spectra (Figs 7.13-7.15) indicated very narrow band peaks. This implied that the frequency resolution, which was adequate to allow interpretation in the frequency domain might not be sufficiently narrow to ensure correct interpretation in the time domain.

(ii) Flows

The auto-correlation curves obtained for the square model oscillating in turbulent with shear, turbulent and smooth flow conditions shown in Fig.7.16 were next considered.

Damping values calculated from these curves show that, while in a T_S flow corresponded closely to the reference value obtained from the trace (Fig.7.1), ξ in the turbulent and

smooth flows was much lower, such that

$$\xi_{T_s} \left(\simeq \xi_{ref}\right) > \xi_T >> \xi_s$$

This indicated that a random forcing input, ie random wind, should be used so that correct damping parameters could be calculated from either time or frequency domain results.

Figs. 7.17 for the circular cylinder oscillations show that while $\xi_s < \xi_{T_s}$, the discrepancy between ξ_{T_s} and ξ_s was not as great for the square model.

(iii) Speed

Figs 7.16.c and 7.16.d show the auto-correlation plots for the square model with minimum applied damping oscillating in a turbulent, shear flow (τ_s) at reference wind speeds of 9.3 m/sec and 5.7 m/sec respectively.

For the higher speed, the auto-correlation plot did not show the heavy co-sinusoidal modulation evidence in the plot for the lower speed. Inspection of their respective spectra, Figs 7.13.c. and 7.13.d. showed only very narrow band response peaks. There was a complete absence of any corrupting secondary peak for the lower-speed spectrum. Hence, this modulation for the lower-speed case was not caused by the 'beating' effect due to the FFT procedure described above.

The explanation for this modulation was sought by inspecting the wake spectra in a smooth flow at a reference wind speed of 6.3 m/sec. This is described more fully in Section VII. 3. ii. e. These spectra showed a peak at 9.63 Hz equal to the resonant frequency

of the square model. It is possible that because of the limit of the resolution bandwidth, the shedding frequency was slightly different from the resonant frequency. This would lead to the 'beat' modulation shown in the auto-correlation plot (Fig.7.16.e) for the low-speed case. This phenomenon of 'beating', brought about by the closeness of the vortex shedding to the resonant oscillations of the model has been noted elsewhere [26].

(iv) Damping

Increase in damping tended to distort the very discrete, narrow band response obtained in tests at low damping values. The very discrete peak was replaced by a cluster of peaks, centred about the resonant. This is seen in the auto-spectra, Figs 7.13 .

The loss of definition was reflected in the auto-correlation curves for high damping (Figs 7.16 – 7.18) by the heavy co-sinusoidal modulation. If an estimate for the damping is to be made from the auto-correlation curves, care must therefore be taken to use only the initial period of the curve to prevent distortions.

Taking such precautions, values of ξ were calculated for maximum applied electro-magnetic damping. Table 7.4 gives the values obtained from auto-correlation plots of the square, circular and wedge models which compare favourably with the standard reference value (ξ_{REF}) of 5.674×10^{-2}.

(v) Degrees of Freedom

Restricting the motion of models from 2 DOF to 1 DOF in the

lateral direction, changed the response of all models dramatically. This can be seen by comparing the auto correlation plots for the lateral oscillations with 2DOF and 1 DOF motion.

In all cases, the auto-correlation curves for the lateral vibration with 1 DOF were less damped than for the 2 DOF case. As a comparison, for the square model in turbulent with shear flow at minimum damping conditions,

$$\xi_{2\,DOF} = 1.343 \times 10^{-2}$$

$$\xi_{1\,DOF} = 4.741 \times 10^{-3}$$

with the reference damping of $\xi_{REF} = 1.518 \times 10^{-2}$

This accounts for the very high fluctuation amplitude of the models with 1 DOF compared to 2 DOF.

c.2. Auto-correlations of In-line Oscillations

All the in-line auto-correlations (Figs7.16-8) showed heavy cosine modulation; a consequency of the non-discrete nature of the resonant responses.

Resonant frequencies could be deduced from the auto-correlation plots but with difficulty because the low signal/noise ratio (compared to the lateral oscillation) reduced the levels of the peaks with respect to the first point, R(o). R(o) was relatively large because it contained the noise component.

When the amplitudes of in-line oscillation decreased, as in the smooth flow cases, the 50 Hz mains-'hum' was picked up. This is shown in Fig. 7.16.a, Therefore the auto-correlation plots of models in smooth flow conditions (Figs 7.16 – 7.18) are contaminated by this dominant

Unlike the lateral case, to get a realistic estimate of ξ from the in-line auto-correlation plots, estimates had to be made by considering the total record of the plots and not just the initial section of the plots. These are given in Table 7.4 and show good correspondence with the reference

As with the lateral oscillations, auto-correlation plots of experiments made in smooth-flow configurations could not be used for estimating ξ

d. Coherence

The coherence between the lateral and in-line oscillations are shown in Fig. 7.20. They indicate the following points.

(i) The square model gave good coherence ($\simeq$ 0.85) at the resonant frequency in turbulent with shear flows. Decreasing the reference speed from 9.3 m/sec to 5.7 m/sec did not alter the coherence value.

(ii) Altering the external applied damping from low to maximum decreased the coherence. In the case of the Sq/T_S configuration, the value decreased from 0.85 to 0.5.

(iii) The coherence plot for the wedge model in turbulent with shear flow did not indicate any dominant frequency.

(iv) The cylinder coherence showed a coherence of 0.7, not at the resonant frequency of 11.5 Hz but at 10.6 Hz. The 10.6 Hz peak corresponded to the 'coupled' mode frequency of the in-line oscillations (Fig. 7.20.a).

(v) Coherence measured in smooth flow (Fig. 7.20) showed the dominance of the 50 Hz mains pick-up by both the lateral and in-line oscillation signals.

e. Vortex Shedding

To explain some of the characteristics seen in the auto-correlation plots (Figs 7.16 – 7.18), some simple wake measurements were made on all models.

The two DISA hot-wire probes were mounted at heights of z/δ = 0.5 and 0.74 (Section VI.2) in the wake of the models.

It was decided to look at the frequency range considered in the vibration analyses, ie dc – 25 Hz. The hot-wire signals were then low-pass filtered at 25 Hz (roll-off rate of 18 dB/octave) and had most of their DC contents backed off with DISA 55 D01 signal conditioners. The conditioned signals were then recorded at a speed of 95.25 mm/sec on magnetic tape.

For subsequent digital analysis, the tape was replayed at a speed of 762 mm/sec through the signal conditioners set up as low-pass filters

at 500 Hz (roll-off of 18 dB/octave). The sampling rate was 1000 samples/sec. For each channel, 16 frames of data, each frame containing 1024 numbers were obtained. Power spectral density plots (Fig. 7.21) were made and all PSD values above the analyses frequency of 200 Hz were discarded.

In this way, the folding back of data below the 200 Hz point was minimised. It should be noted that the analysis frequency range of $0 \longrightarrow 200$ Hz corresponded to the true model-scale frequency range of $0 \rightarrow 25$ Hz.

The rest of this section deals with the converted model-scale frequencies. The following points can be noted from the power spectral density plots (Fig. 7.21).

(i) Any discrete vortex shedding in turbulent flow (Fig.7.21) was masked by the turbulence in the flow.

(ii) Wake spectra in smooth flow indicated vortex-shedding peaks.

For the square, at $\bar{U}_{ref} = 9.72$ m/sec, $n_s = 14.63$ Hz

This gave a Strouhal number, $S = 0.1133$ for the square model. This value was at variance with the often quoted 0.14 for an infinite square-section model [13]. From the amplitude response curve with reduced wind speed for an oscillating square cylinder, Davenport [83] gives a critical Strouhal number of 0.11.

Using S = 0.1133, the vortex-shedding frequency at the reference wind speed of 6.30 m/sec was 9.47 Hz. But the spectra for the particular test (Fig. 7.21) indicated a shedding frequency of 9.63 Hz. Since the resonant frequency of the square model was 9.63 Hz, this indicated the possible capture of the vortex shedding by the oscillation of the model.

(iii) For the wedge, spectra showed a shedding frequency of 106.5 Hz. This gives a Strouhal number of 0.1

VIII DISCUSSION AND FINAL CONCLUSIONS

This chapter is aimed at presenting a cohesive and short summary of the previous chapers and the final conclusions drawn from this study.

It comprises four sections: Section VIII - 1, a recapitulation of the objectives of this research. Section VIII - 2, a review of the previous chapters including any particularly interesting observations; Section VIII - 3, proposals for future work arising from this research; and Section VIII - 4, which describes the achievements of the research and possible significant contributions made to the study of wind effects on bluff bodies.

VIII.1 Aims and Requirements of the Research

The aim of the research was to compare the wind-excited response of a bluff structure free to respond with two degrees of freedom with a structure limited to one degree of freedom of motion.

To achieve this, tests were made in a wind-tunnel and the following requirements had to be satisfied. The bluff body chosen was a model of an existing tall building, and due care had therefore to be taken in constructing the model. For the prototype the excitation is caused by natural winds, and so a model of the atmospheric boundary layer had to be generated in the wind-tunnel. The third requirement was to design and construct a gimbal system which would allow the model to move in two mutually orthogonal directions or in either one direction. It was also necessary to set up a random-data acquisition and analysis system to cope with the

digital analyses of the fluctuating signals from the model deflections and from the turbulence of the generated wind.

VIII.2. Review

2.i. Chapter I

Chapter I began with a brief history of the destructive power of the natural wind on man-made bluff structures, particularly tall buildings. The section that followed defined the aims of the research and discussed the need for such an investigation. Finally, the mechanisms of the dynamic response of bluff structures caused by wind-excitation were discussed. Emphasis was placed particularly on square-section structures.

2.ii. Chapter II

This chapter on 'Analogue Data and its Analyses' was divided into three sections. The first dealt with the different transducers that monitored the deflection of the models and the turbulent structure of the generated wind. The second section discussed the standard concepts of random-data signal analyses used for analysing the analogue signals given out by the transducers. The final section concerned the analogue analyses instruments used.

2.iii. Chapter III

Chapter III gave a detailed description of the setting up of a digital-analysis system to analyse the structure of random signals. The three stages of digital analyses, acquisition of analogue signals, analogue-to-digital conversion and the digital analyses, were described in great

depth. In the section on analogue-to-digital conversion, a complete description was given of the combined use of an analogue system and a digital system.

2.iv. Chapter IV

Simplified descriptions of the atmospheric boundary layer under strong-wind, neutral conditions were discussed in this chapter. A spectral form for the longitudinal wind component of the turbulent wind, obtained by Kaimal et al [61] in full-scale conditions was suggested as a better form for modelling than the more conventional forms suggested by Davenport [49] and Harris [59]. This was justified on the grounds that both Davenport and Harris used length scales of turbulence, the evaluation of which have been the subject of some controversy.

The remainder of Chapter IV described the design and construction of the turbulence generators that were used to generate the model of the atmospheric boundary layer under strong-wind, neutral conditions.

2.v. Chapter V

The design and construction of the experimental hardware used was described in Chapter V. Section V.1 described the construction of the models, designed to satisfy similarity with full-scale prototypes. The next section, Section V.2 dealt with the design and construction of the two-degree-of-freedom gimbal system upon which the whole investigation depended.

Section V.3 described the construction of the damping system used to provide the necessary external damping to the models. The section concluded with a description of the rig that housed and supported the models, gimbals and dampers.

2.vi. Chapter VI

Chapter VI described the analyses of the turbulent structure of the generated boundary layer. The results, obtained variously from analogue and digital analyses, showed a good representation to the model of the atmospheric boundary layer, described in Chapter IV. The use of Kaimal's form for the full-scale longitudinal wind spectra showed excellent fit with the simulated boundary layer, leading to the conclusion that Kaimals' form be considered for any future simulation of the atmospheric boundary layer.

2.vii. Chapter VII

This chapter, contained the final results of the investigation. From the many vibration results described, the observations, most salient to the investigation were noted:

(a) It was shown that the damping parameter ξ for a model under test can be evaluated either from forced-displacement traces in still-wind conditions or from auto spectrum/correlation plots of the model vibrating in generated turbulent winds. Values of ξ obtained using these different methods showed very close correspondence with each other.

(b) With zero applied damping, ξ showed a significant difference between 2 DOF and 1 DOF, for all models. For example, for the square model,

$$\xi_{1\ DOF} = 0.35\ \xi_{2\ DOF}$$

(c) When the external damping was increased to the maximum, the differences decreased. Considering the square model again,

$$\xi_{1\ DOF} = 0.86\ \xi_{2\ DOF}$$

(d) In smooth flow conditions, ξ evaluated from spectra-correlations did not show correspondence to the values evaluated from still-wind conditions. There were no significant differences between ξ calculated from 2 DOF and ξ calculated from 1 DOF.

(e) The decrease in damping of the models when the in-line motion was suppressed shown to significantly increase the lateral response of all models in turbulent flows. In smooth flow, however, the reverse occurs.

(f) Joint probability density analyses indicated a correlation between lateral and in-line motions. This correlation was seen to decrease with increasing structural damping.

(g) Coherence analyses indicated high coherence between lateral and in-line motions for low damping. This decreased as the structural damping increased. For example, for the square model in turbulent flow, $\gamma^2 = 0.85$ for low damping and $\gamma^2 = 0.5$ for high damping.

(h) It was also shown that a shear profile impressed on a turbulent flow increased the response characteristics of all the models more than when the profile is not impressed. This affected both the fluctuating and the static component. The largest percentage difference was seen in the in-line component of vibration.

(i) Analyses of the wake structure behind the oscillating square cylinder indicated a vortex-shedding Strouhal number of 0.113 different to the often-quoted value of about 0.14.

The results given in Chapter VII showed that, for a lightly-damped structure with a small frequency difference between the principal axes of vibration, coupling between the lateral and in-line vibration modes occurred. This indicated a tendency by the lateral mode to re-distribute to the in-line mode, the energy imparted to it by the turbulence of the wind.

VIII.3. Proposals for Future Work

On the basis of the research described here, further investigations on the following lines are suggested.

(a) Work should be done on the influence of varying the frequency difference between the principal axes of vibration and on the resulting in-line/lateral coupling effect.

(b) The recently completed World Trade Centre has been instrumented and tests are under way to obtain full-scale results. It would be useful to compare the full-scale results with the values obtained in this model study.

(c) Most of this work could be re-tested in a tunnel capable of covering a much wider range of wind speeds. This would make unnecessary the use of bi-planar screens to reduce the wind speed.

(d) More digital analyses could be made to replace analogue analyses thus giving greater confidence to the results. This would require an on-line digital analyses system.

VIII 4. Final Conclusions

Model testing is a powerful technique for assessing, at an early stage, the performance of a full-scale prototype. The closeness of

the results from the model tests to those from the prototype depend on the correctness of the modelling.

In the past it has been thought that certain similarity requirements do not influence the final results appreciably and can therefore be neglected. One such assumption questioned here was that, since the dominant response of a structure to a wind is in the lateral direction, models can be constructed to vibrate with only 1 DOF. The investigation has shown that this assumption may be open to question in certain conditions. It has been shown that, under certain conditions coupling between the lateral and in-line modes can take place. This coupling leads to an increase in structural damping which is not indicated on 1 DOF model. This results in the 1 DOF model showing larger amplitudes of lateral vibration. A 2 DOF model therefore gives a more accurate representation of the prototype as it does not show inflated values of lateral vibrations.

To sum up, therefore, care should be taken in model testing to use models free to vibrate in the in-line as well as in the lateral direction.

In conclusion, it is to be hoped that, with more testing and verification of these results, practising engineers might look at the possibility of increasing the damping of slender, tall structures by decreasing the frequency difference between the principal modes of vibration. This would encourage coupling to take place, thus re-distributing the energy imparted to the structure by the prevailing, turbulent wind.

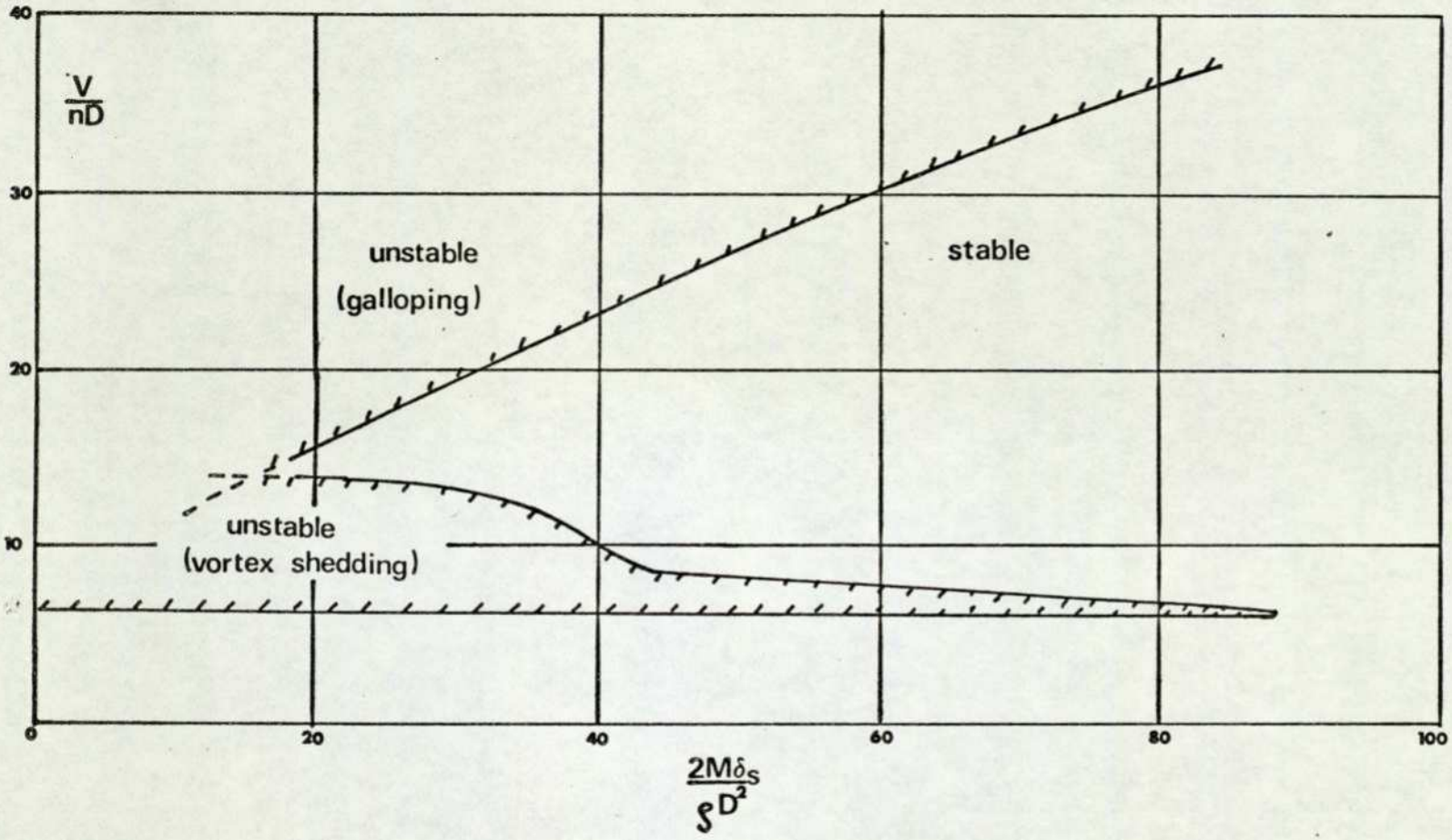

Aerodynamic stability diagram for a two-dimensional square-section prism (Scruton [24]).

FIGURE 1.1

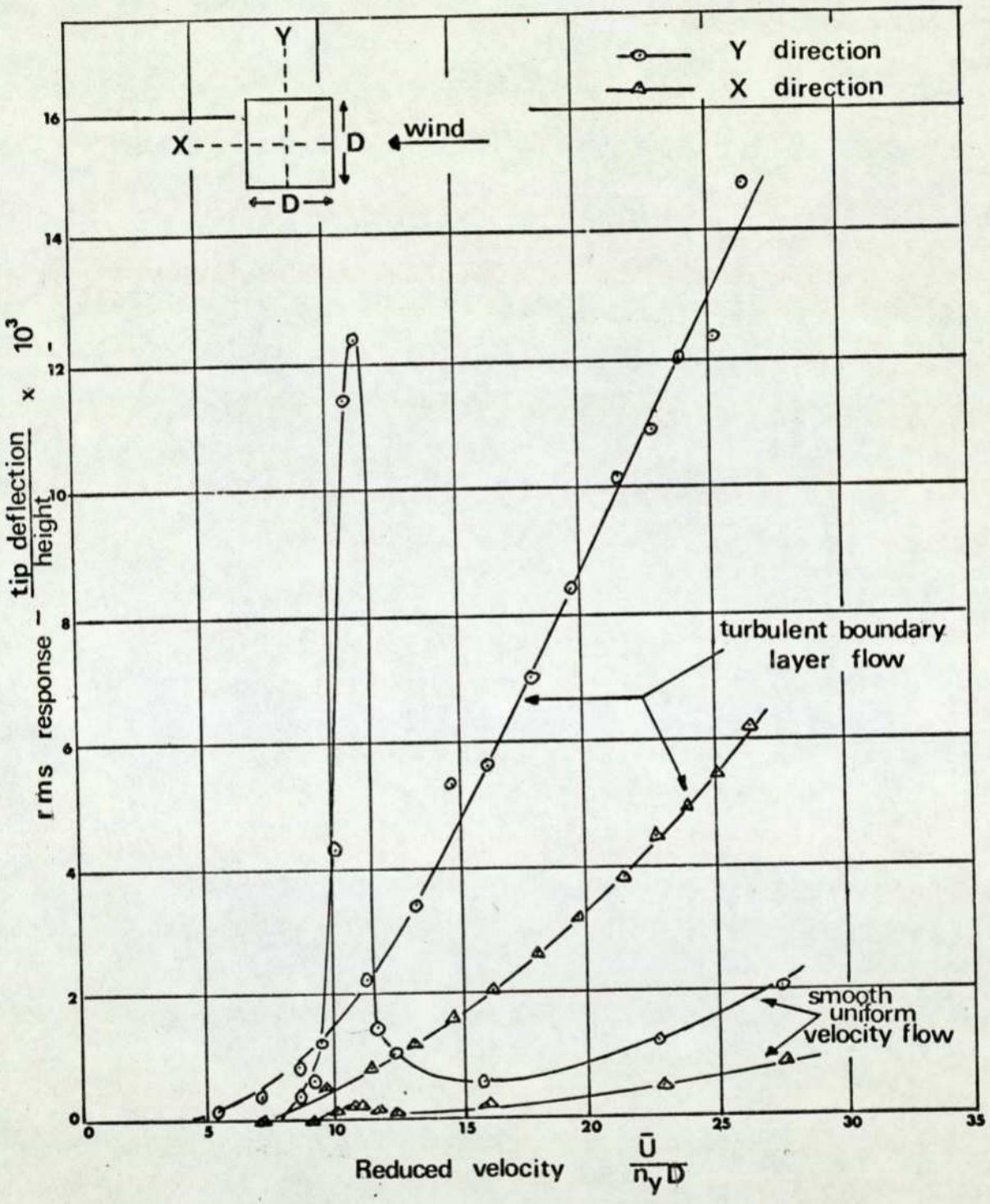

Comparison of dynamic response in smooth and turbulent flow for square model [30]

FIGURE 1.2

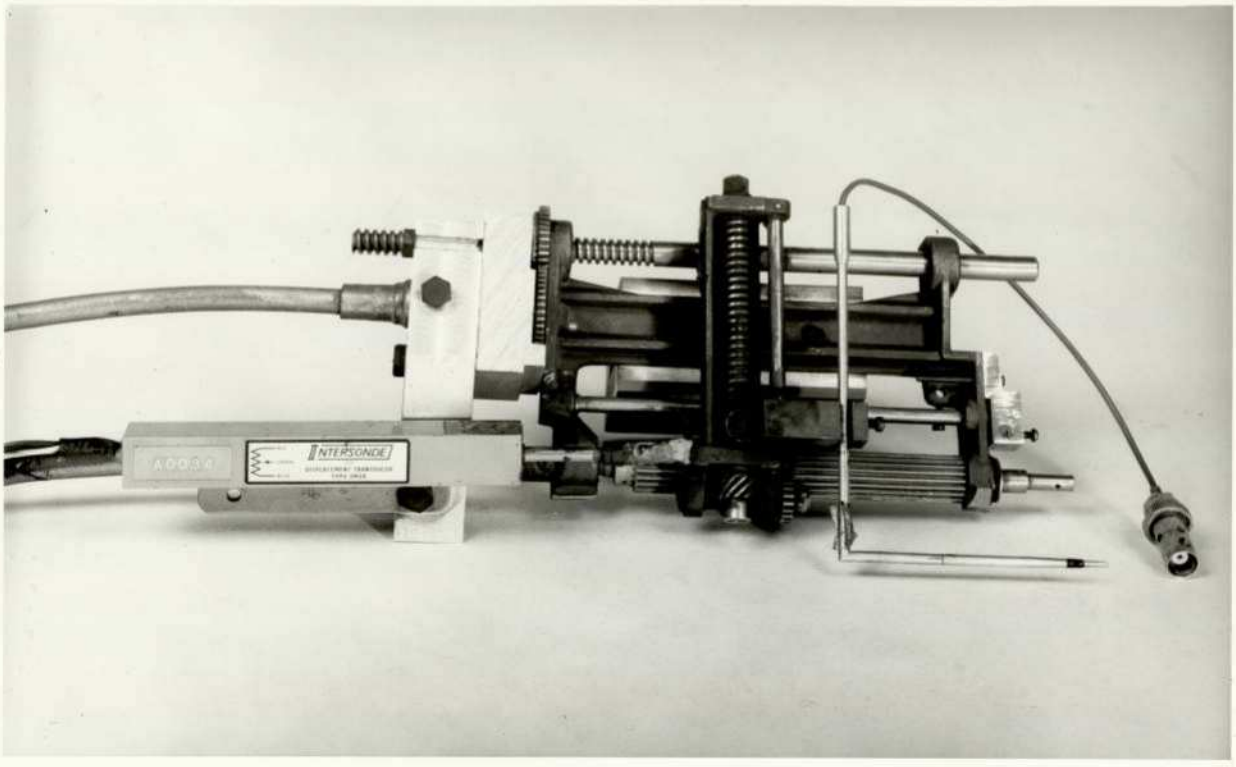

Traverse mechanism

FIGURE 2.1

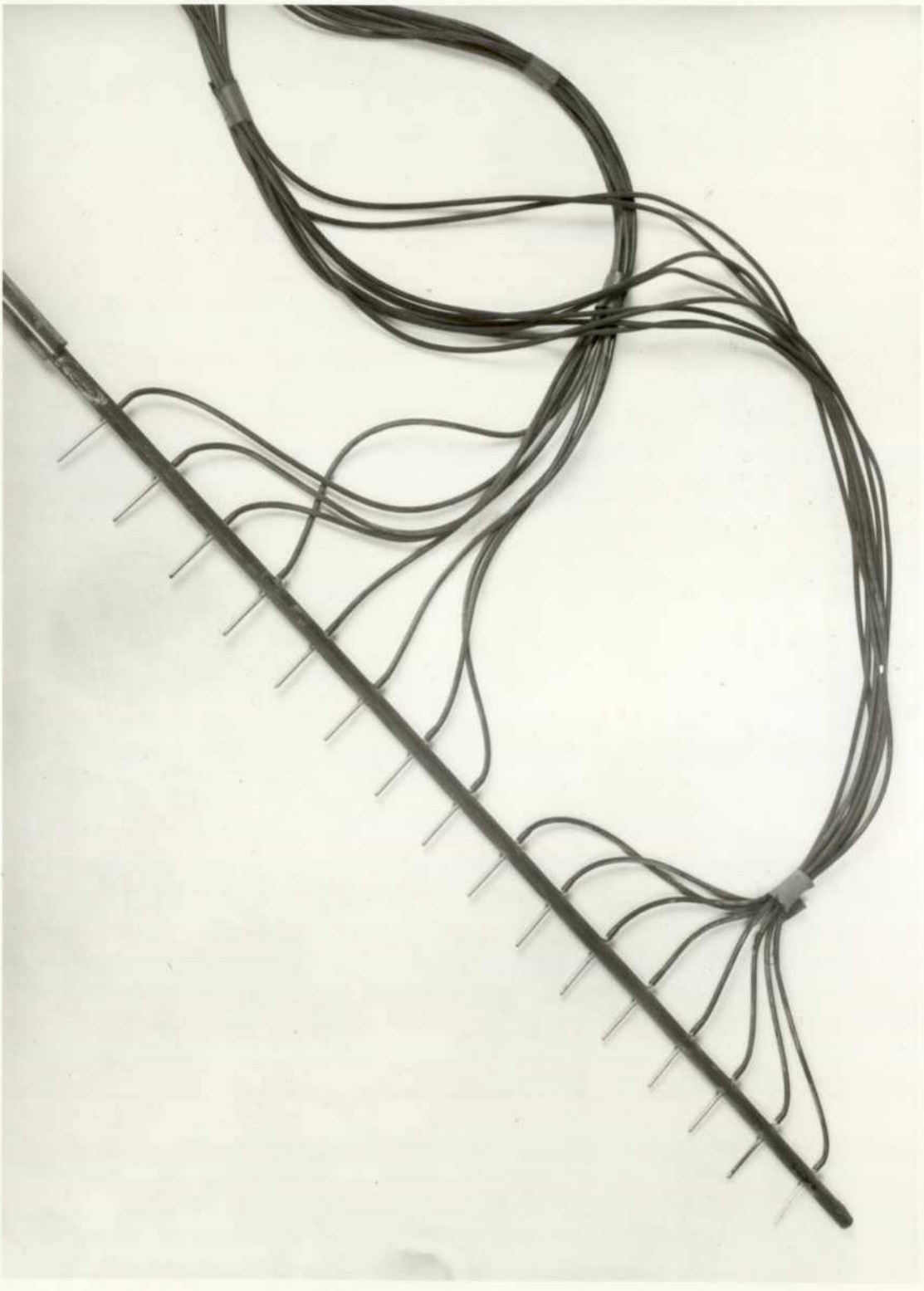

Pitot rake

FIGURE 2.2

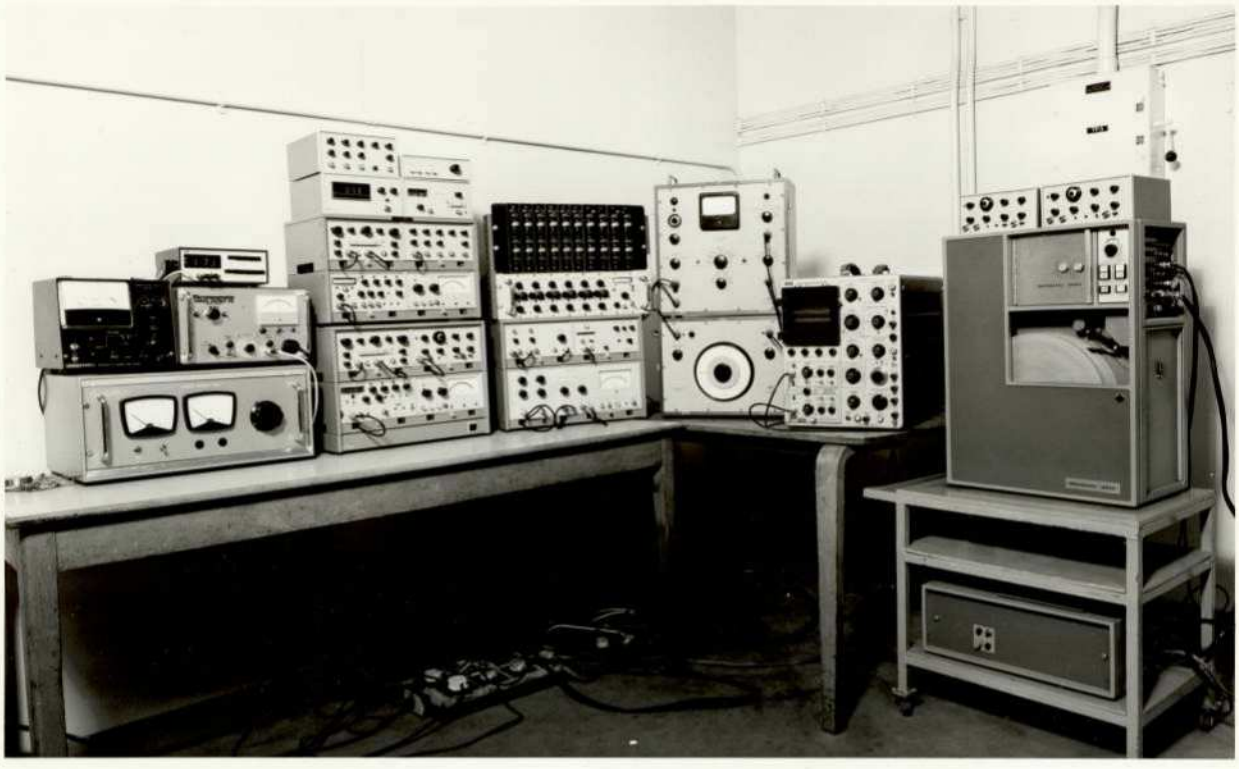

Analogue equipment

FIGURE 2.3

Patch Panel Wiring Diagram

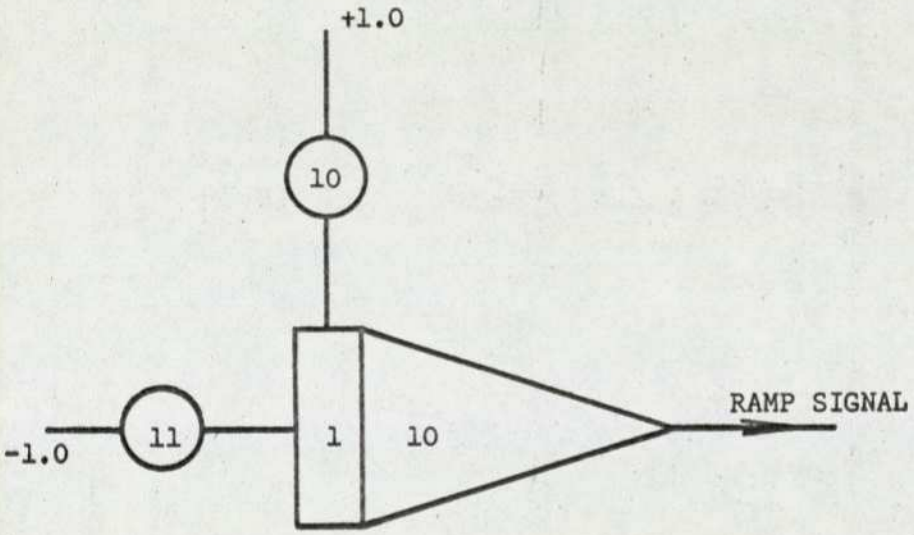

PATCHING REQUIRED FOR RAMP TEST-GENERATOR

FIGURE 3.1.a

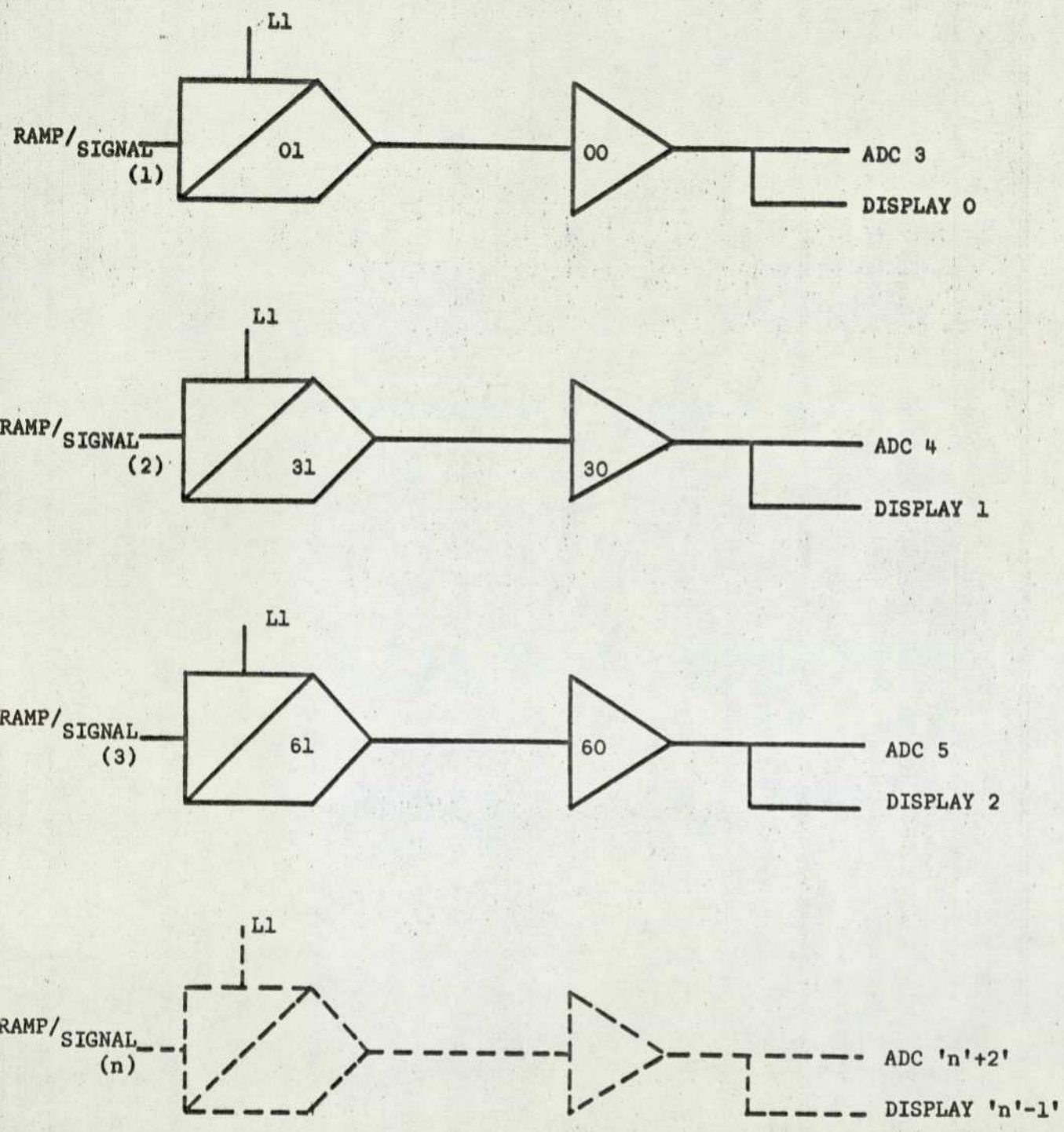

ANALOG PATCHING REQUIRED FOR EACH DATA CHANNEL

FIGURE 3.1.b

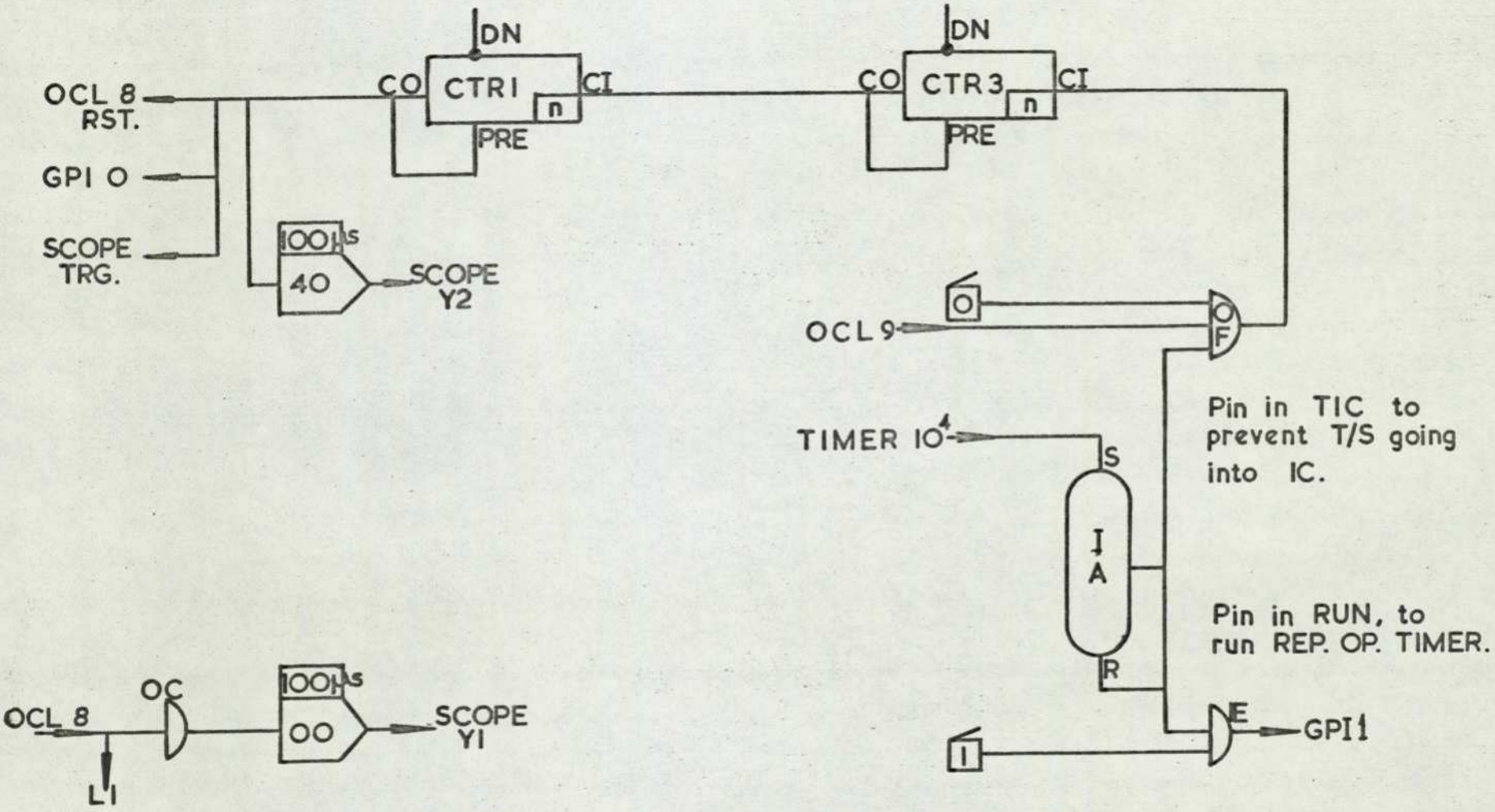

Logic Patching Required for Multi-Channel A/D Conversion.

FIGURE 3.1.c

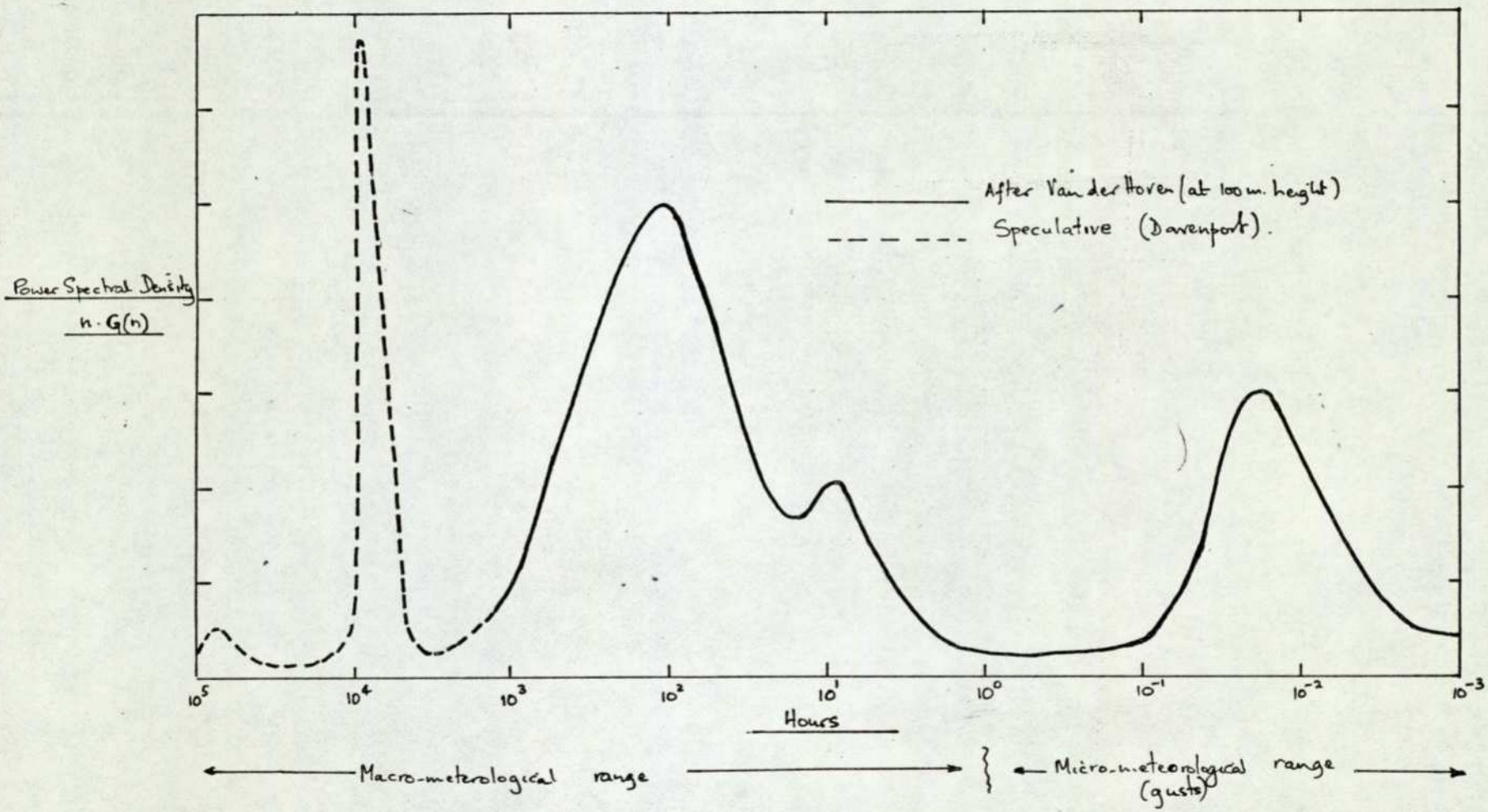

Van der Hoven's spectrum of horizontal wind speed near the ground (at 100m. height) [ ]

FIGURE 4.1

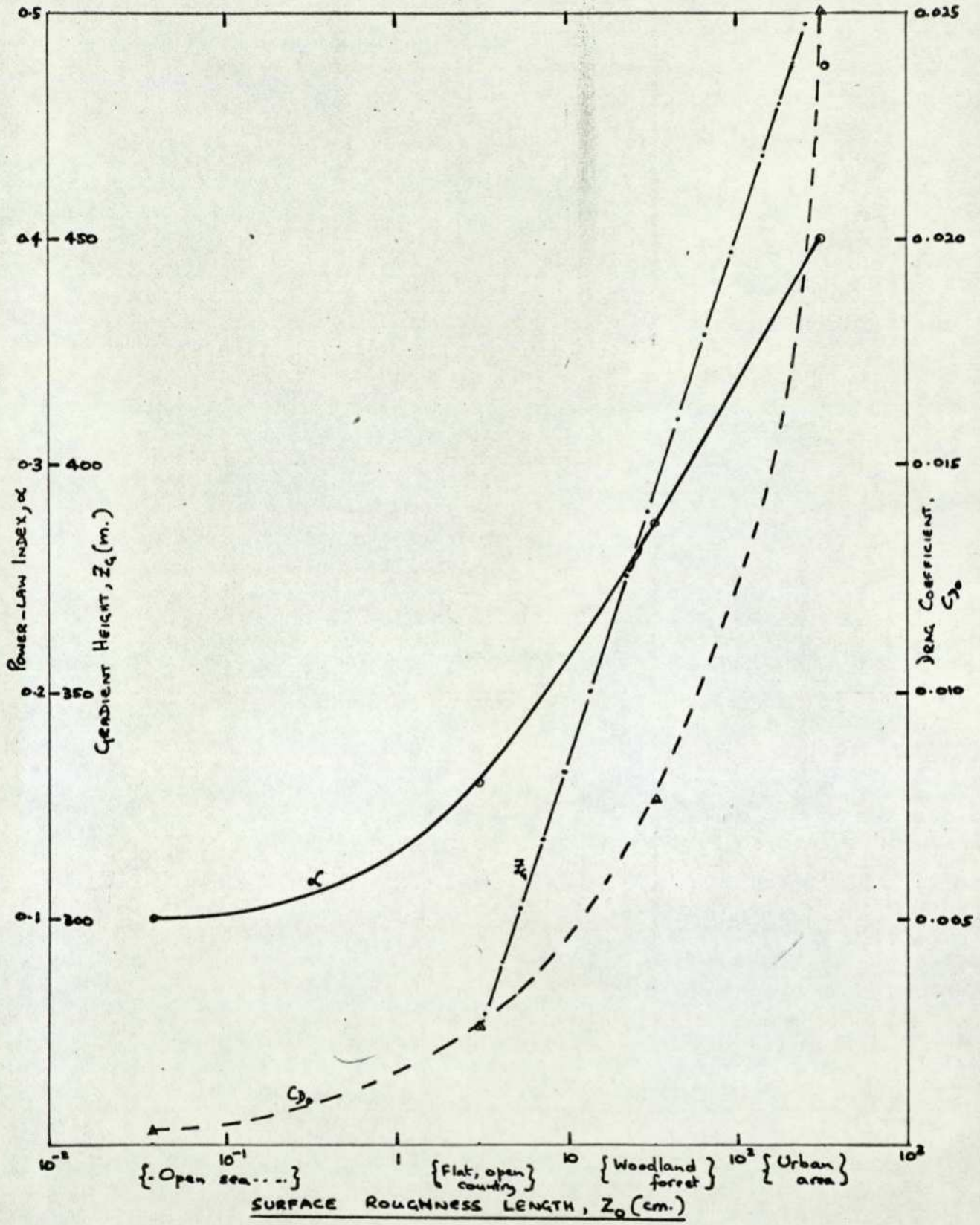

Parameters of wind profile for different surfaces [ ]

FIGURE 4.2

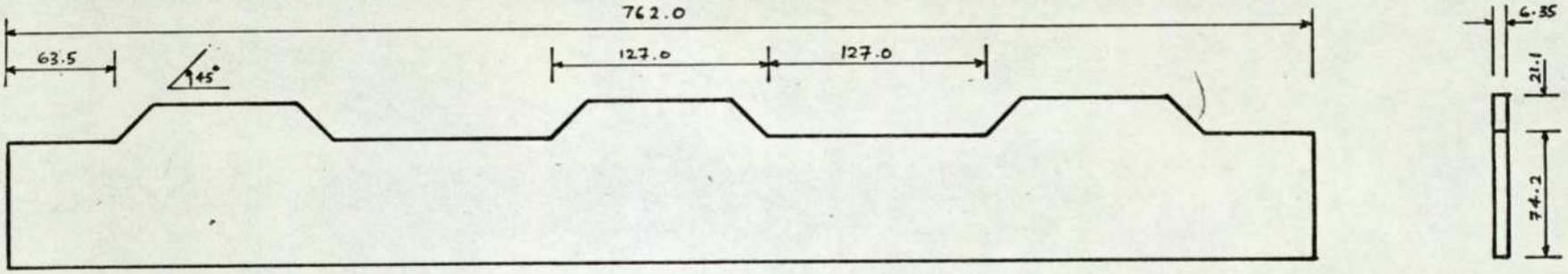

MATERIAL: Plywood

SCALE: 1/4

Castellated barrier

FIGURE 4.3.a

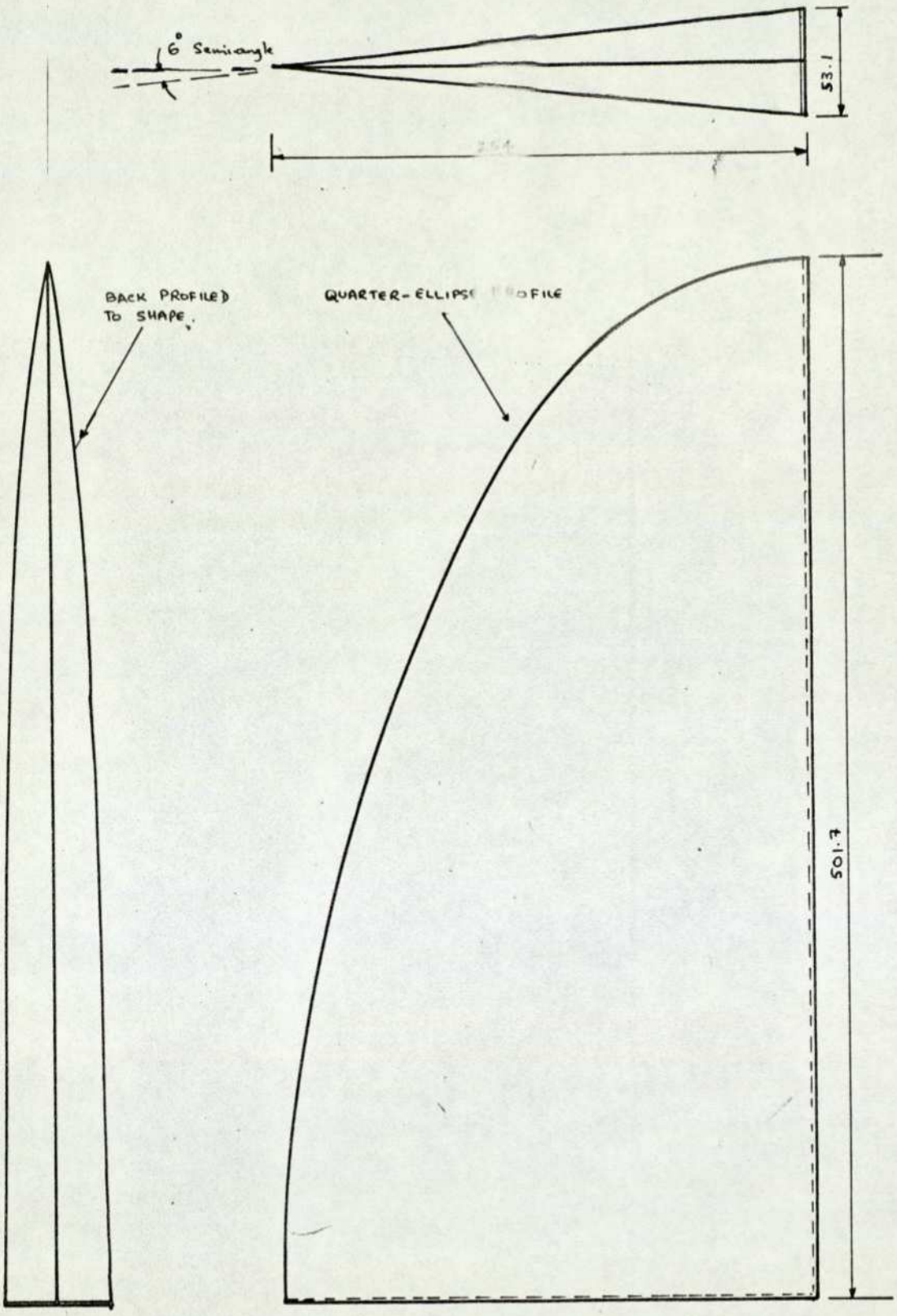

MATERIAL: Brass skin covering a plywood skeleton of back and base, and triangular stiffeners distributed along the generator height.

SCALE : 1 / 3

VORTEX GENERATOR

FIGURE 4.3.b

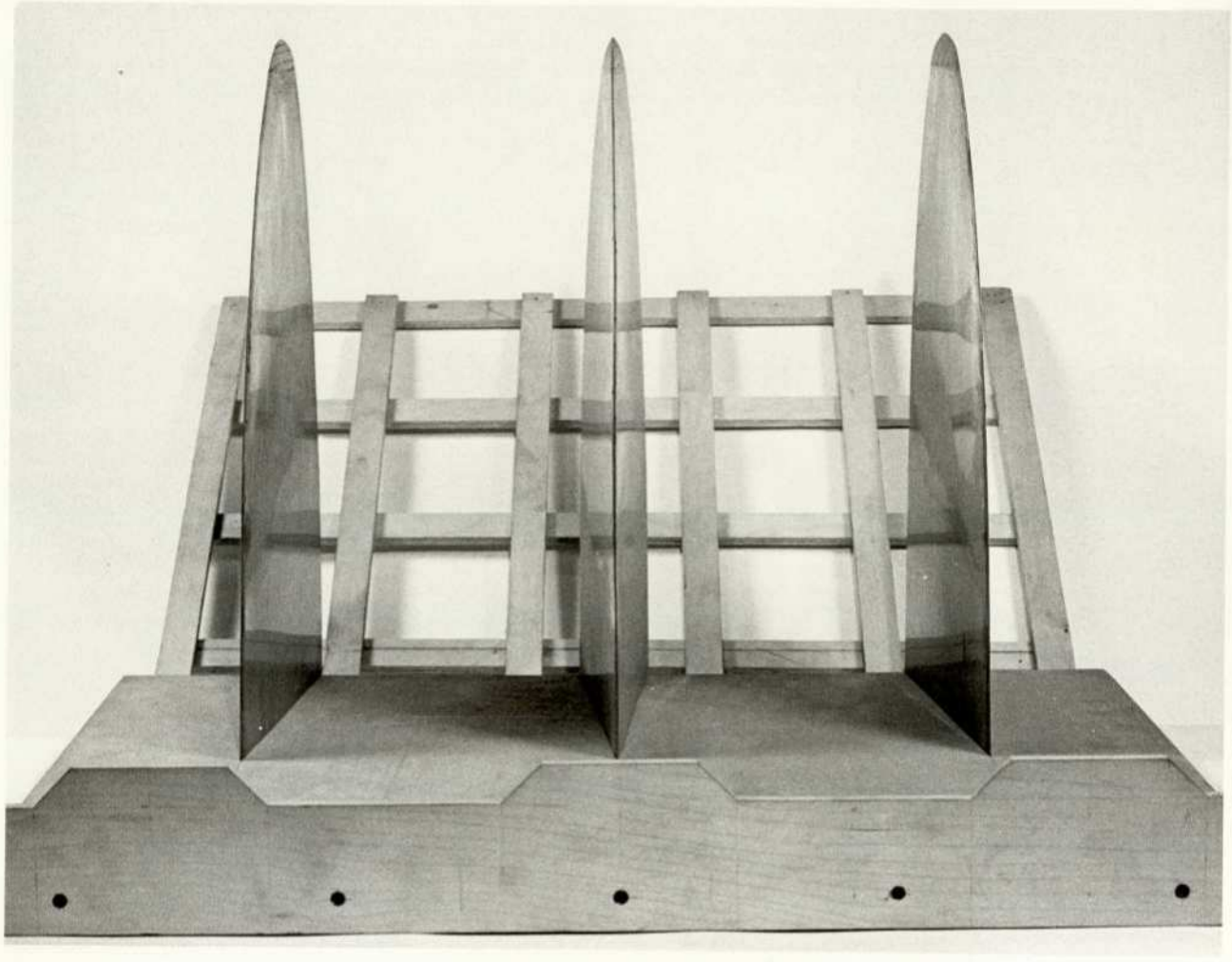

Mounting of vortex generators on board: a bi-planar screen is shown at the back

FIGURE 4.4

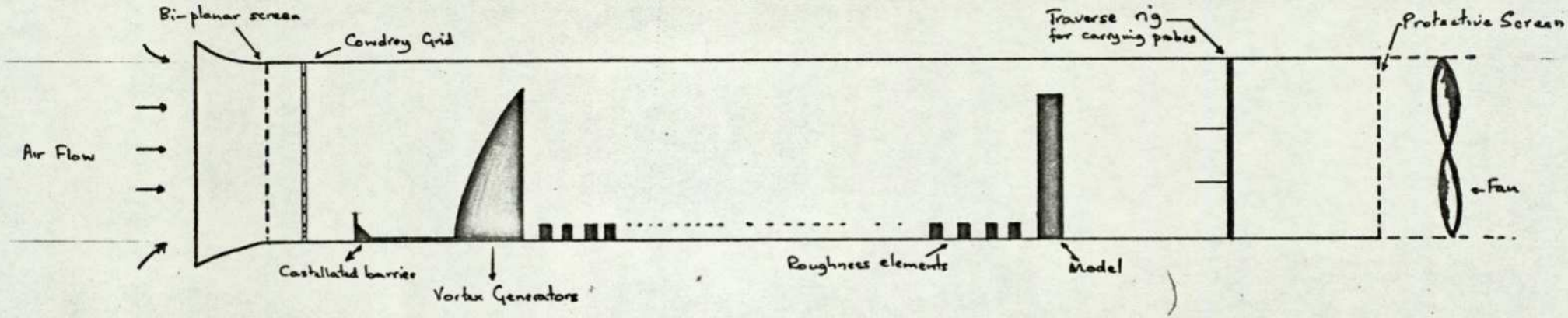

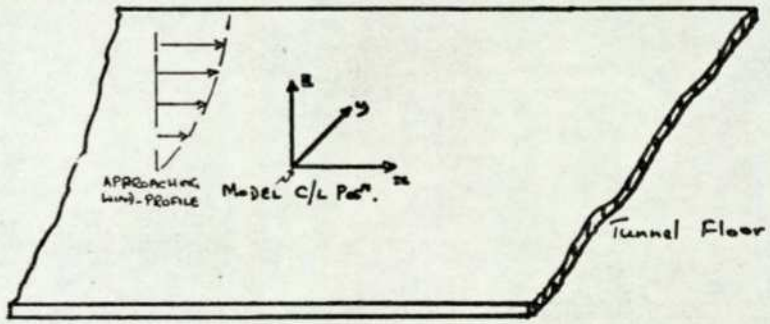

Co-ordinate system

Positioning of turbulent-shear-flow generators in wind-tunnel and origin of co-ordinate system

FIGURE 4.5

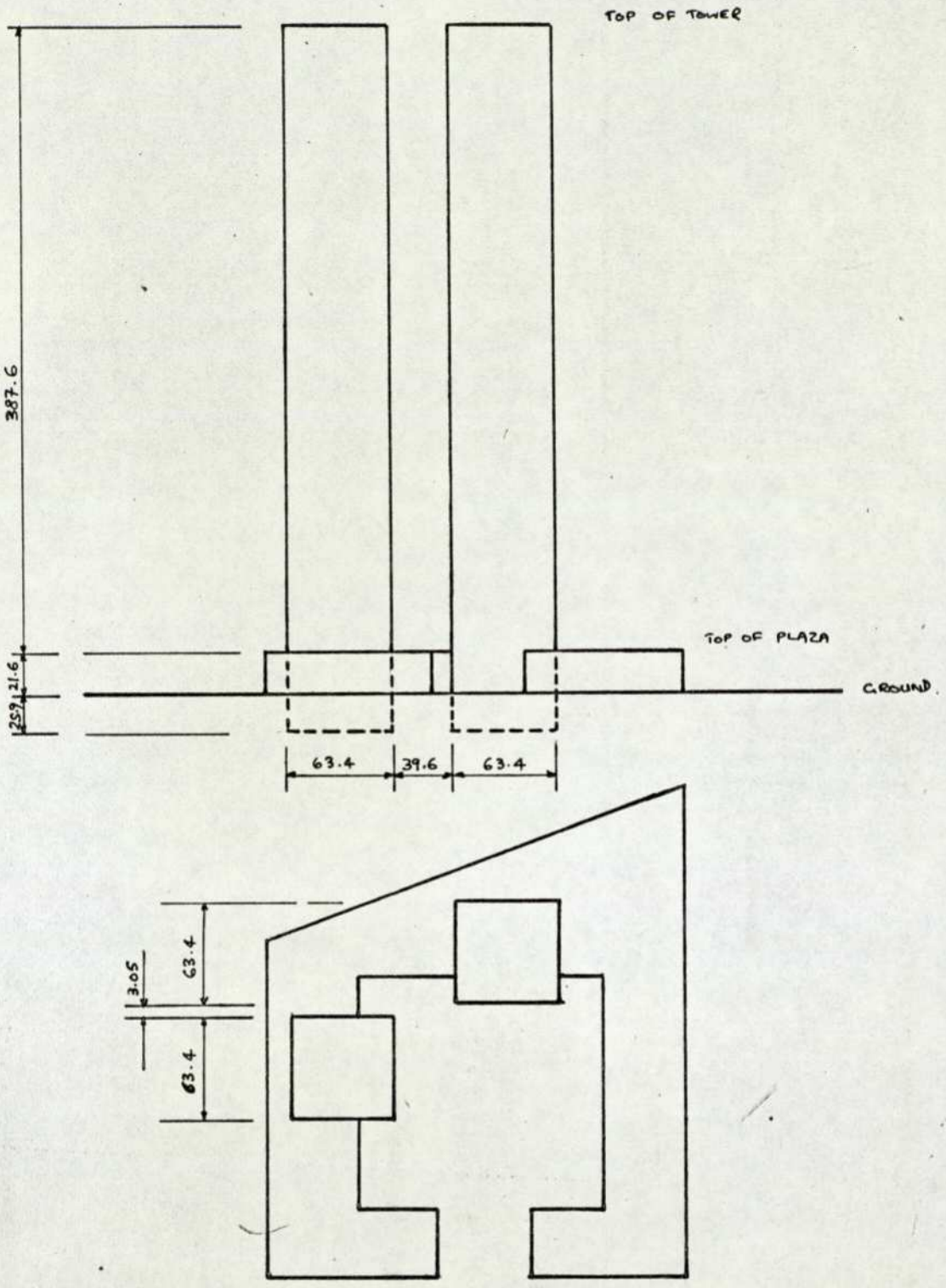

All dimensions in metres

The World Trade Centre

FIGURE 5.1

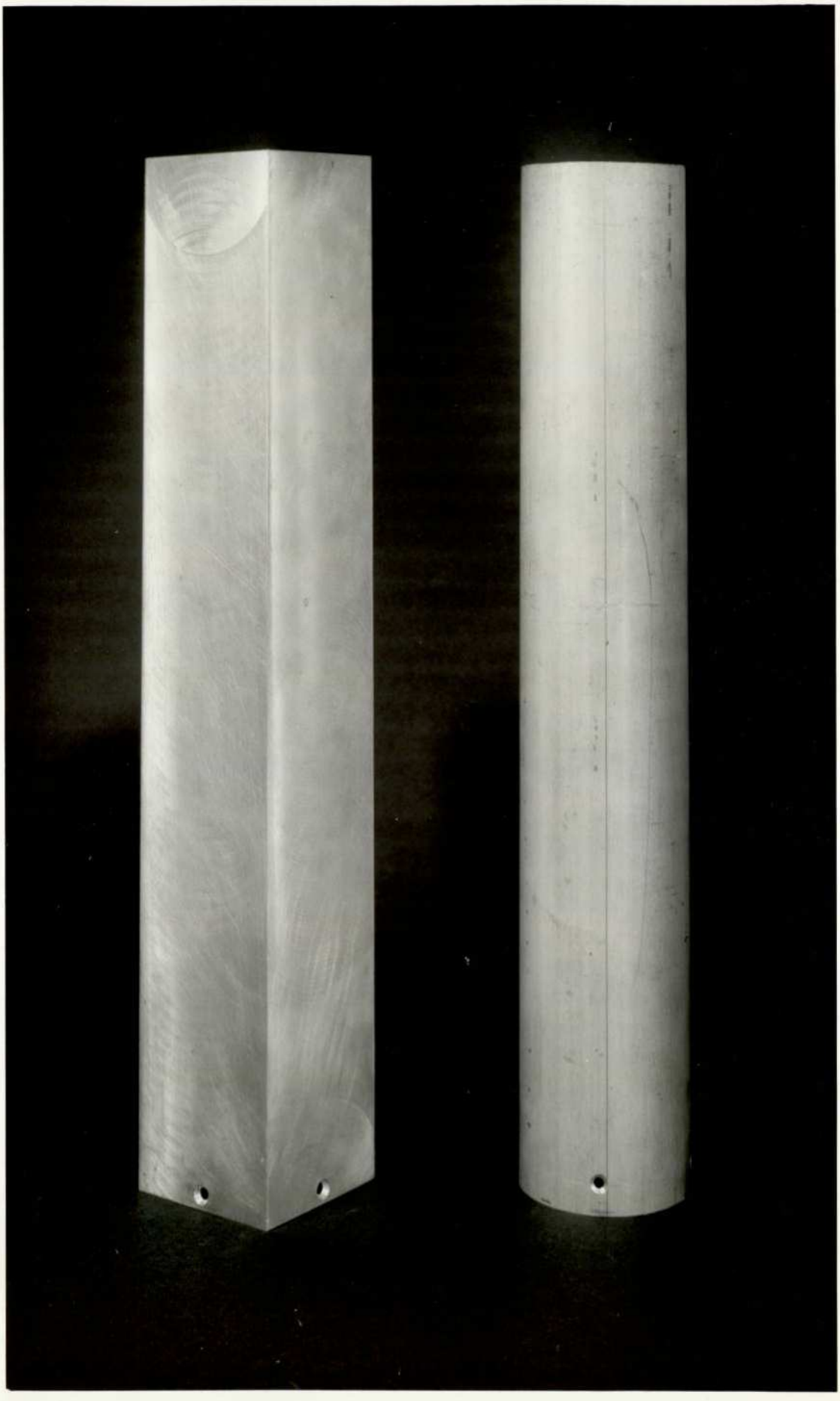

Models used in the experiments

FIGURE 5.2

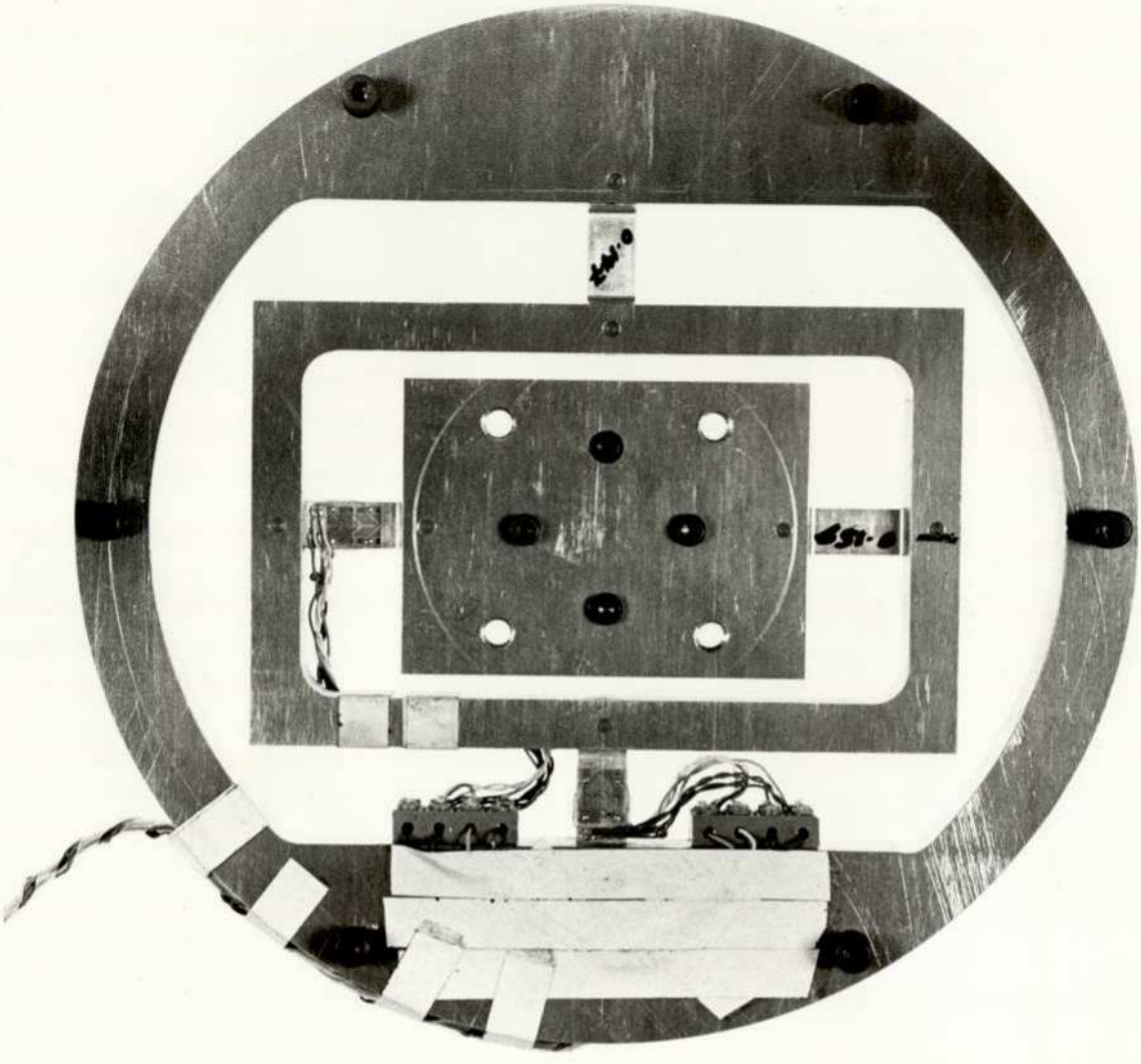

Gimbal system

FIGURE 5.3

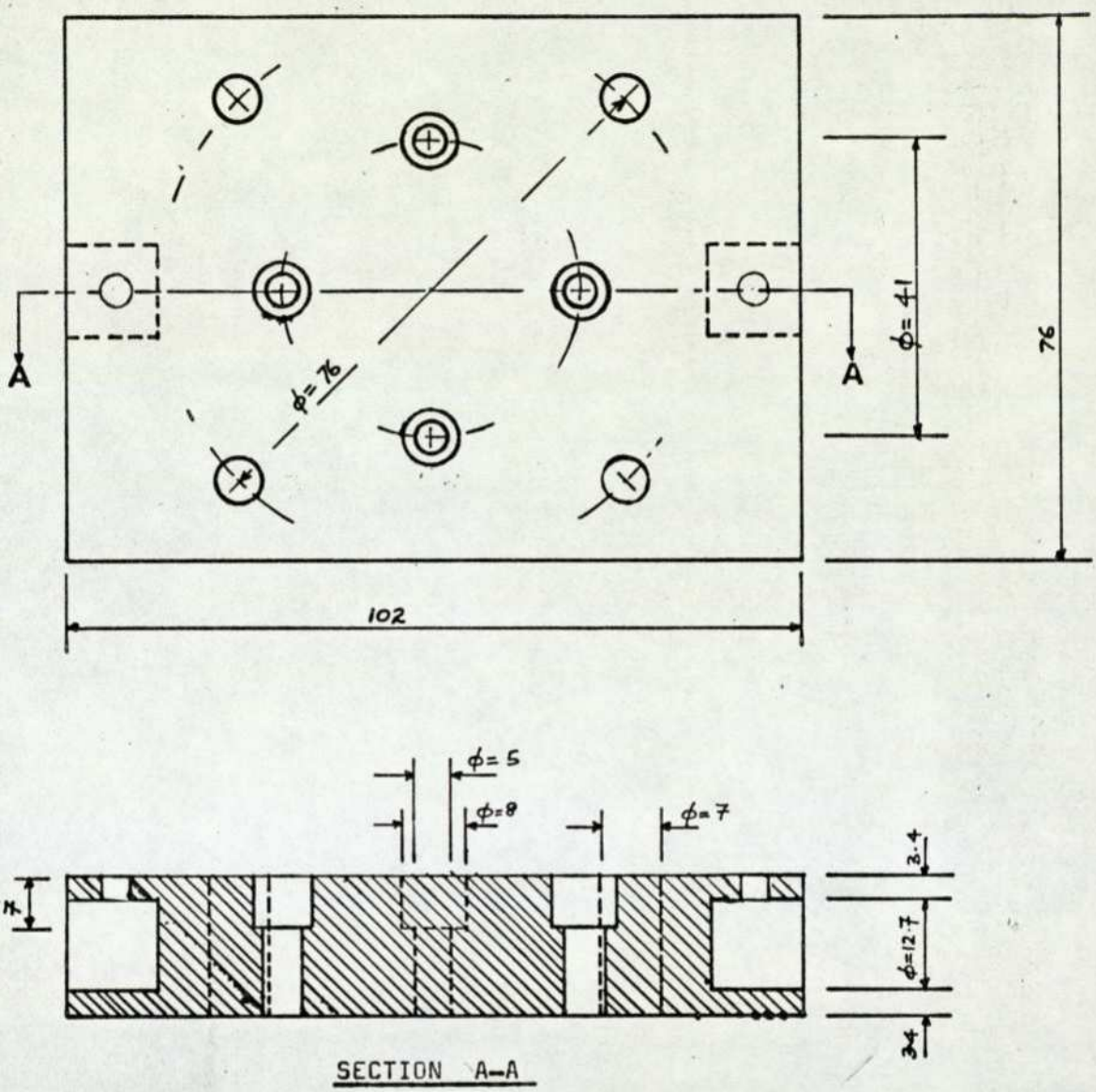

SECTION A–A

MATERIAL: Duraluminum

SCALE : 1 / 1

Centre block of gimbal system

FIGURE 5.3.a

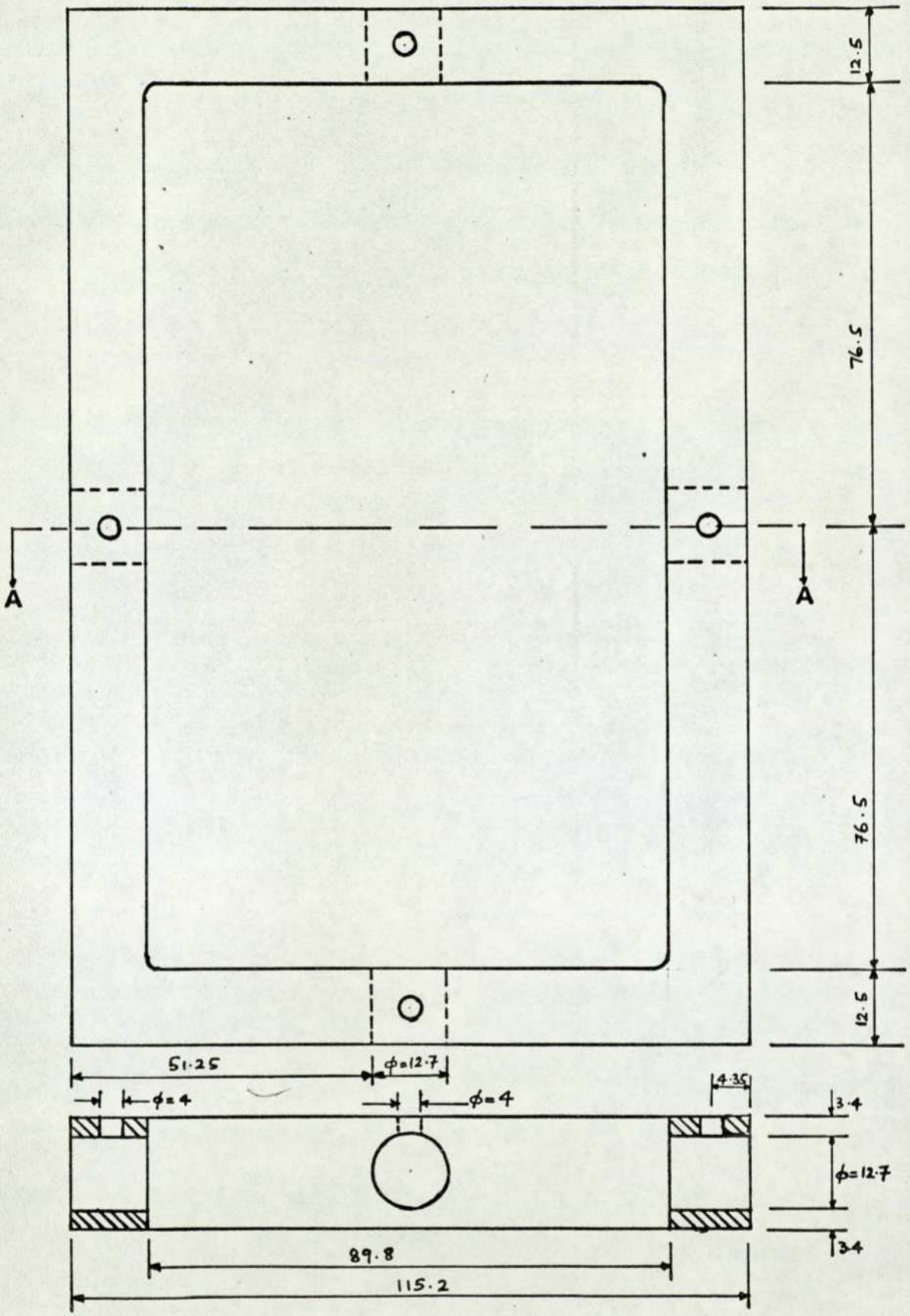

SECTION A–A

MATERIAL: Duraluminum

SCALE : 1 / 1

Intermediate ring of gimbal system

FIGURE 5.3.b

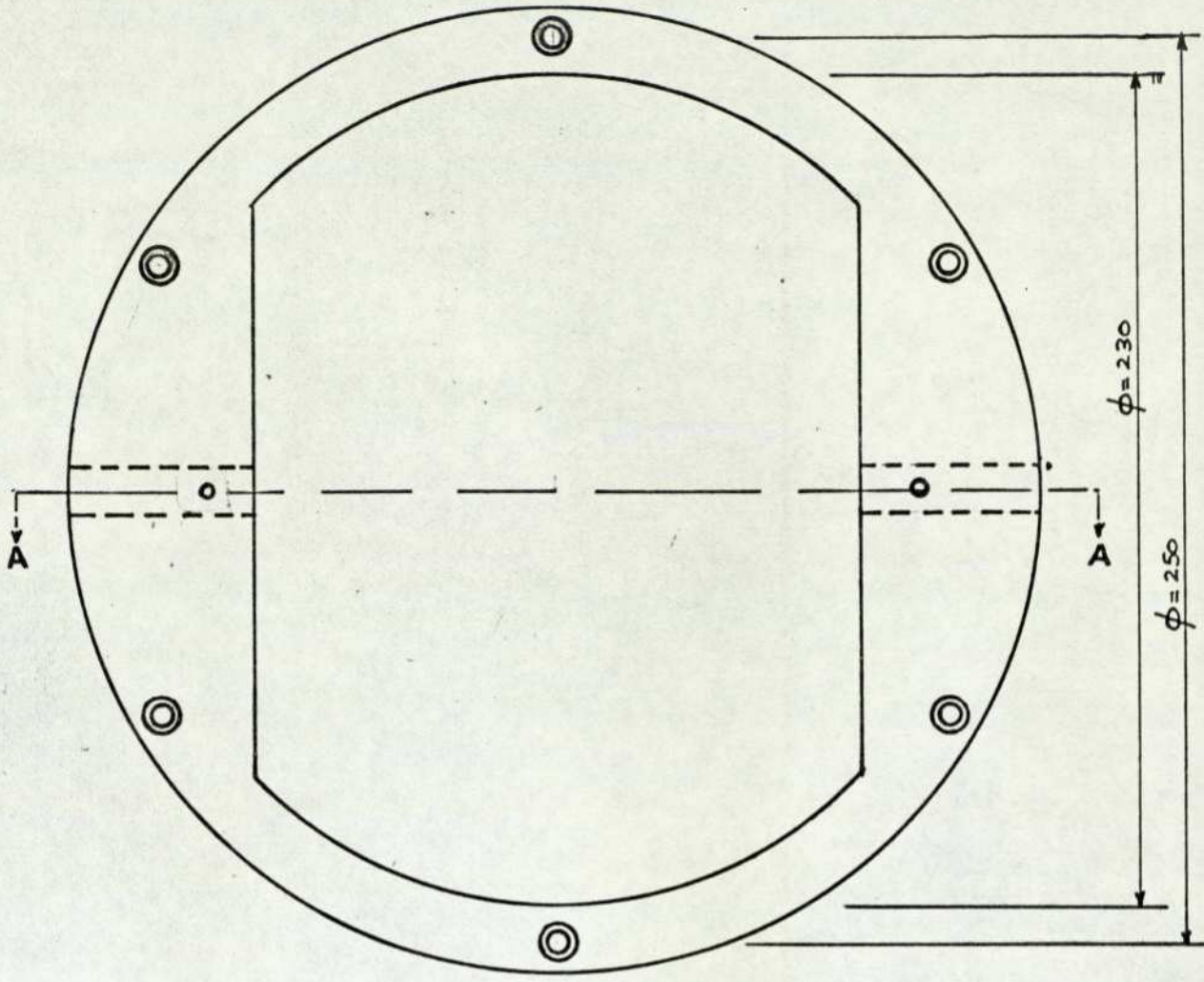

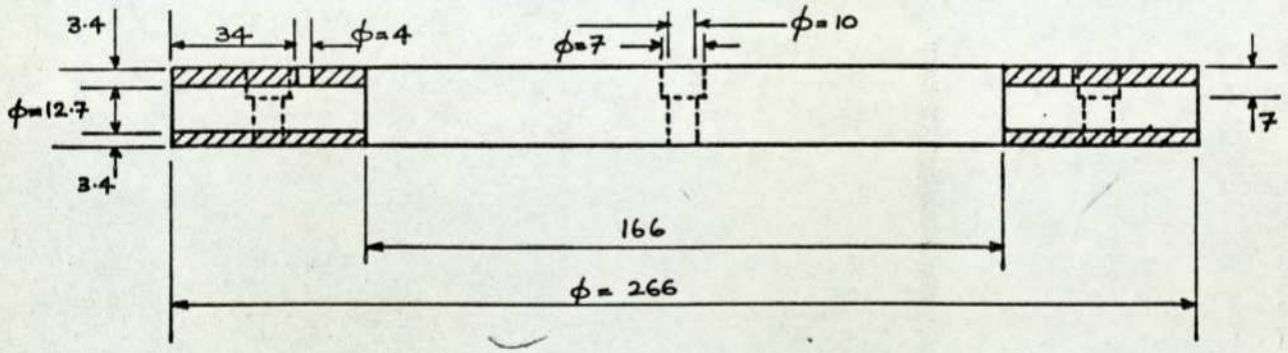

SECTION A–A

MATERIAL: Duraluminum

SCALE : 1 / 2

Support ring of gimbal system

FIGURE 5.3.c

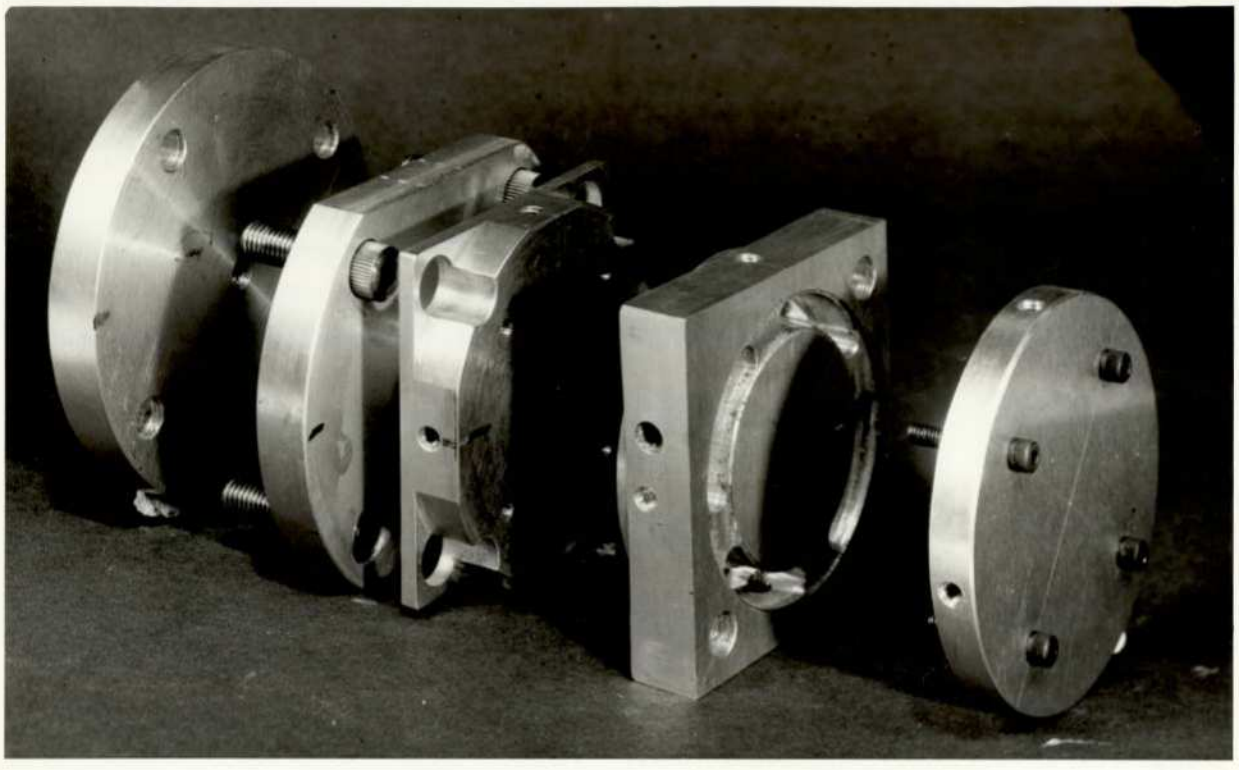

Attachment linkage

FIGURE 5.4

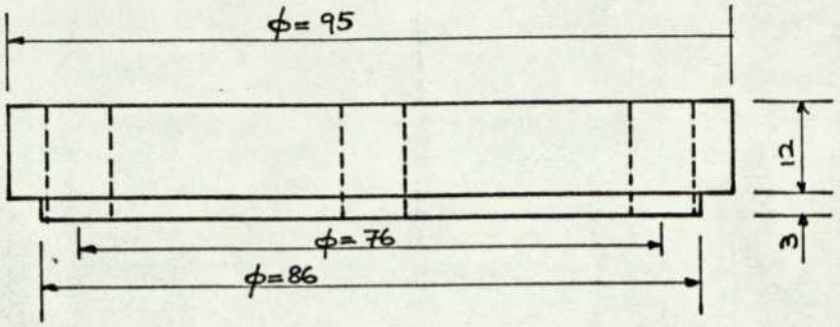

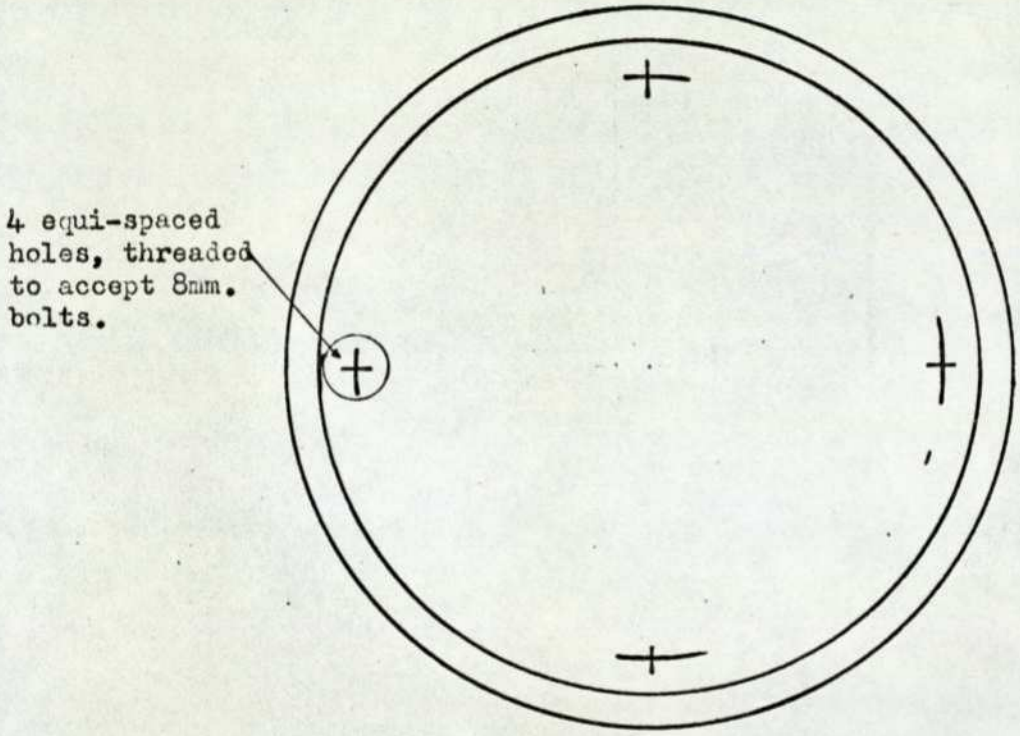

MATERIAL : Duraluminum

SCALE : 1/1

Spacer link

FIGURE 5.4.a

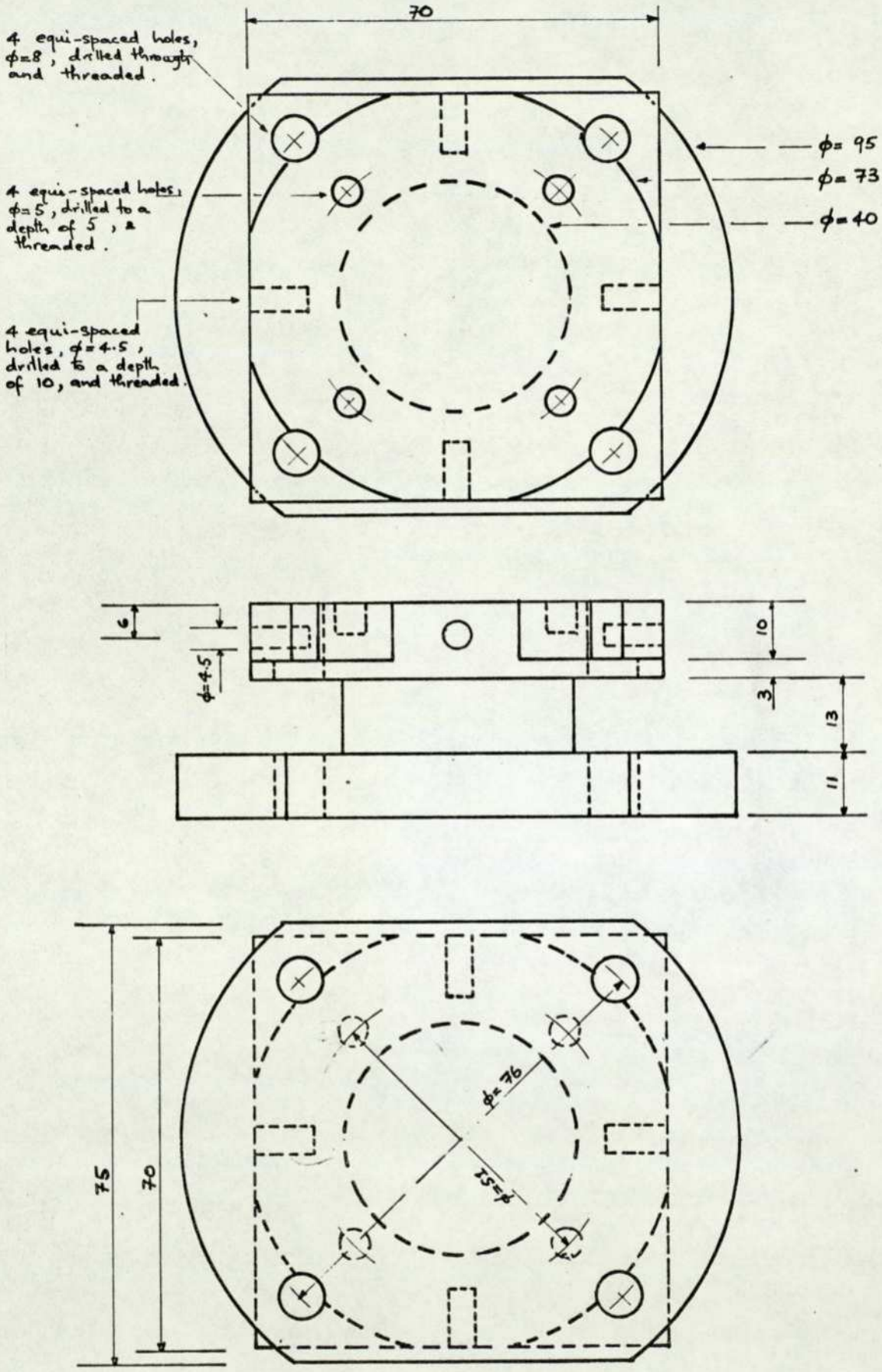

MATERIAL: Duraluminum

SCALE : 1 / 1

THIRD-ANGLE PROJECTION

Spacer

FIGURE 5.4.b

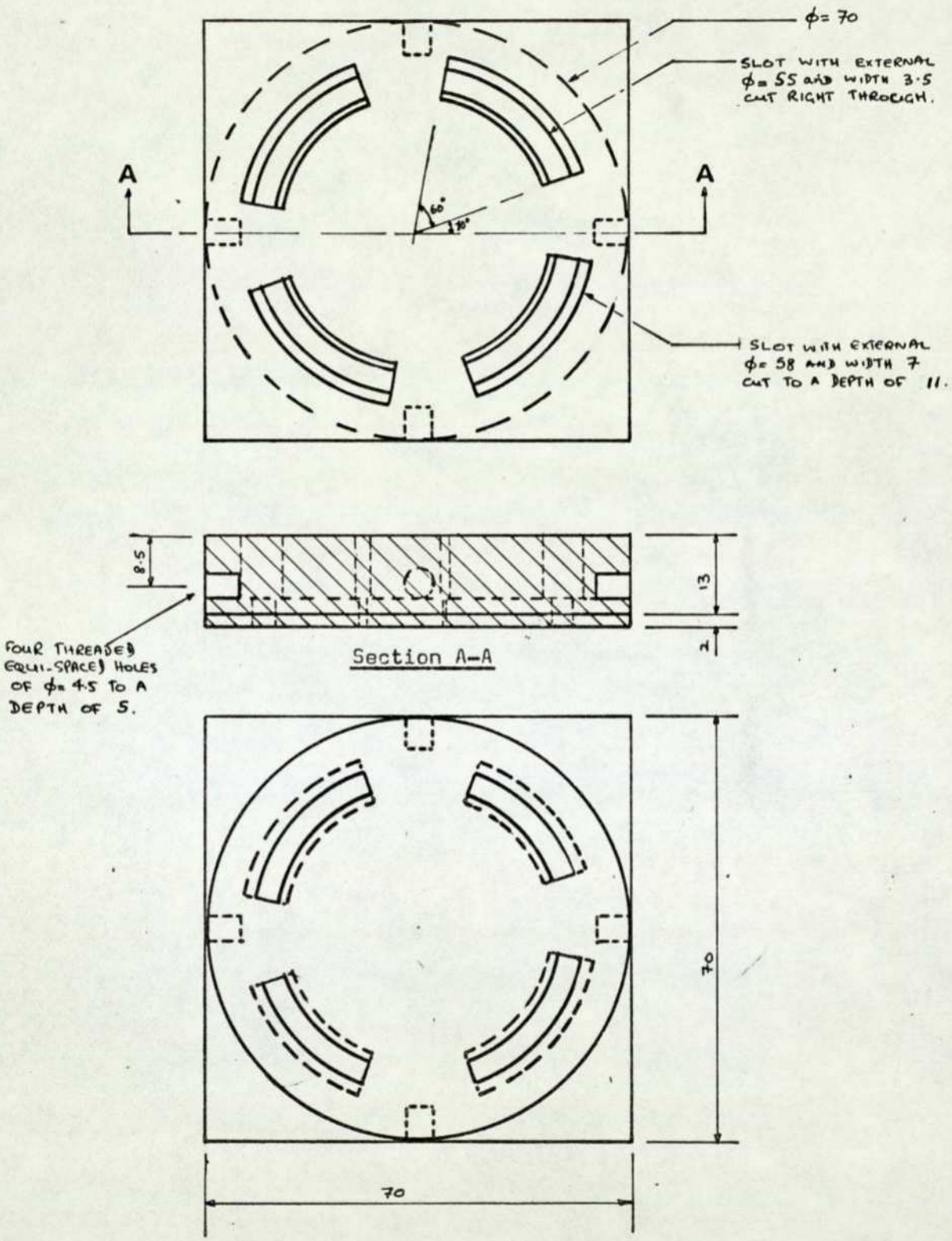

MATERIAL: Duraluminum

SCALE : 1 / 1

THIRD ANGLE PROJECTION

Square plug

FIGURE 5.4.c.i

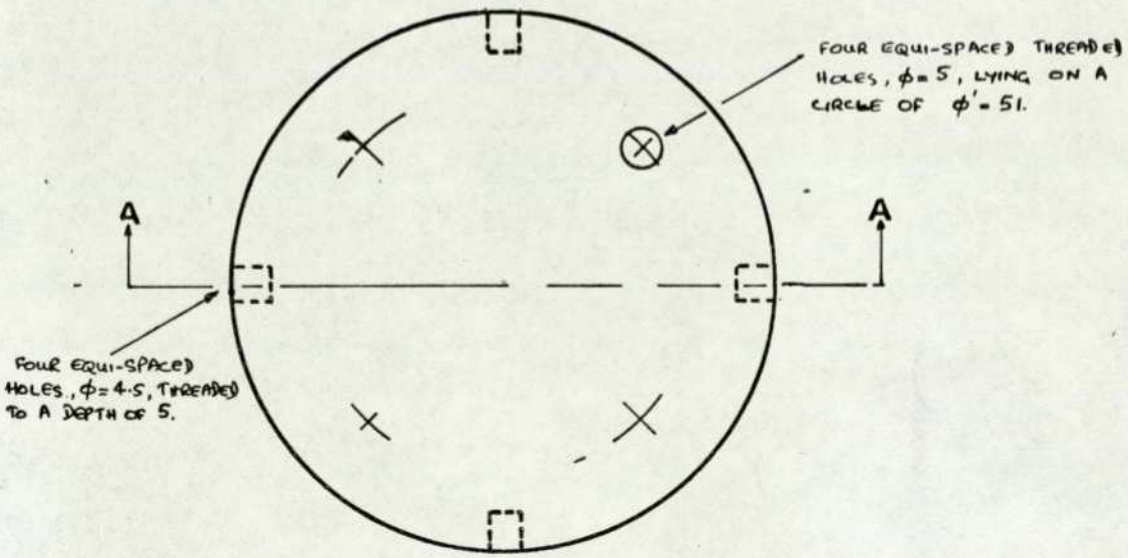

SECTION A–A

MATERIAL: Duraluminum

SCALE : 1 / 1

THIRD ANGLE PROJECTION

Circular plug

FIGURE 5.4.c.ii

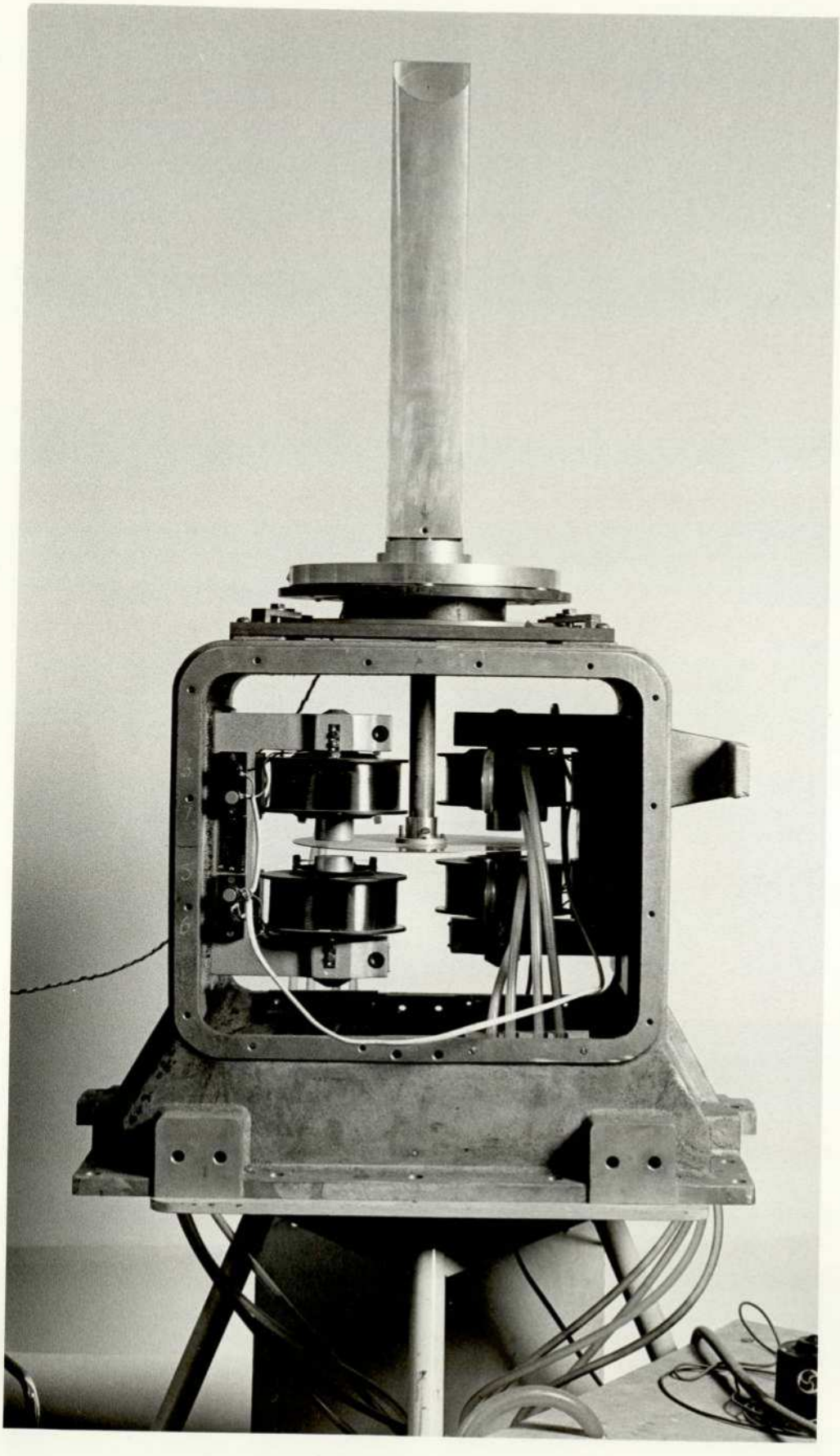

Model mounted on the experimental rig

FIGURE 5.5

Tube and collar of the damping system

FIGURE 5.6

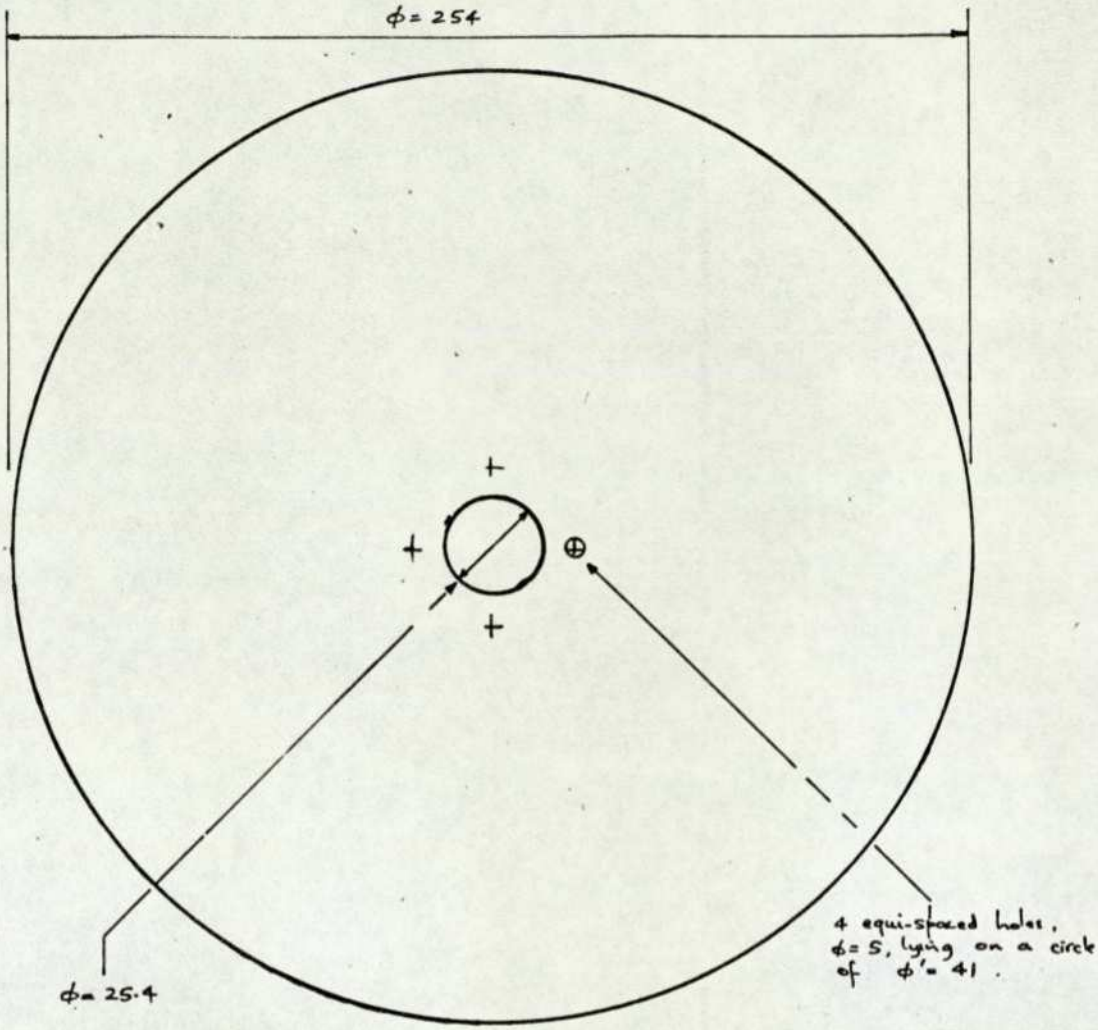

MATERIAL: 1 mm thick copper plate

SCALE : 1 / 2

Copper plate

FIGURE 5,6,a

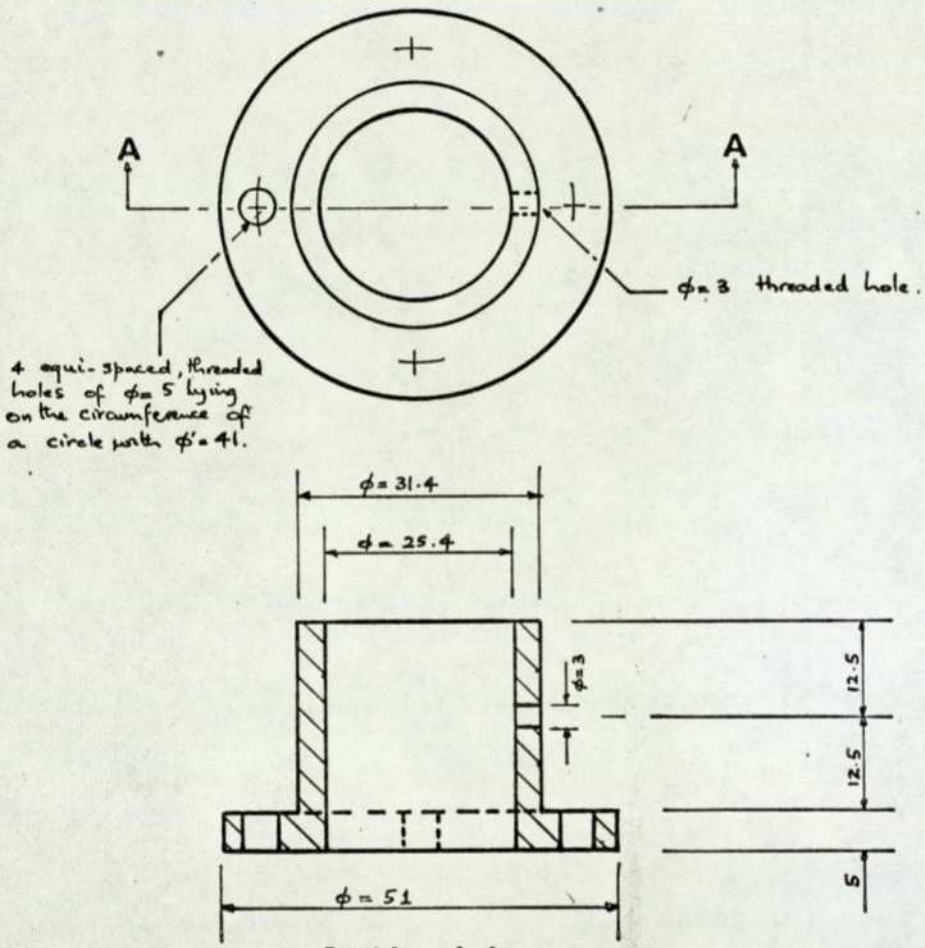

Section A–A

MATERIAL: Duraluminum

NO. REQUIRED: 2

SCALE : 1 / 1

THIRD–ANGLE PROJECTION

Collar

FIGURE 5.6.b

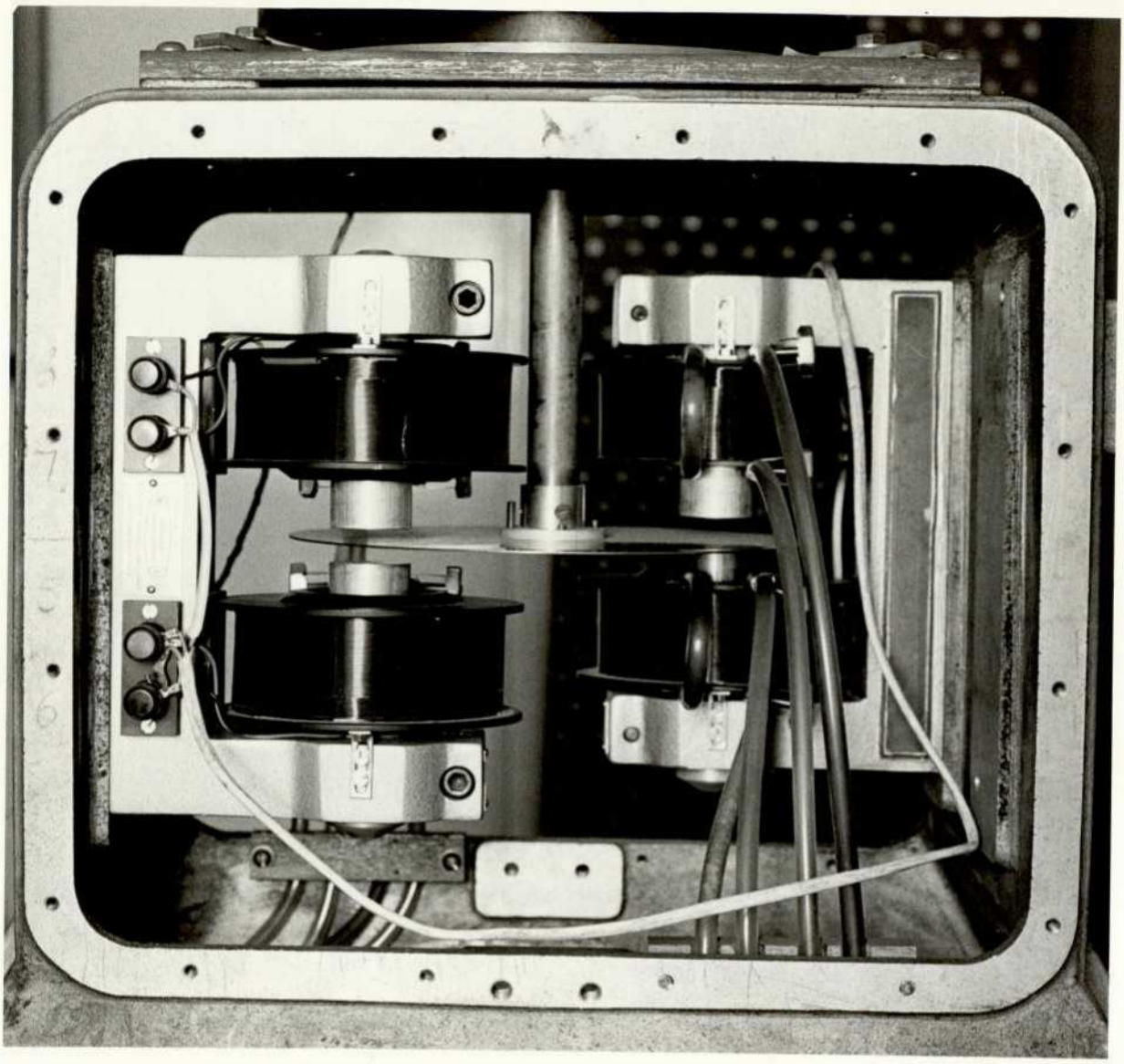

Mounting of electro-magnets

FIGURE 5.7

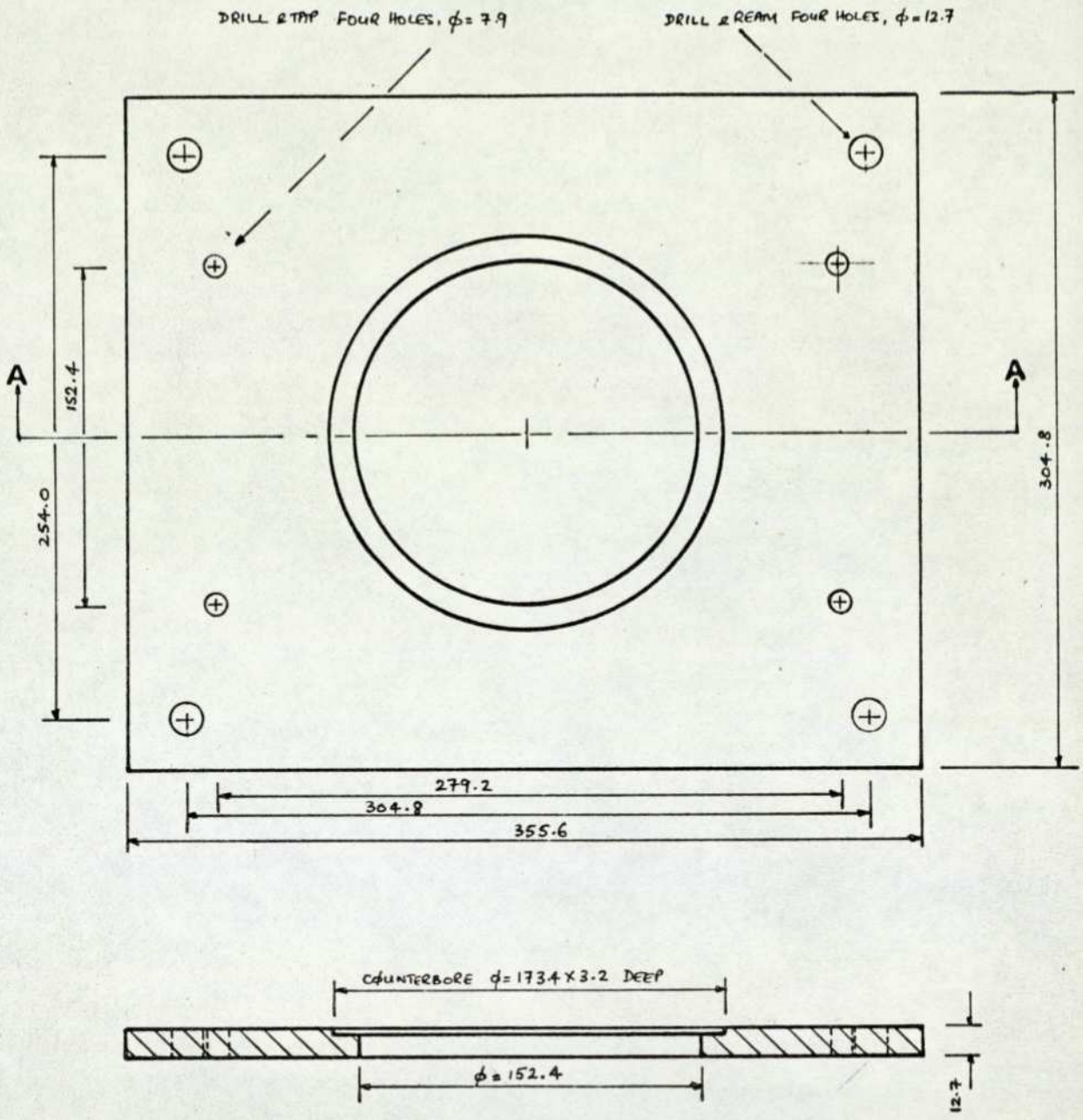

SECTION A–A

MATERIAL: Mild-steel plate

SCALE : 1 / 3

Support plate

FIGURE 5.8

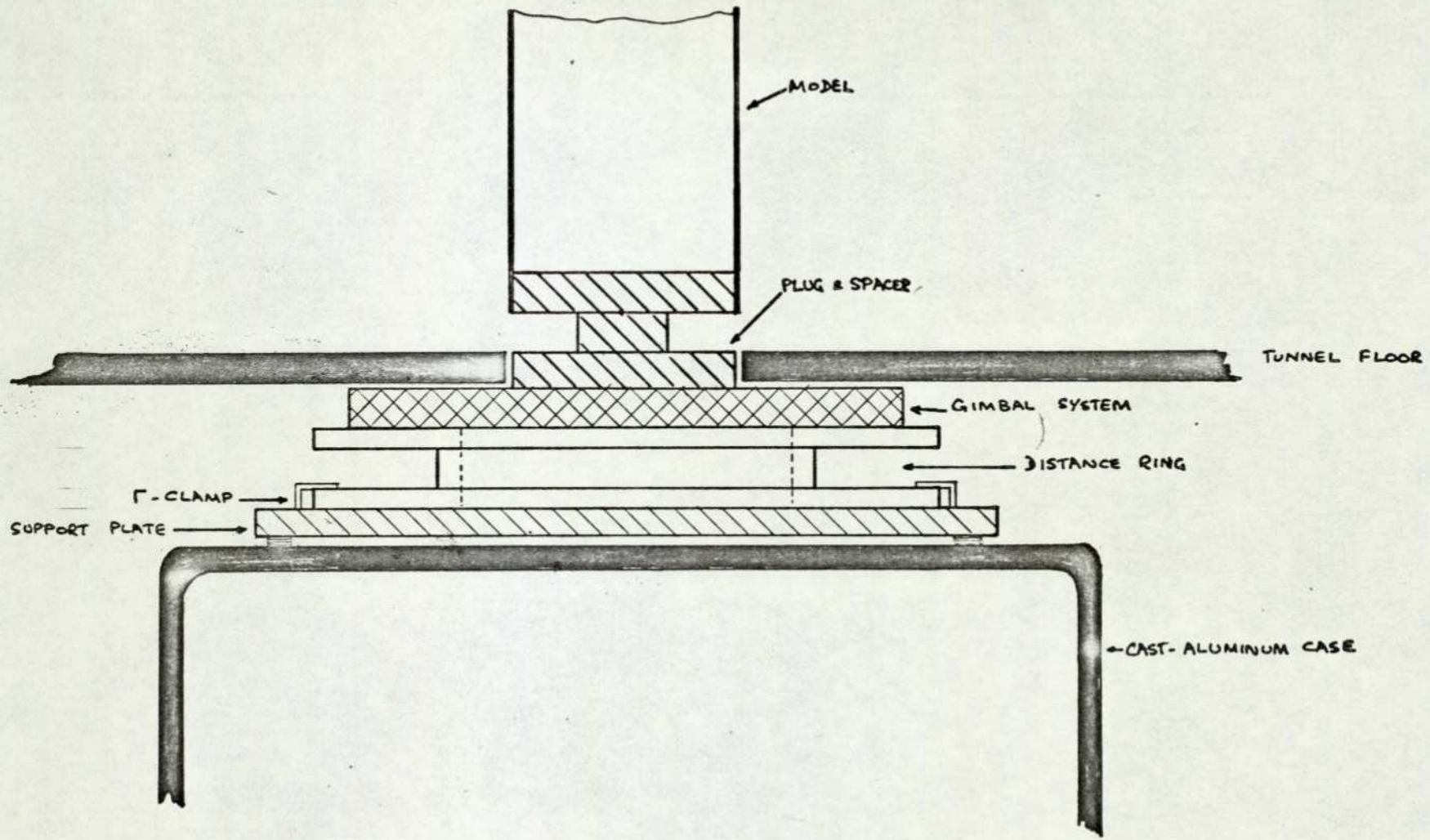

Schematic showing clearance between wind-tunnel floor and model mounted on vibration rig

FIGURE 5.9

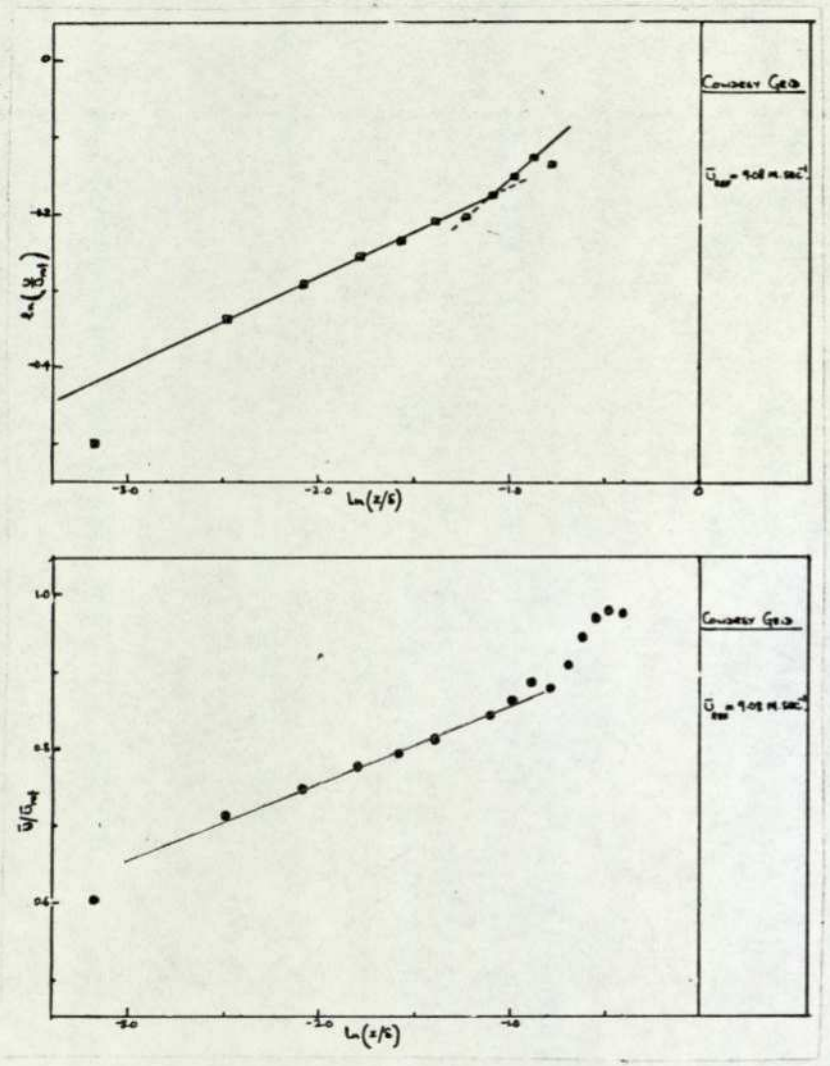

Velocity profile: Generated flow with Cowdrey grid only

FIGURE 6.1.a

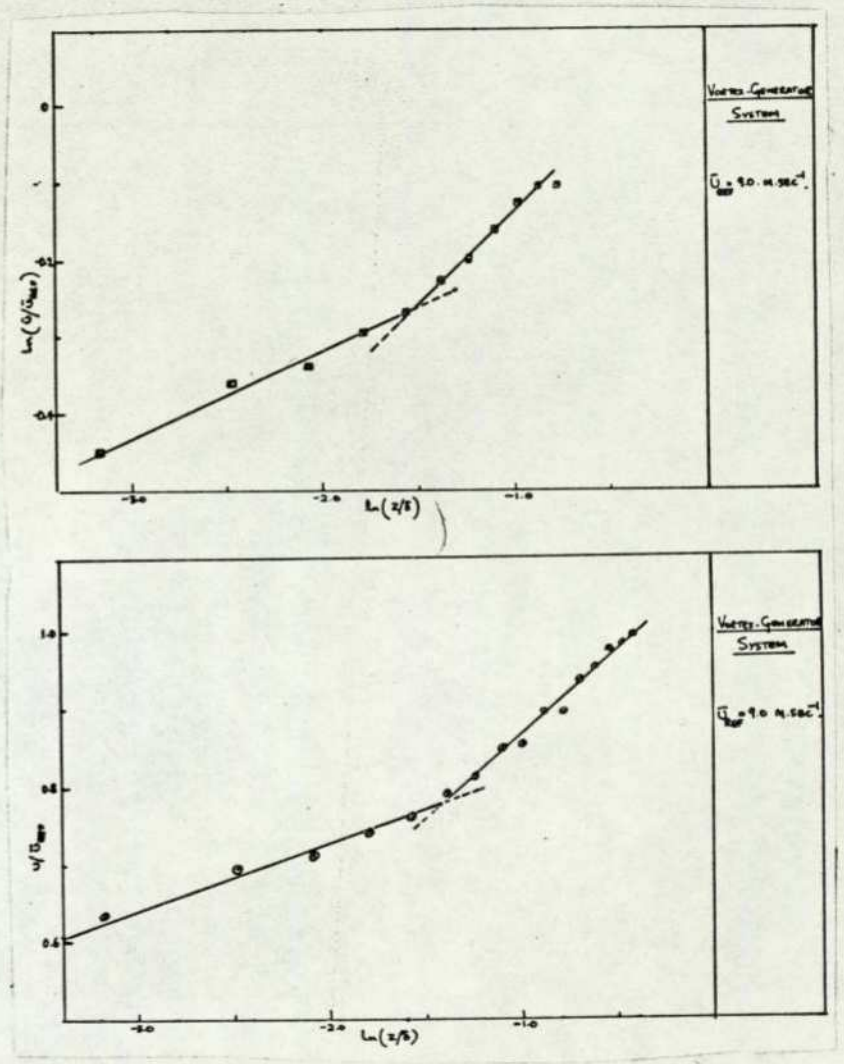

Velocity profile: Generated flow with vortex generator system only

FIGURE 6.1.b

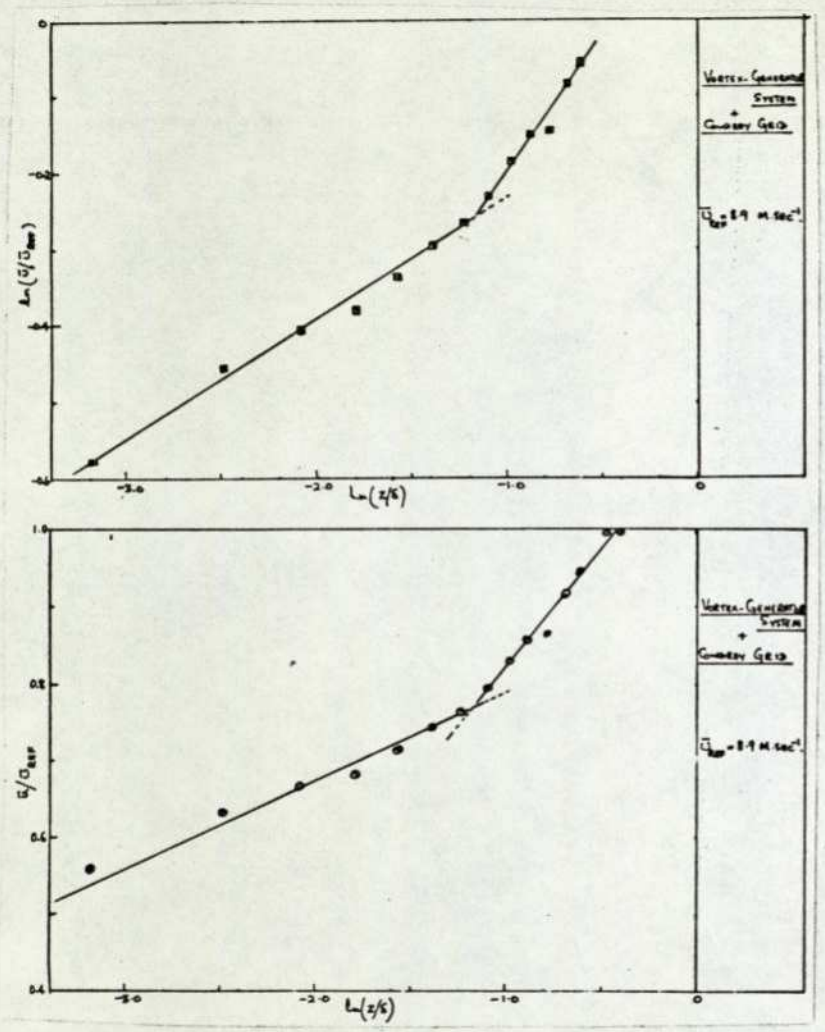

Velocity profile: Generated flow with vortex generator system and Cowdrey grid but without roughness elements

FIGURE 6.1.c

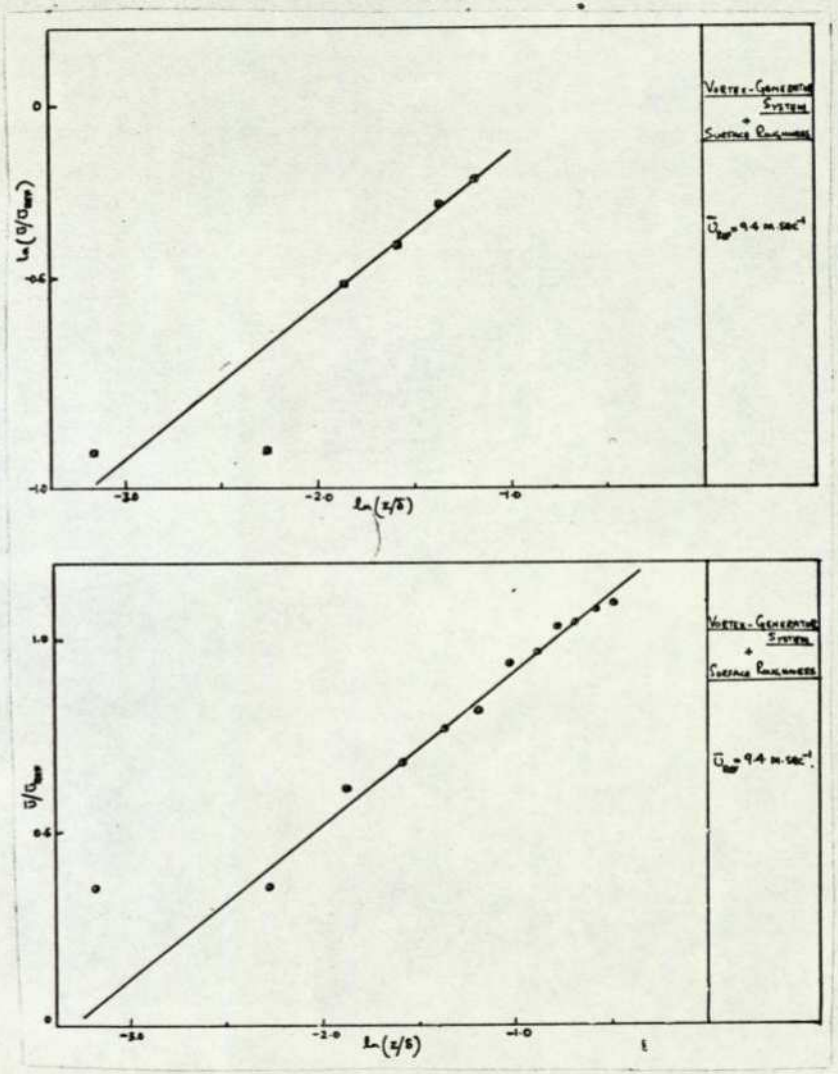

Velocity profile: Generated flow (T_s)

FIGURE 6.1.d

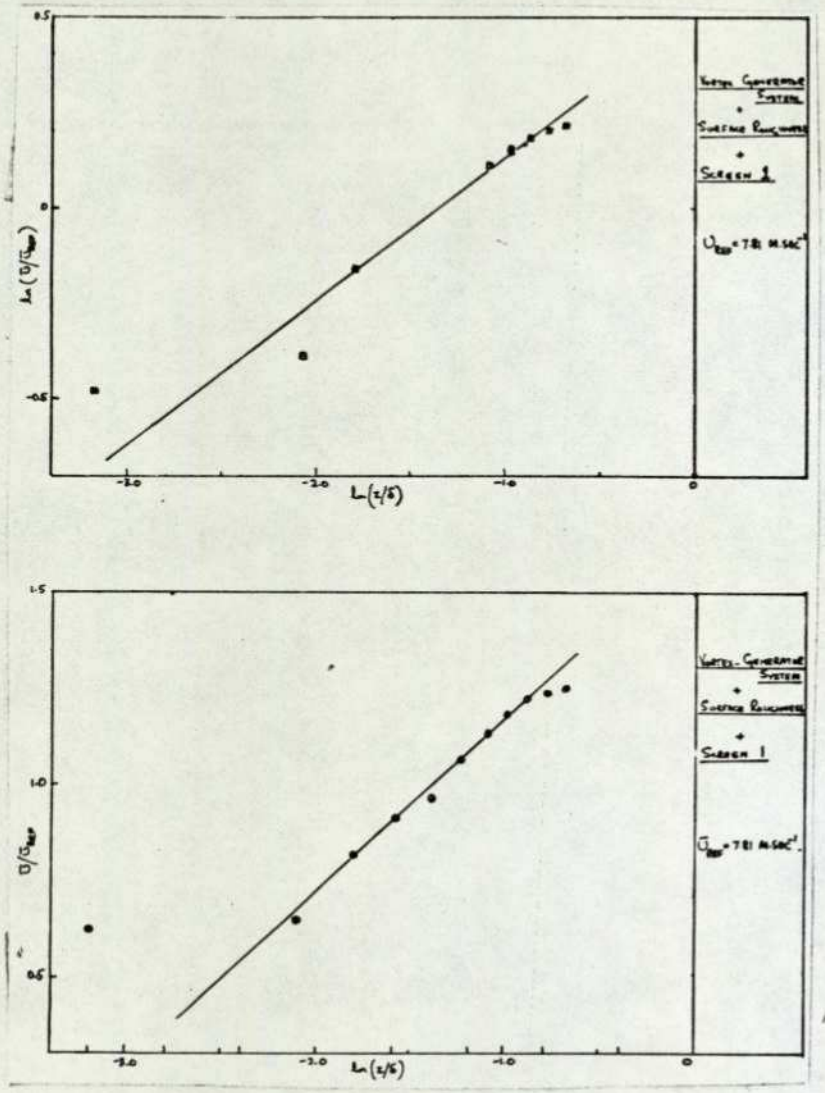

Velocity profile: Generated flow (T_s+1)

FIGURE 6.1.e

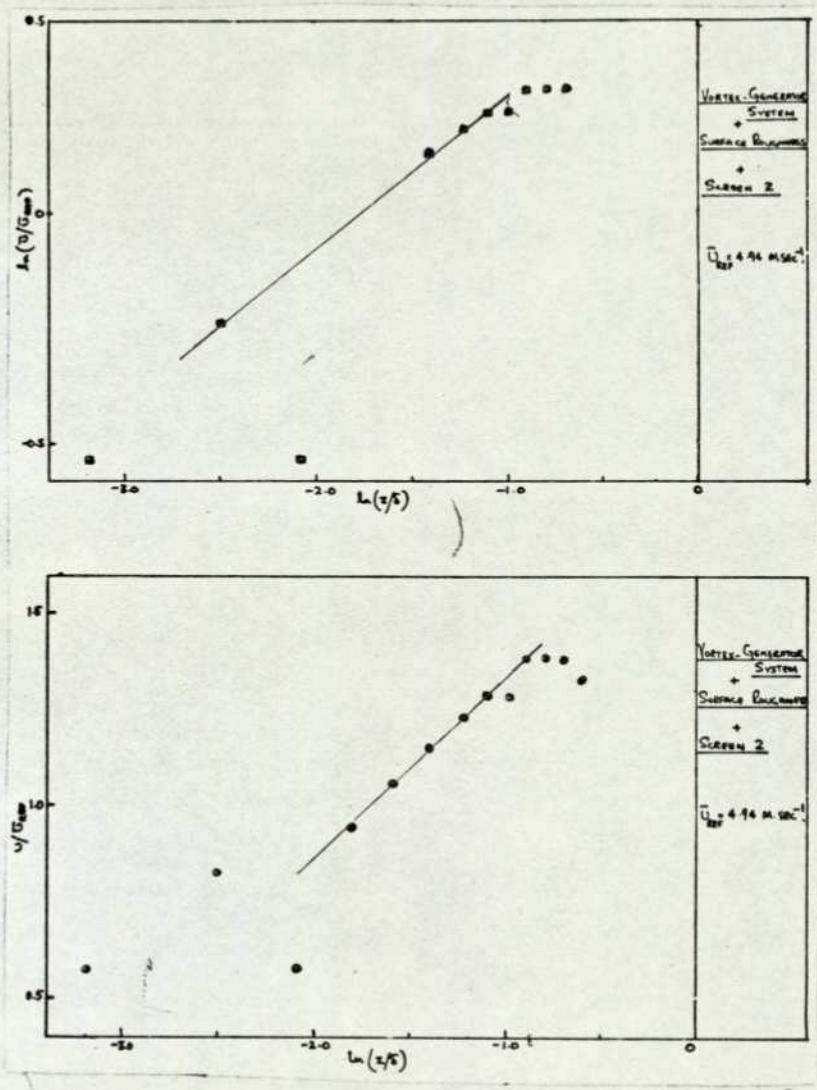

Velocity profile: Generated flow (T_s+2)

FIGURE 6.1.f

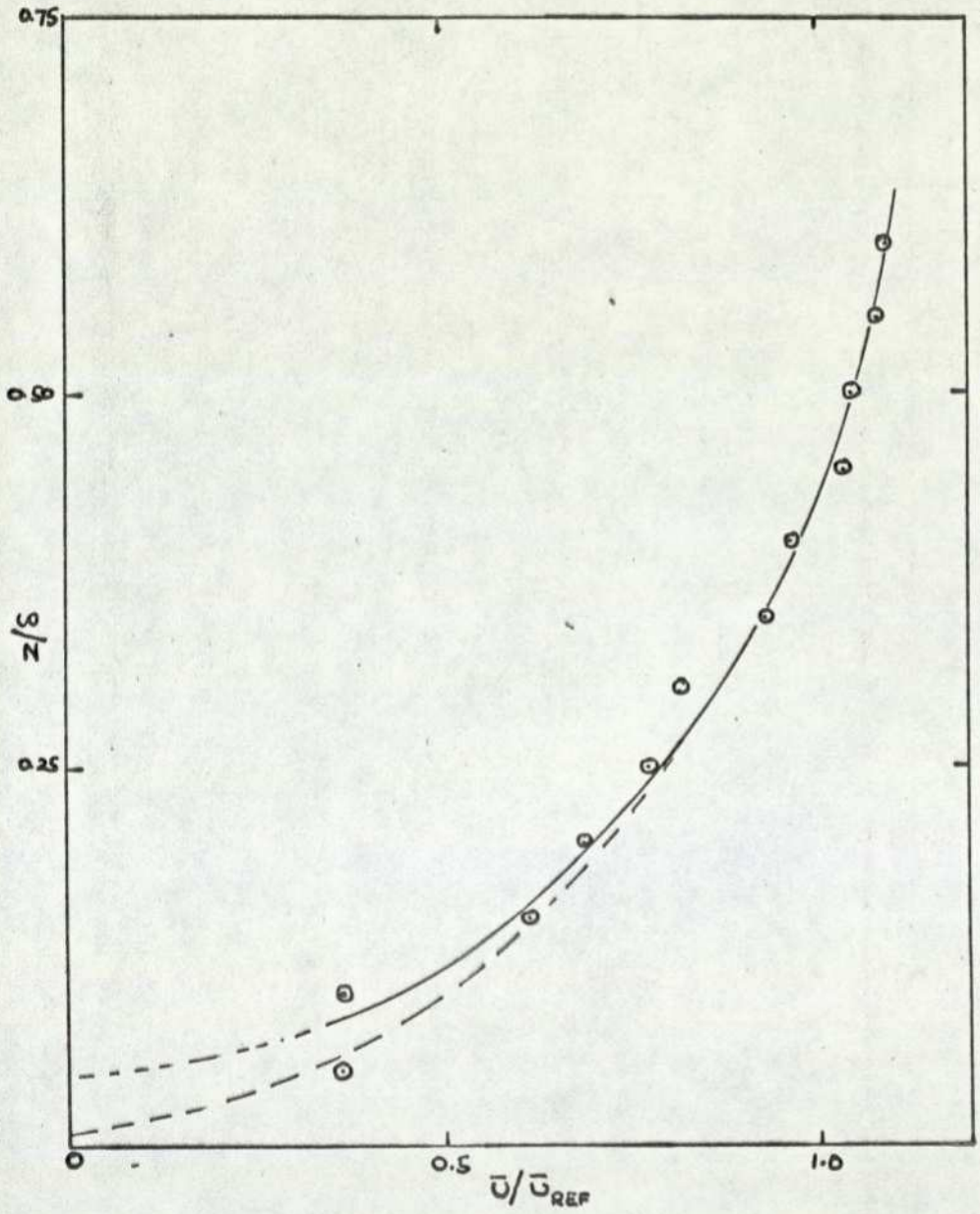

Velocity profile plot to obtain possible zero-plane displacement

FIGURE 6.1.g

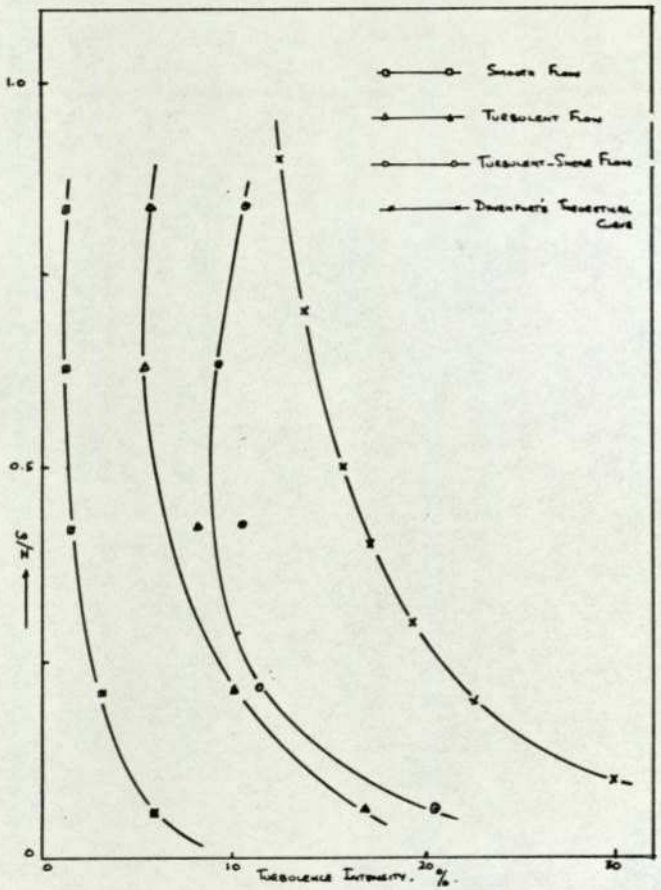

Turbulent intensity profile: Generated flow without roughness

FIGURE 6.2.a

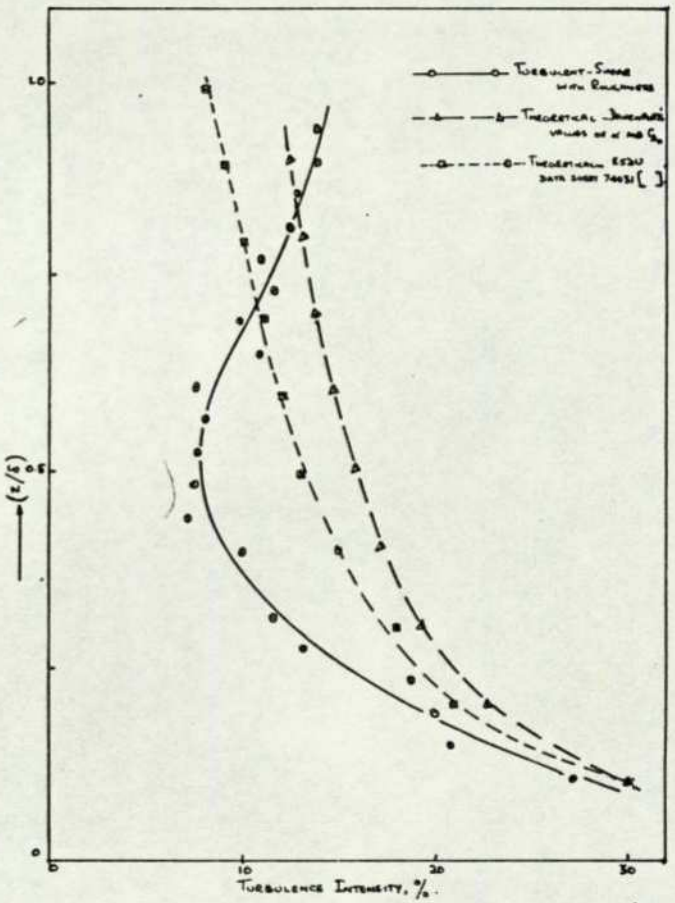

Turbulent intensity profile: Generated flow with roughness

FIGURE 6.2.b

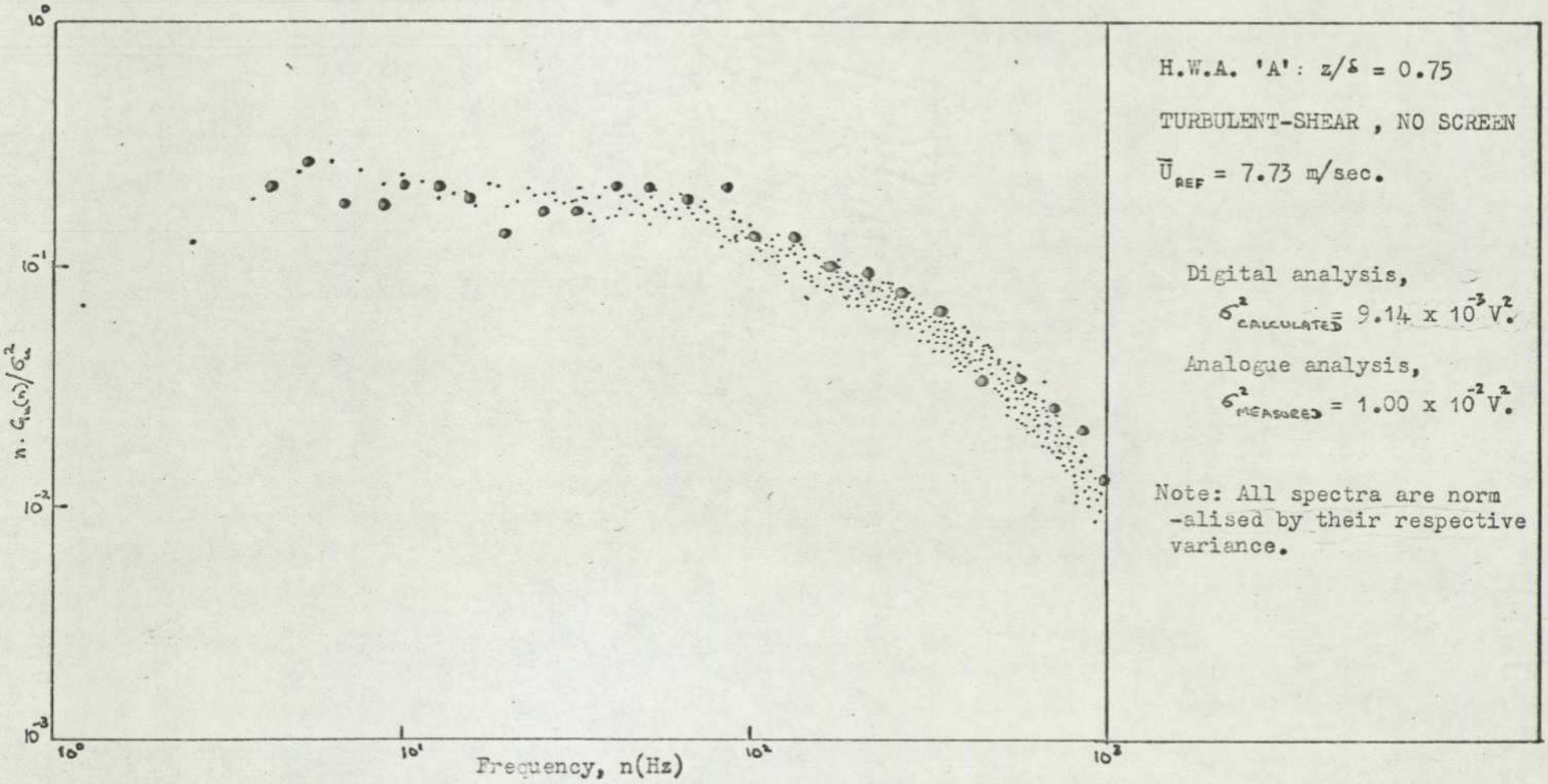

Comparison of turbulence spectra obtained by digital and analogue methods.

FIGURE 6.3

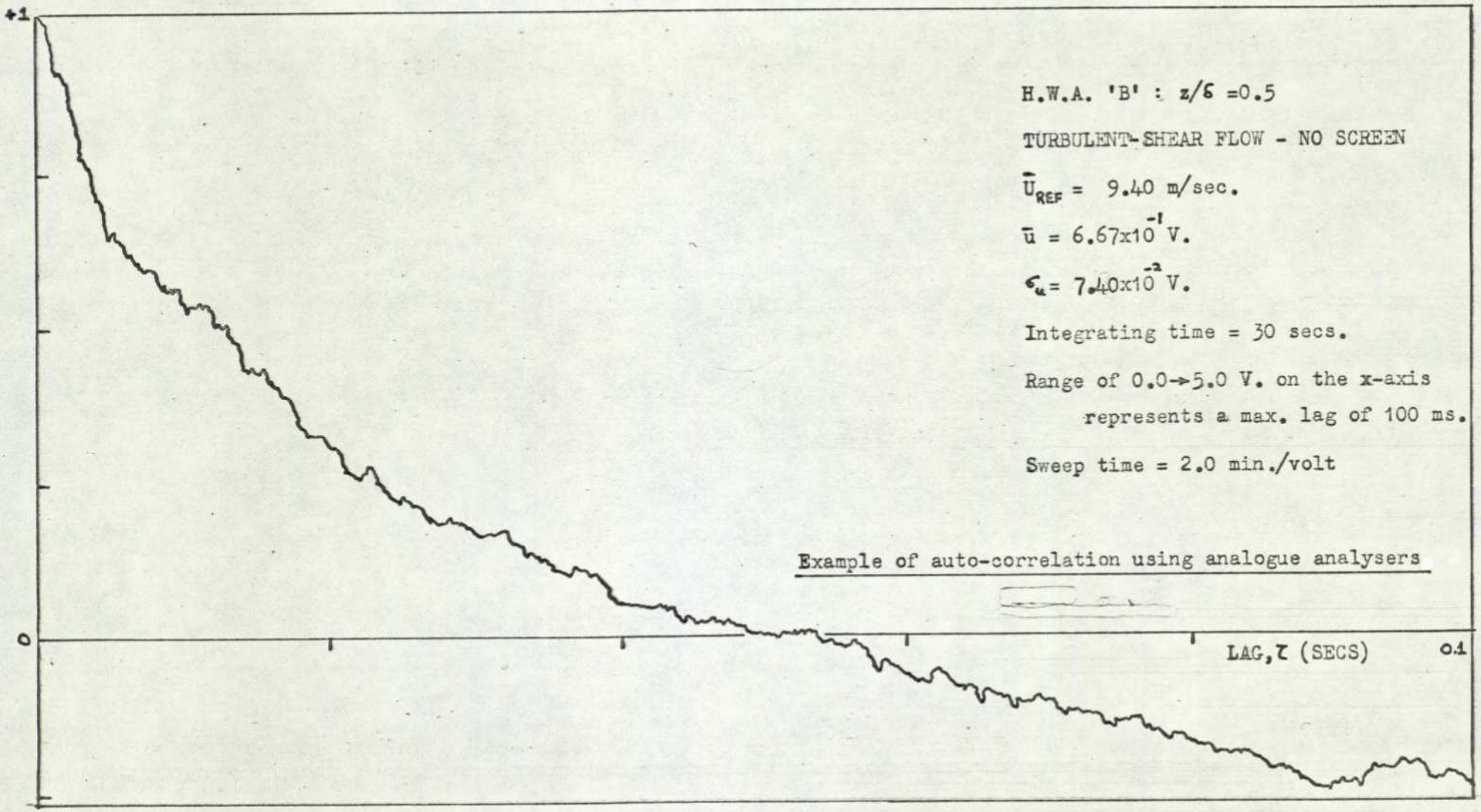
+1
0
H.W.A. 'B' : z/δ =0.5
TURBULENT SHEAR FLOW - NO SCREEN
$\bar{U}_{REF}$ = 9.40 m/sec.
$\bar{u}$ = 6.67x10^{-1} V.
σ_u = 7.40x10^{-2} V.
Integrating time = 30 secs.
Range of 0.0→5.0 V. on the x-axis represents a max. lag of 100 ms.
Sweep time = 2.0 min./volt
Example of auto-correlation using analogue analysers
LAG, τ (SECS)
0.1

FIGURE 6.4

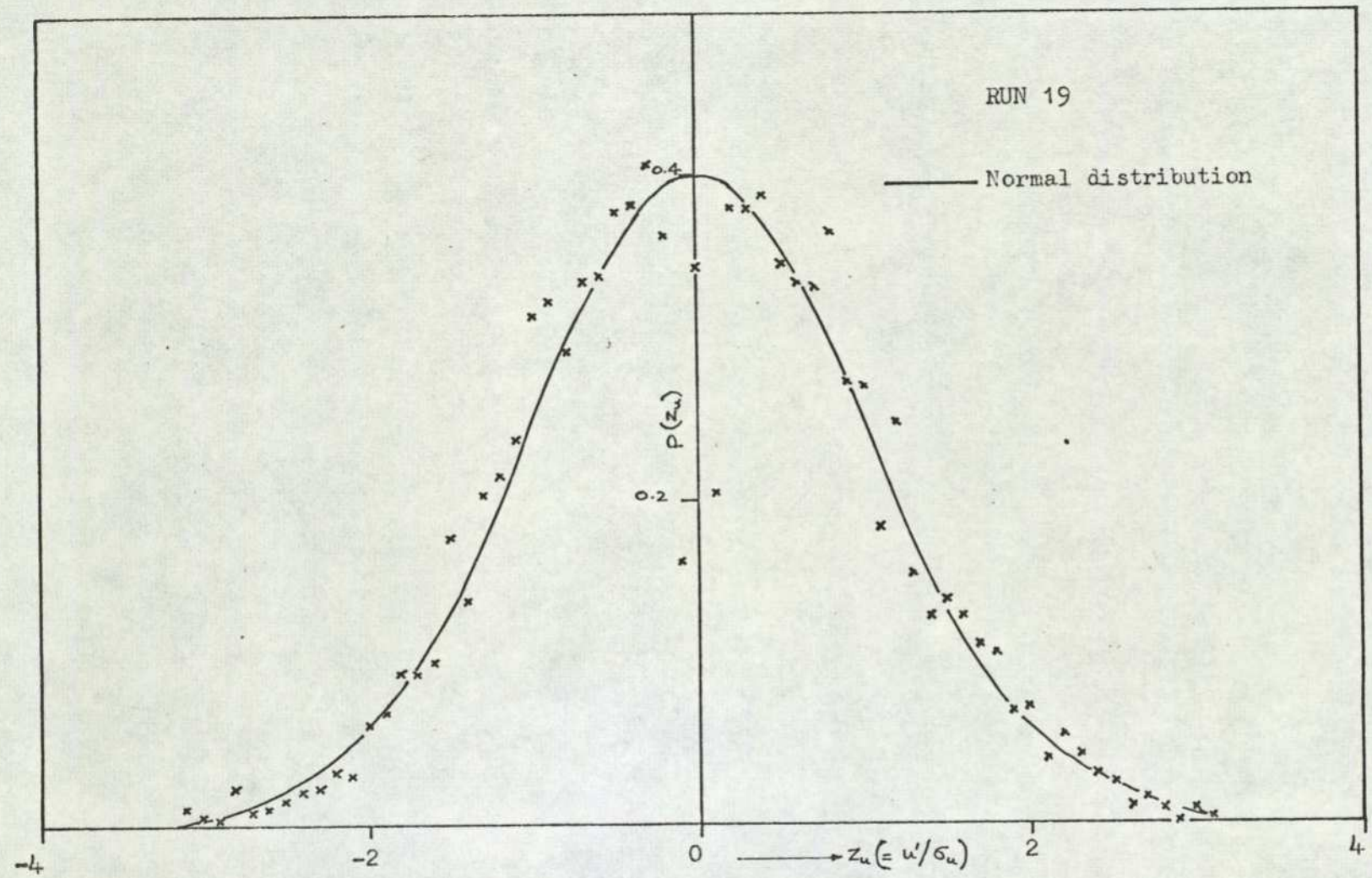

Probability density distribution for the longitudinal wind velocity at $z/\delta = 0.75$

FIGURE 6.5.a

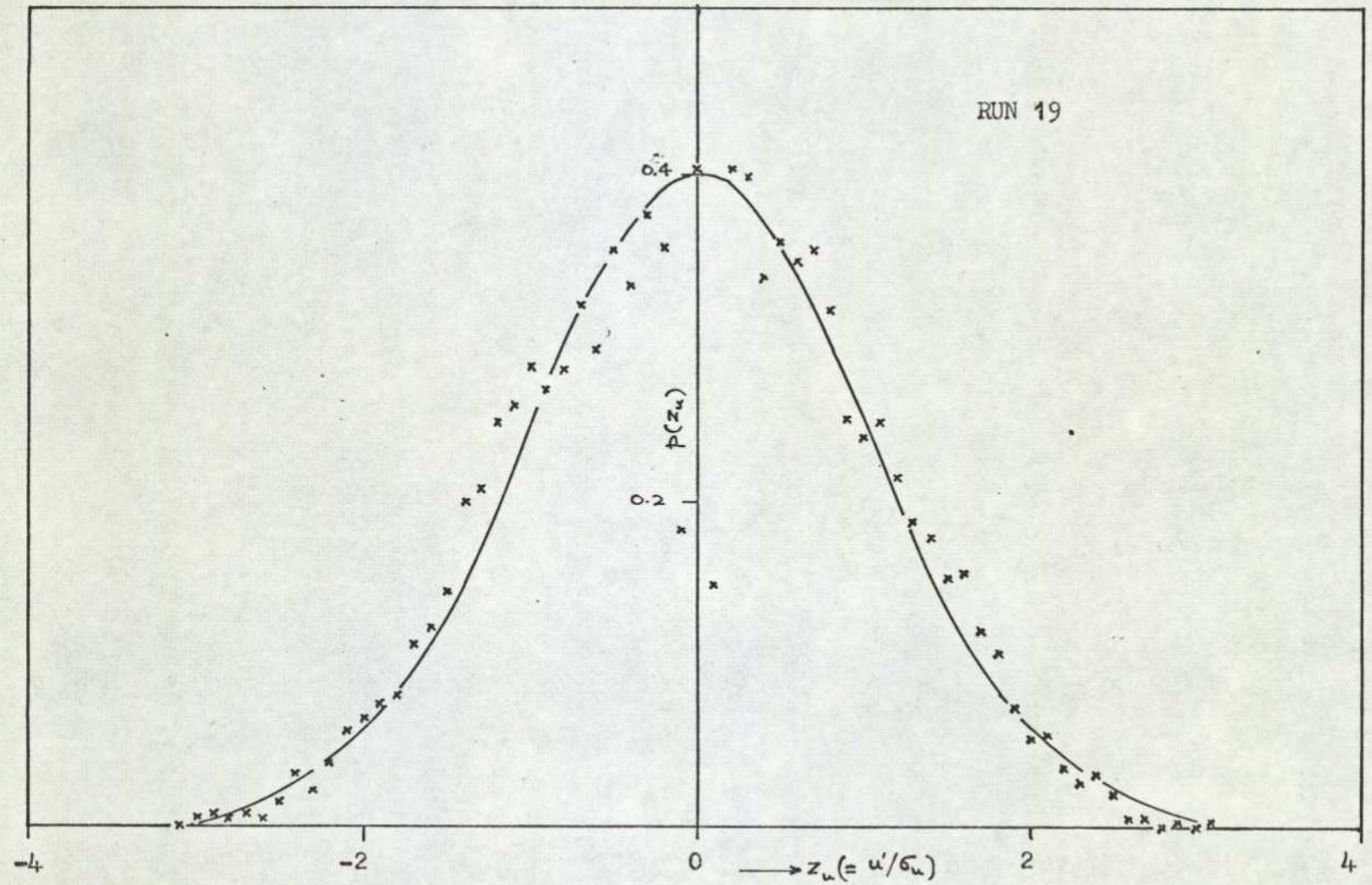

Probability density distribution for the longitudinal wind velocity at $z/\delta = 0.50$

FIGURE 6.5.b

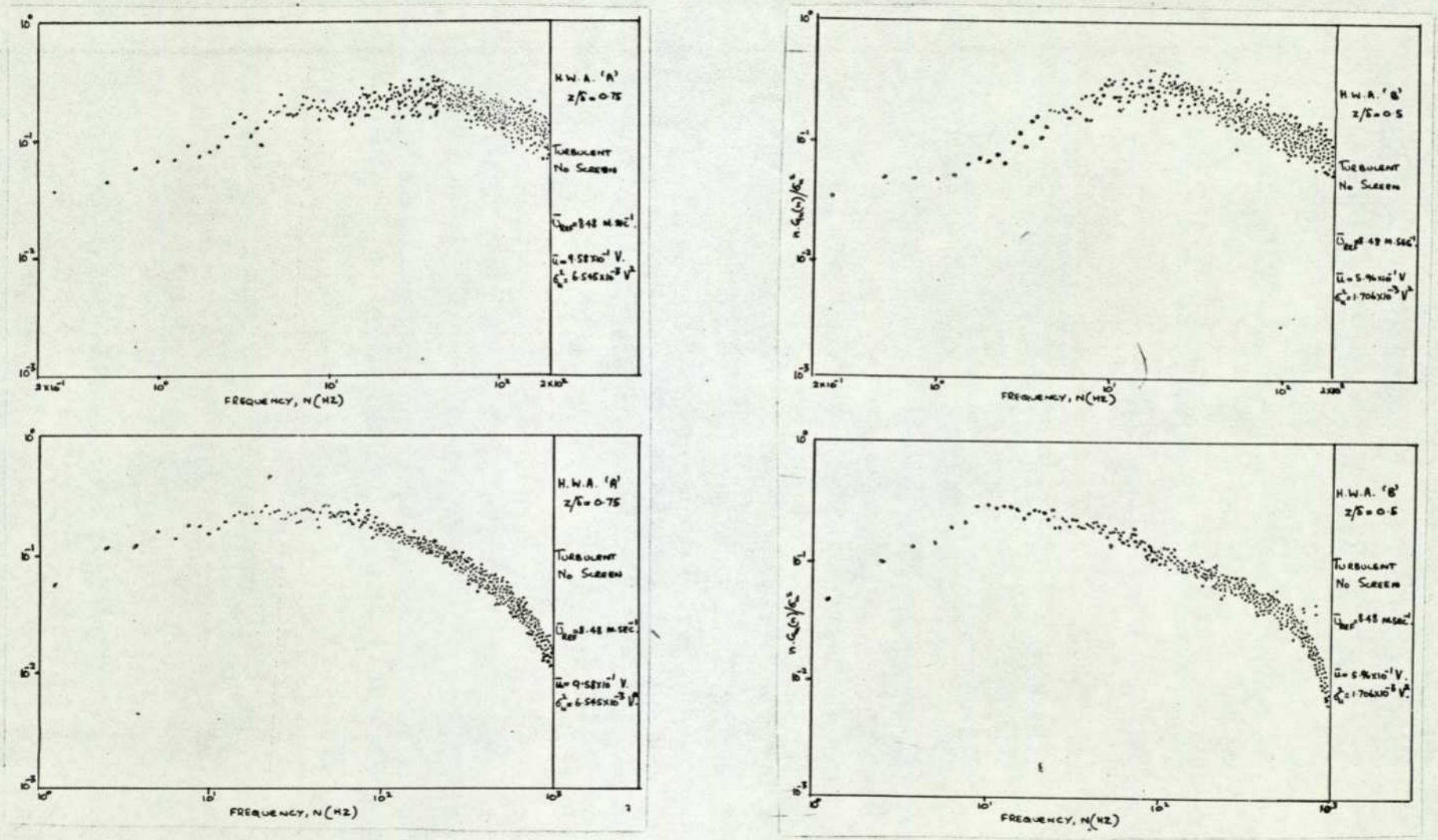

Auto-spectrum: Generated flow (T)

FIGURE 6.6.a

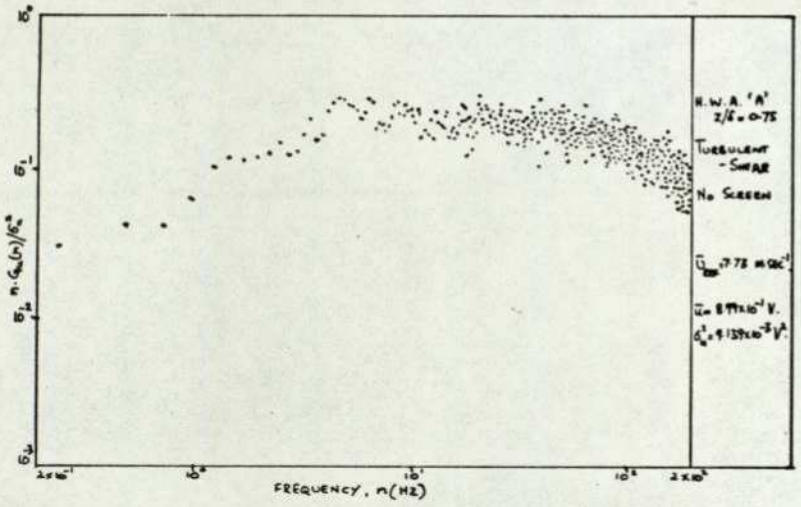

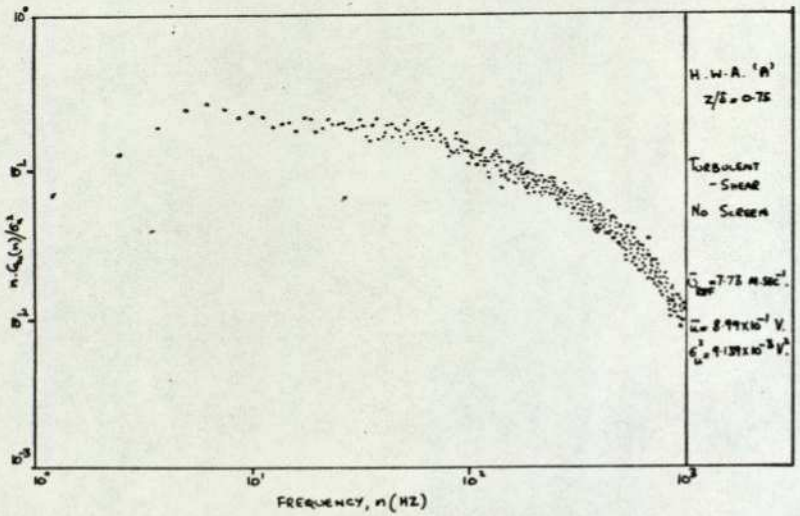

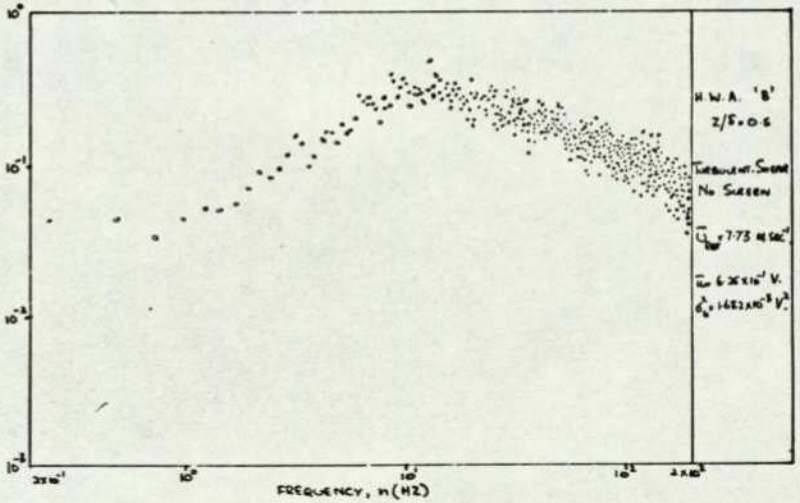

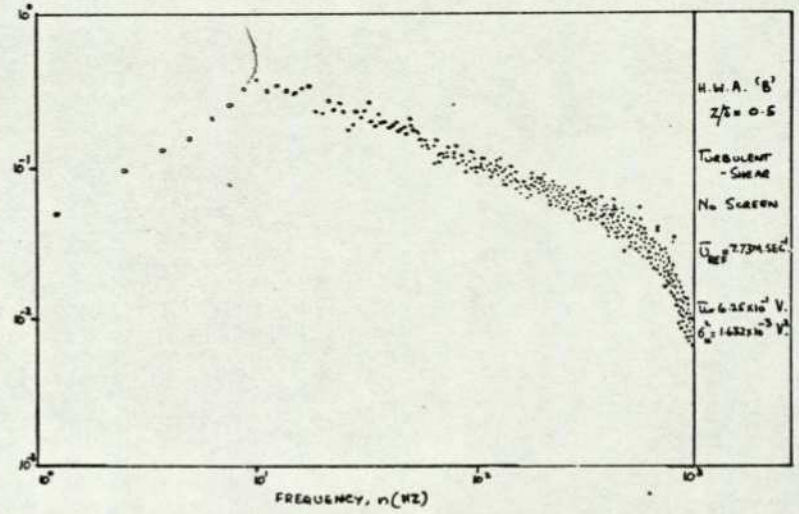

Auto-spectrum: Generated flow (T_S) — low speed

FIGURE 6.6.b

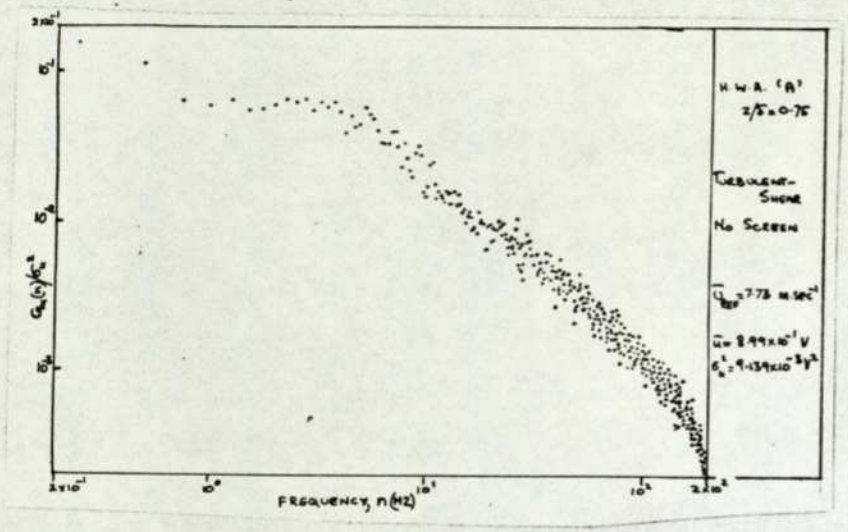

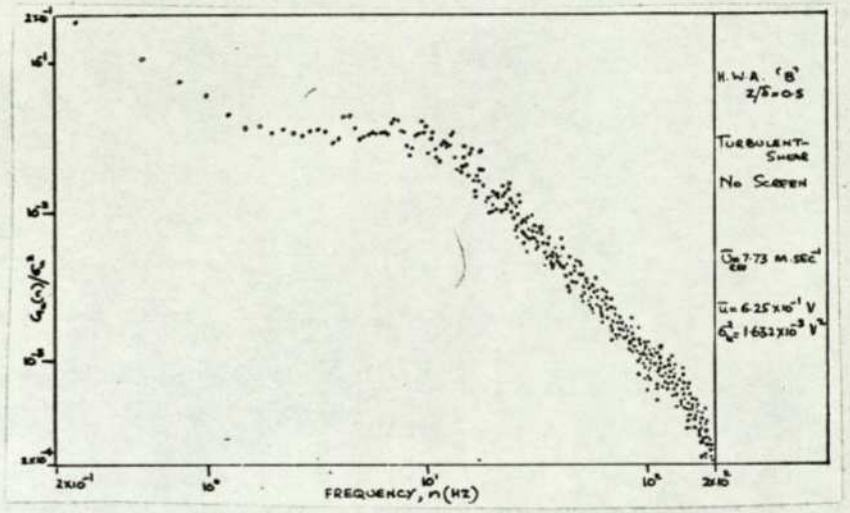

Auto-spectrum: Generated flow (T_s) — $\ln\{G_u(n)/\sigma_u^2\}$ vs $\ln\{n\}$

FIGURE 6.6.b.i

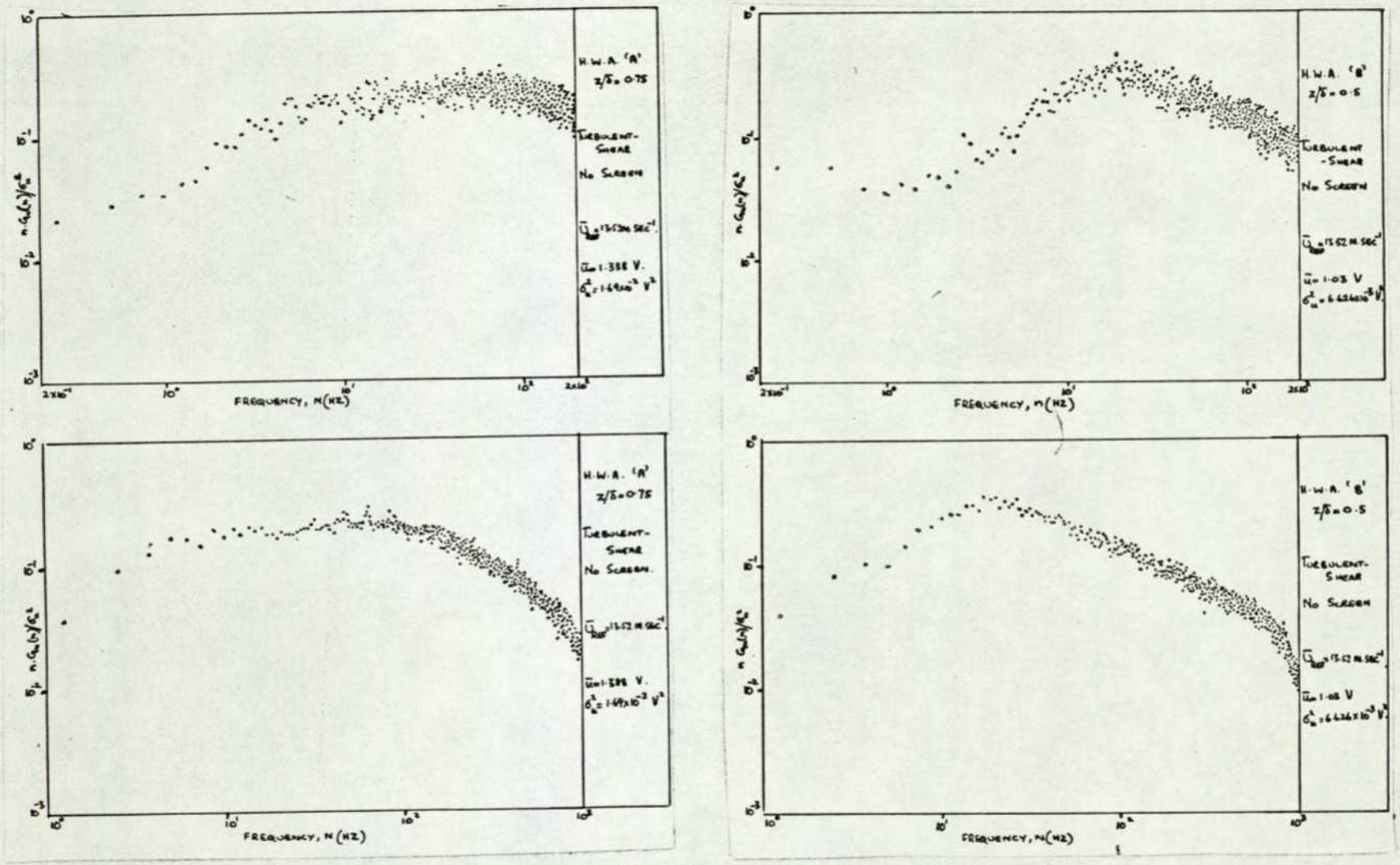

Auto-spectrum: Generated flow (T_S) -- high speed

FIGURE 6,6,c

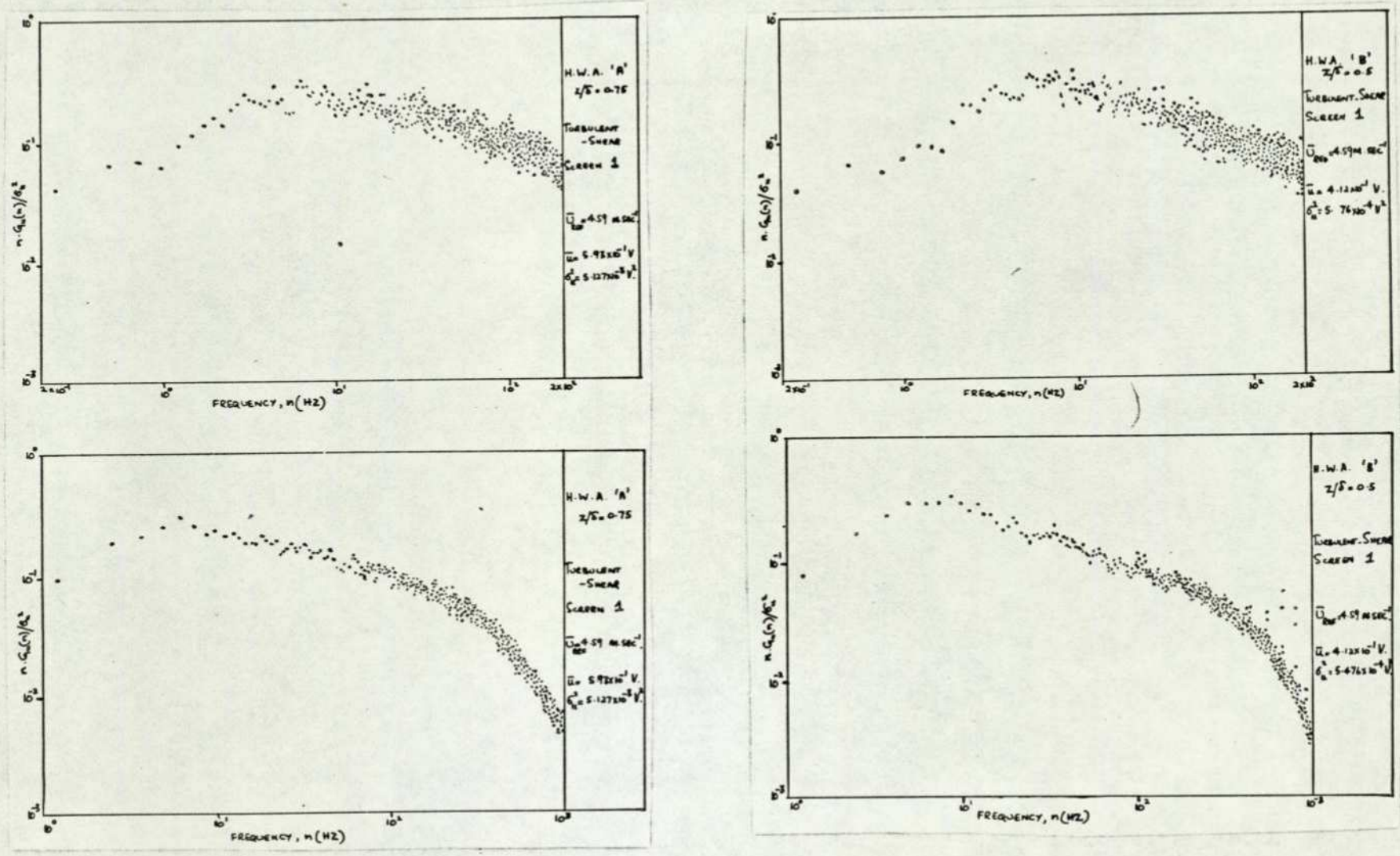

Auto-spectrum: Generated flow (T_S + 1)

FIGURE 6.6.d

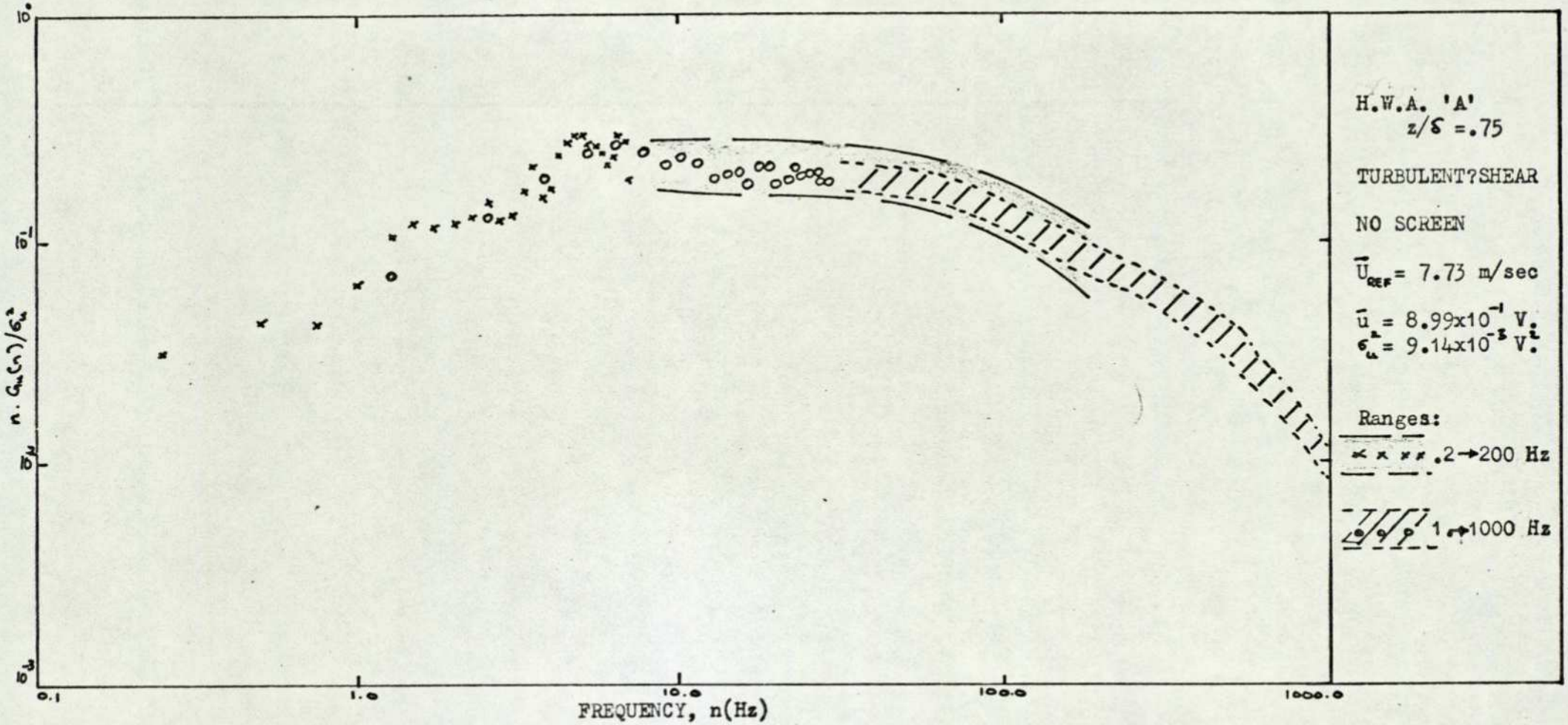

Composite spectra of generated turbulence (digital analysis)

FIGURE 6.6.e

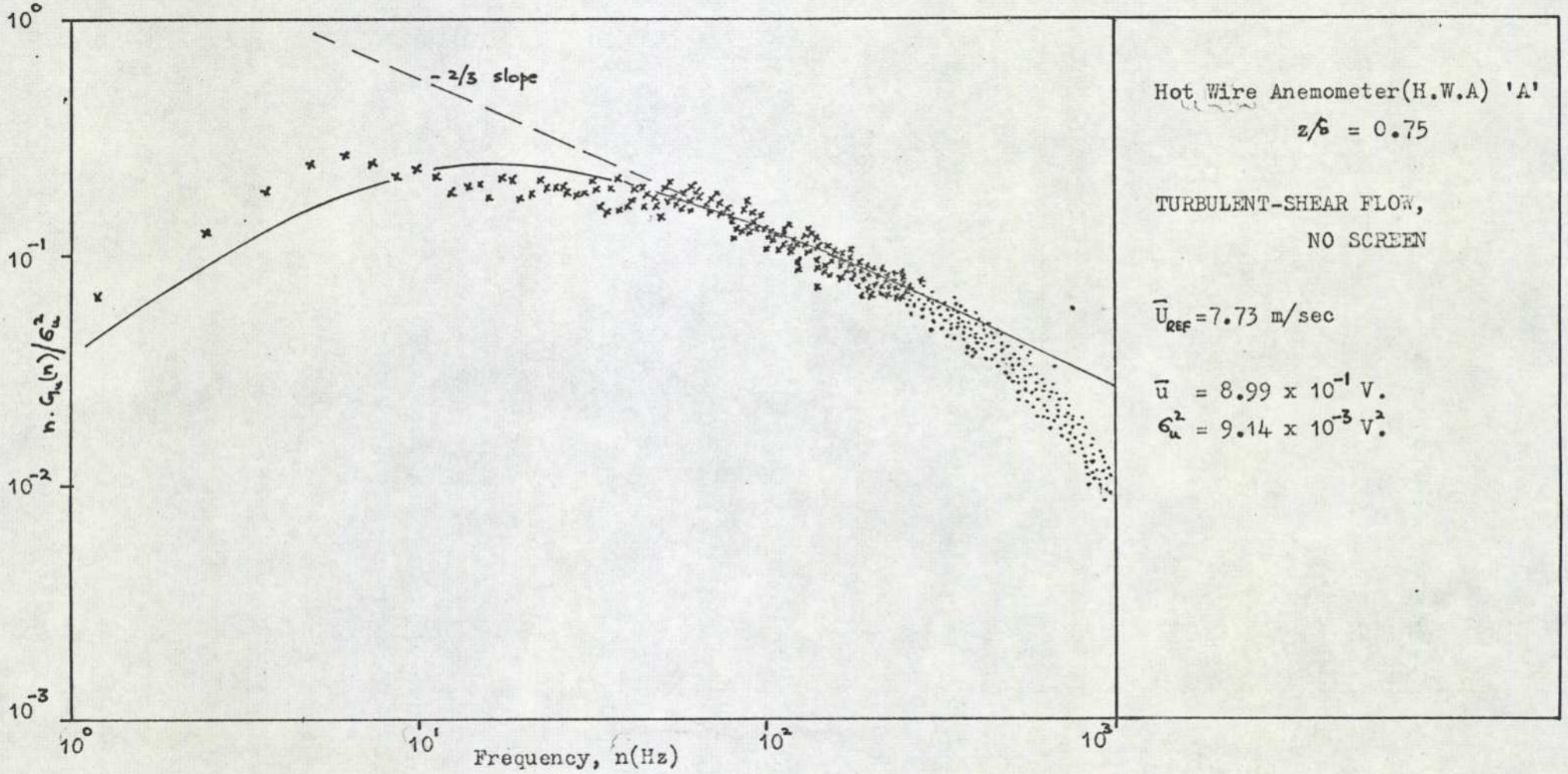

Fitting of Kaimal equation for longitudinal fluctuating wind velocity spectrum

FIGURE 6.6.f

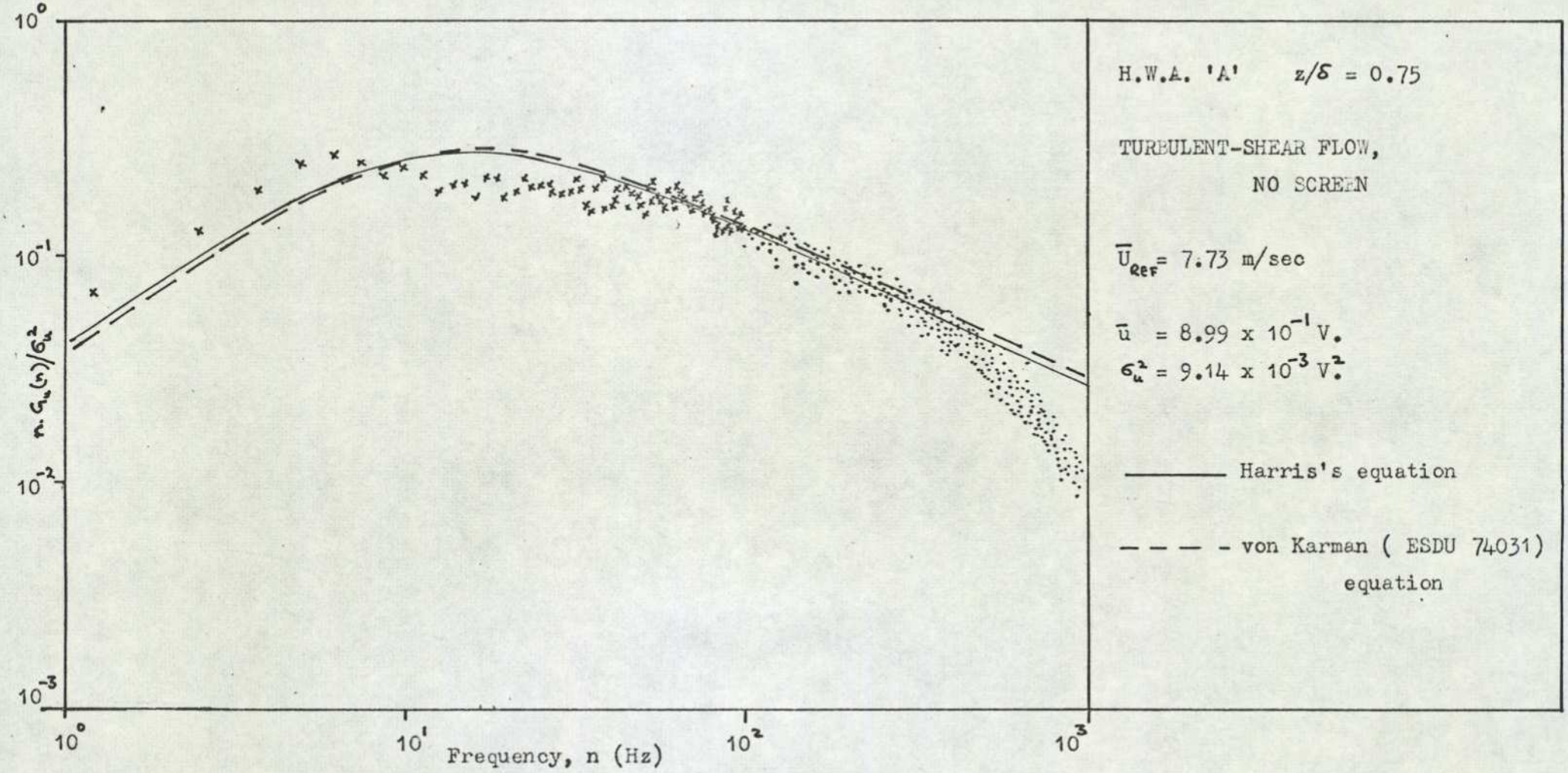

Fitting of Harris and von Karman equations to the longitudinal fluctuating wind velocity spectrum

FIGURE 6.6.g

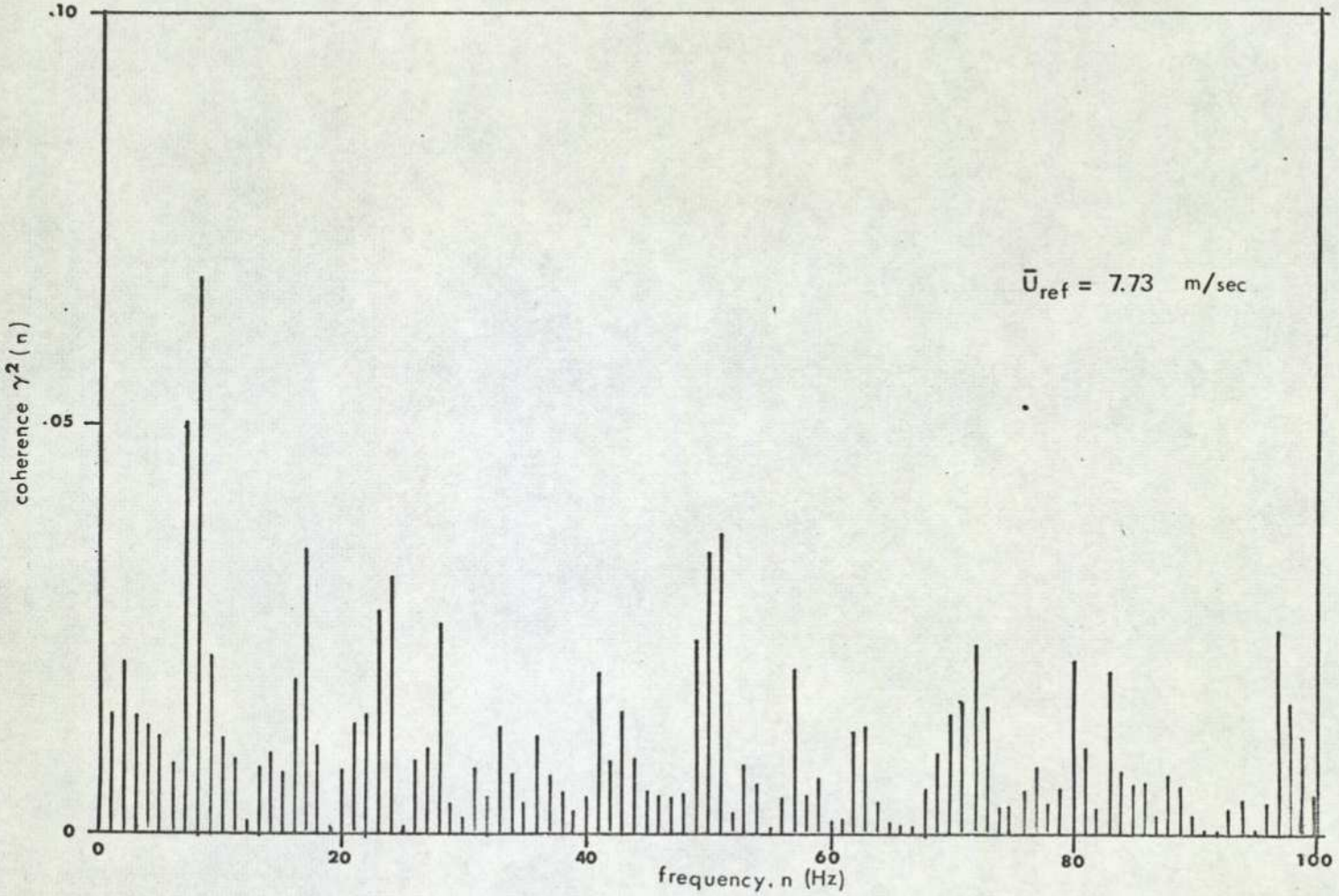

Coherence between hot-wire anemometers A($z/\delta = 0.75$) and B ($z/\delta = 0.50$) in turbulent shear flow

FIGURE 6.7

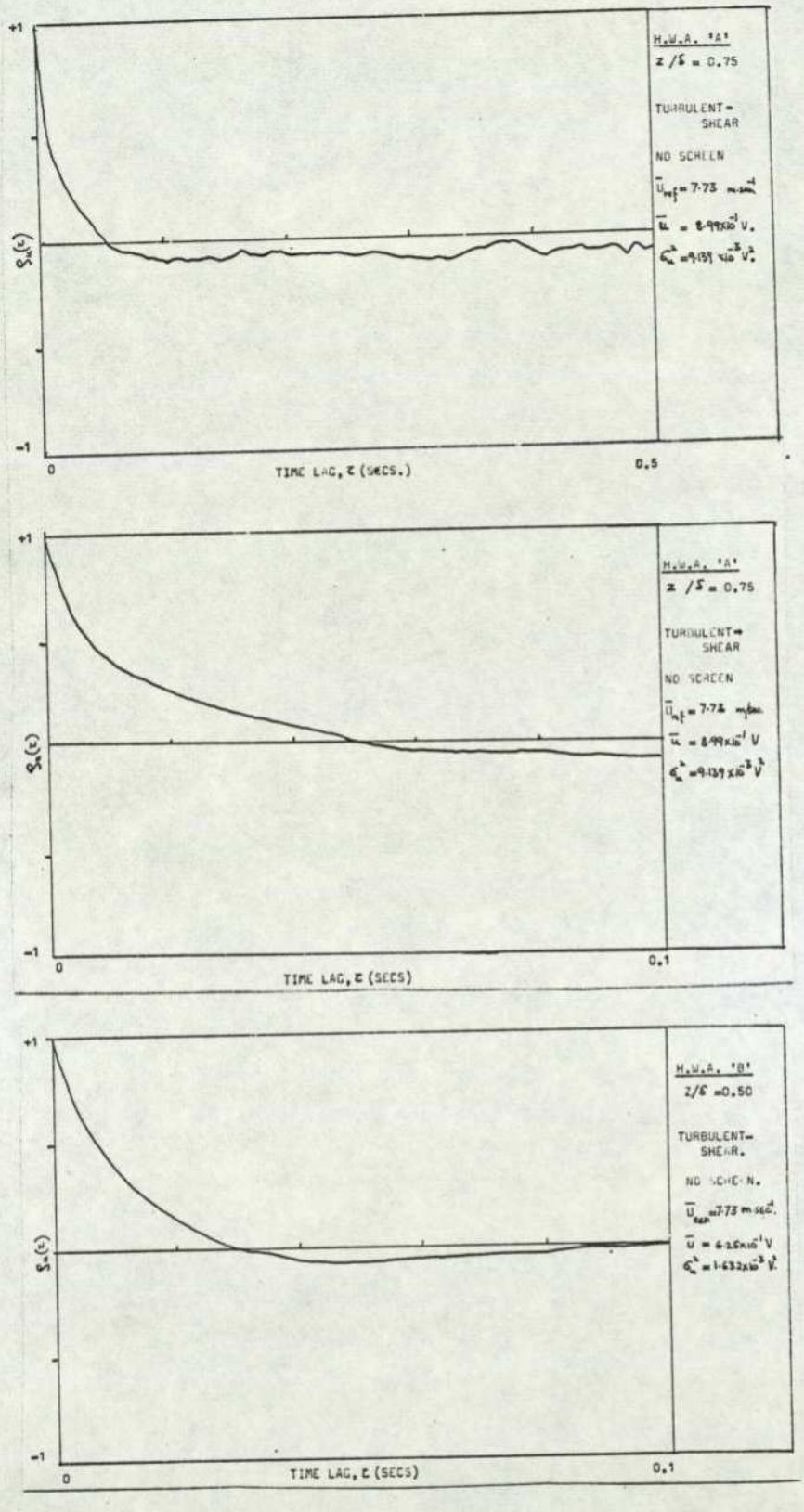

Auto-correlation: Generated flow (T_s) -- low speed

FIGURE 6.8.a

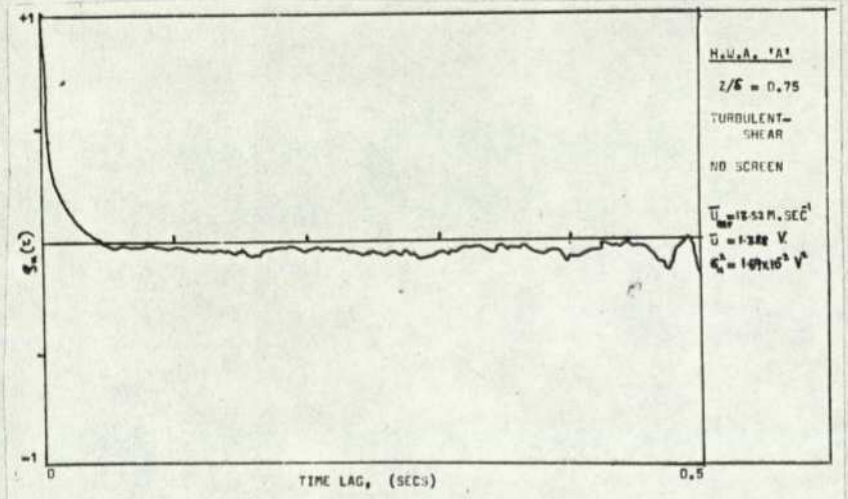

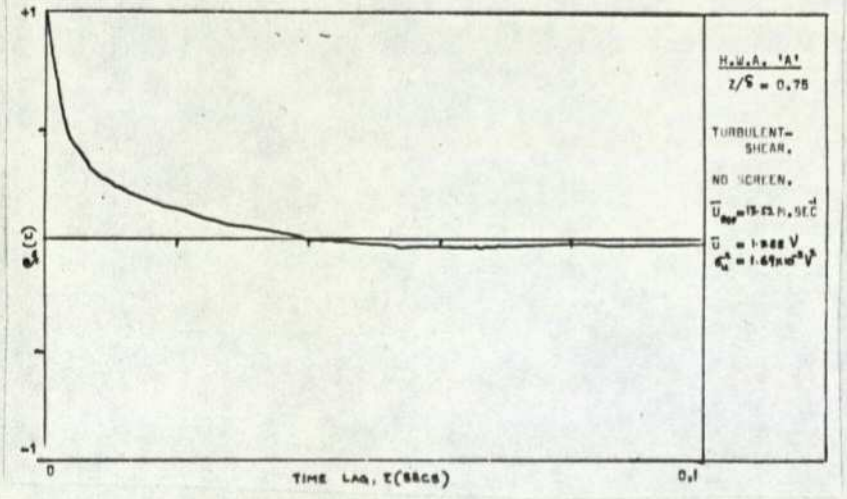

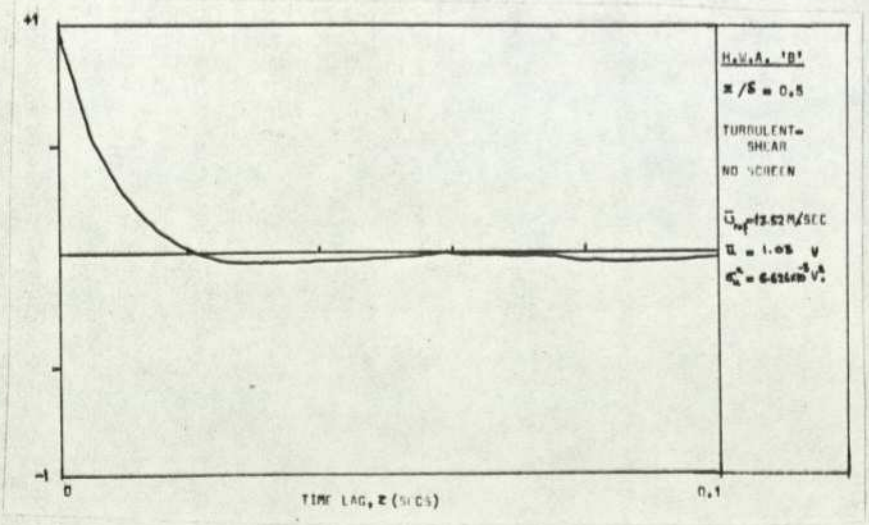

Auto-correlation: Generated flow (T_s) — high speed

FIGURE 6.8.b

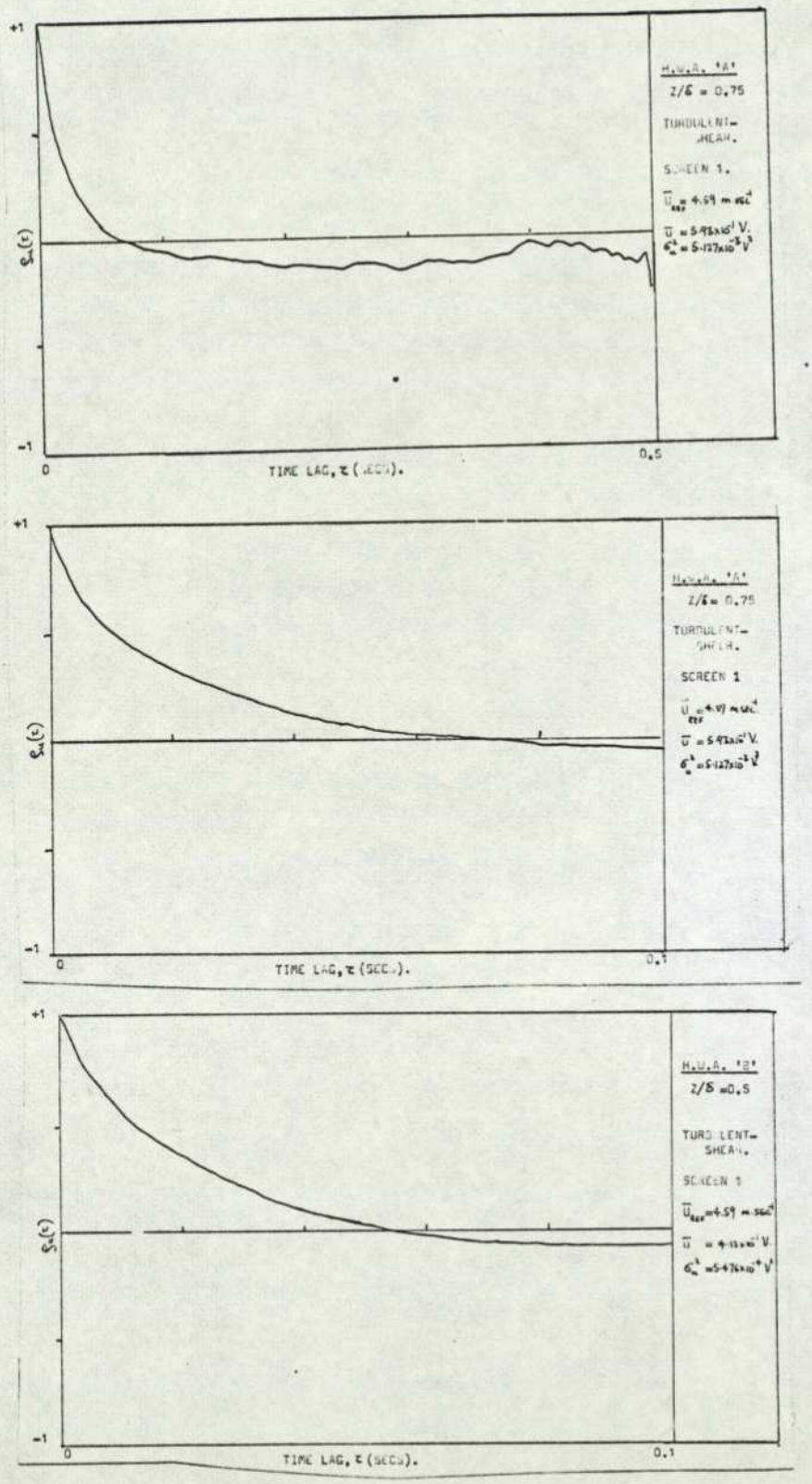

Auto-correlation: Generated flow (T_s + 1)

FIGURE 6.8.c

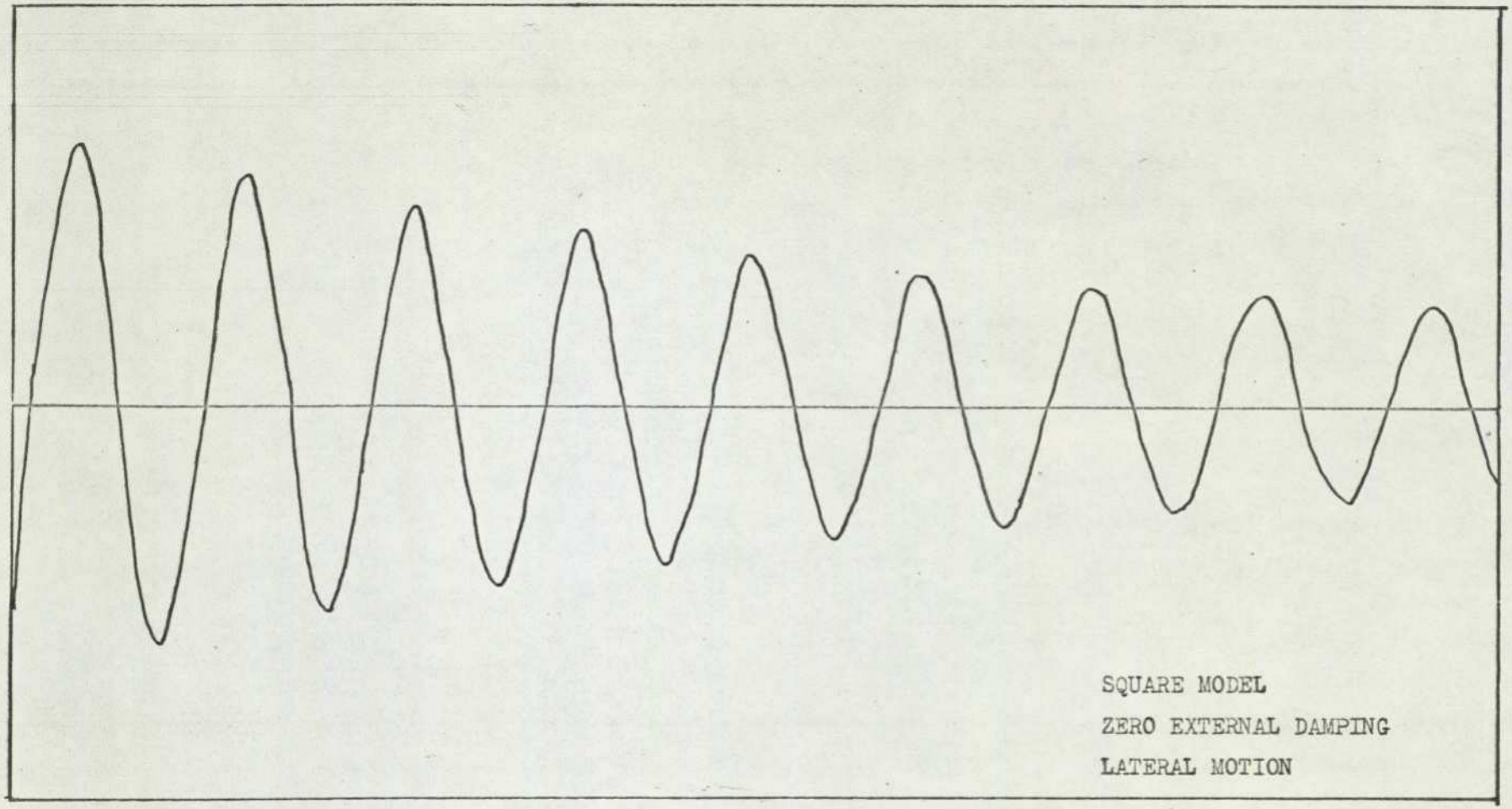

NATURAL DECAY TRACE IN STILL-WIND CONDITION (FROM UV TRACE)

FIGURE 7.1.a

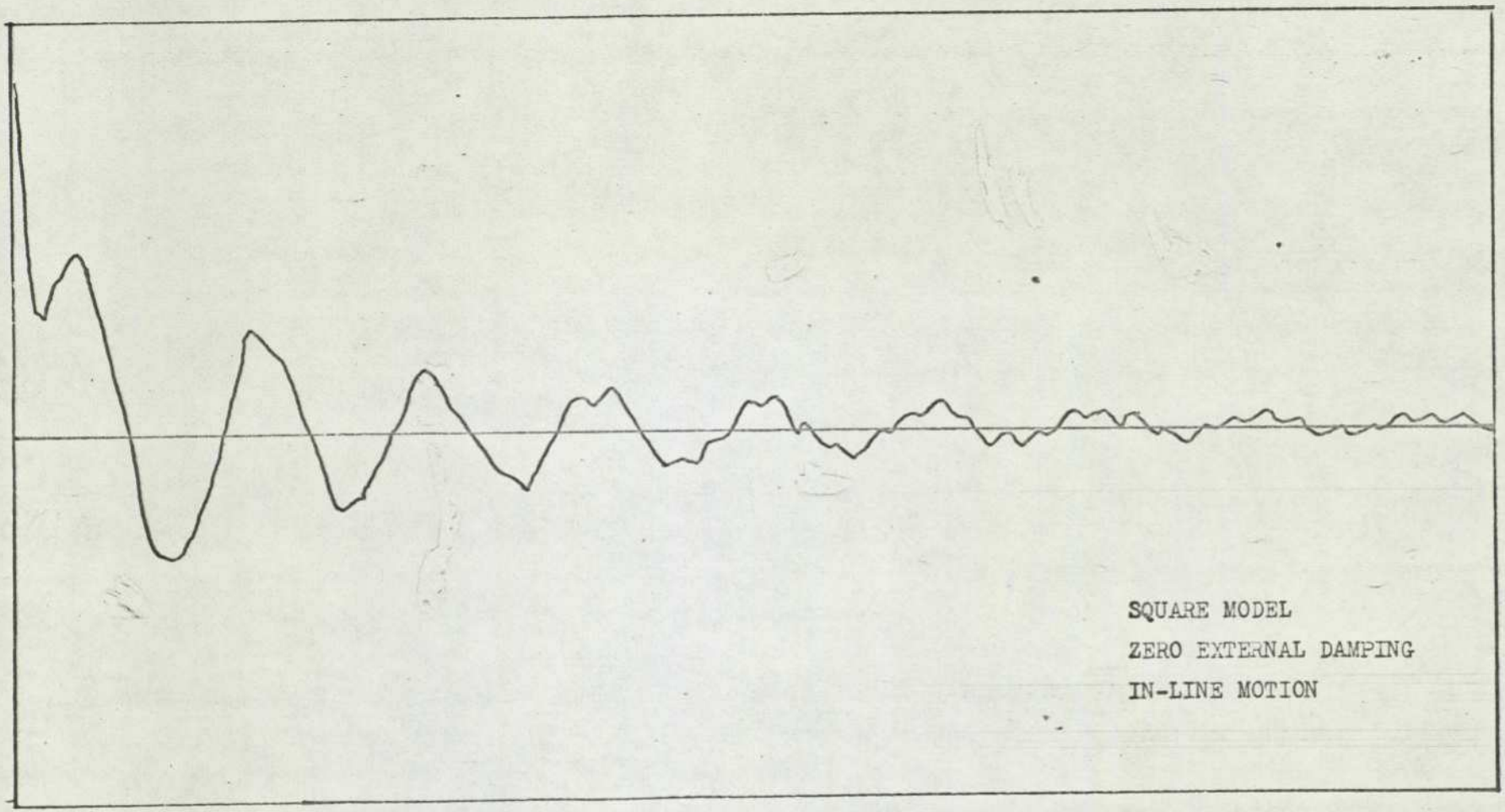

NATURAL DECAY TRACE IN STILL-WIND CONDITION (FROM UV TRACE)

FIGURE 7 1 b

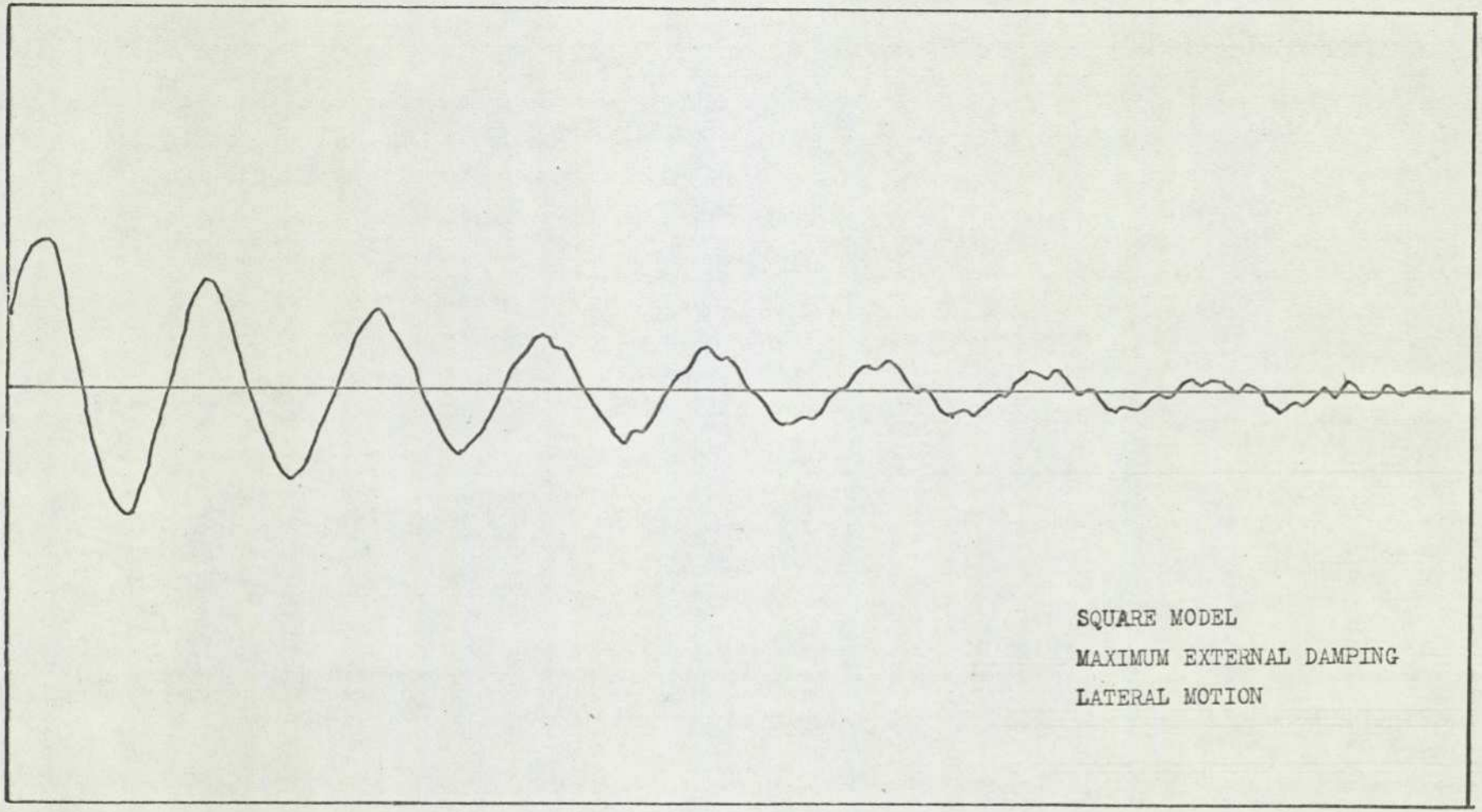

NATURAL DECAY TRACE IN STILL-WIND CONDITION (FROM UV TRACE)

FIGURE 7.1.c

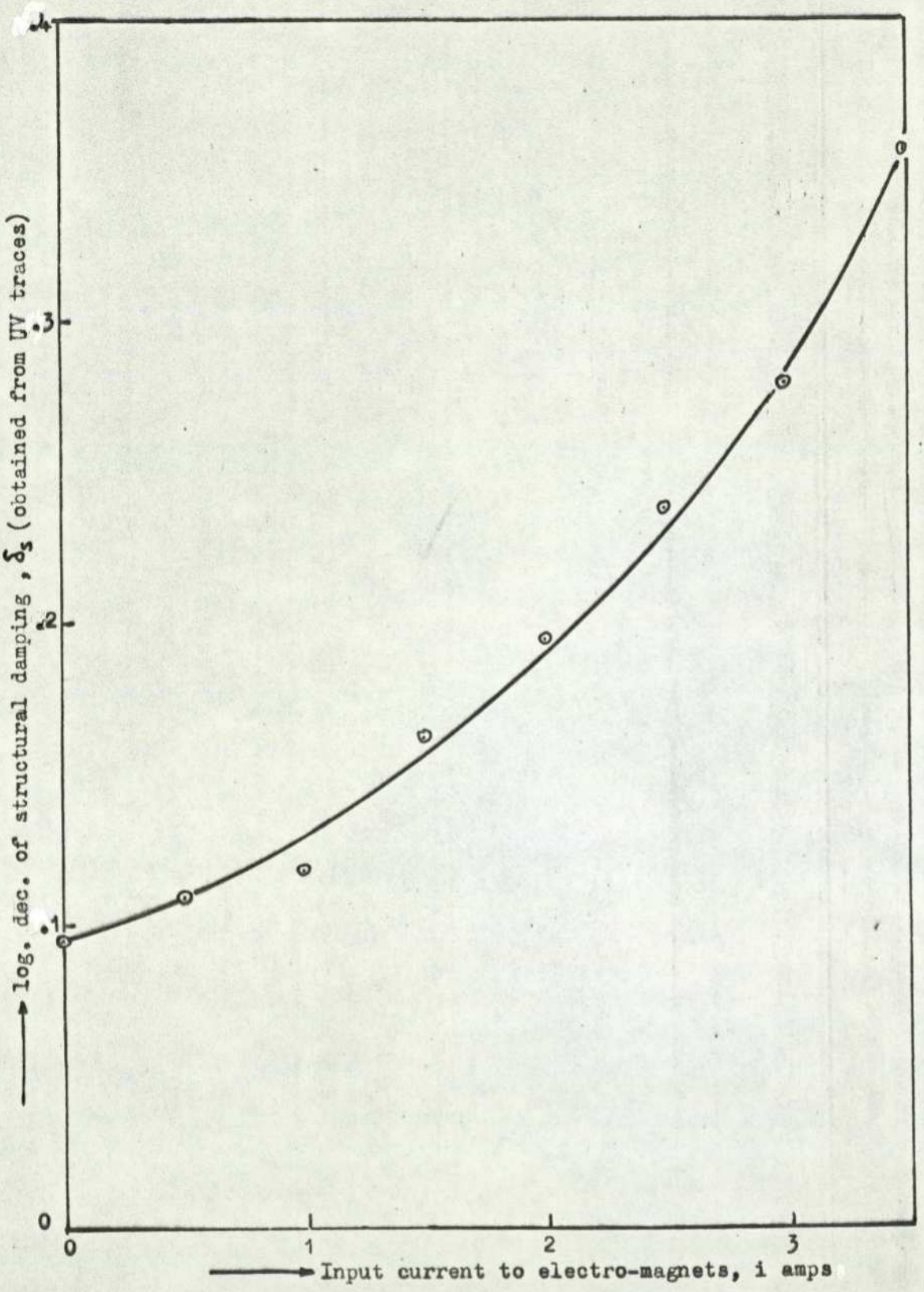

External structural damping induced by the electro-magnets

FIGURE 7.2

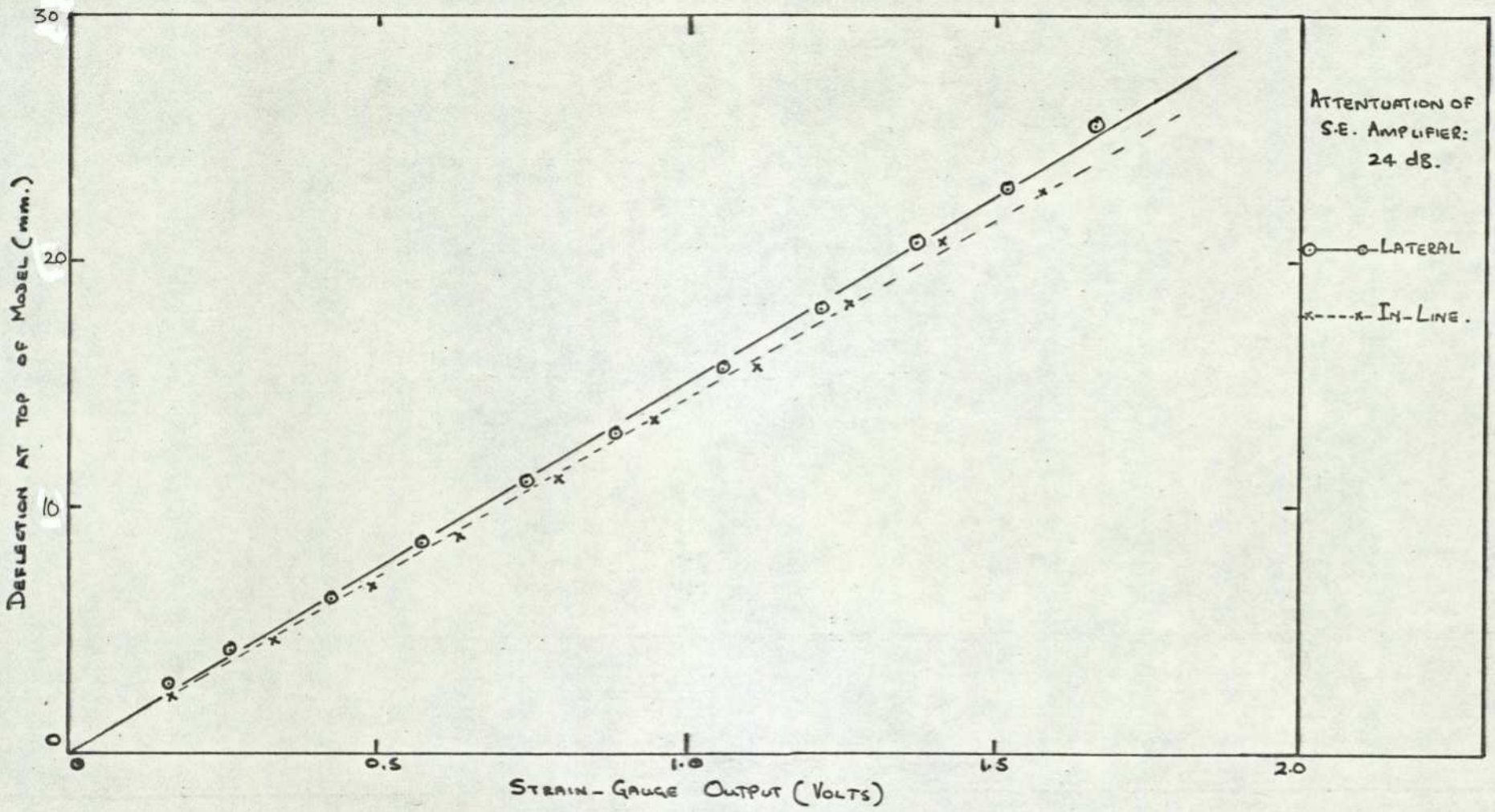

Calibration of strain-gauge system

FIGURE 7.3

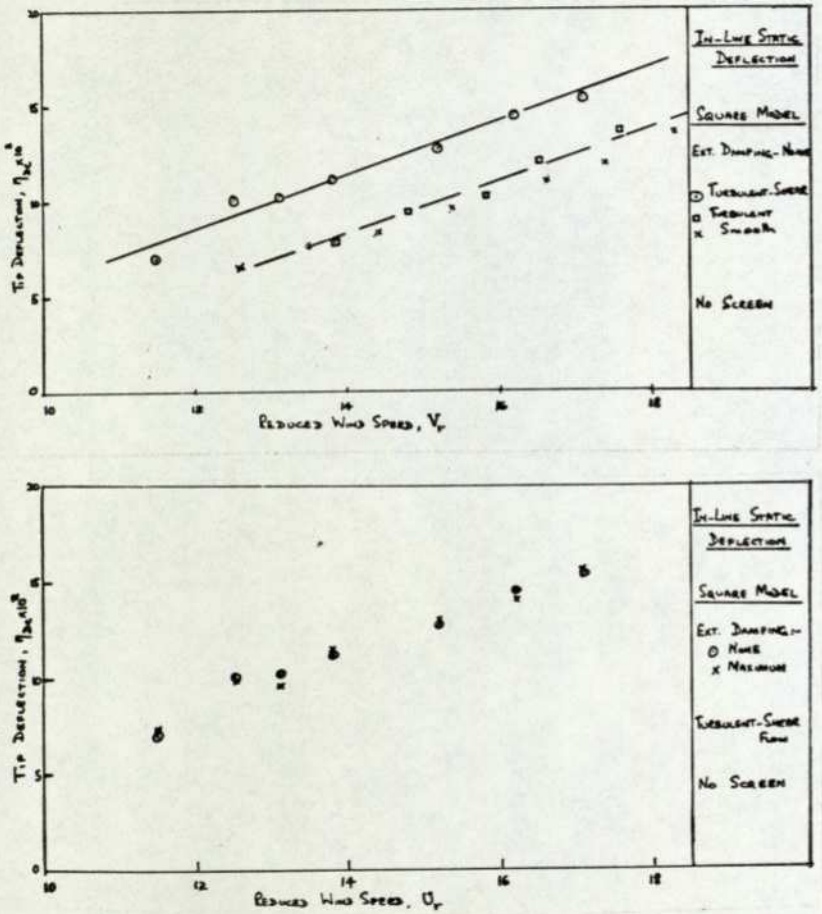

In-line static deflection: Square model with various damping/flow configurations

FIGURE 7.4.a

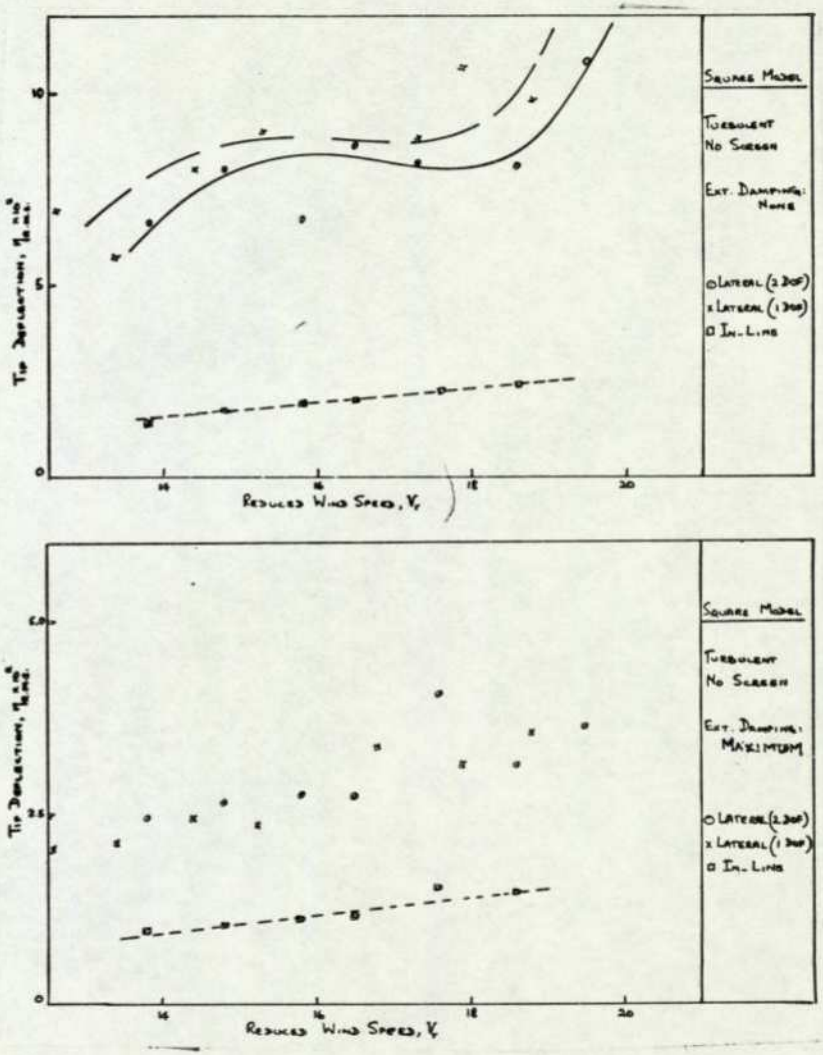

Fluctuating deflection: Square model in turbulent flow

FIGURE 7.4.b

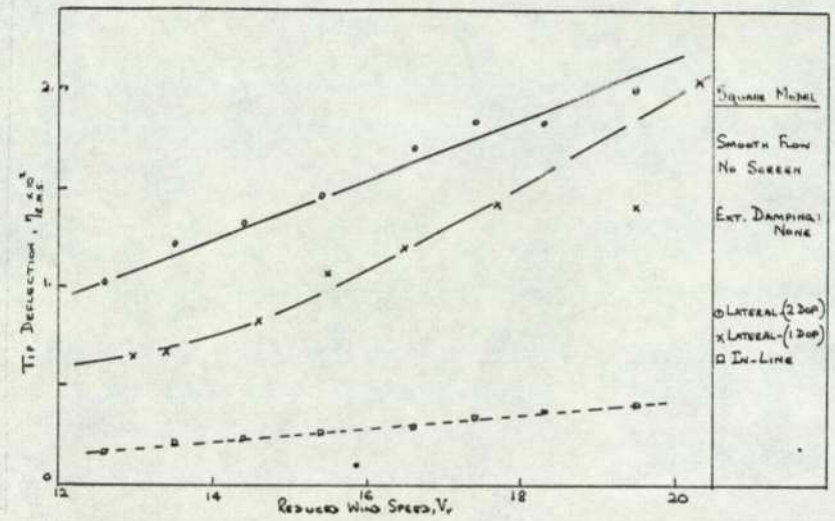

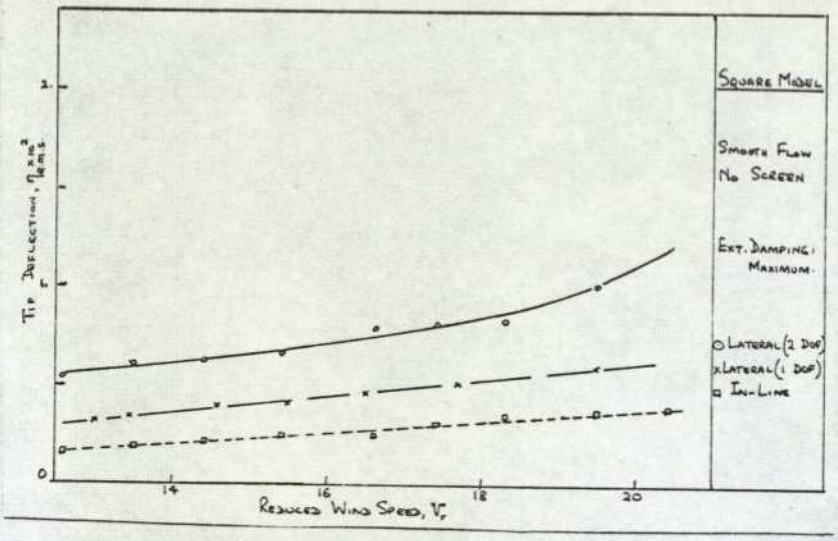

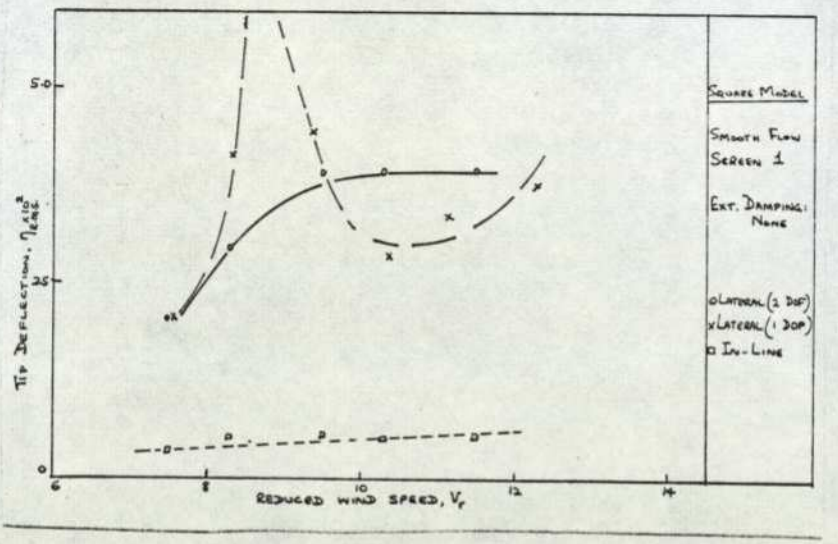

Fluctuating deflection: Square model in smooth flow

FIGURE 7.4.c

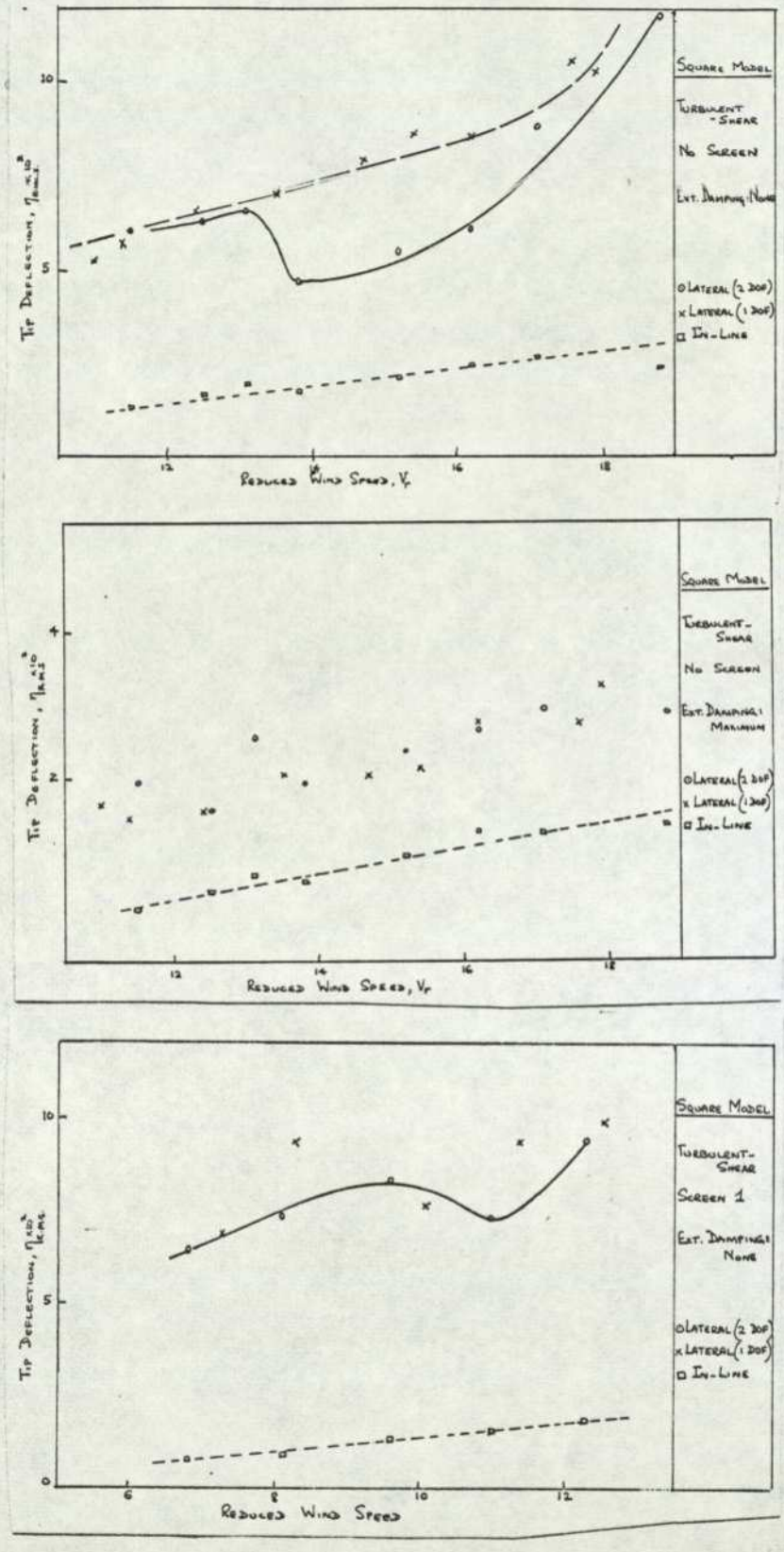

Fluctuating deflection: Square model in turbulent shear flow

FIGURE 7.4.d

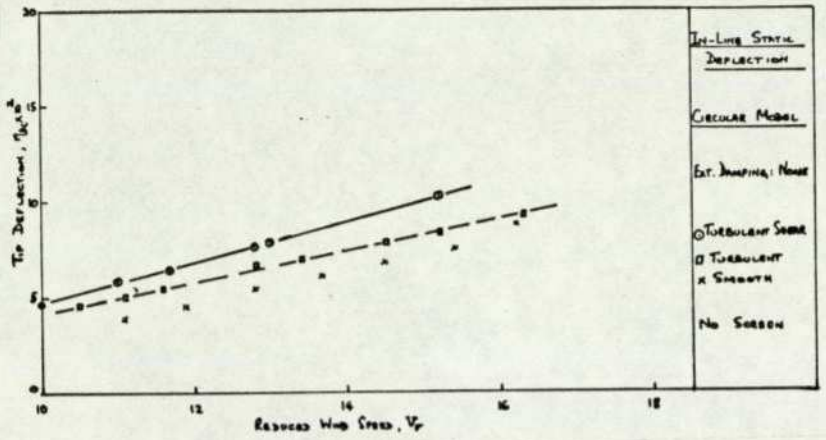

In-line static deflection: Circular model with various flow configurations

FIGURE 7.5.a

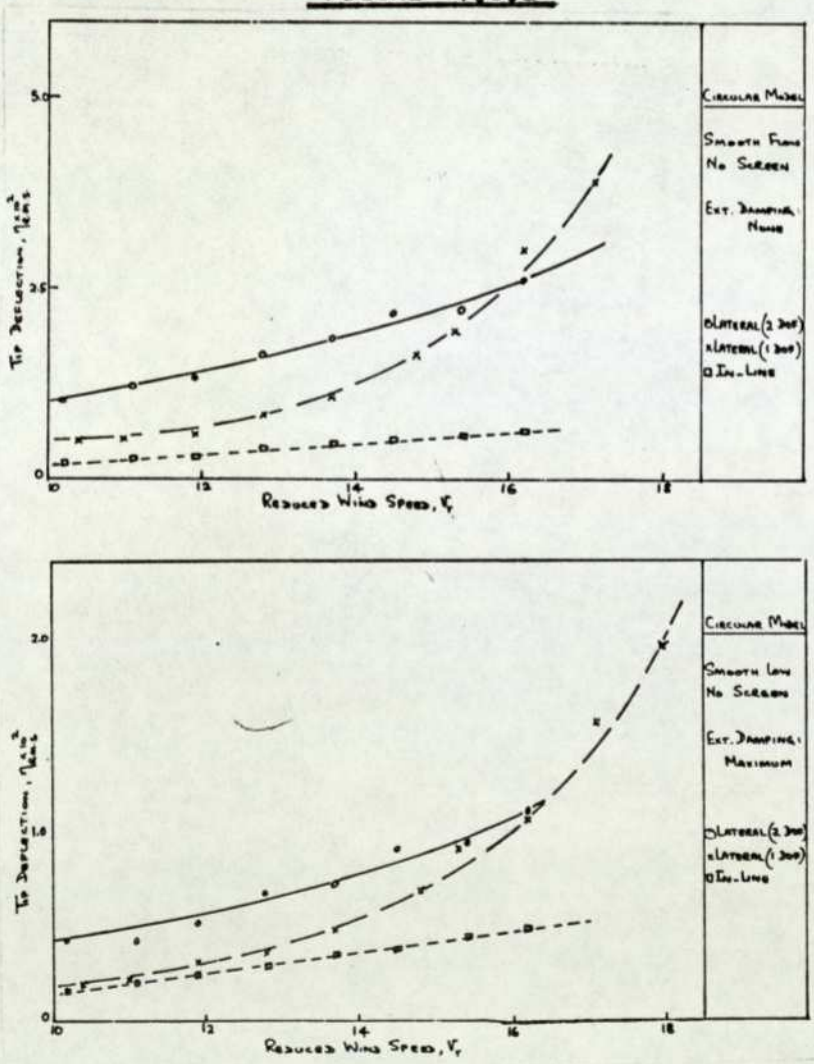

Fluctuating deflection: Circular model in smooth flow

FIGURE 7.5.b

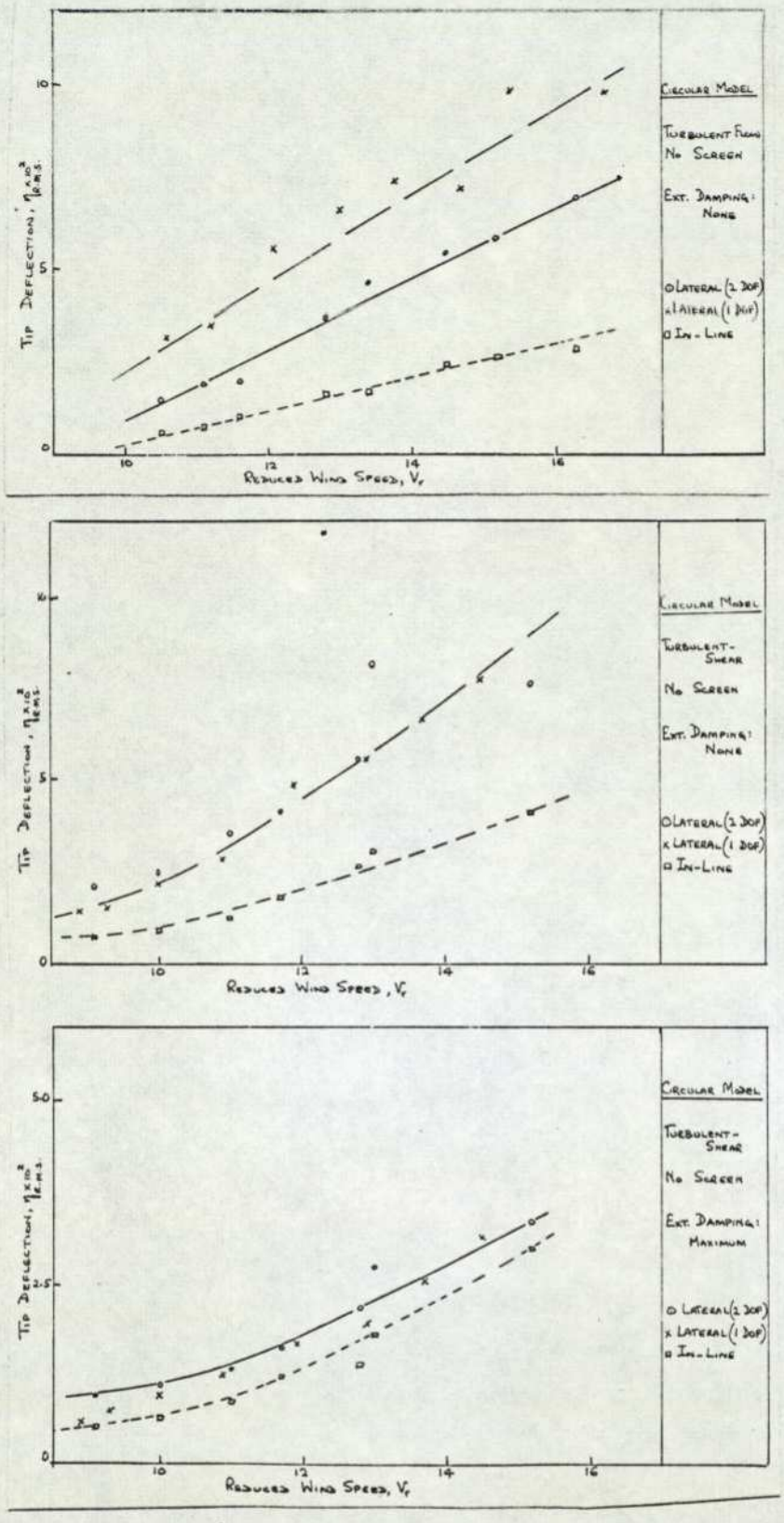

Fluctuating deflection: Circular model in turbulent and turbulent shear flow

FIGURE 7.5.c

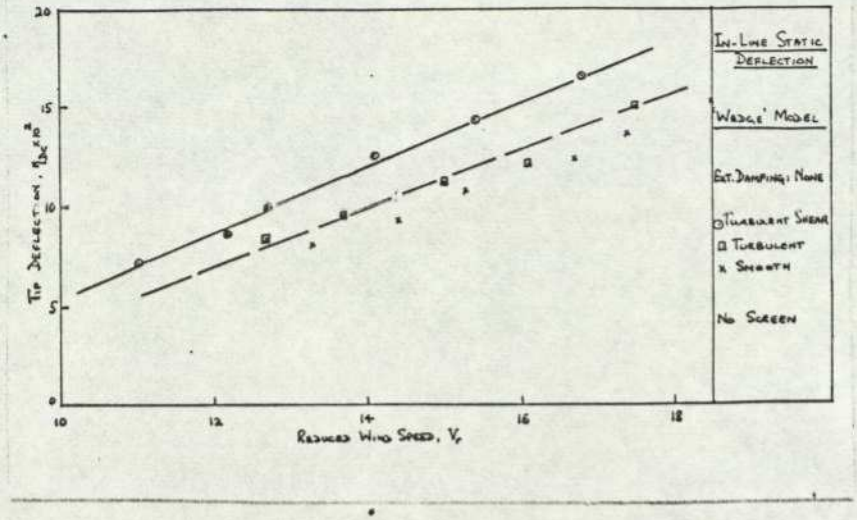

In-line static deflection: Wedge model with various flow configurations

FIGURE 7.6.a

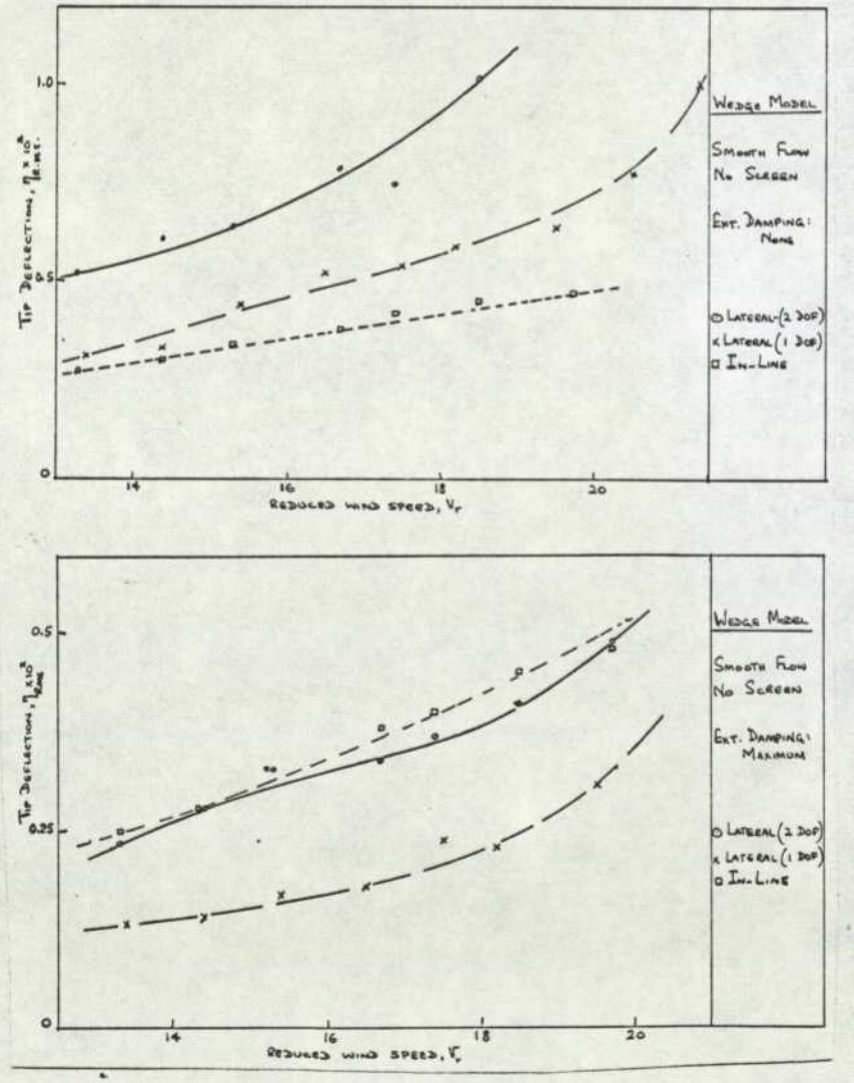

Fluctuating deflection: Wedge model in smooth flow

FIGURE 7.6.b

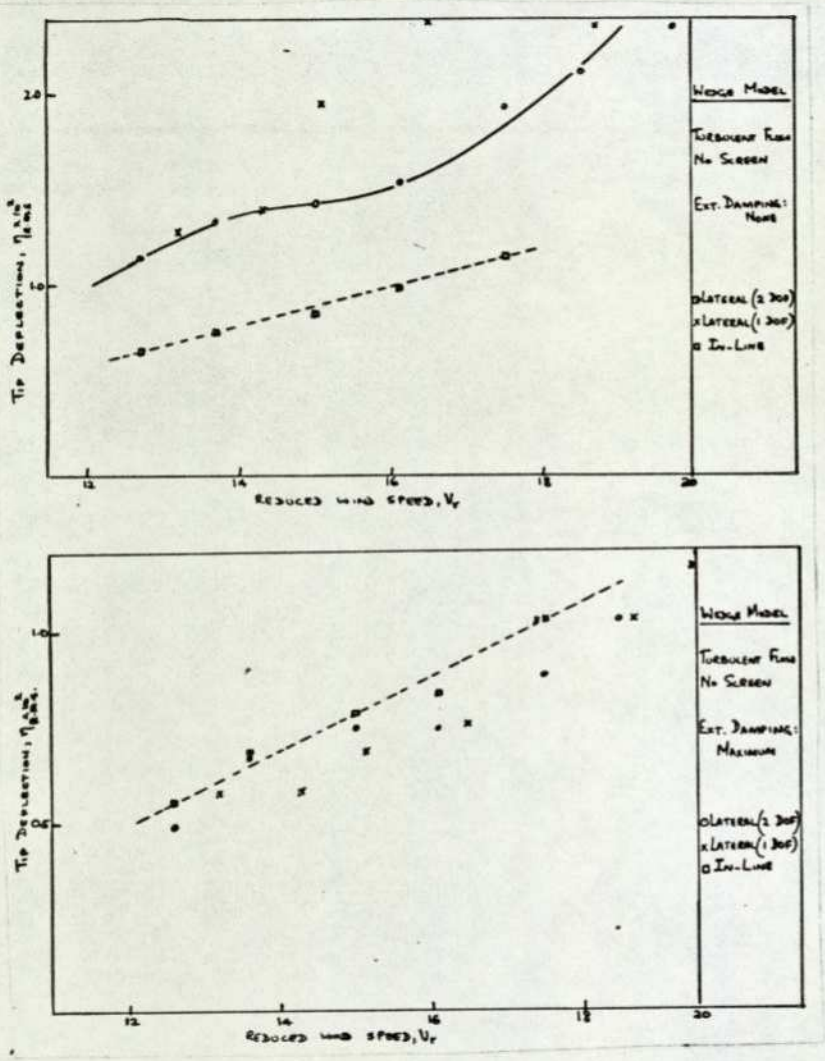

Fluctuating deflection: Wedge model in turbulent flow

FIGURE 7.6.c

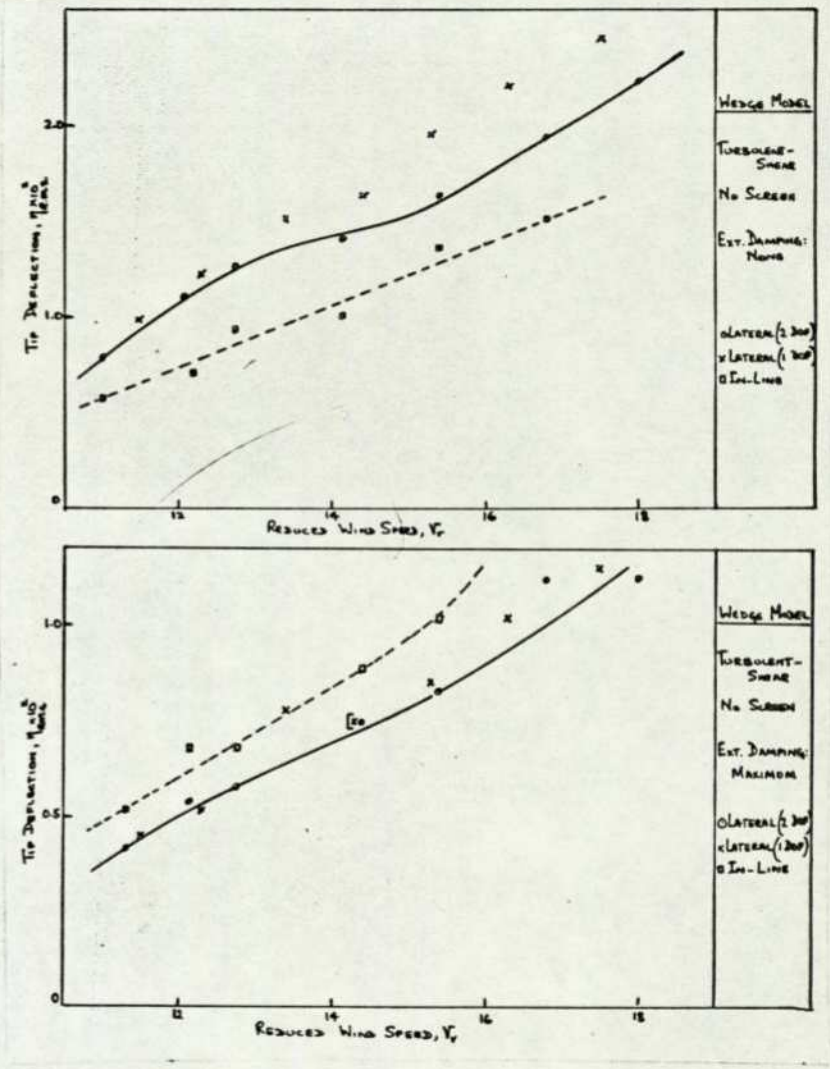

Fluctuating deflection: Wedge model in turbulent shear flow

FIGURE 7.6.d

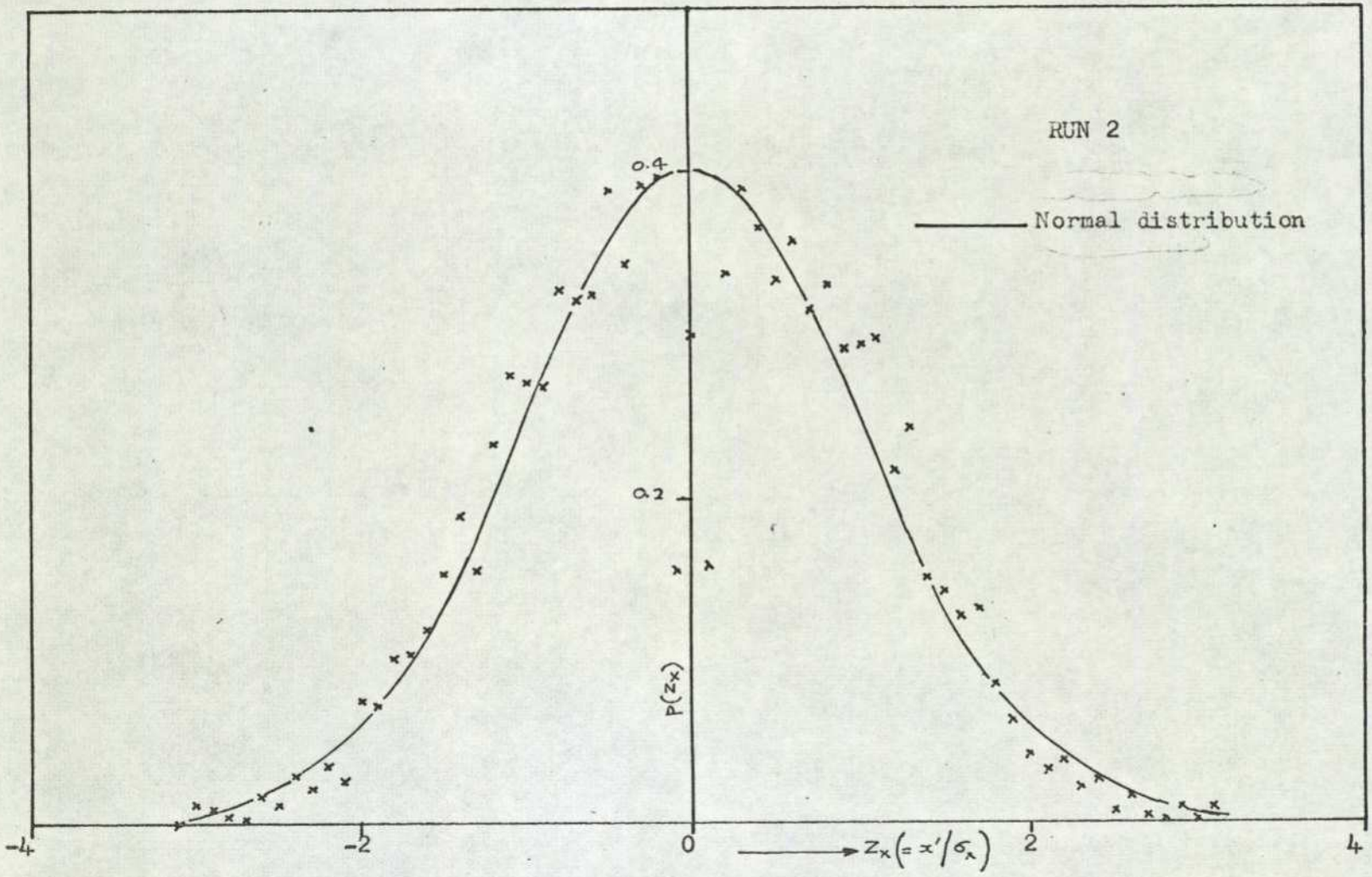

Probability density distribution of the in-line motion of the square model in T_s flow

FIGURE 7.7.a

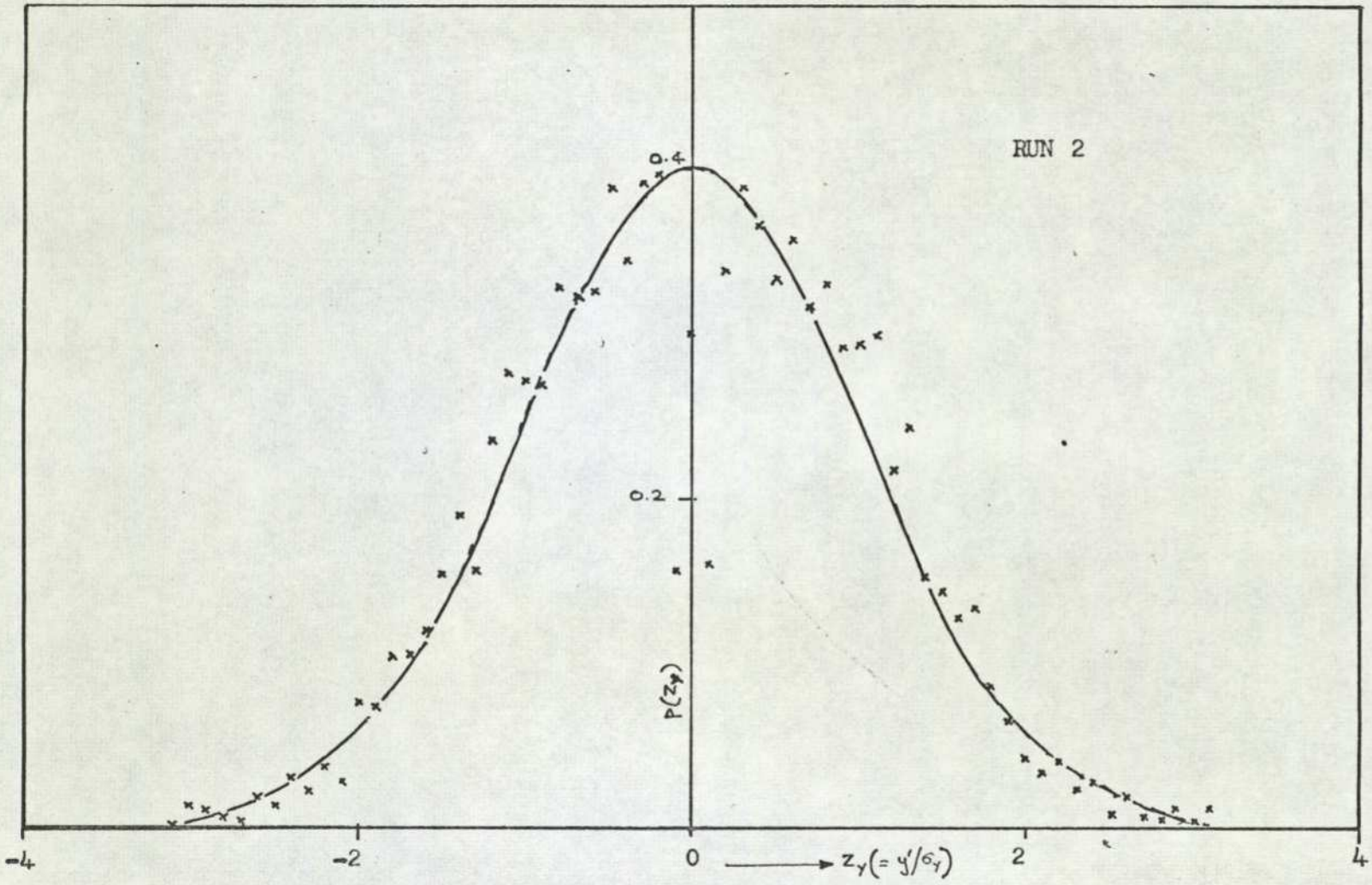

Probability density distribution of the lateral motion of the square model in T_s flow

FIGURE 7.7.b

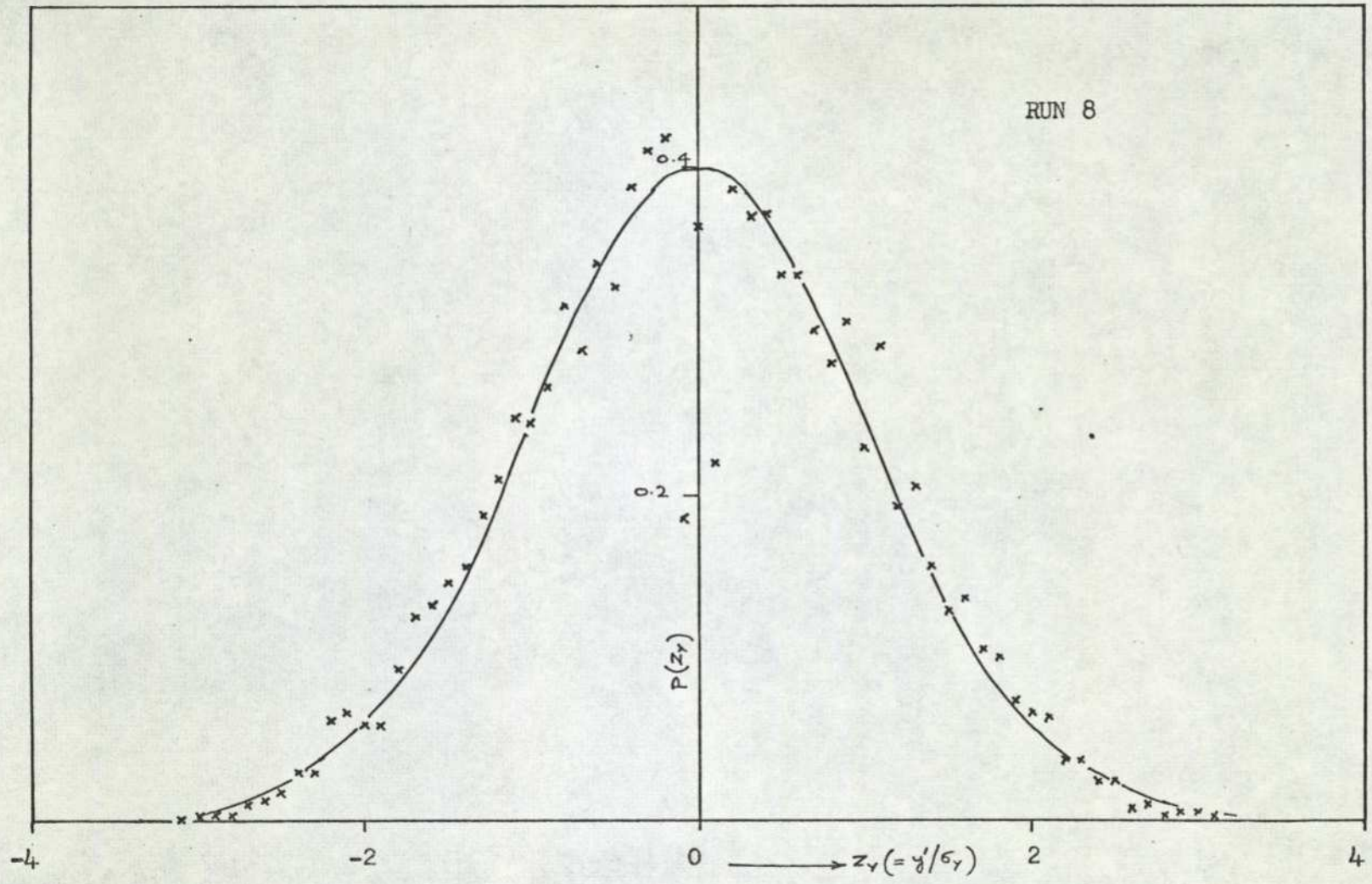

Probability density distribution of the lateral motion for the circular model in T_s flow

FIGURE 7.8.a

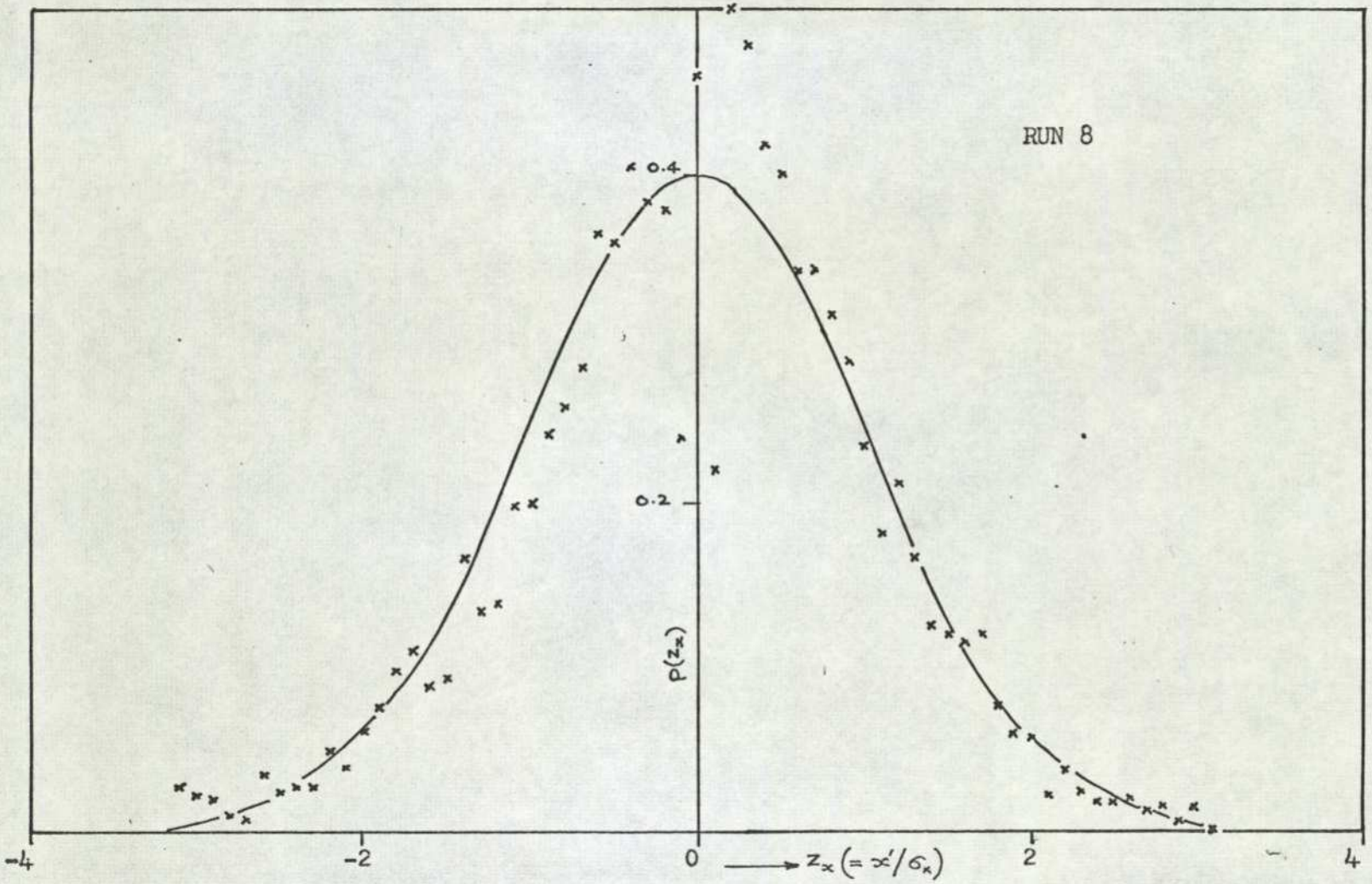

Probability density distribution of the in-line motion for the circular model in T_s flow

FIGURE 7.8.b

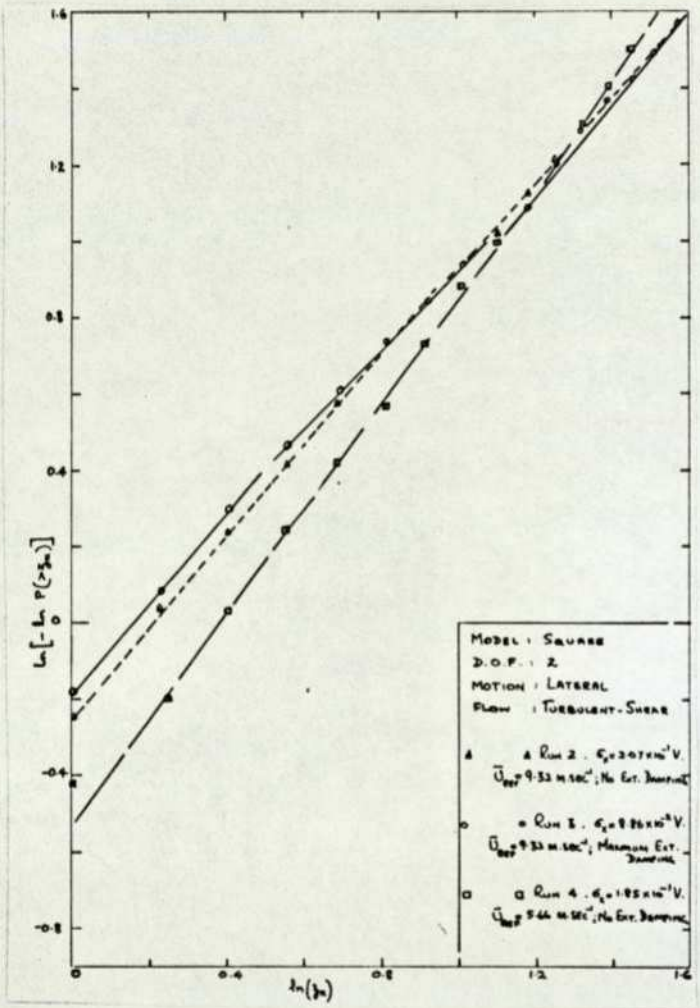

Cumulative probability distribution

FIGURE 7.9

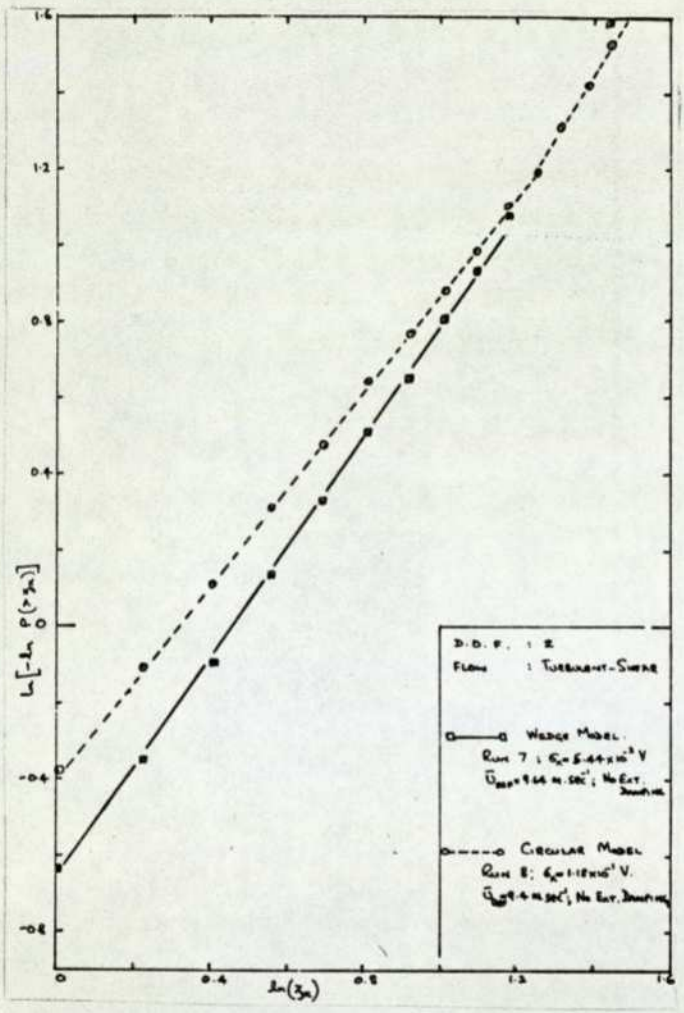

Cumulative probability distribution

FIGURE 7.10

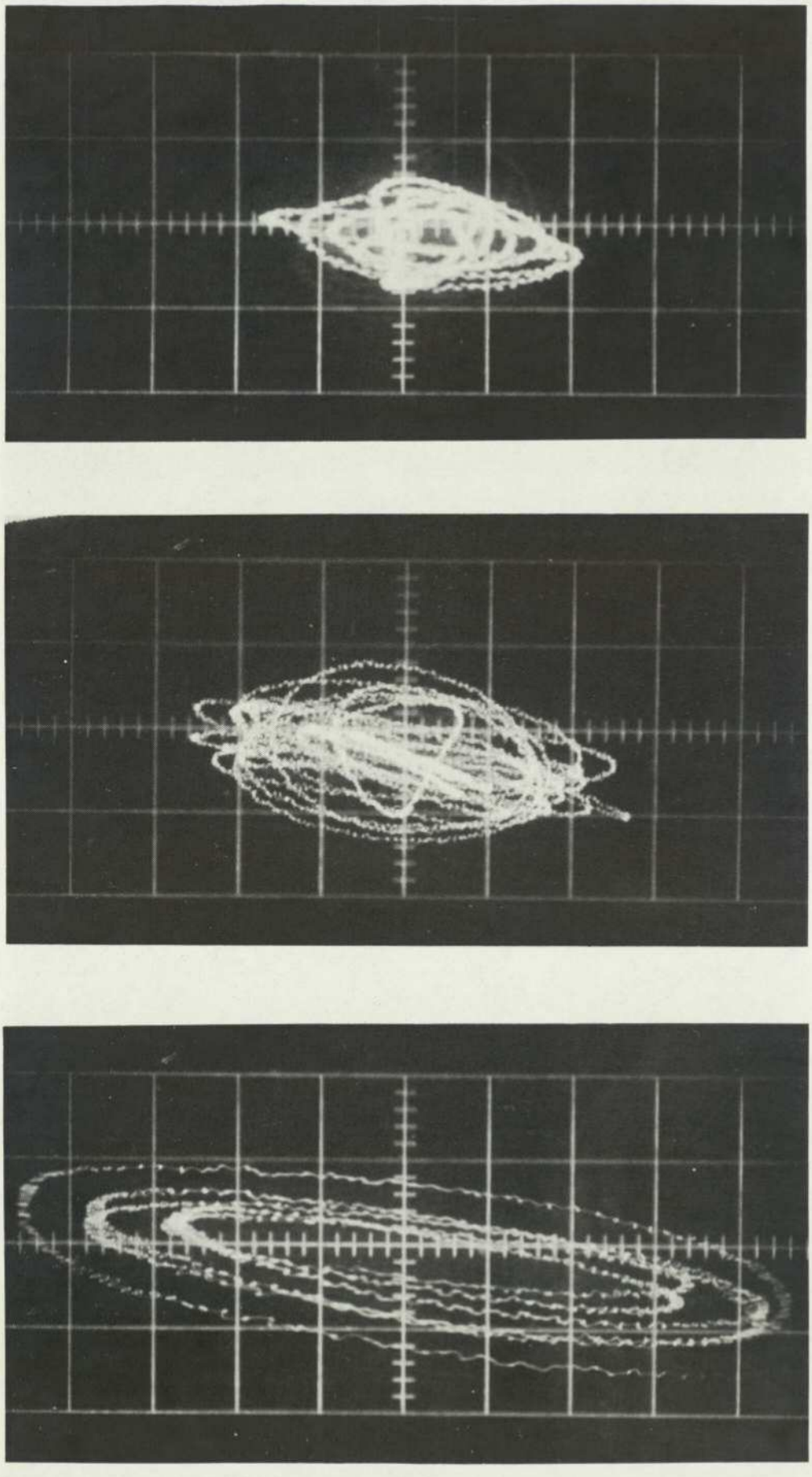

Phases of oscillation of a square model with low damping in T_s flow

FIGURE 7.11

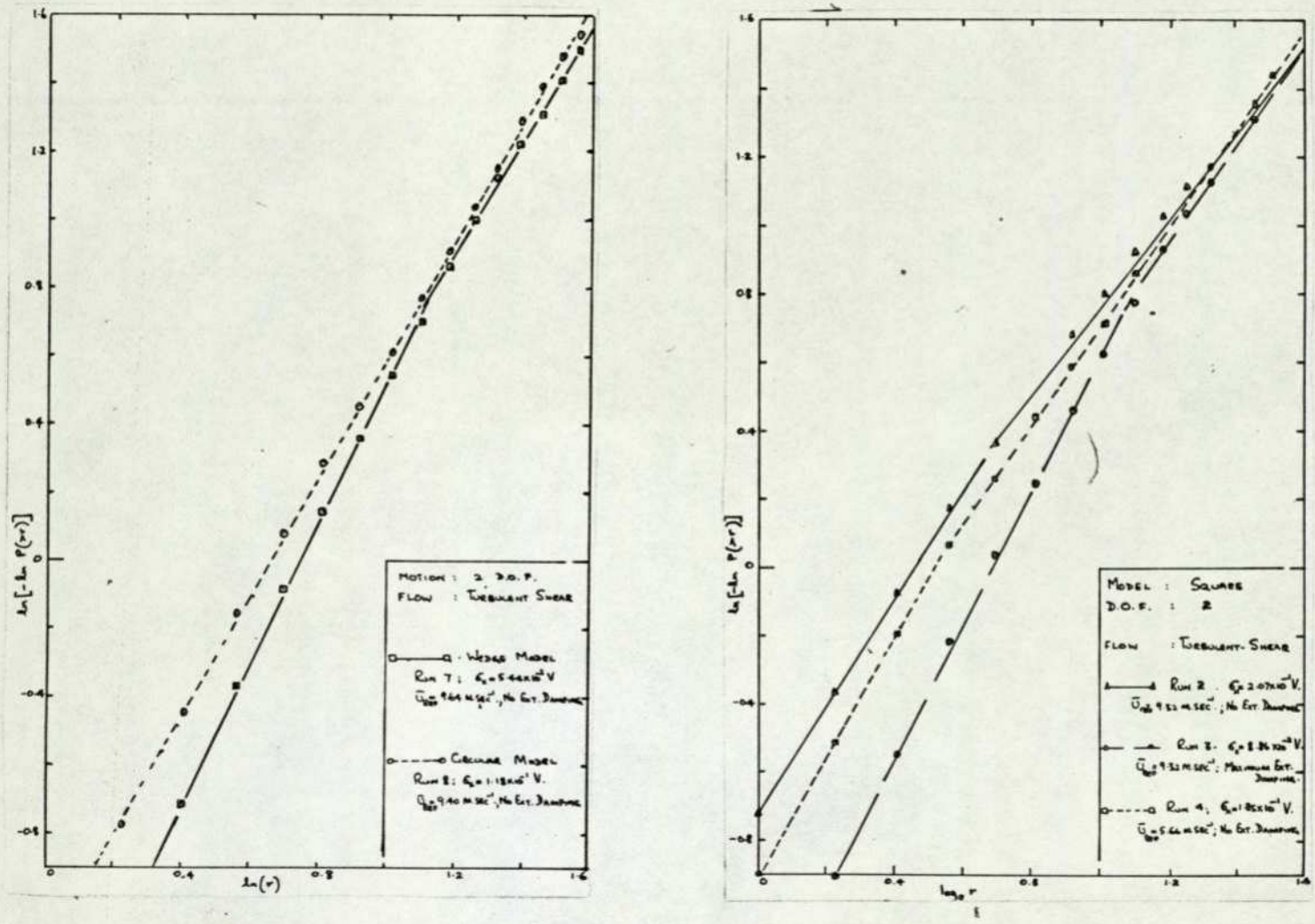

Envelope of fluctuations

FIGURE 7.12

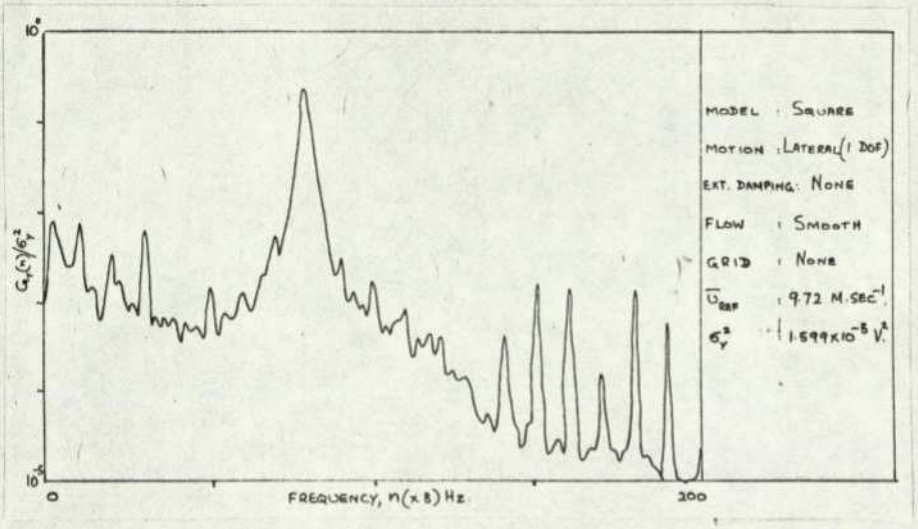

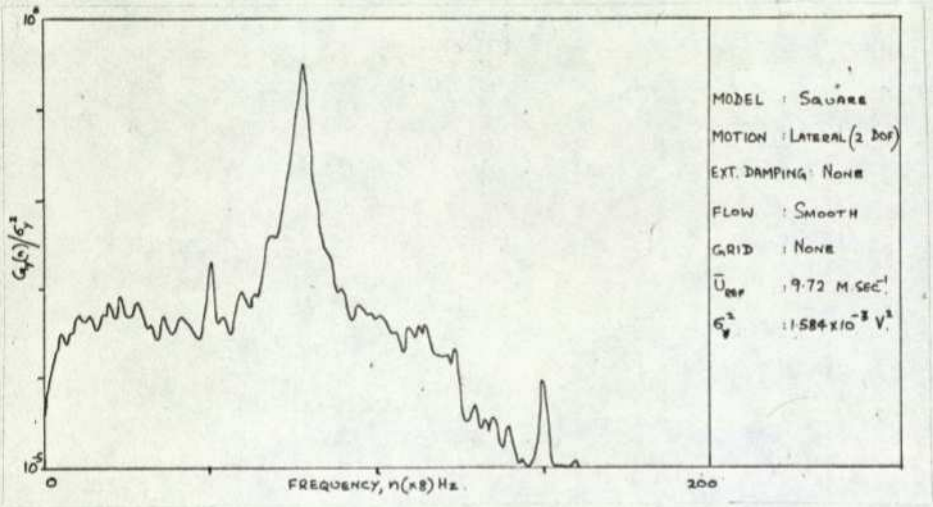

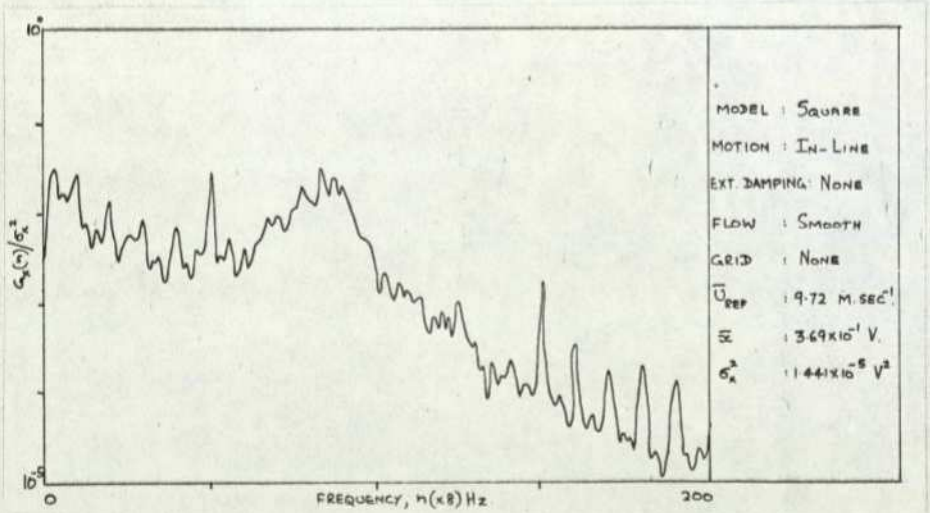

Auto-spectrum: Square model in smooth flow without applied damping

FIGURE 7.13.a

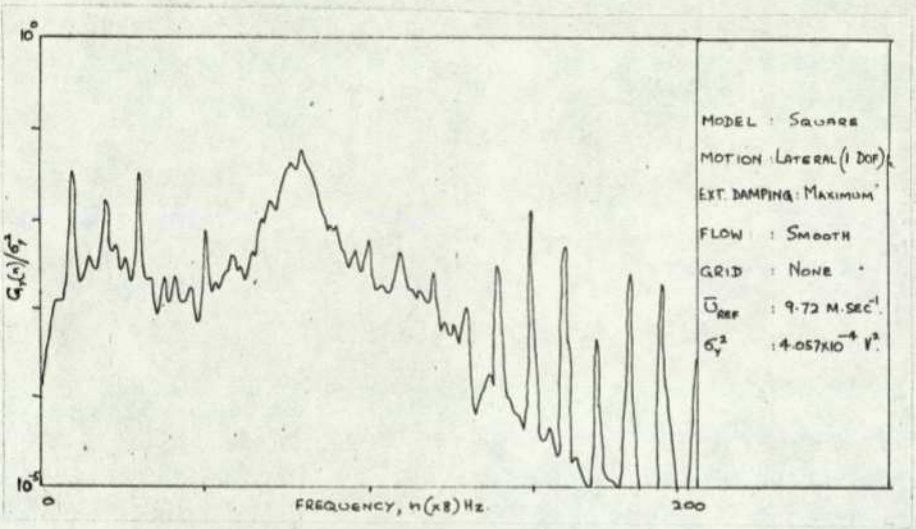

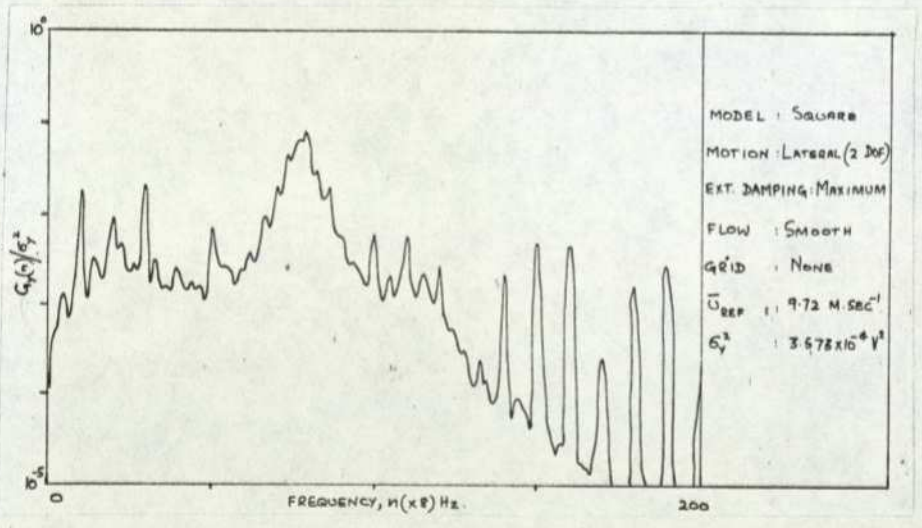

Auto-spectrum: Square model in smooth flow with maximum applied damping

FIGURE 7.13.b

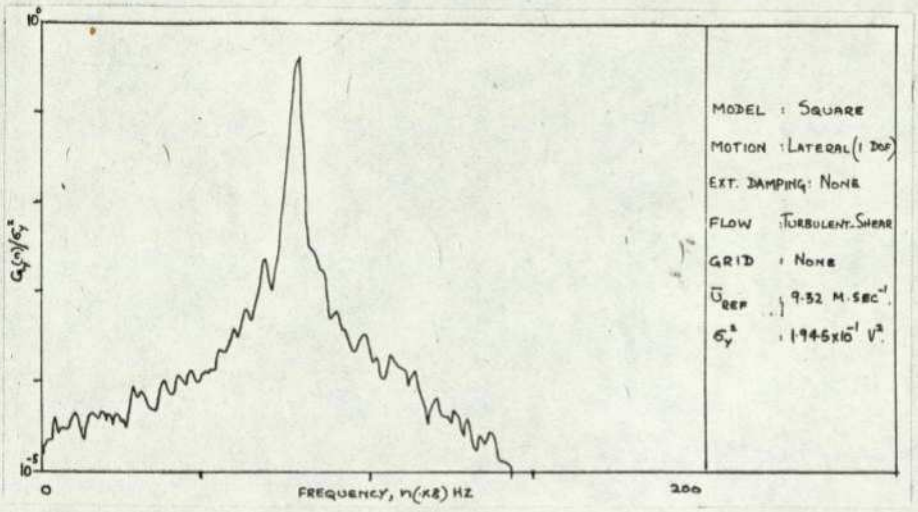

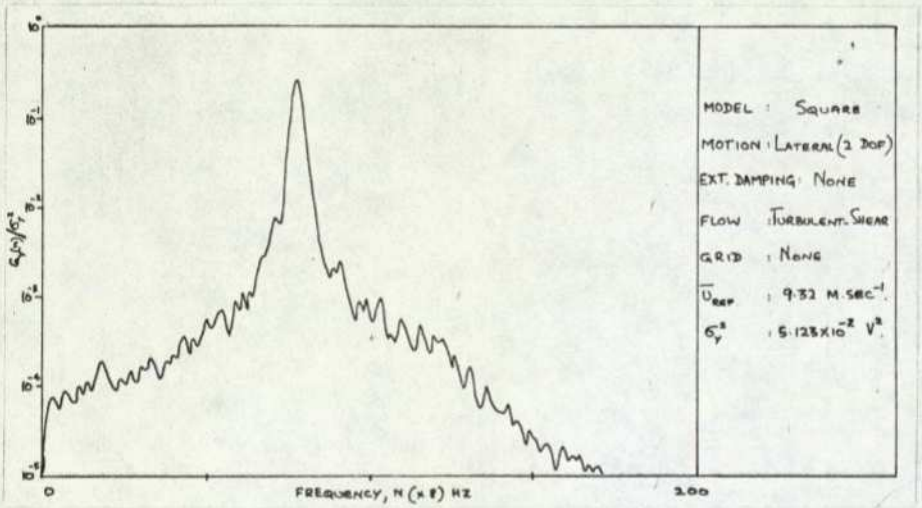

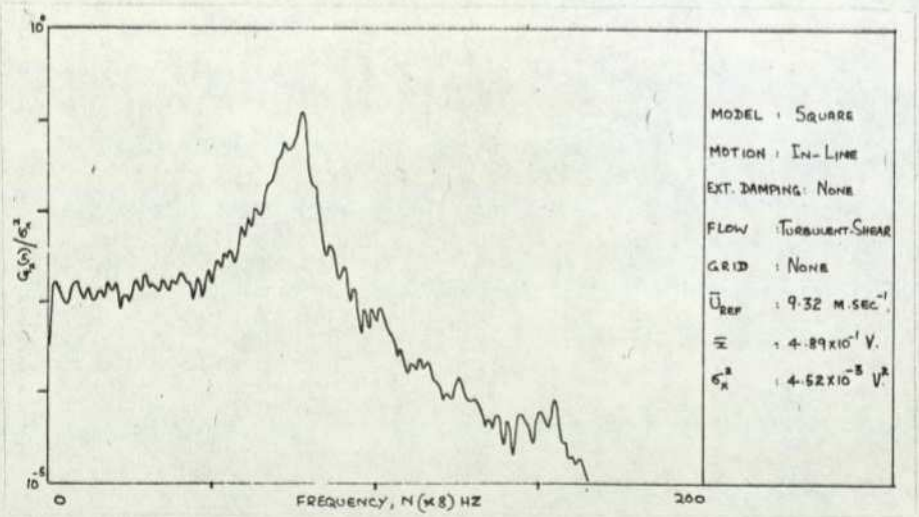

Auto-spectrum: Square model in turbulent shear flow without applied damping

FIGURE 7.13.c

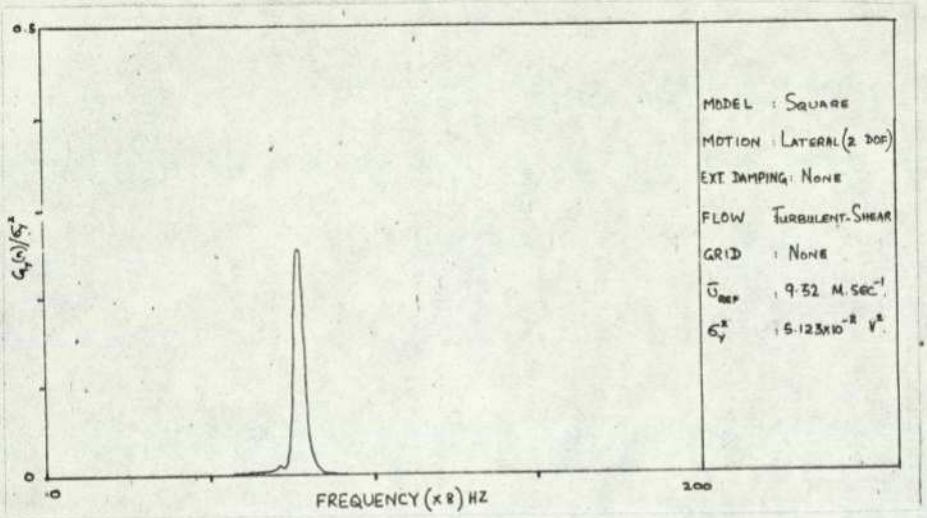

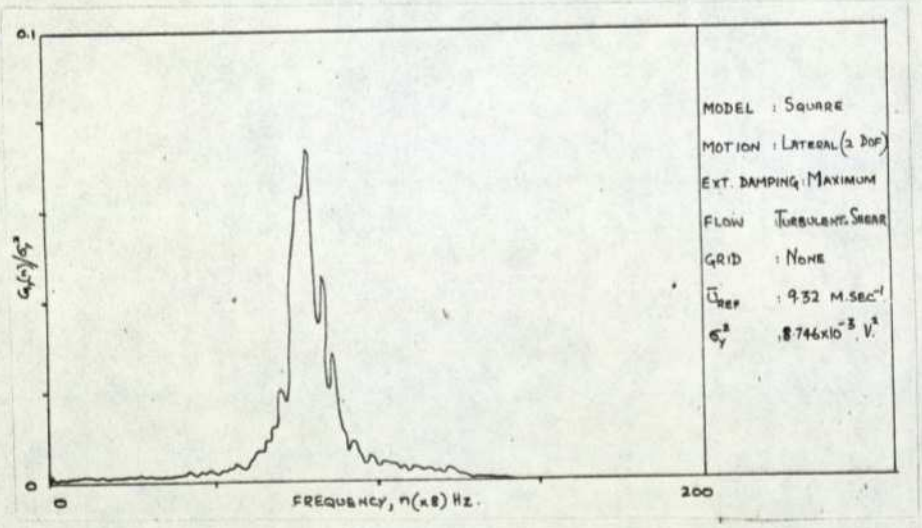

Auto-spectrum (linear plot): Square model in turbulent shear flow with and without applied damping

FIGURE 7.13.d

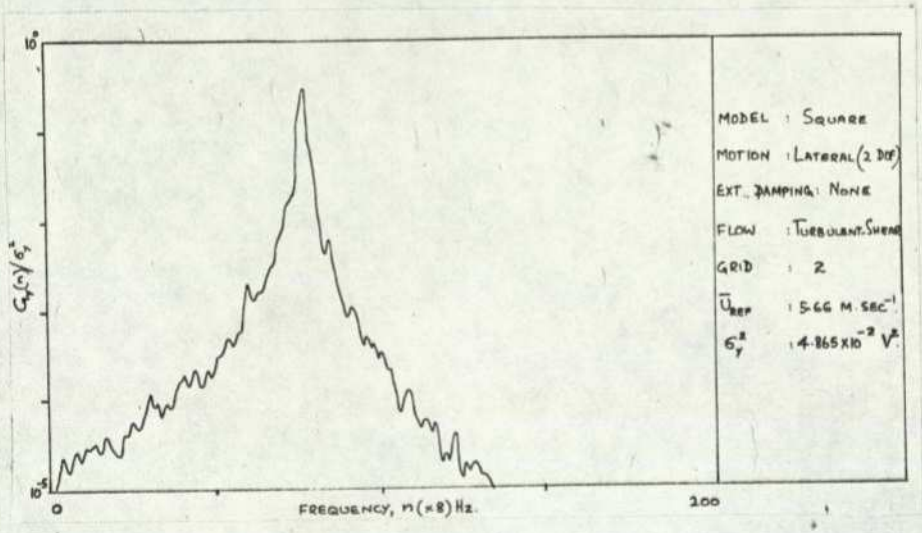

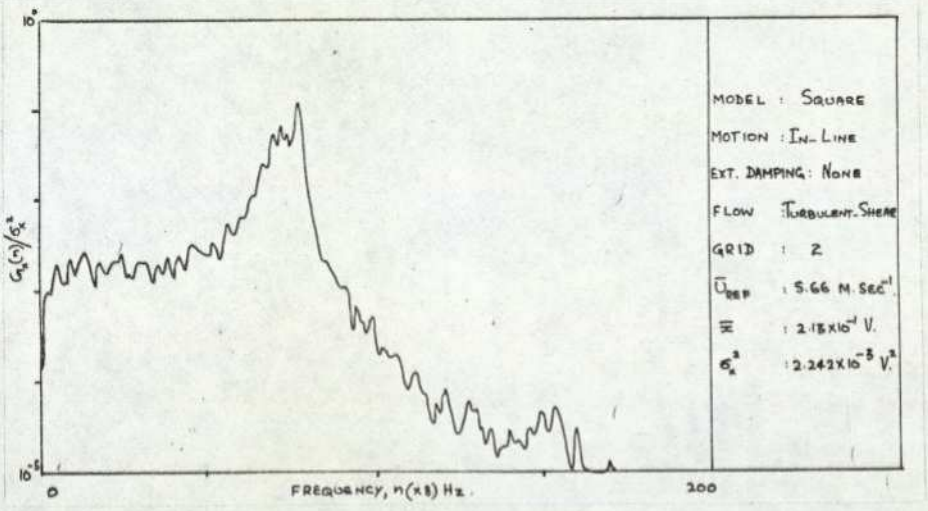

Auto-spectrum: Square model in turbulent shear flow (screen 2) without applied damping

FIGURE 7.13.e

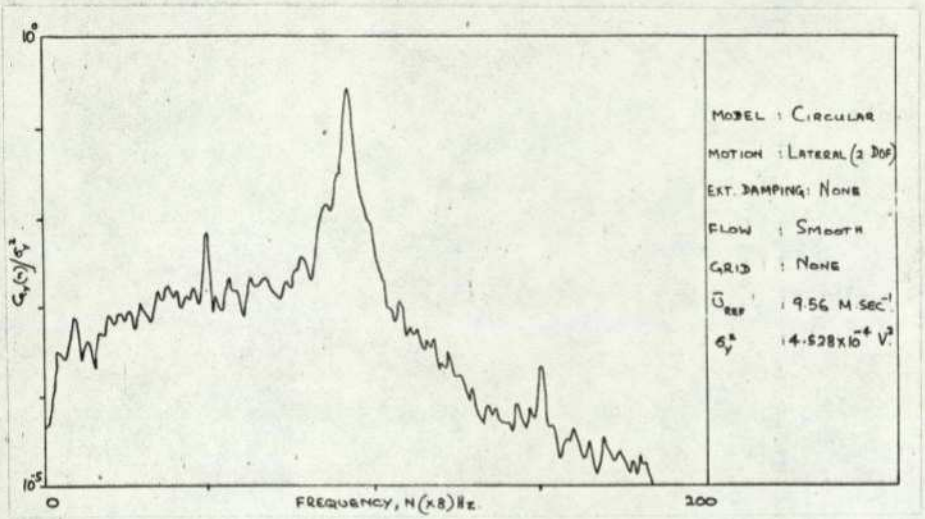

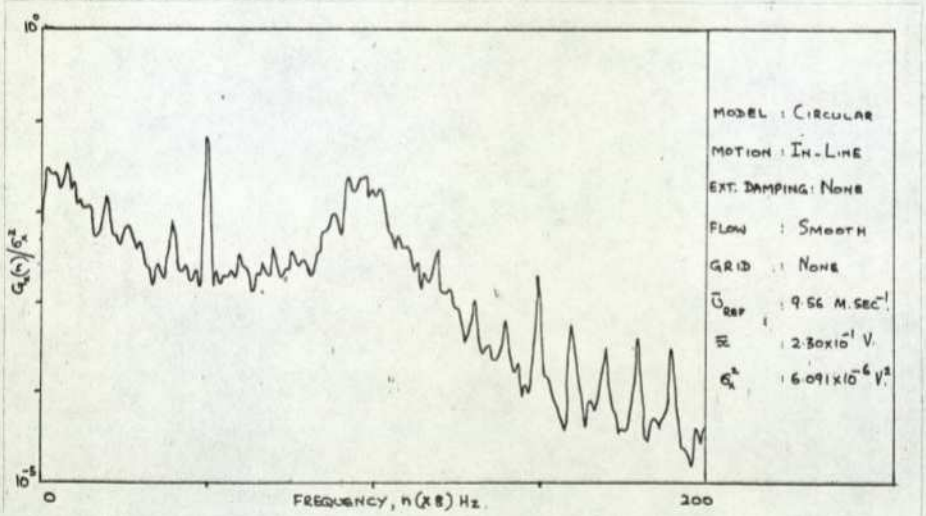

Auto-spectrum: Circular model in smooth flow without applied damping

FIGURE 7.14.a

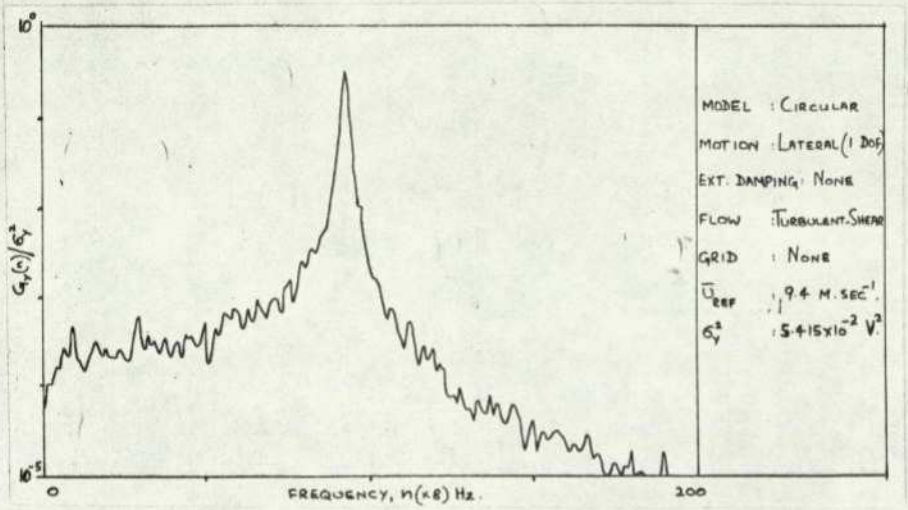

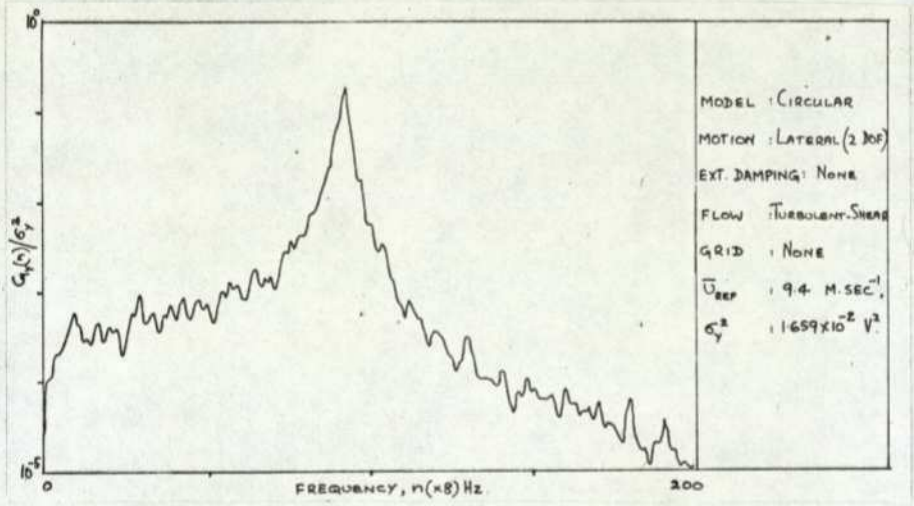

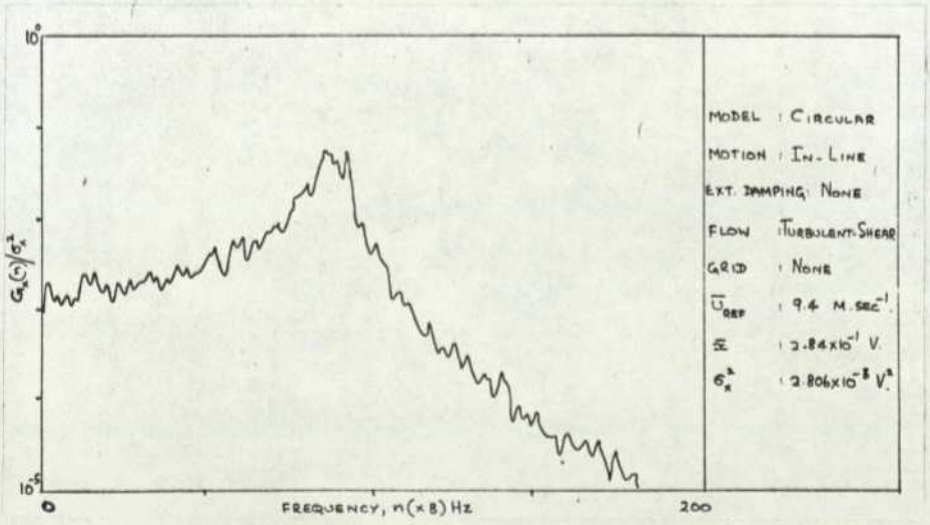

Auto-spectrum: Circular model in turbulent shear flow without applied damping

FIGURE 7.14.b

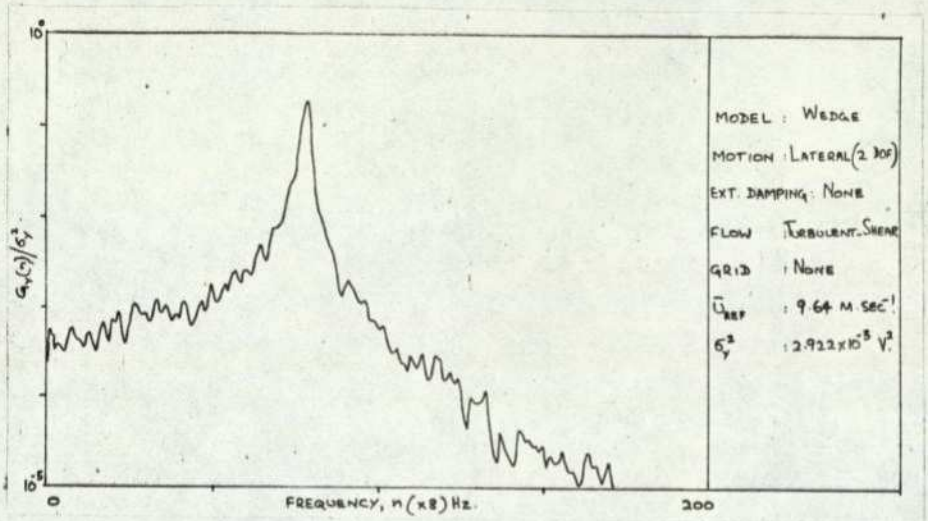

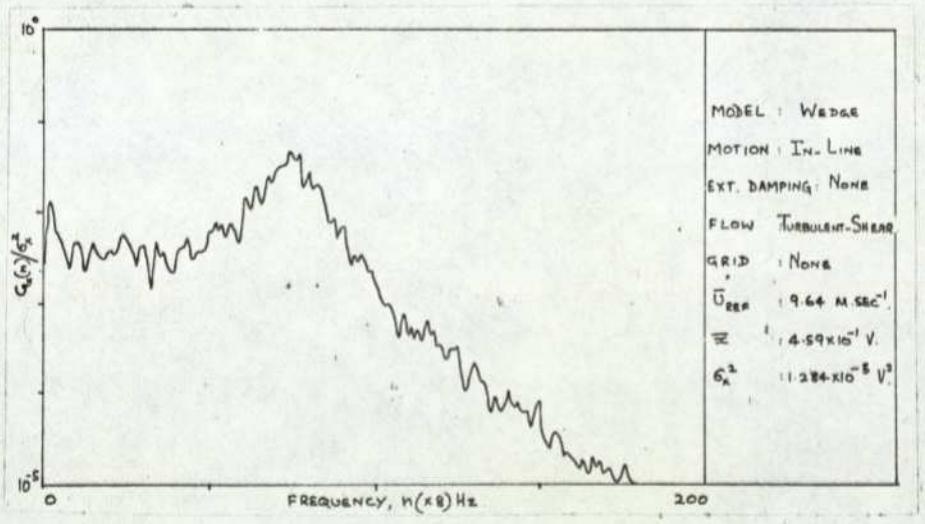

Auto-spectrum: Wedge model in turbulent shear flow without applied damping

FIGURE 7.15

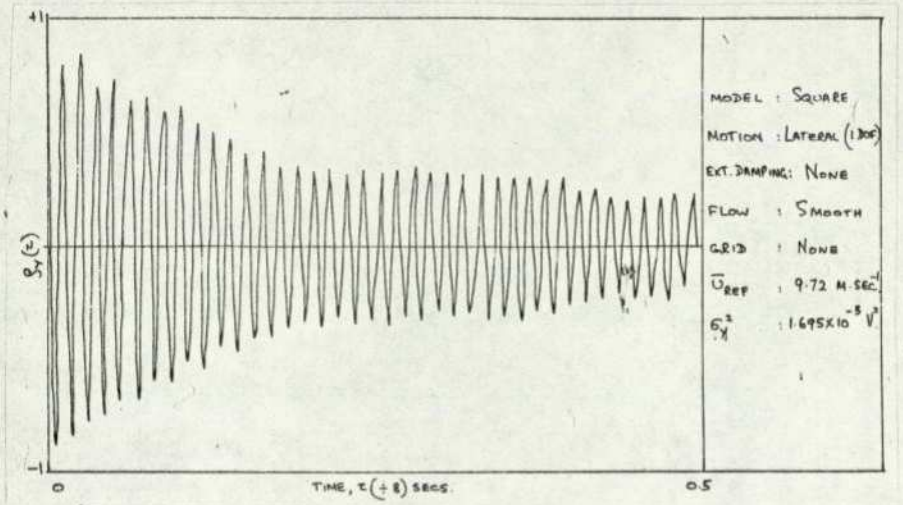

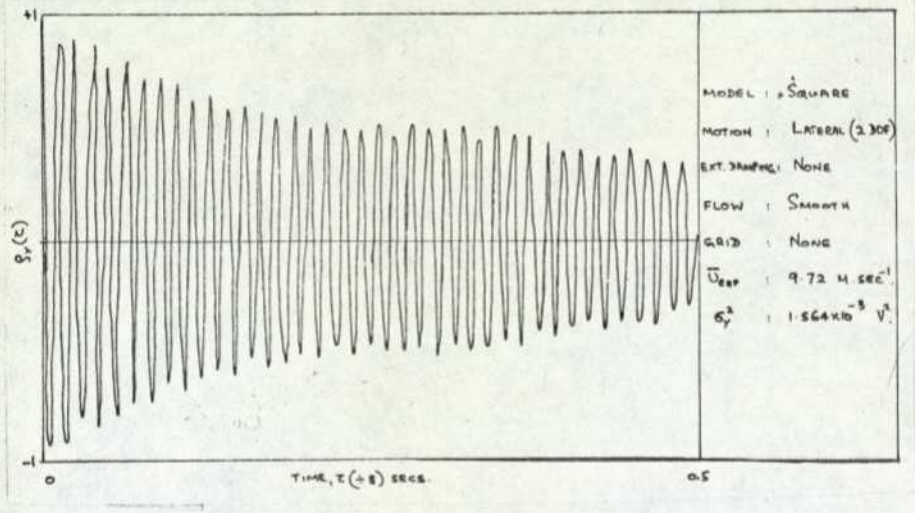

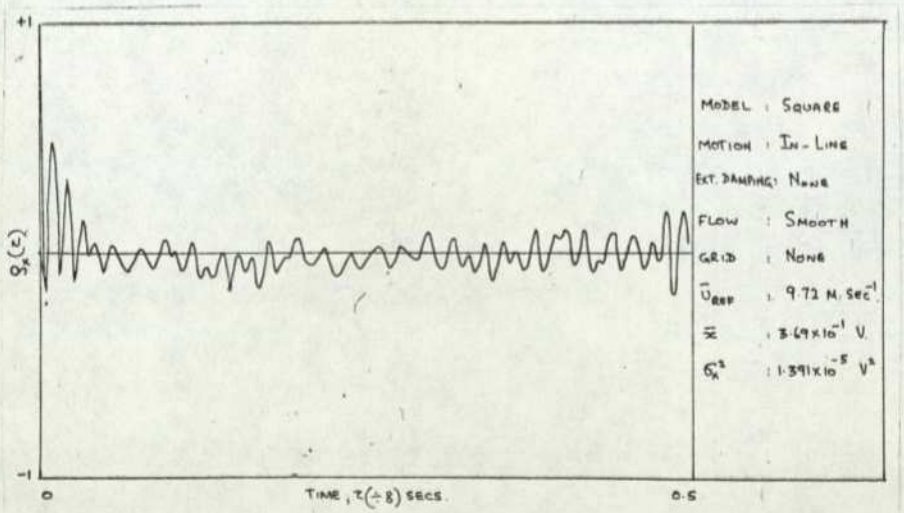

Auto-correlation: Square model in smooth flow without applied damping

FIGURE 7.16.a

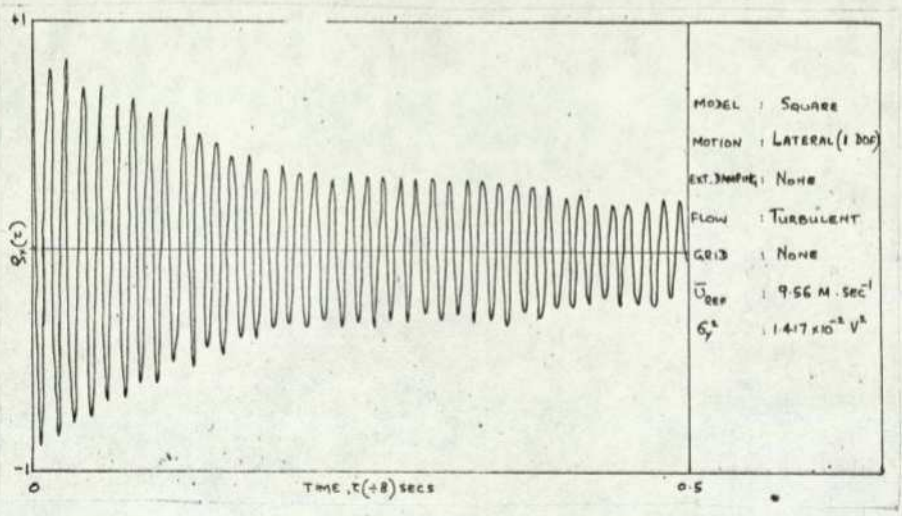

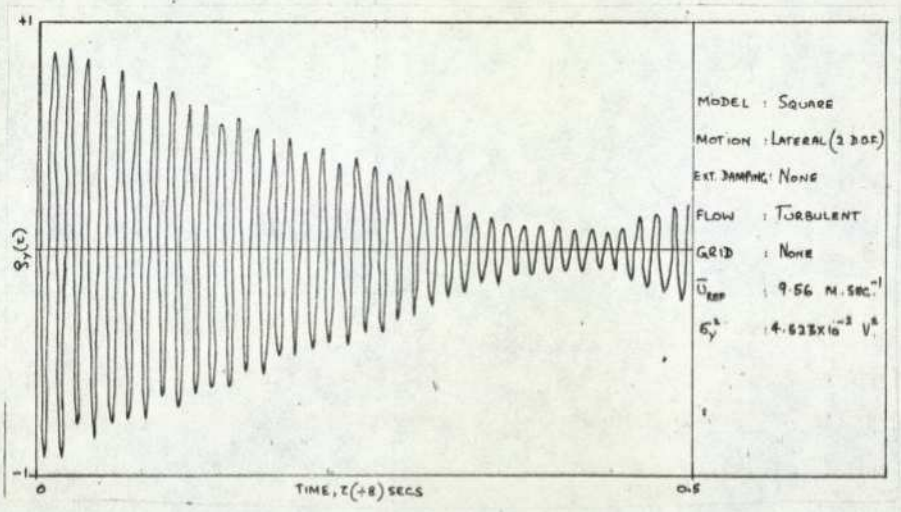

Auto-correlation: Square model in turbulent flow without applied damping

FIGURE 7.16.b

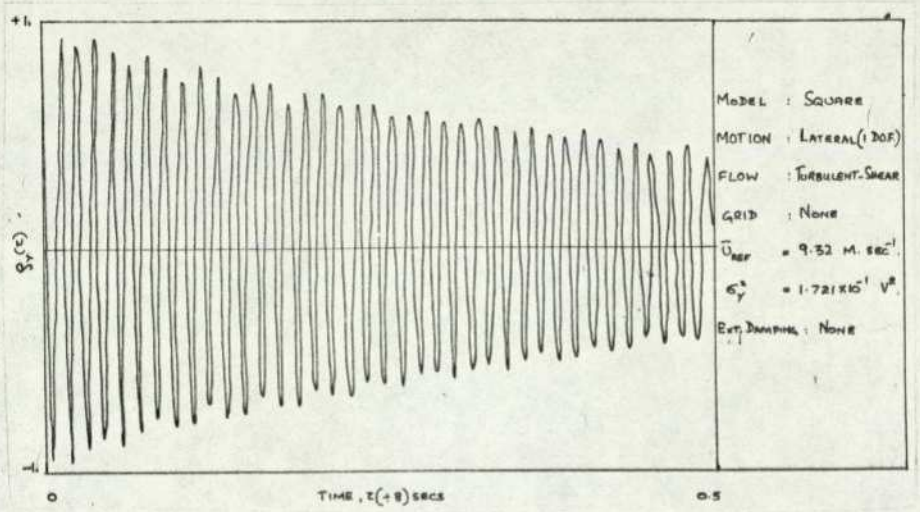

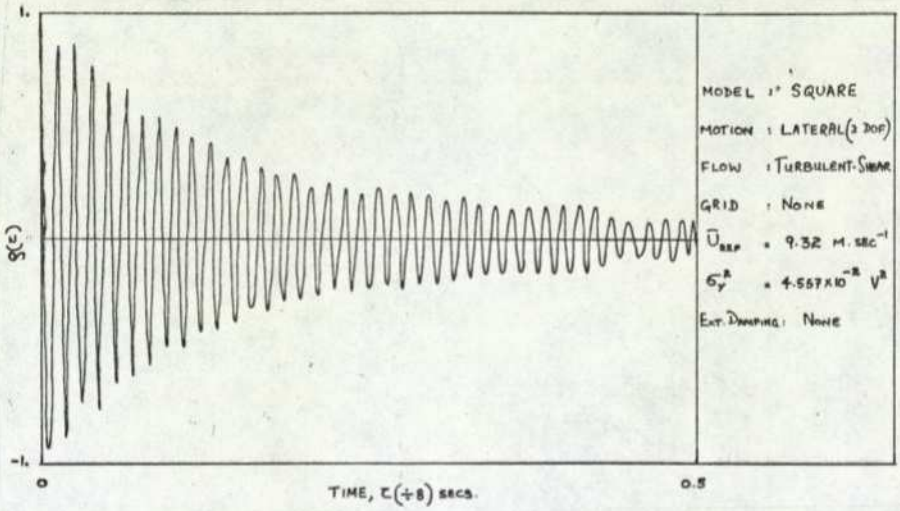

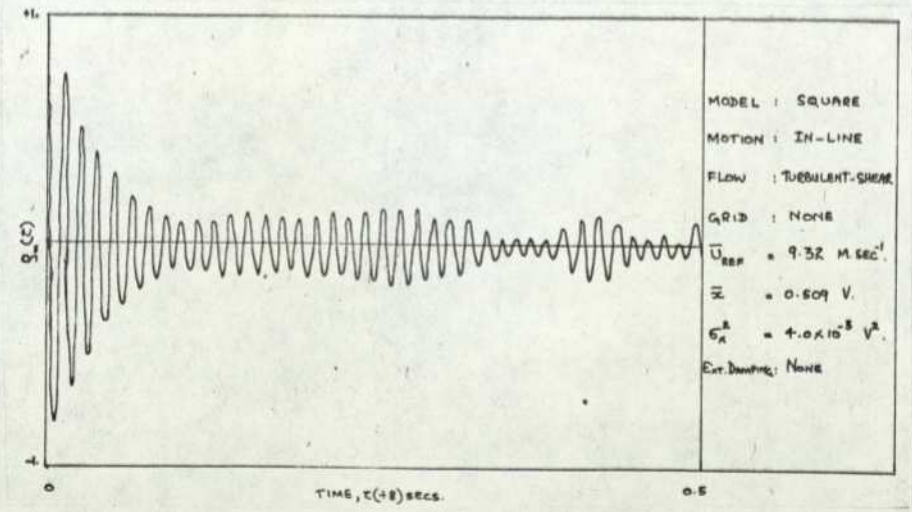

Auto-correlation: Square model in turbulent shear flow without applied damping

FIGURE 7.16.c

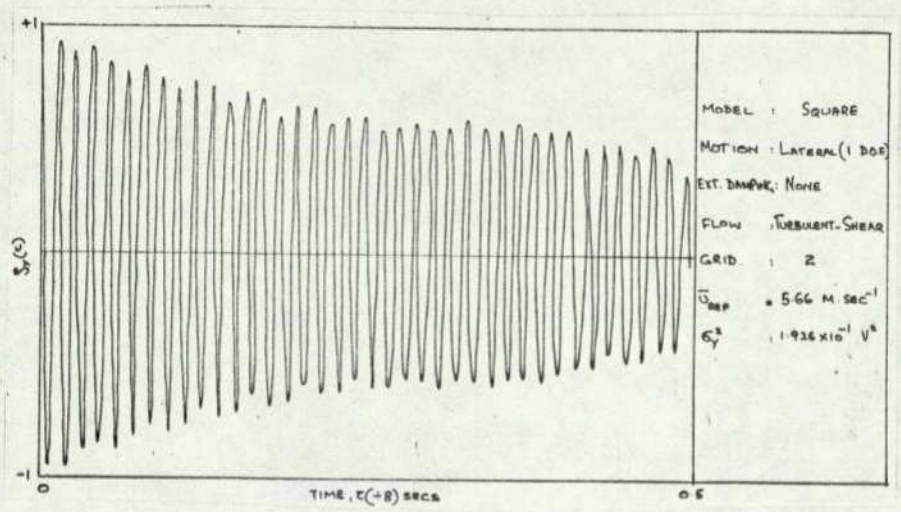

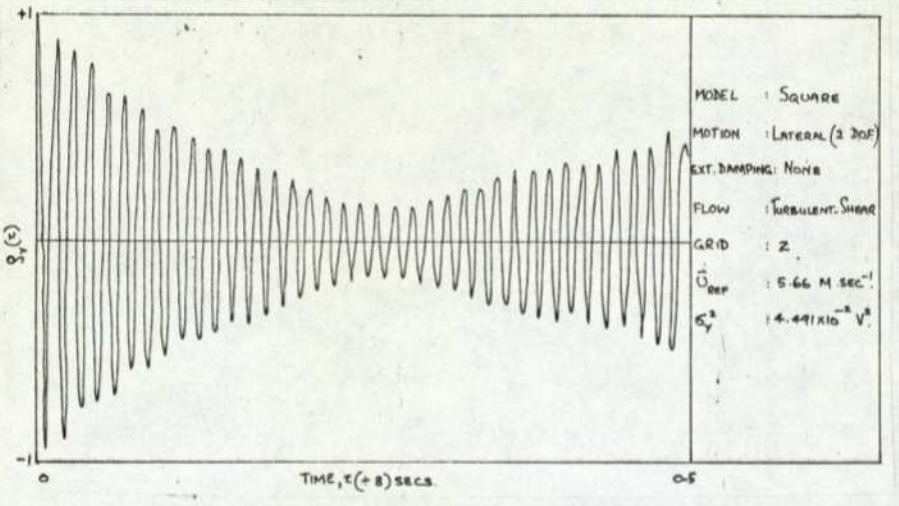

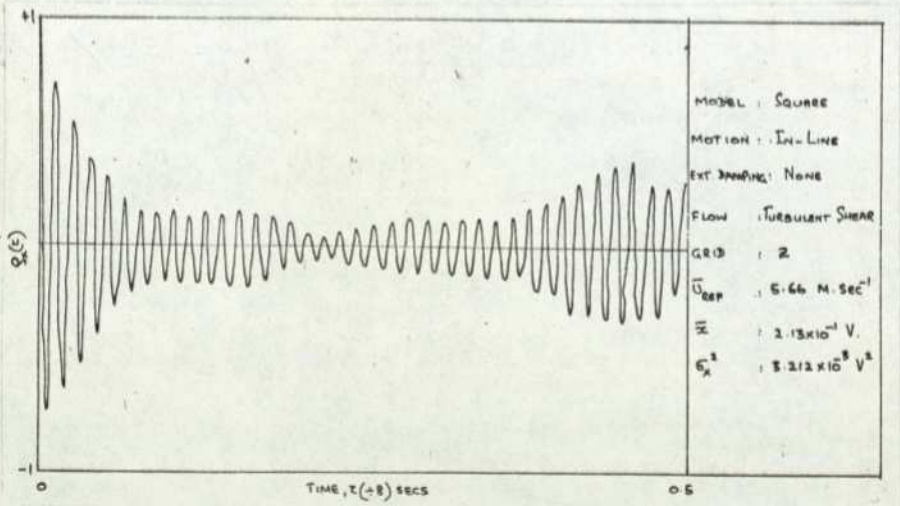

Auto-correlation: Square model in turbulent shear flow (screen 2) without applied damping

FIGURE 7.16.d

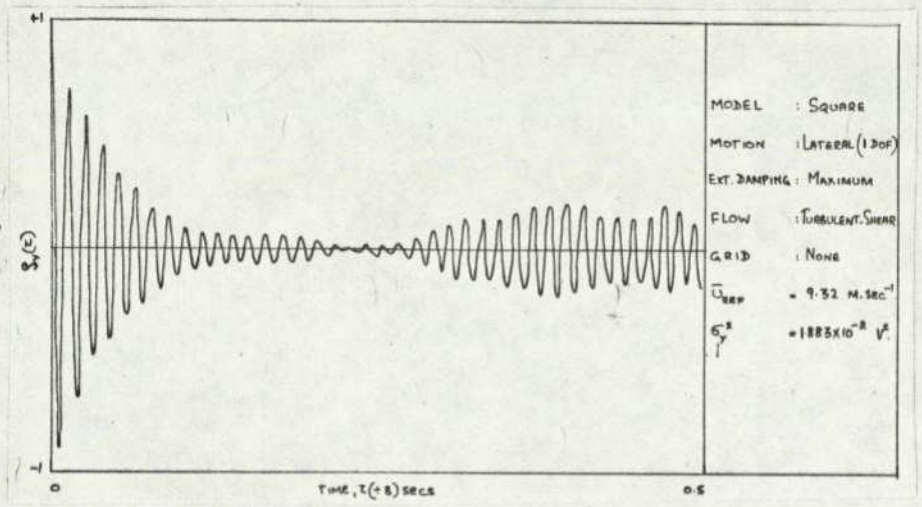

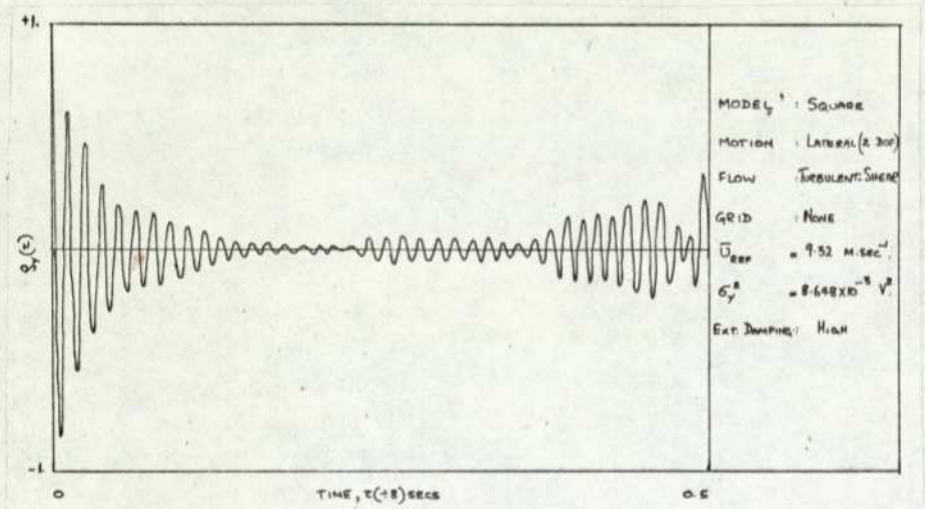

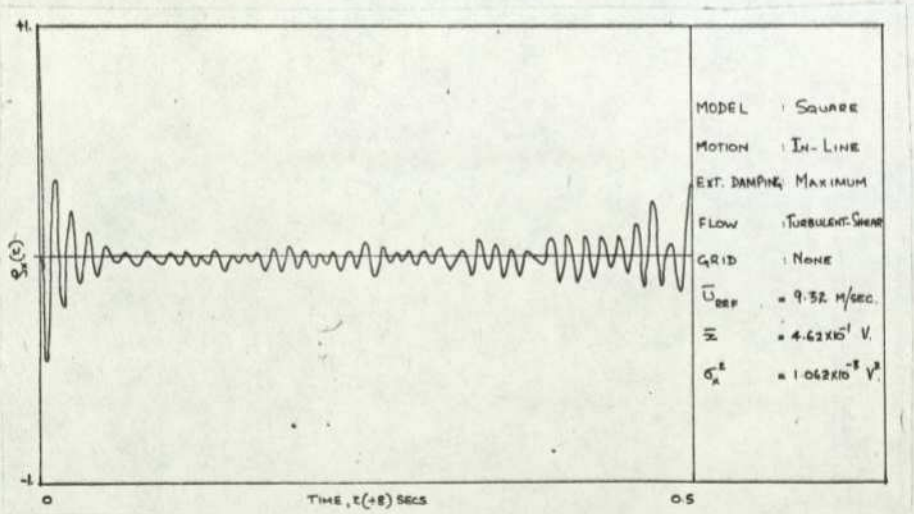

Auto-correlation: Square model in turbulent shear flow with maximum applied damping

FIGURE 7.16.e

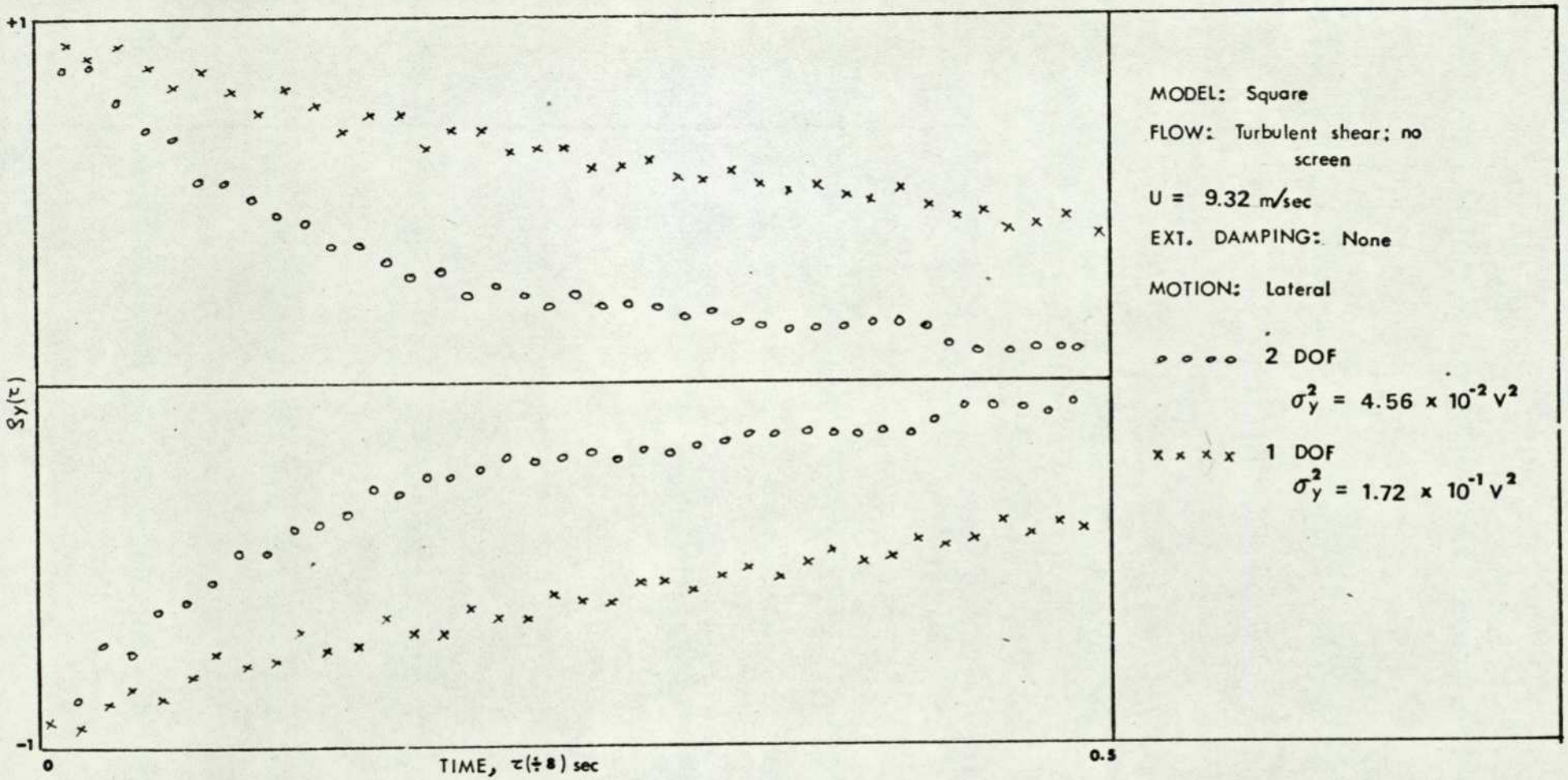

Comparison between 2 DOF and 1 DOF motion: Maxima and minima points of the respective auto-correlations

FIGURE 7.16.f

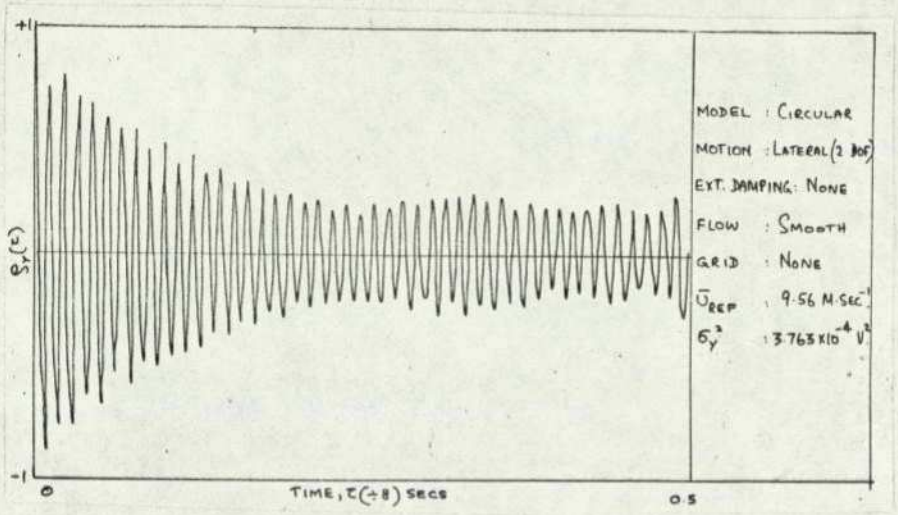

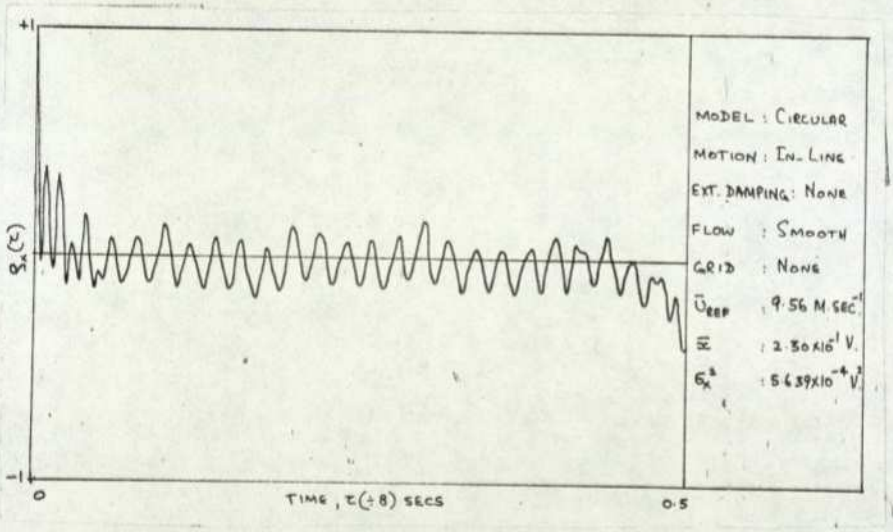

Auto-correlation: Circular model in smooth flow without applied damping

FIGURE 7.17.a

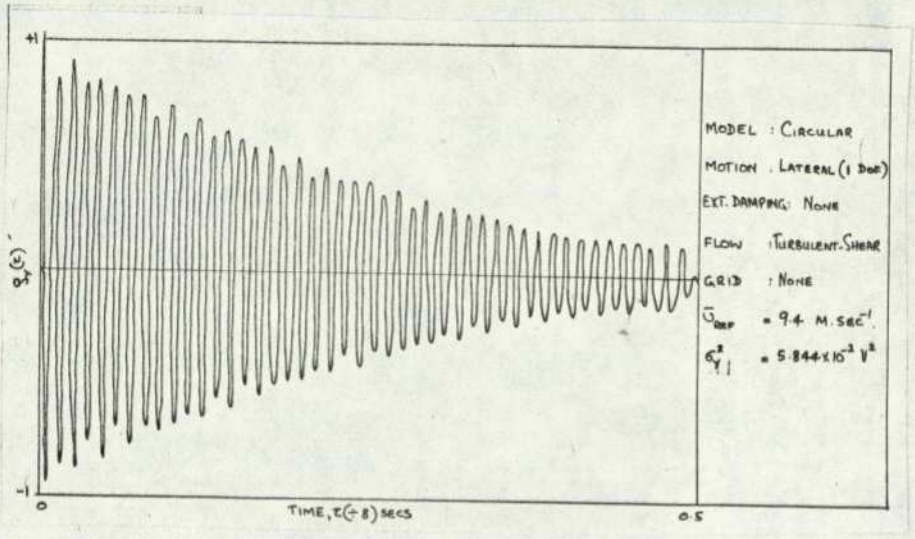

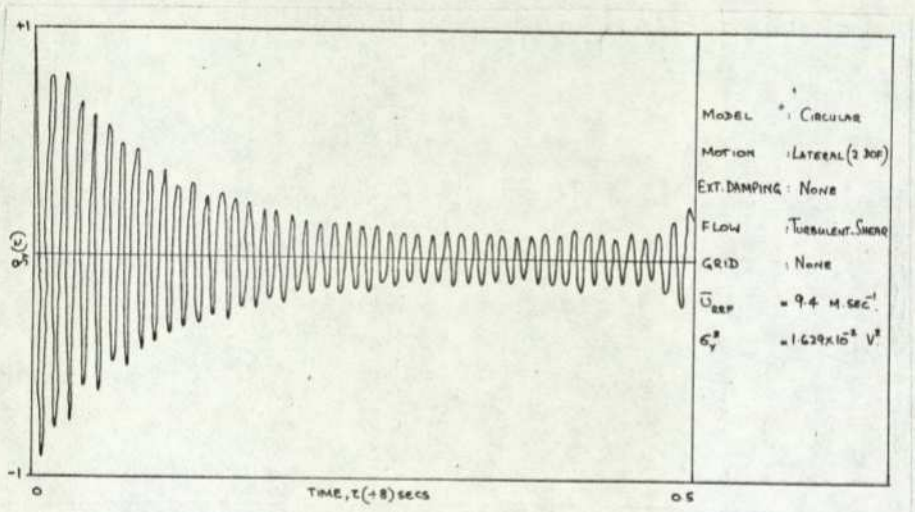

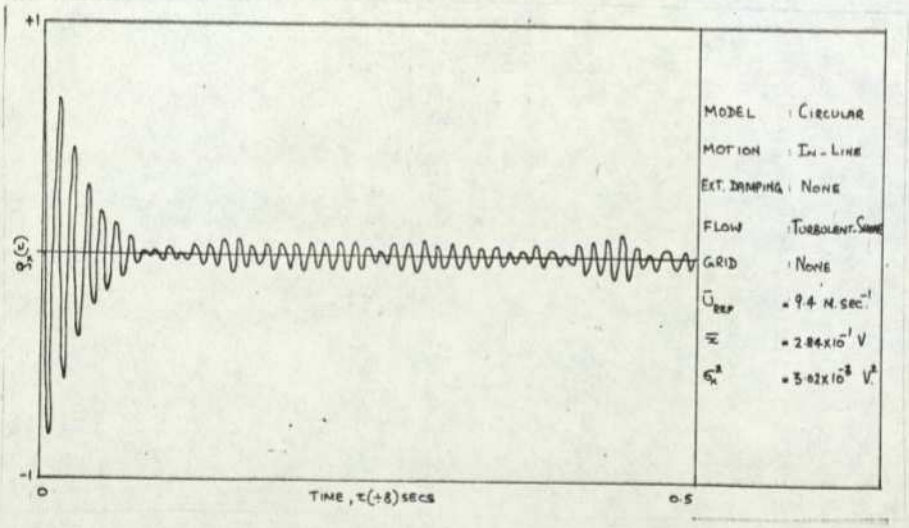

Auto-correlation: Circular model in turbulent shear flow without applied damping

FIGURE 7.17.b

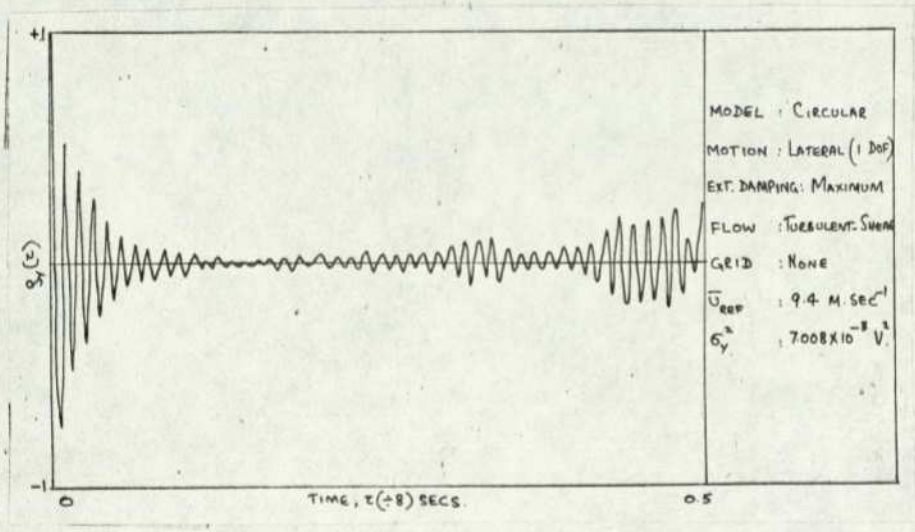

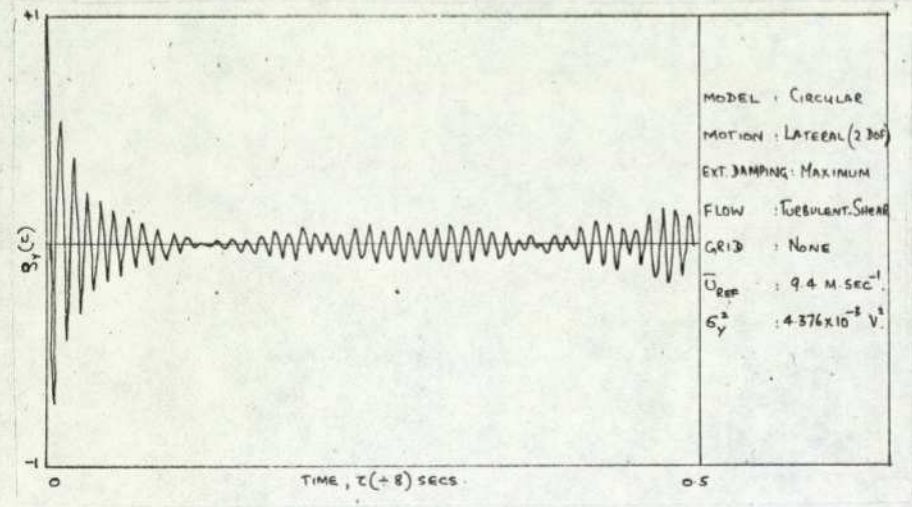

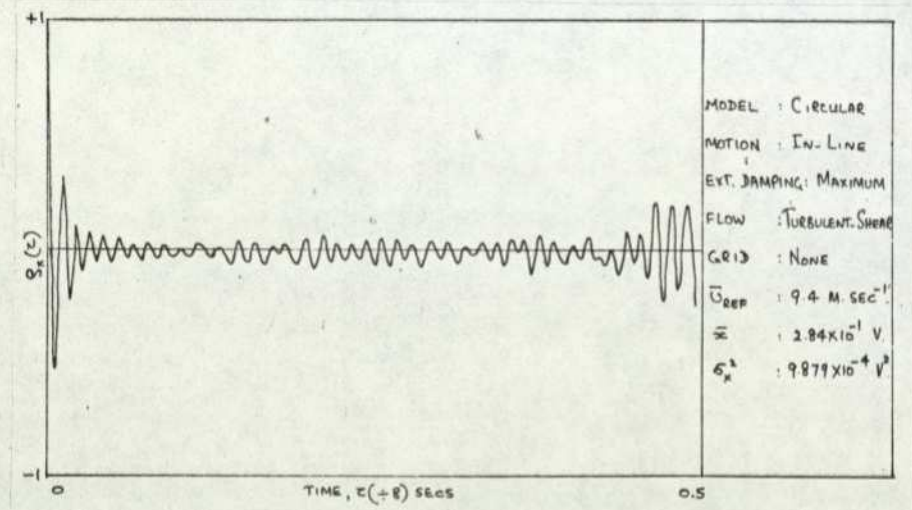

Auto-correlation: Circular model in turbulent shear flow with maximum applied damping

FIGURE 7.17.c

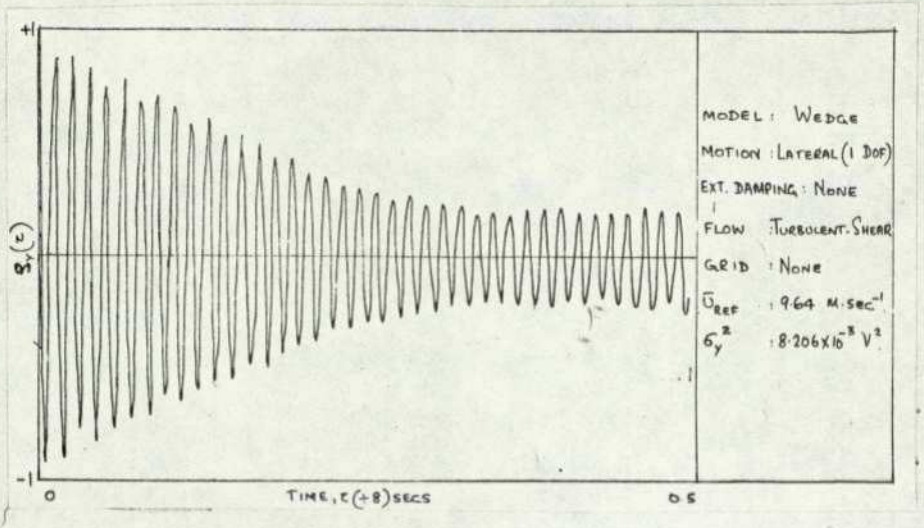

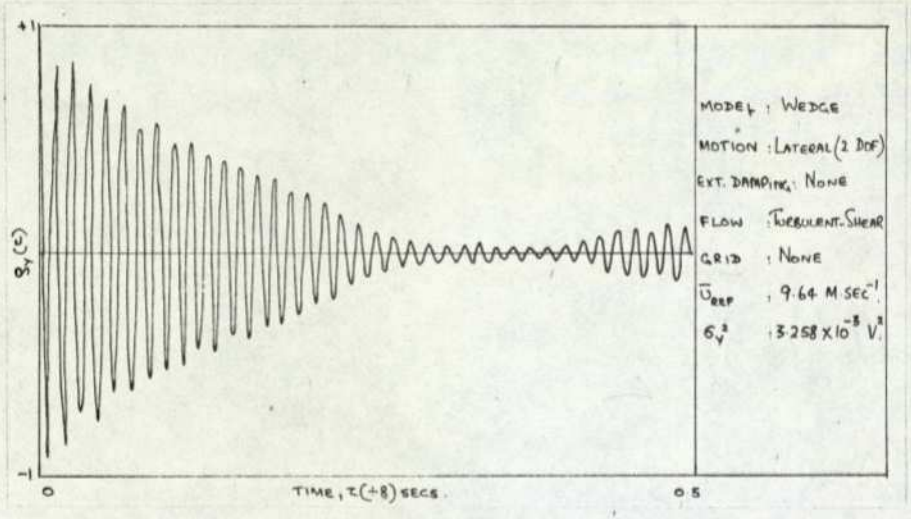

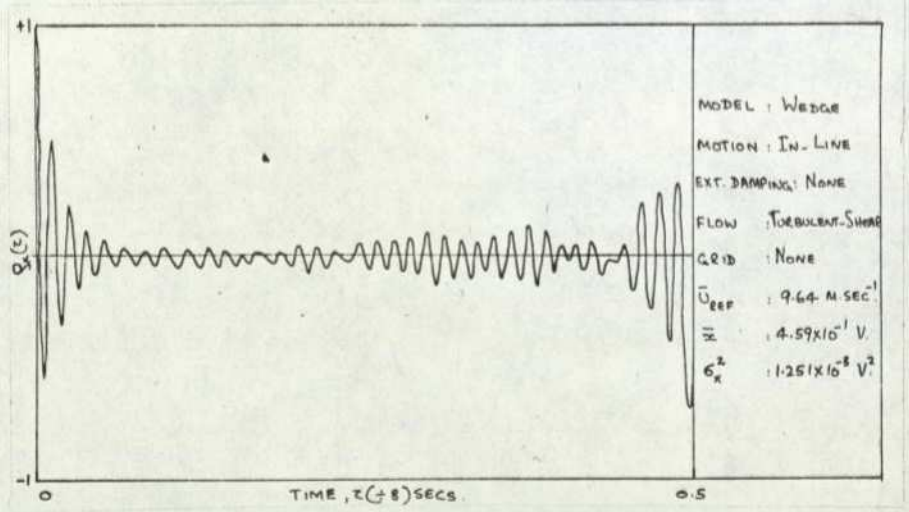

Auto-correlation: Wedge model in turbulent shear flow without applied damping

FIGURE 7.18.a

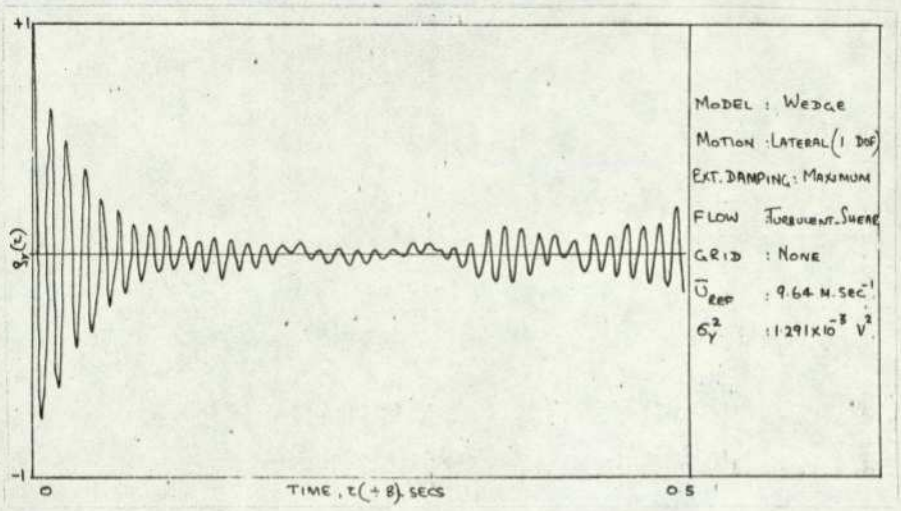

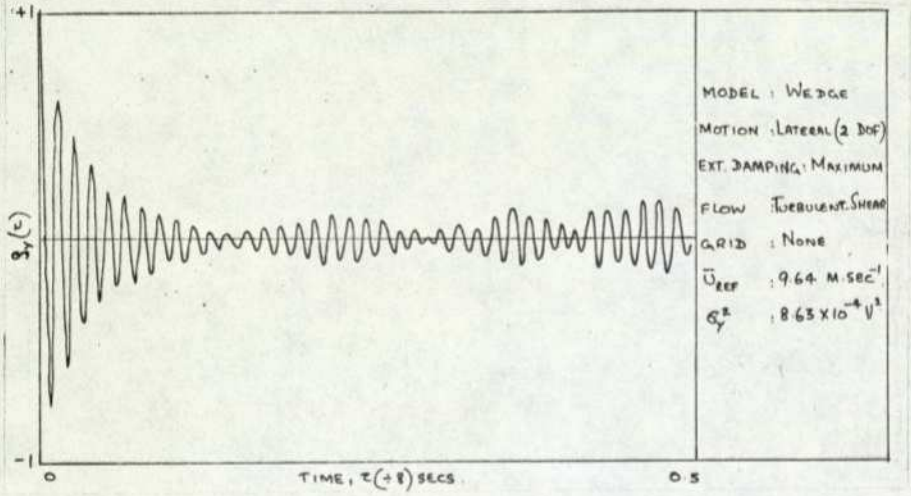

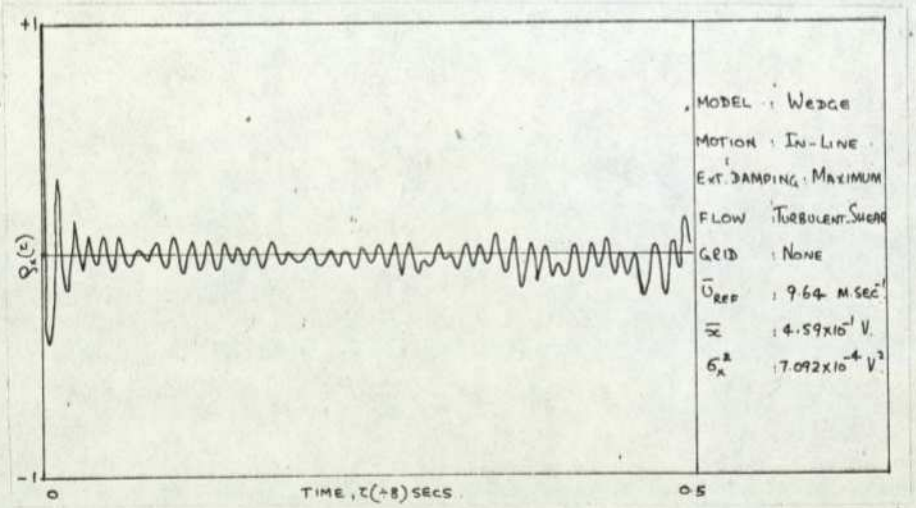

Auto-correlation: Wedge model in turbulent shear flow with maximum applied damping

FIGURE 7.18.b

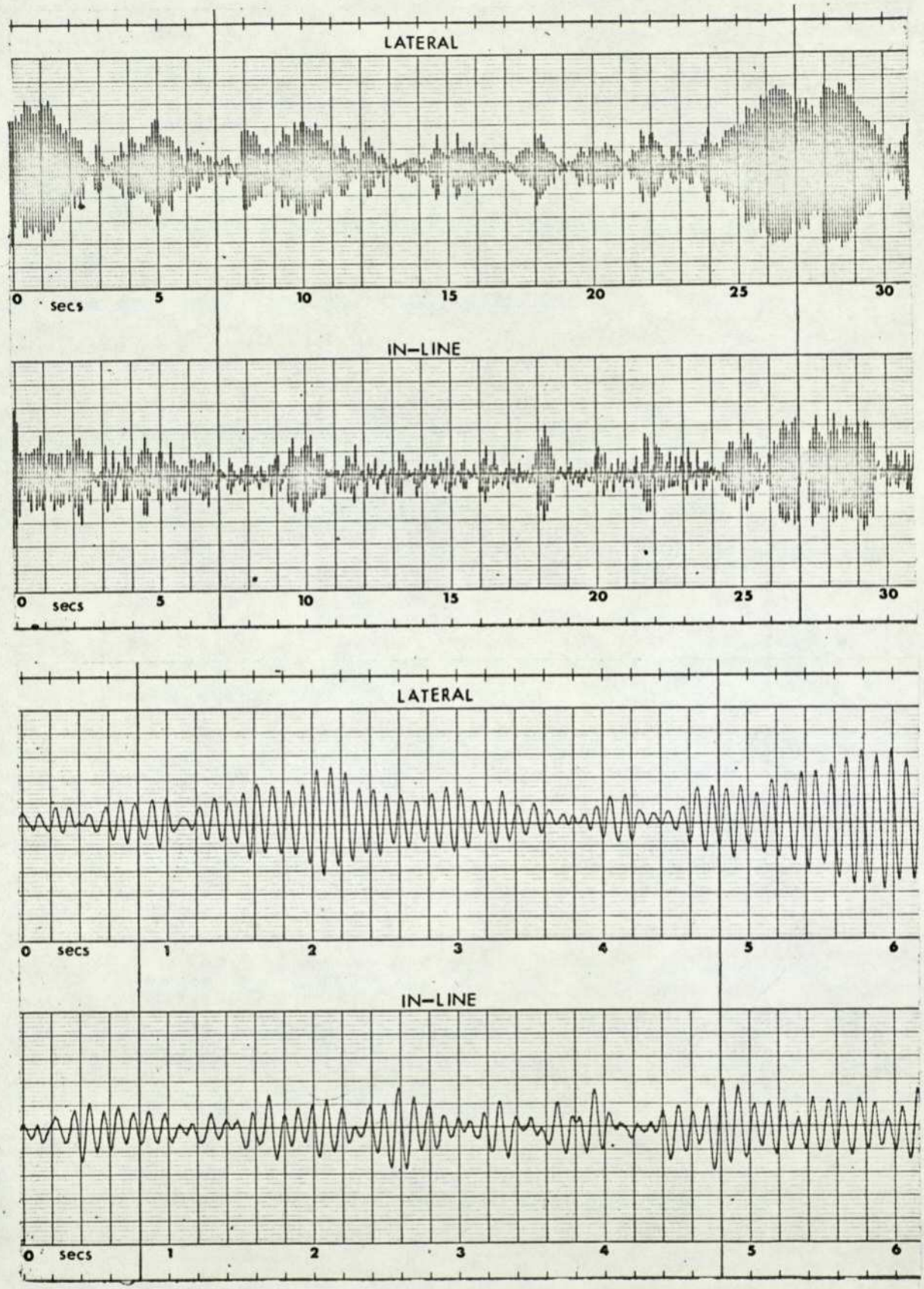

Square model oscillating in turbulent shear flow → no screen $\bar{U}_{ref}$ = 7.73 m/sec

Strain-guage signals

FIGURE 7.19

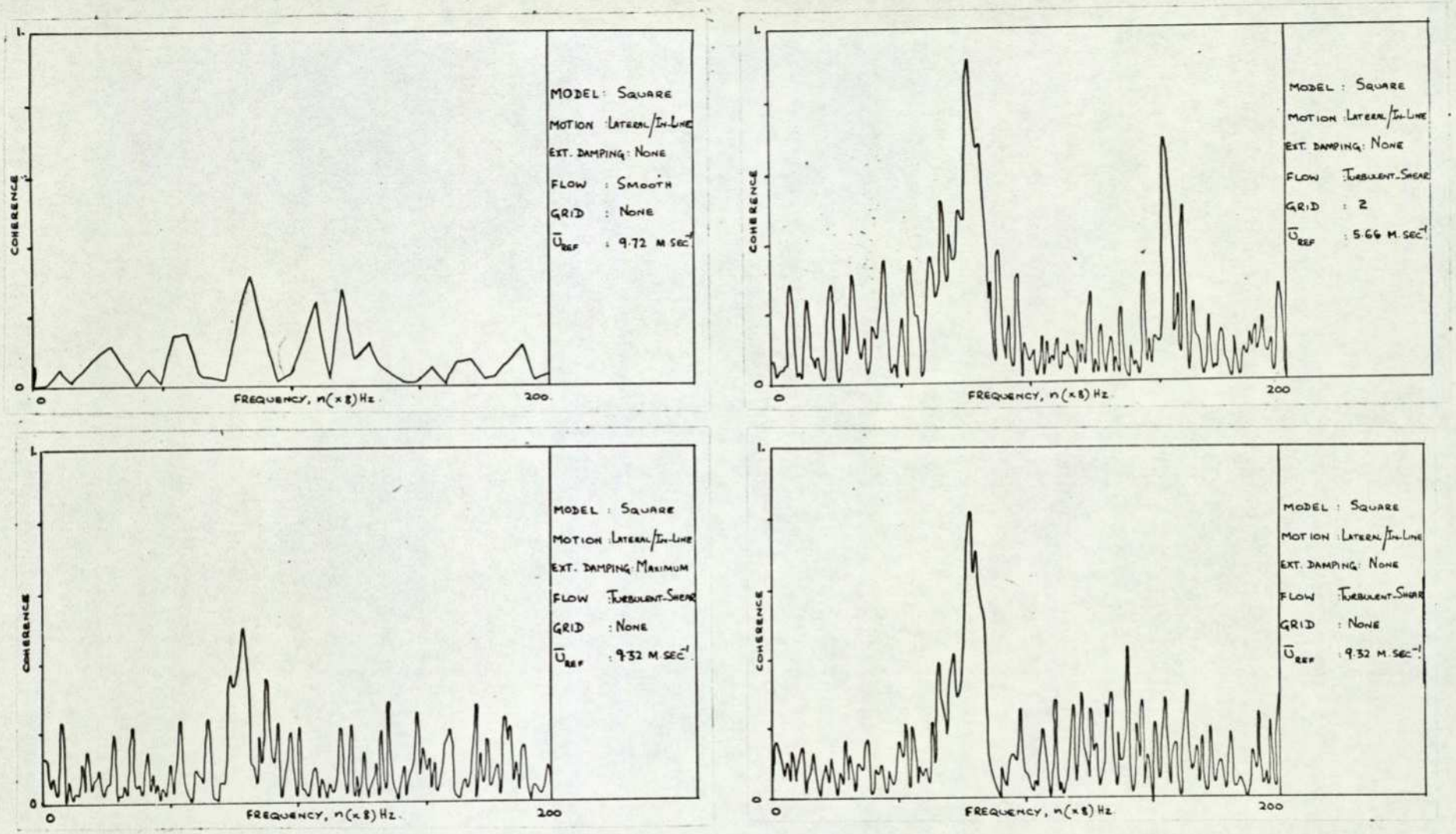

Coherence: Square model for various damping/flow configurations

FIGURE 7.20.a

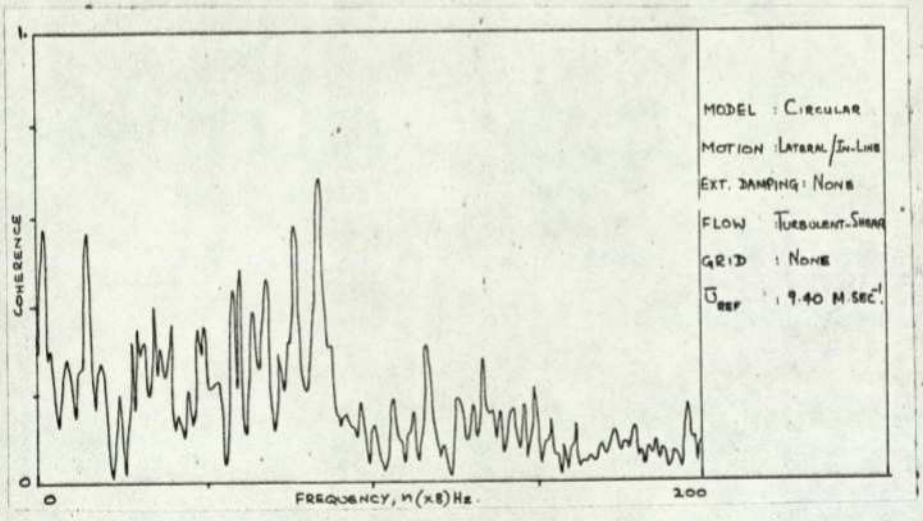

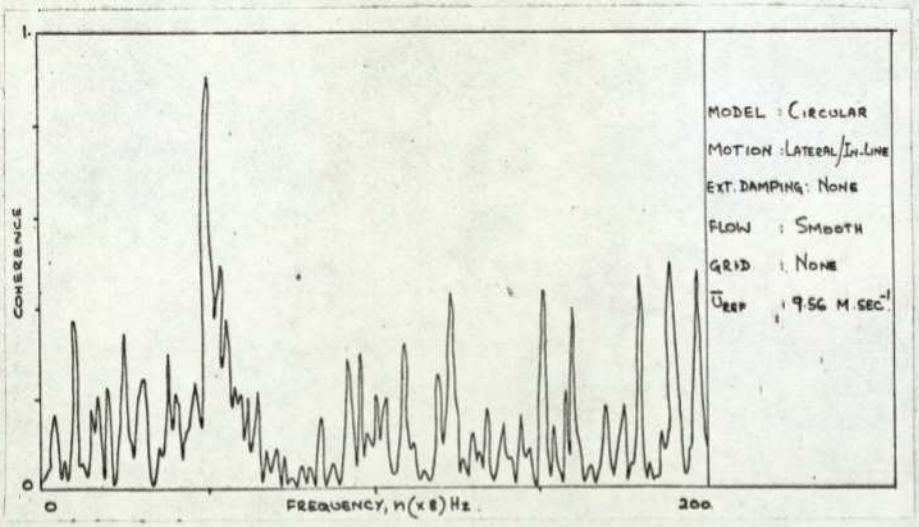

Coherence: Circular model in turbulent shear and smooth flow

FIGURE 7.20.b

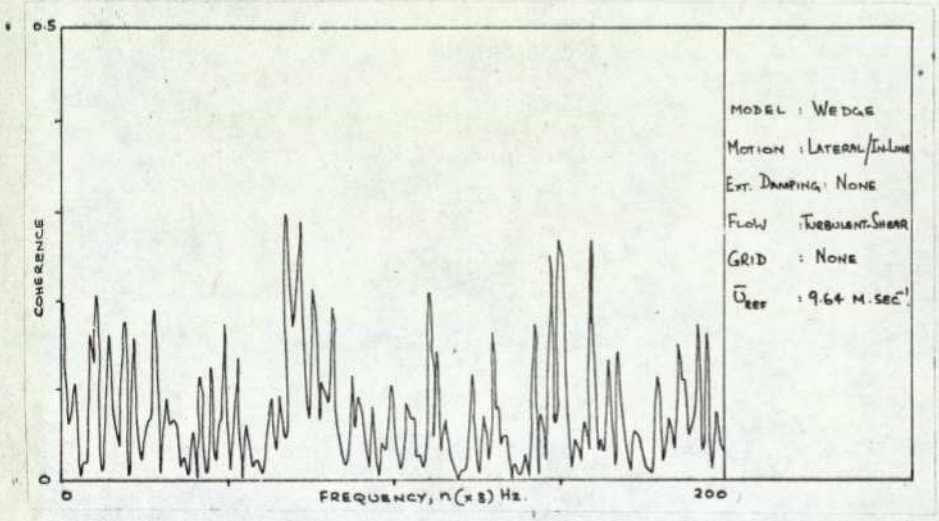

Coherence: Wedge model in turbulent shear flow

FIGURE 7.20.c

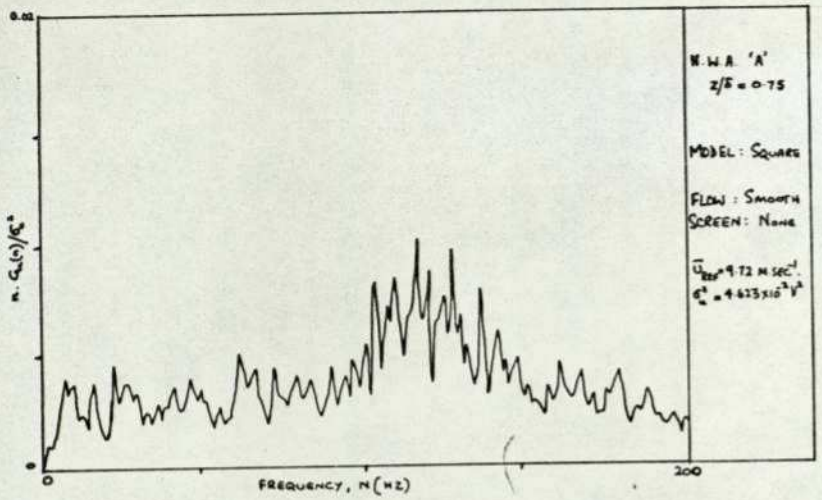

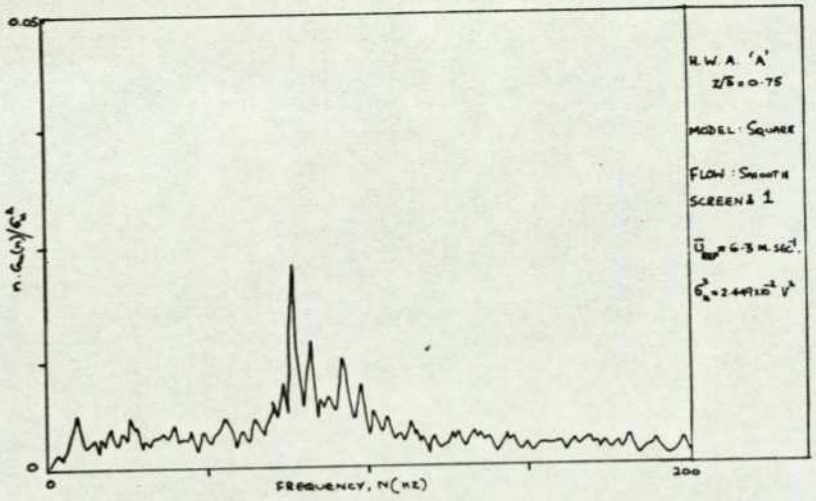

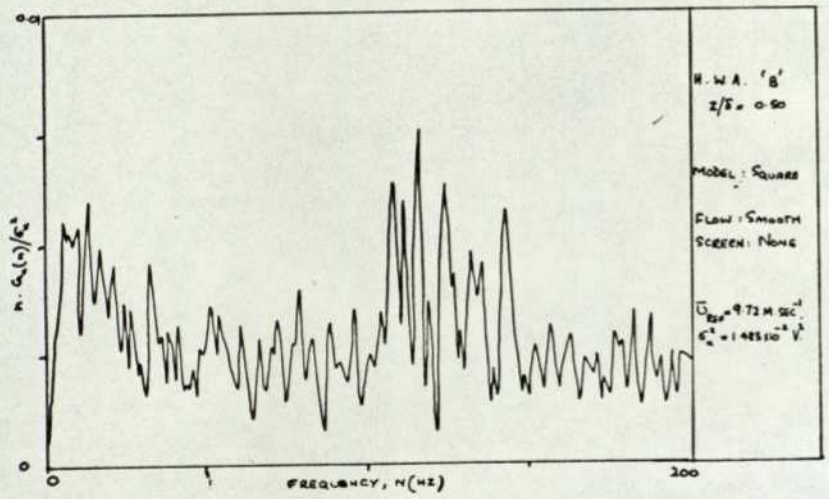

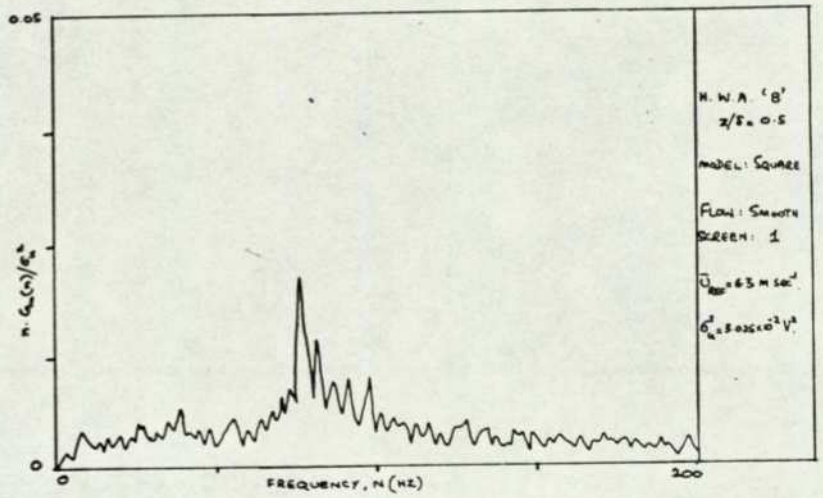

Wake spectra behind square model in smooth flow

FIGURE 7.21.a

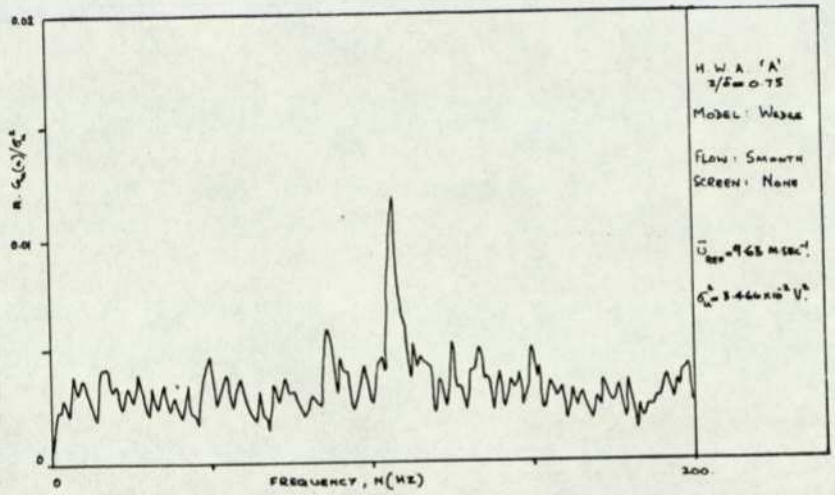

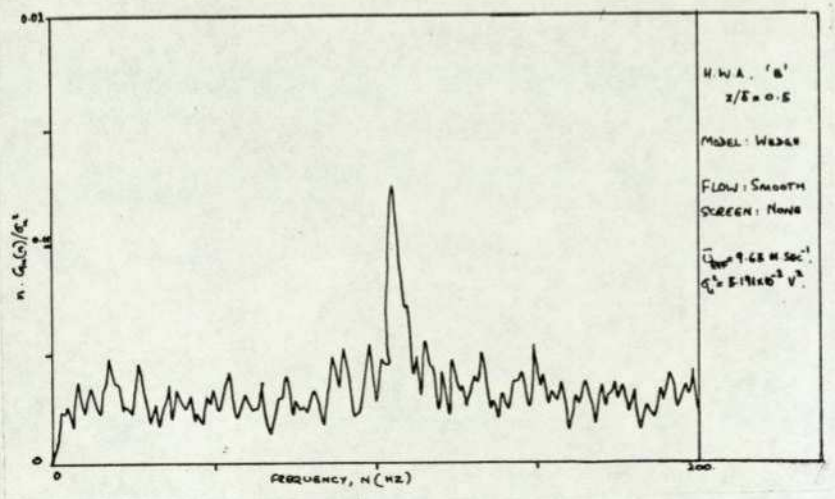

Wake spectra behind wedge model in smooth flow

FIGURE 7.21.b

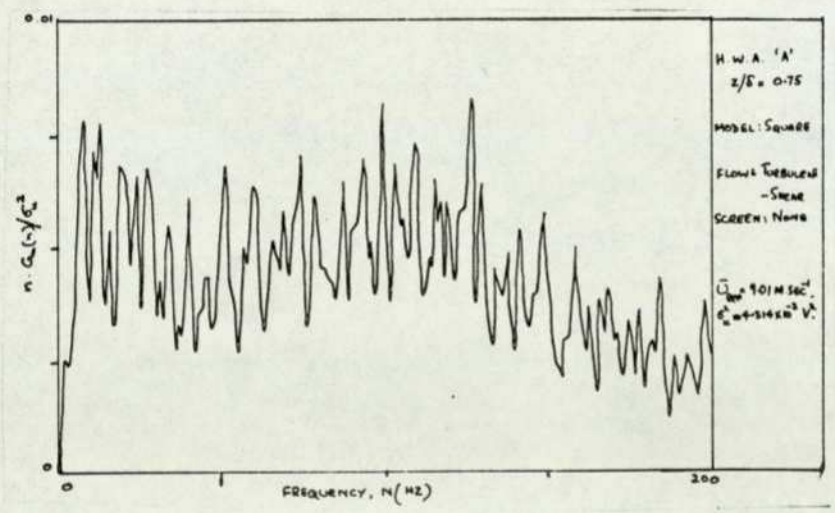

Wake spectrum behind square model in turbulent shear flow

FIGURE 7.21.c

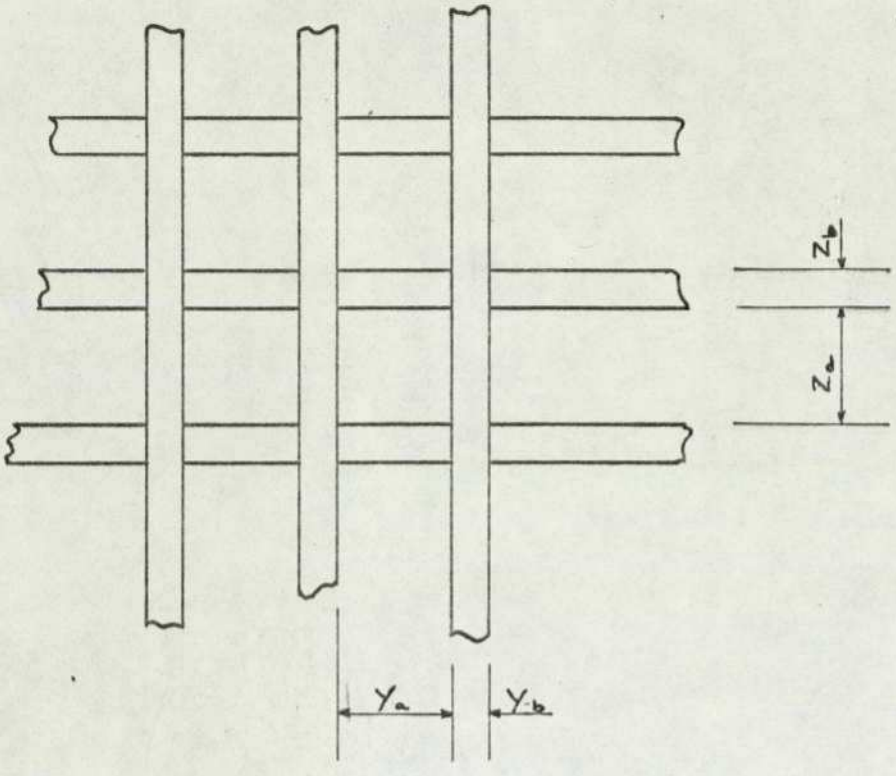

SCREEN NO.	MESH DIMENSIONS (MM.)				BLOCKAGE
	Y_a	Y_b	Z_a	Z_b	%
1	121	32	121	32	45
2	102	51	102	51	50
3	83	57	83	57	71

Bi-Planar screens

TABLE 4.1

FLOW GENERATOR	PROFILE EXPONENT α_u	α_L	SURFACE DRAG COEFFICIENT C_{D_u}	C_{D_L}	SURFACE ROUGHNESS z_{o_u} $x10^{-2}$(m.)	z_{o_L}	MACRO-VISCOSITY N_u $x10^{-4}$ (m^2./sec)	N_L	FRICTION VELOCITY u_{*u} $x10^{-2}$(m/sec.)	u_{*L}
Cowdrey grid (α=0.143)	0.218	0.127	0.015	0.0028	0.44	0.0028	35.	0.095	79.5	33.9
Vortex-generator(V.G) system	0.23	0.11	0.017	0.0026	0.51	0.0028	42.	0.090	83.0	32.2
V.G. system + Cowdrey grid (α=0.4)	0.335	0.16	0.029	0.0039	1.34	0.0166	143.	0.650	107.0	39.2
V.G. + C.Grid + roughness	0.39		0.039		1.253		284.		226.	
V.G. + C.Grid + roughness + Screen 2	0.45		0.083		1.60		161.		100.	
V.G. + C.Grid + roughness + Screen 3	0.48		0.074		1.89		165.		88.	

Characteristics of generated velocity profiles obtained from Fig. 6.1

TABLE 6.1

RUN NO.	GENERATED FLOW	U_{REF} m/sec	BACKED-OFF D.C. $\bar{U}_A$ (V). $\bar{U}_B$	R.M.S. $\sigma_{u,A}$ $\sigma_{u,B}$ x10² (V.)	SKEWNESS $\alpha_{3,A}$ $\alpha_{3,B}$ x 10²	KURTOSIS $\alpha_{4,A}$ $\alpha_{4,B}$
18	T	8.48	0.958 0.596	8.09 4.13	23. 6.	3.09 2.60
19	T_S	7.73	0.899 0.625	9.56 4.04	0. -2.	2.88 2.58
20	T_S + (1)	4.59	0.593 0.412	7.16 2.34	-4. -2.	2.52 2.54
21	T_S + (2)	3.07	0.439 0.325	4.29 2.19	15. -1.	2.91 2.51
22	T_S + (3)	1.56	0.312 0.244	3.62 1.62	7. 4.	2.62 2.75
23	T_S	7.73	0.899 0.625	9.56 4.46	-56. -47.	3.17 3.08
24	T_S	13.52	1.388 1.030	13.00 8.14	1. -36.	2.92 2.80

Note: All runs, except 23, sampled at 2500 s/sec, with play-back ratio, r=1.
Run 23, sampled at 500 s/sec, with play-back ratio, r=8.

Amplitude-domain characteristics of turbulent generated flows - a sample of the digitised runs.

TABLE 6.2

FLOW GENERATED	$\bar{U}$ m/sec	H.W.A.	von KARMAN SPECTRUM Hz	$x10^{2}$(m.)	HARRIS SPECTUM Hz	$x10^{1}$(m)	$x10^{2}$(m)	KAIMAL SPECTRUM Hz	$x10^{2}$(m)	AUTO CORRELATION $x10^{-3}$(sec)	$x10^{2}$(m)
T	9.58	A	25.00	5.579	25.00	6.637	5.587	7.50	5.109		
	5.96	B	16.00	5.424	16.00	6.452	5.431	5.00	4.768		
T_s	13.88	A	38.75	5.215	36.46	6.594	5.550	10.27	5.406	8.90	12.360
	10.30	B	18.02	8.322	17.00	10.490	8.834	4.69	8.785	6.81	7.019
T_s	8.99	A	16.00	8.181	16.00	9.732	8.192	4.60	7.817	8.57	7.707
	6.25	B	12.56	7.245	13.07	8.282	6.972	3.76	6.649	6.83	4.270
T_s + (1)	5.93	A	11.13	7.757	11.13	9.228	7.768	3.20	7.413	10.46	6.202
	4.12	B	9.48	6.328	9.48	7.527	6.336	2.73	6.037	11.01	4.535
T_s + (2)	4.39	A	8.40	7.609	8.57	8.872	7.469	2.42	7.266		
	3.25	B	6.09	7.710	6.09	9.243	7.781	1.79	7.263		
T_s + (3)	3.12	A	5.00	9.085	5.00	10.830	9.119	1.46	8.548		
	2.44	B	6.34	5.604	6.34	6.666	5.611	1.75	5.577		
T + (1)	7.24	A	17.00	6.201	17.66	7.101	5.977	5.00	5.792		
	4.43	B	9.30	6.936	9.30	8.250	6.945	2.90	6.110		
T + (2)	5.36	A	10.69	7.300	10.69	8.684	7.310	3.08	6.961		
	3.20	B	5.00	9.318	5.00	11.080	9.331	1.75	7.314		
T + (3)	3.88	A	6.00	9.415	5.97	11.260	9.476	1.67	9.293		
	2.43	B	4.00	8.845	4.00	10.520	8.857	1.13	8.602		
T	15.01	A	53.30	4.100	49.19	52.850	4.449	17.66	3.400		
	9.28	B	21.60	6.255	21.60	74.410	6.264	6.47	5.737		

Length-scales of turbulence of some cases of the generated flows, calculated using various methods

TABLE 6.3

RUN NO.	MODEL	D.O.F.	FLOW	U m/sec	EXT. DAMPING	MOTION	D.C x10 V.	R.M.S. x10 V.	SKEWNESS	KURTOSIS
2	Sq	2	T_s	9.32	None	Lateral	0.046	2.070	-0.023	2.75
						In-line	4.660	0.762	-0.180	3.53
3	Sq	2	T_s	9.32	Maximum	Lateral	0.046	0.886	-0.006	2.89
						In-line	4.640	0.397	-0.275	3.55
4	Sq	2	T_s+(2)	5.66	None	Lateral	0.046	1.850	-0.006	2.59
						In-line	1.690	0.517	0.017	3.31
5	Sq	2	T	9.56	None	Lateral	0.044	2.020	-0.007	2.47
						In-line	3.550	0.615	-0.080	3.14
6	W	2	T	9.64	None	Lateral	0.043	0.418	0.009	2.60
						In-line	3.740	0.260	-0.196	2.92
7	W	2	T_s	9.64	None	Lateral	0.042	0.544	-0.010	2.47
						In-line	4.700	0.453	-0.485	3.87
8	C	2	T_s	9.40	None	Lateral	0.041	1.180	-0.008	2.71
						In-line	2.430	0.624	-0.183	3.50
9	C	2	T	9.40	None	Lateral	0.040	0.757	-0.013	2.46
						In-line	1.980	0.399	-0.161	3.62
15	Sq	1	T_s	9.32	None	Lateral	0.036	3.620	-0.002	2.02
16	W	1	T_s	9.64	None	Lateral	0.039	0.672	0.001	2.53
17	C	1	T_s	9.40	None	Lateral	0.038	1.910	0.001	2.26

Amplitude domain characteristics of model vibrations - a sample of digitised runs

TABLE 7.1

U (M/SEC)	9.32	9.32	5.66
EXTERNAL DAMPING	None	Maximum	None
$z_y = y'/\sigma_y$	P ($> z_y$)		
0.25	.84	.87	.85
0.50	.68	.75	.71
0.75	.56	.63	.58
1.00	.43	.52	.46
1.25	.34	.44	.36
1.50	.26	.36	.28
1.75	.20	.28	.22
2.00	.16	.22	.17
2.25	.12	.17	.13
2.50	.098	.13	.099
2.75	.077	.09	.078
3.00	.064	.066	.062
3.25	.051	.047	.047
3.50	.036	.037	.035
3.75	.026	.025	.025
4.00	.020	.017	.020
4.25	.016	.011	.016
4.50	.011	.0063	.013
4.75	.0078	.0044	.0088
5.00	.0066	.0034	.0066

Cumulative probability distributions for the lateral vibrations of the Square model in turbulent with shear flow

TABLE 7.2

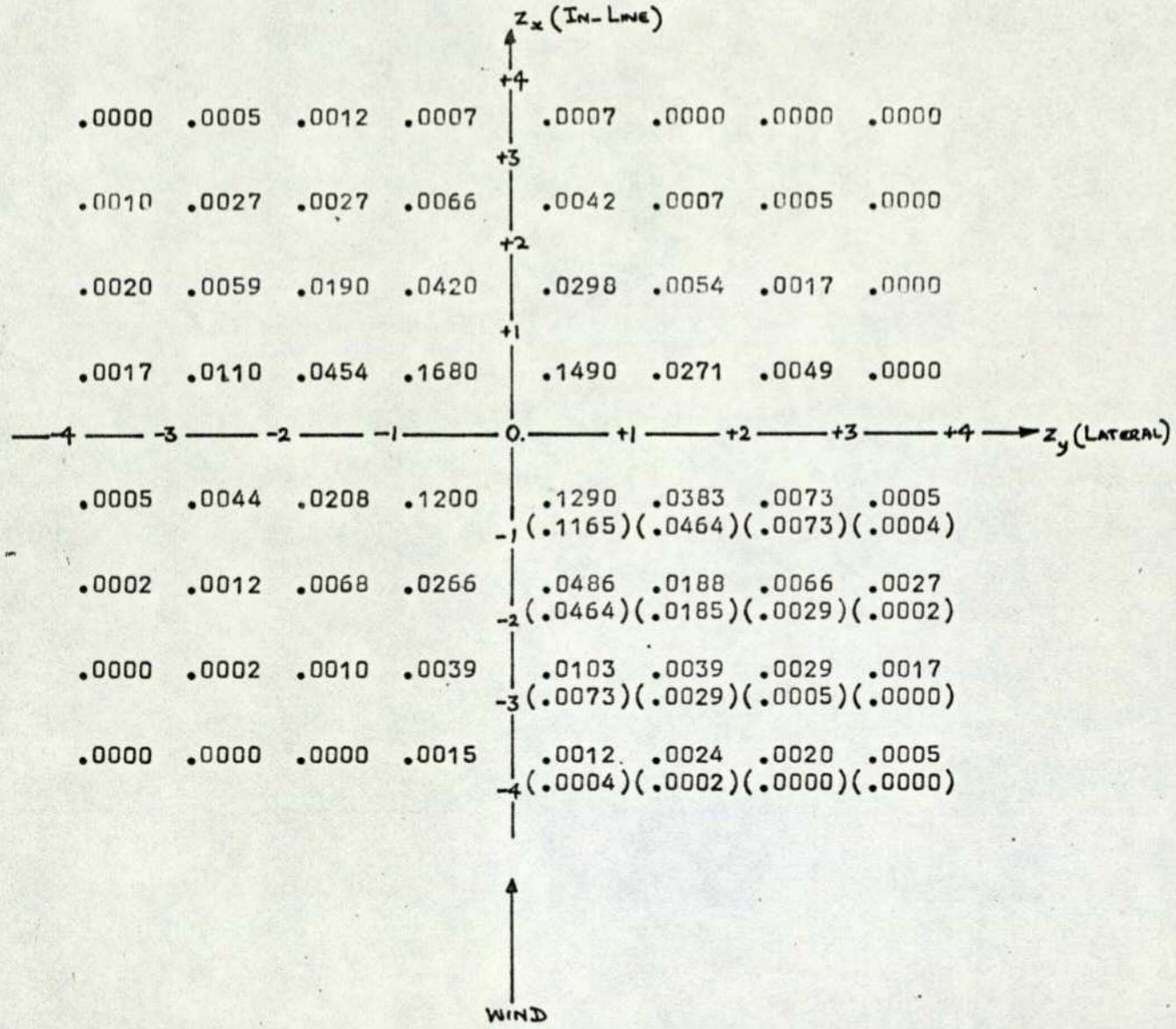

Note: Figures within brackets are the theoretical values of a bi-variate normal distribution

$\bar{U}_{REF}$ = 9.32 m/sec.

EXT. DAMPING: None

Joint probability distribution

for square model oscillating in turbulent shear flow

TABLE 7.3.a

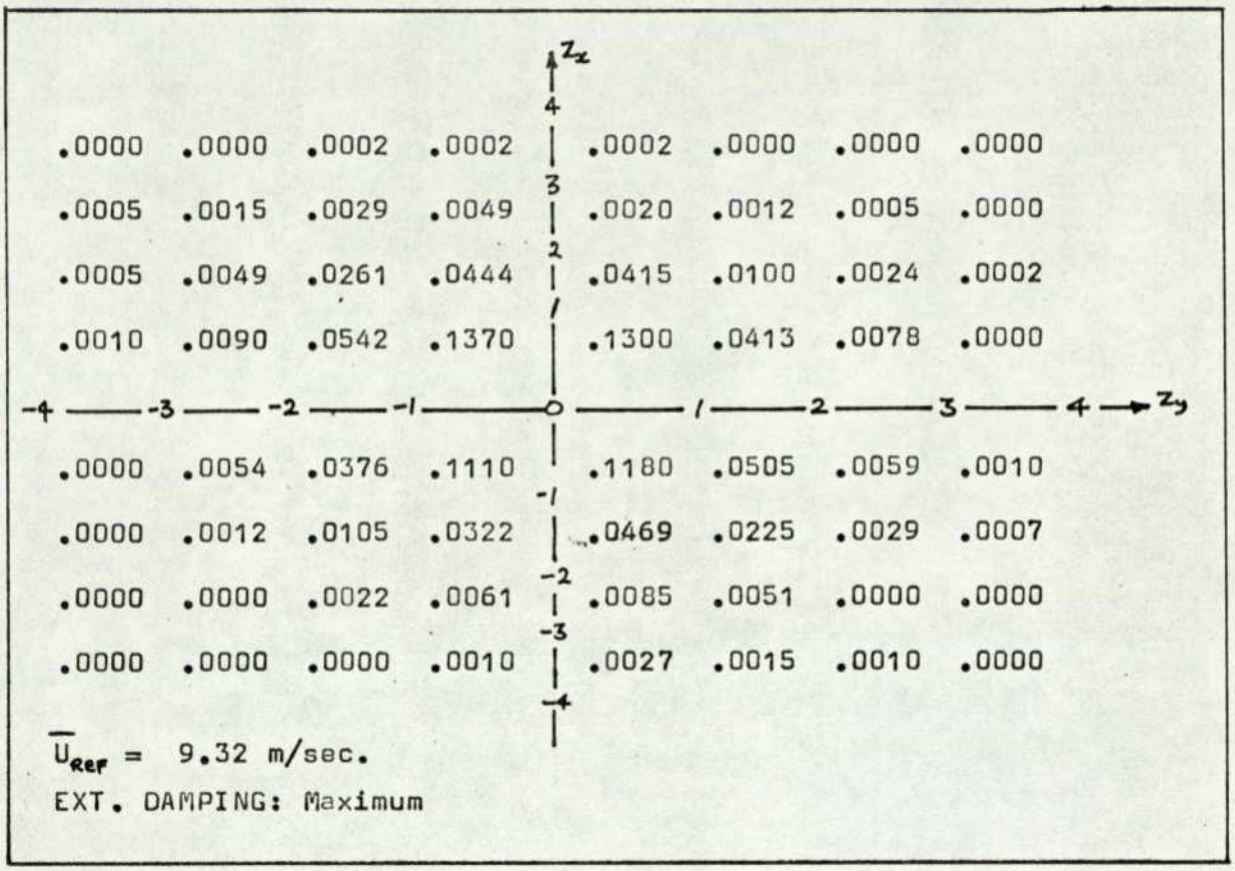

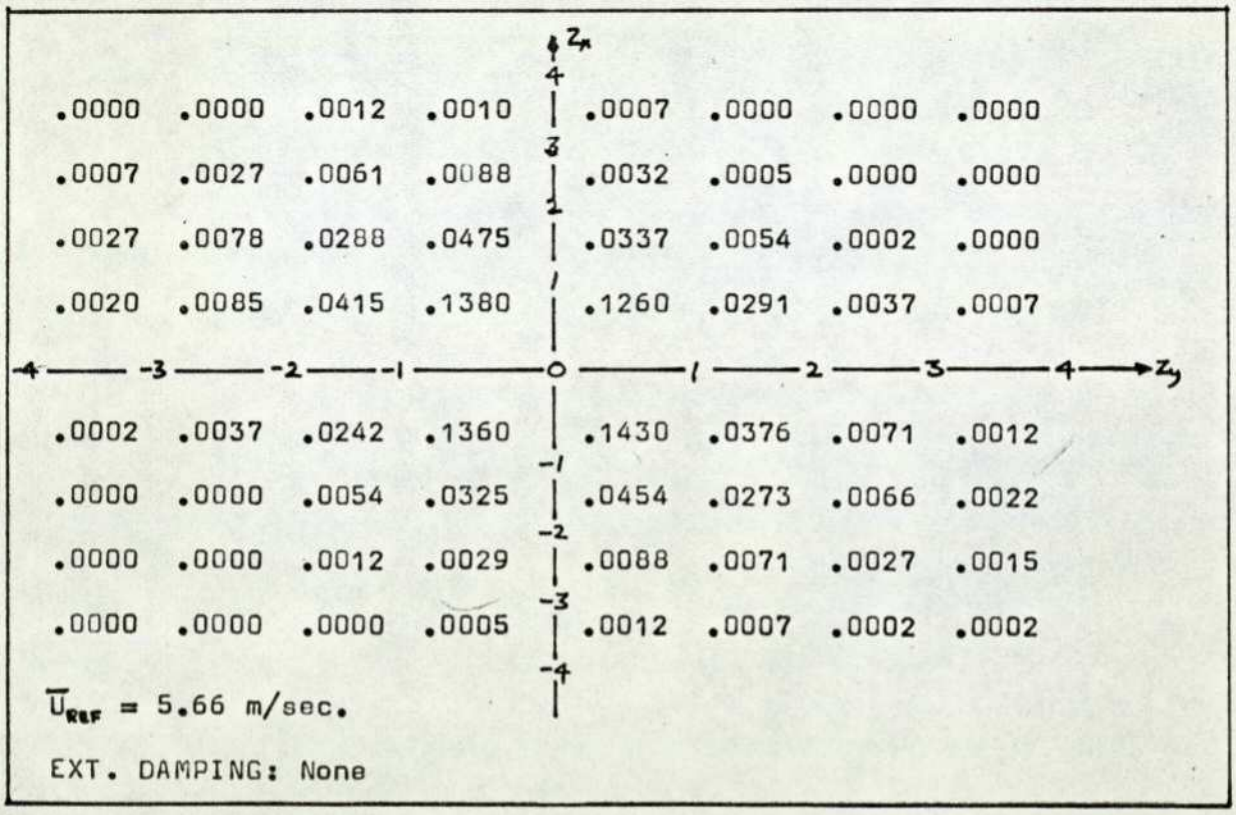

Joint probability distributions
for square model oscillating in turbulent shear flow

TABLE 7.3.b

Damping evaluated from UV trace with model displaced in still-wind conditions:

Method	Maxima	Area	Decay
Ext. Damping		$\xi \times 10^2$	
None	1.872	1.518	2.120
Maximum	5.193	5.674	5.010

MODEL	DAMPING	FLOW	Auto-spectra				Auto-correlation		
			Lateral		In-line		Lateral		In-line
			2 DOF	1 DOF	NORMAL	EXTRA	2 DOF	1 DOF	NORMAL
						$\xi \times 10^2$			
Sq	None	T_s	1.677	1.336	1.560	3.367	1.343	0.474	1.245
		S	1.518	1.448			0.627		
C	None	T_s	1.407	1.257	1.304	4.741	1.353		
		S	1.055						
W	None	T_s	1.991		1.991	4.054	1.260		
Sq	Maximum	T_s	4.973		4.340		5.462	4.690	
C	Maximum	T_s					5.595		
W	Maximum	T_s					4.894		

Sample of damping values evaluated by various methods

TABLE 7.4

APPENDIX 2A. CALIBRATION OF HOT-WIRE ANEMOMETERS

A formula, which is usually used for the calibration of hot-wire anemometers is the empirical equation

$$E^2 = A_1 + B_1 U^n$$

where E is the mean voltage drop across the hot-wire for a mean flow velocity U, normal to the axis of the wire. A_1, B_1 and n are constants made to fit the calibration.

A disadvantage of the above equation is that the assumption of a linear relationship between E^2 and U^n has not always given the desired accuracy in fitting a suitable curve to the experimental calibration data. This has lead Siddall and Davies [84], among others, to propose a second-degree calibration curve of the form.

$$E^2 = A_2 + B_2 U^n + C_2 U^{2n}$$

Davies and Patrick [85] have confirmed that the second degree form gives good fit to experimental data for wind speed range, $0 < U\ (m/sec) < 160$.

The hot-wire anemometers were calibrated using a DISA calibration rig, 55 D42. The turbulence intensity in the calibration flow was given to be less than 1%.

The output voltage from the hot-wires was monitored on the DC voltmeter, DISA 55D30. The dynamic pressure, and hence the flow speed, was indicated by an inclined manometer, supplied by DISA.

Fig. ^a shows a calibration curve for a particular wire. The excellent fit of the second order equation compared with the first order can be seen.

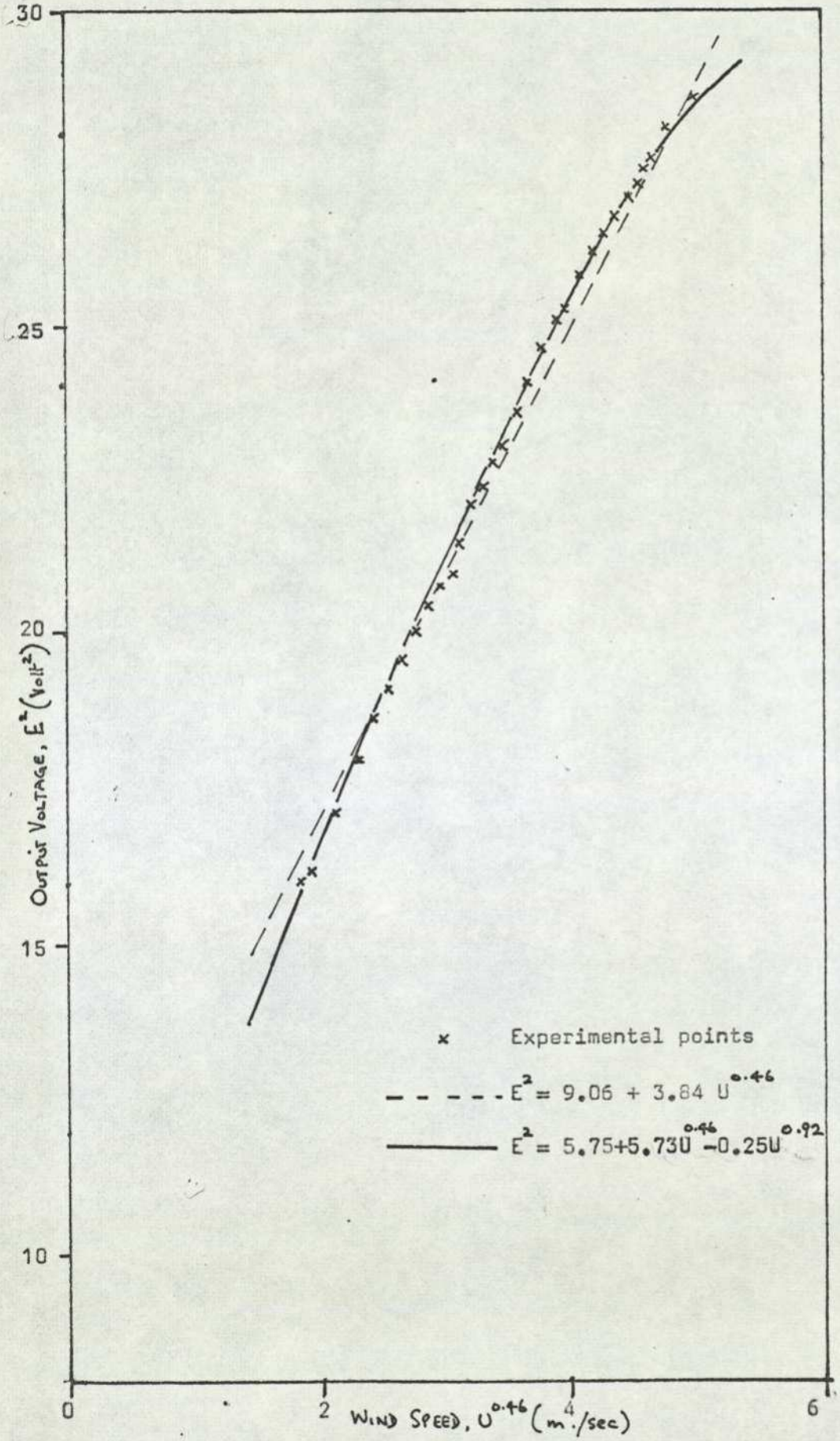

Calibration curve for a hot-wire anemometer

FIGURE a

APPENDIX 3.A: ANALOGUE TO DIGITAL CONVERSION PROGRAM — ADCN.

Note: The 'assembler' programme of ADCN written by P Saward has been 'microfiched' and is contained in a wallet at the back.

Flow Diagram for ADCN Computer Program

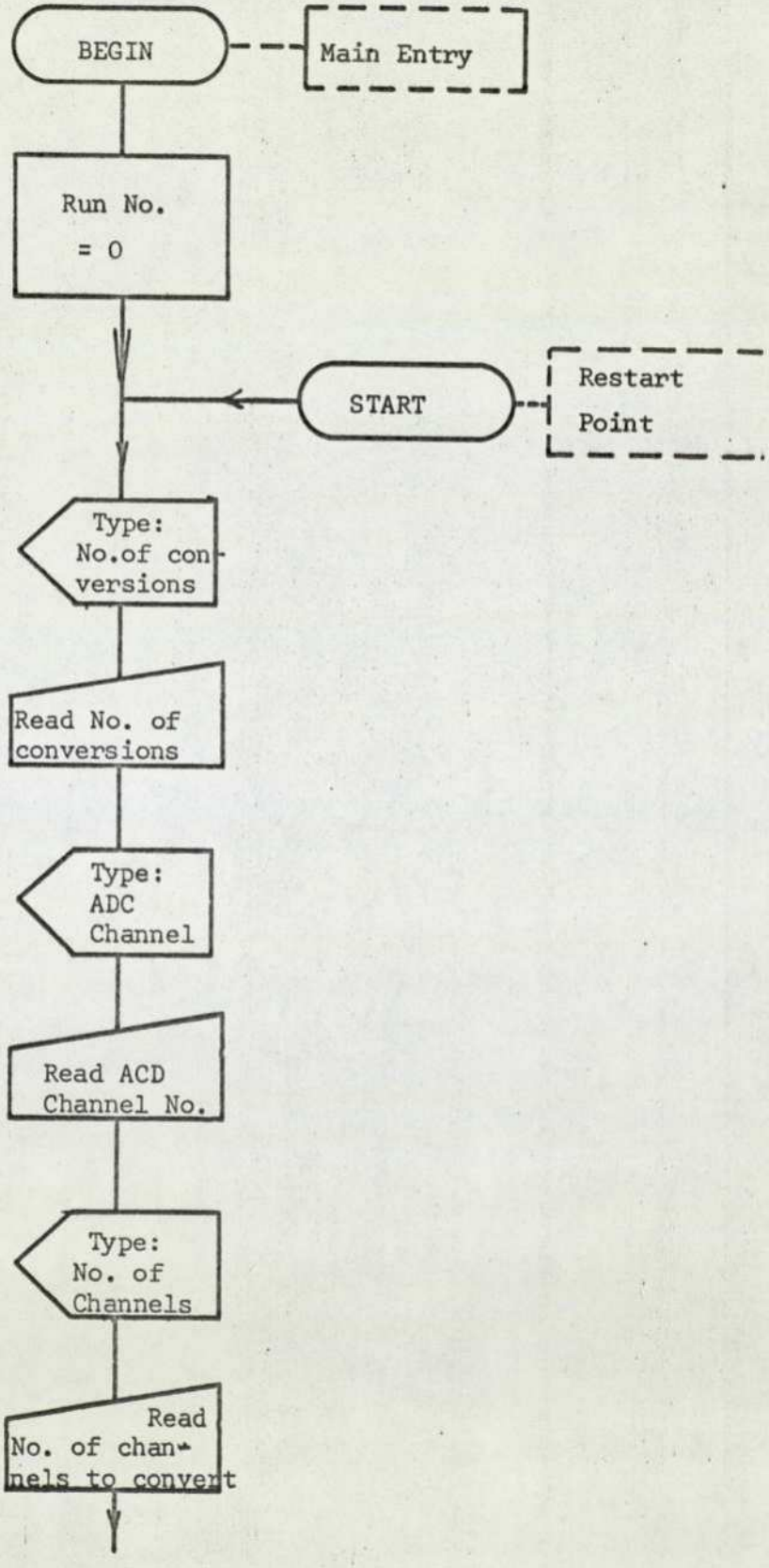

1

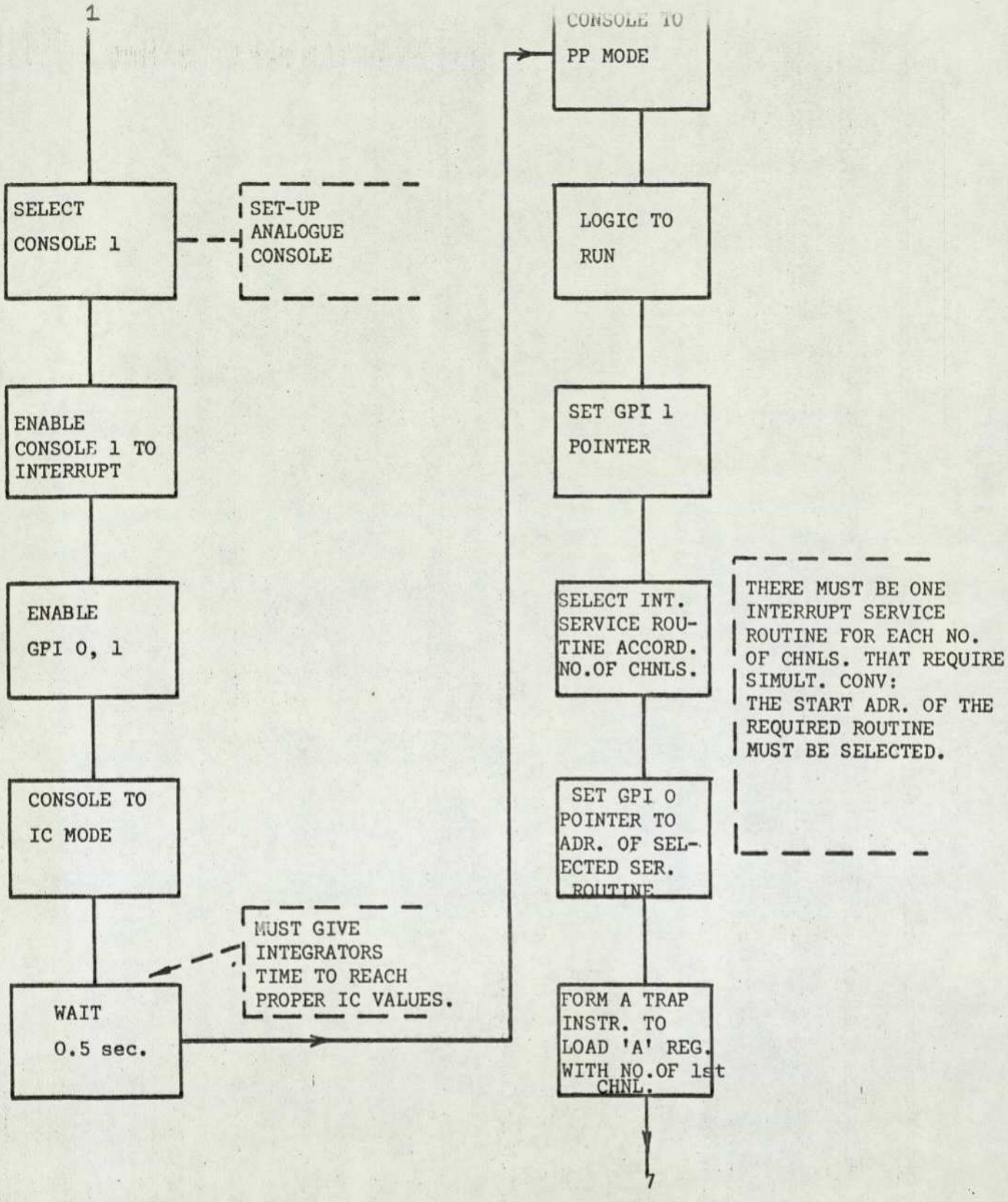
1
SELECT CONSOLE 1
SET-UP ANALOGUE CONSOLE
ENABLE CONSOLE 1 TO INTERRUPT
ENABLE GPI 0, 1
CONSOLE TO IC MODE
WAIT 0.5 sec.
MUST GIVE INTEGRATORS TIME TO REACH PROPER IC VALUES.
CONSOLE TO PP MODE
LOGIC TO RUN
SET GPI 1 POINTER
SELECT INT. SERVICE ROUTINE ACCORD. NO.OF CHNLS.
THERE MUST BE ONE INTERRUPT SERVICE ROUTINE FOR EACH NO. OF CHNLS. THAT REQUIRE SIMULT. CONV: THE START ADR. OF THE REQUIRED ROUTINE MUST BE SELECTED.
SET GPI 0 POINTER TO ADR. OF SELECTED SER. ROUTINE
FORM A TRAP INSTR. TO LOAD 'A' REG. WITH NO.OF 1st CHNL.
7

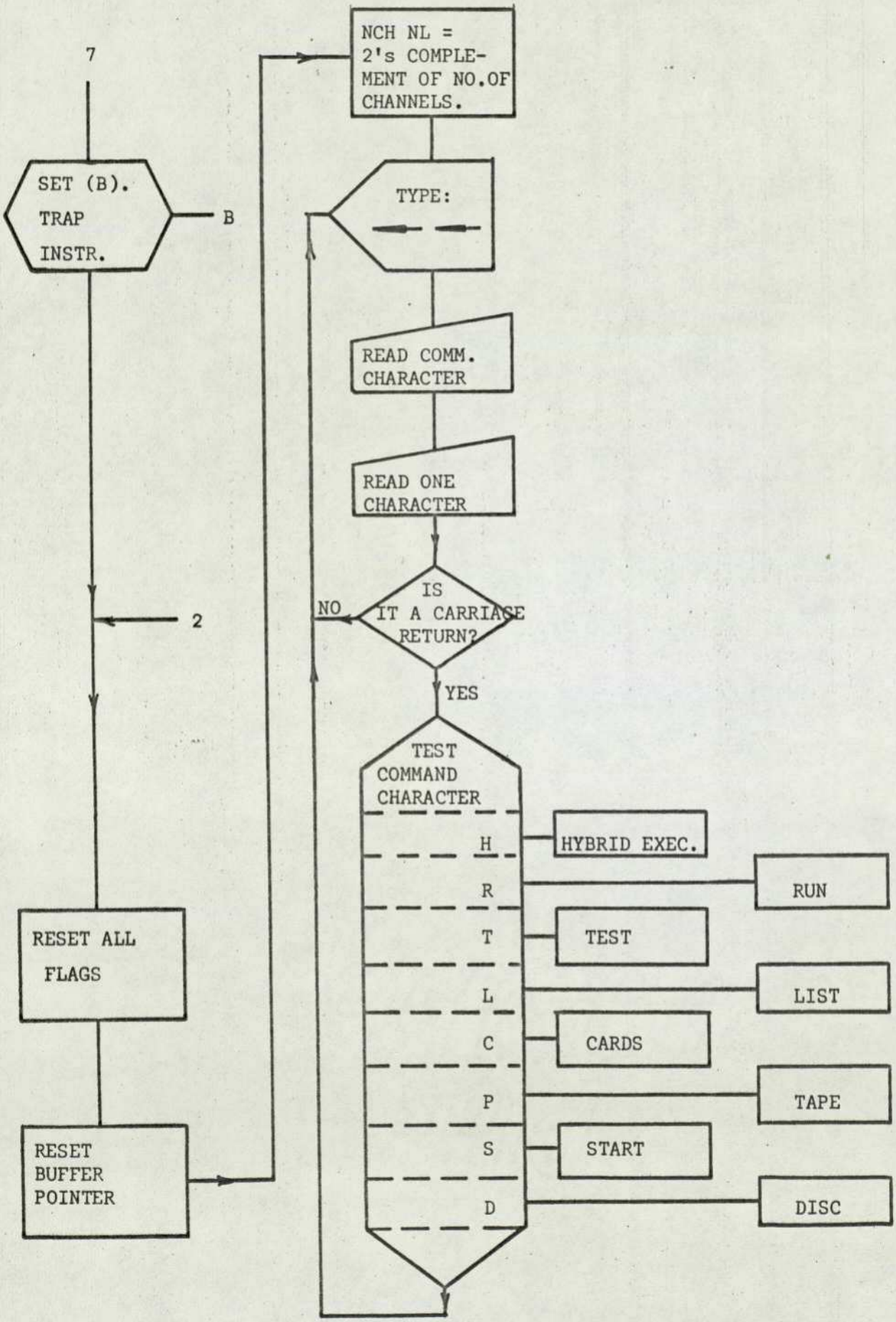
7
NCH NL =
2's COMPLE-
MENT OF NO.OF
CHANNELS.
SET (B).
TRAP
INSTR.
B
TYPE:
READ COMM.
CHARACTER
READ ONE
CHARACTER
2
NO
IS
IT A CARRIASE
RETURN?
YES
TEST
COMMAND
CHARACTER
H
HYBRID EXEC.
R
RUN
T
TEST
L
LIST
C
CARDS
P
TAPE
S
START
D
DISC
RESET ALL
FLAGS
RESET
BUFFER
POINTER

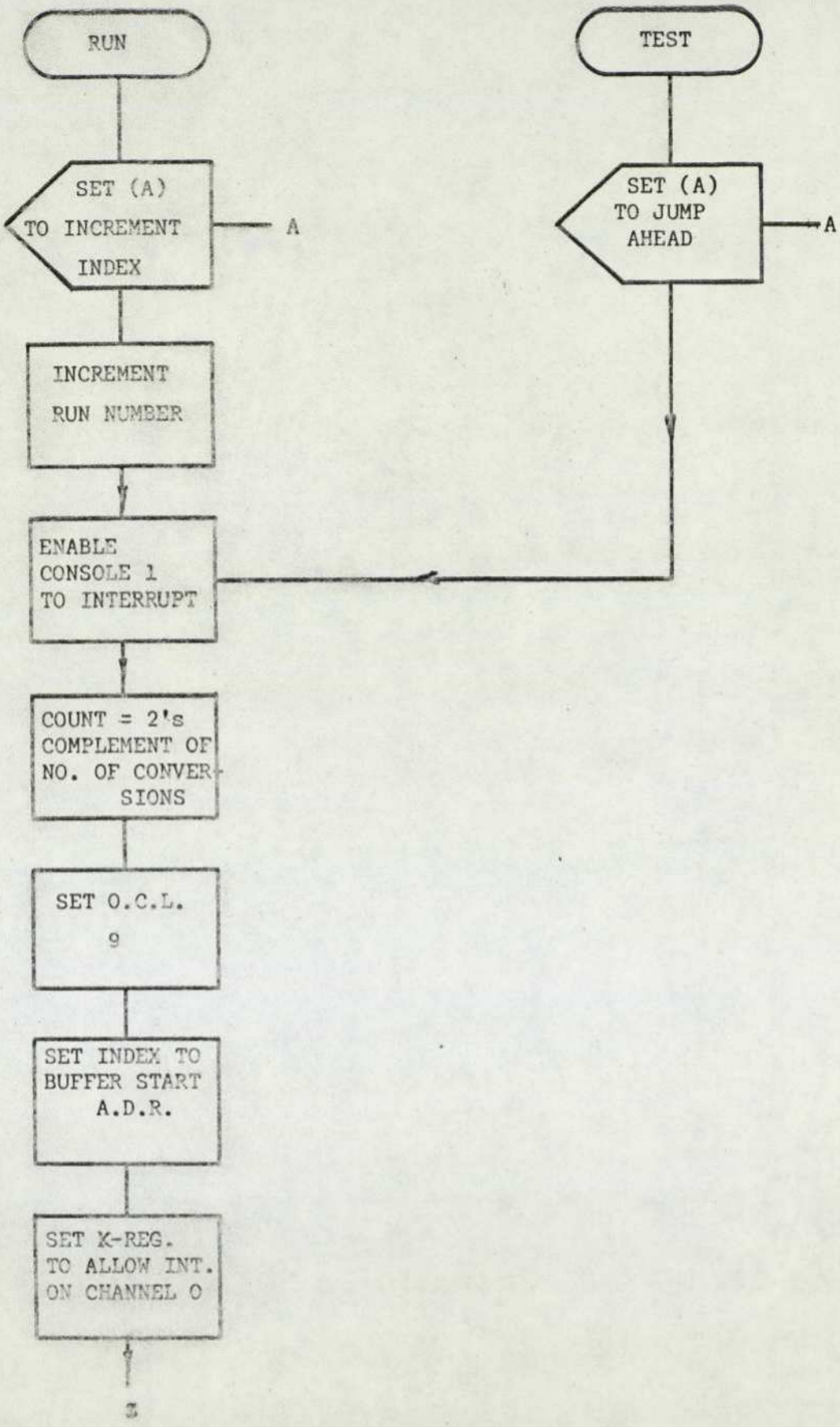
RUN
TEST
SET (A) TO INCREMENT INDEX
A
SET (A) TO JUMP AHEAD
A
INCREMENT RUN NUMBER
ENABLE CONSOLE 1 TO INTERRUPT
COUNT = 2's COMPLEMENT OF NO. OF CONVERSIONS
SET O.C.L. 9
SET INDEX TO BUFFER START A.D.R.
SET X-REG. TO ALLOW INT. ON CHANNEL 0
3

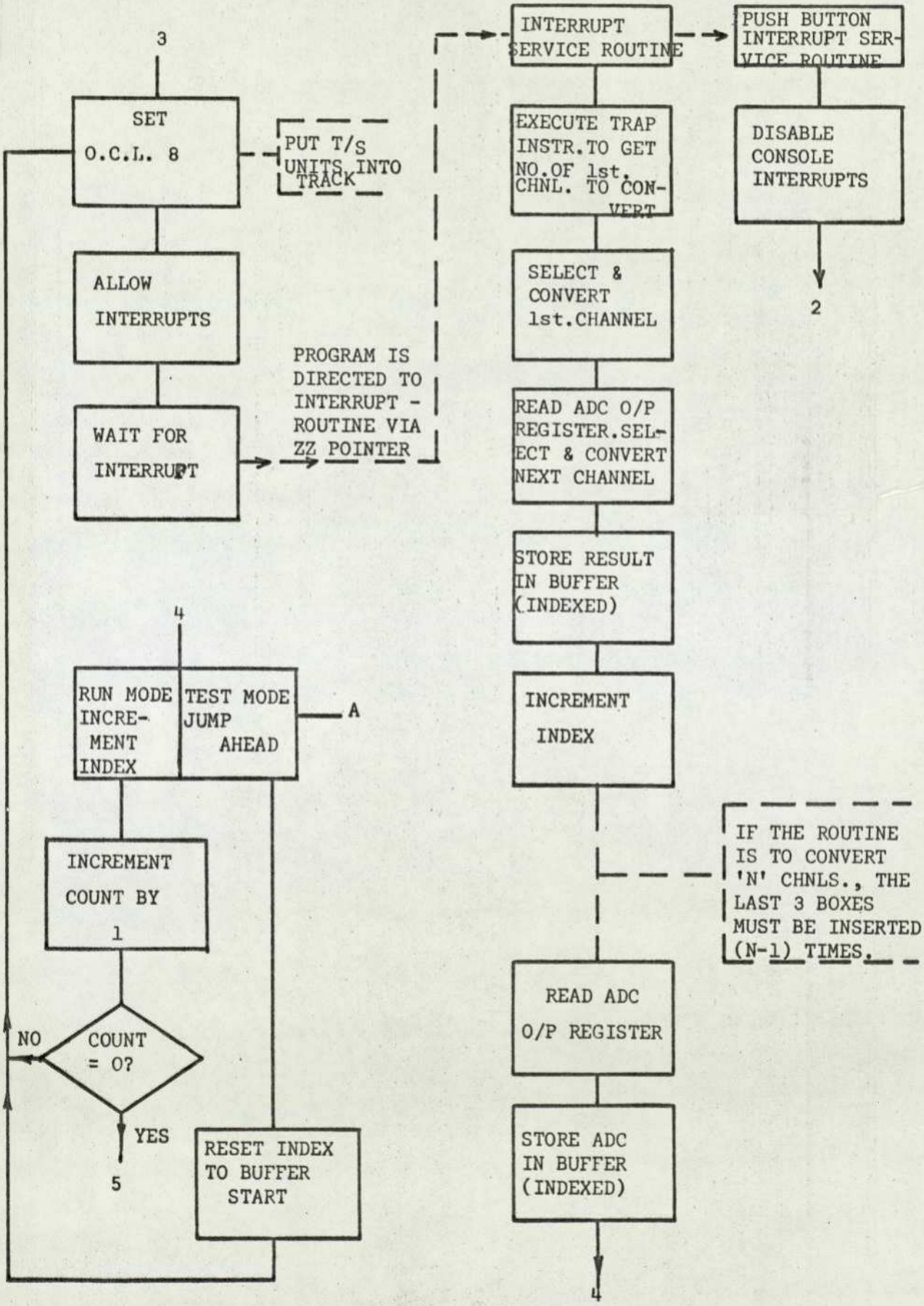
3
SET O.C.L. 8
PUT T/S UNITS INTO TRACK
ALLOW INTERRUPTS
WAIT FOR INTERRUPT
PROGRAM IS DIRECTED TO INTERRUPT - ROUTINE VIA ZZ POINTER
INTERRUPT SERVICE ROUTINE
PUSH BUTTON INTERRUPT SERVICE ROUTINE
EXECUTE TRAP INSTR. TO GET NO. OF 1st. CHNL. TO CONVERT
DISABLE CONSOLE INTERRUPTS
2
SELECT & CONVERT 1st. CHANNEL
READ ADC O/P REGISTER. SELECT & CONVERT NEXT CHANNEL
STORE RESULT IN BUFFER (INDEXED)
INCREMENT INDEX
IF THE ROUTINE IS TO CONVERT 'N' CHNLS., THE LAST 3 BOXES MUST BE INSERTED (N-1) TIMES.
READ ADC O/P REGISTER
STORE ADC IN BUFFER (INDEXED)
4
4
RUN MODE INCREMENT INDEX
TEST MODE JUMP AHEAD
A
INCREMENT COUNT BY 1
NO
COUNT = 0?
YES
5
RESET INDEX TO BUFFER START

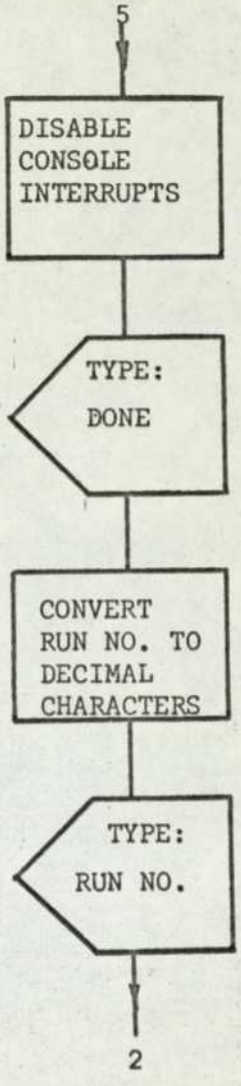
5
DISABLE CONSOLE INTERRUPTS
TYPE: DONE
CONVERT RUN NO. TO DECIMAL CHARACTERS
TYPE: RUN NO.
2

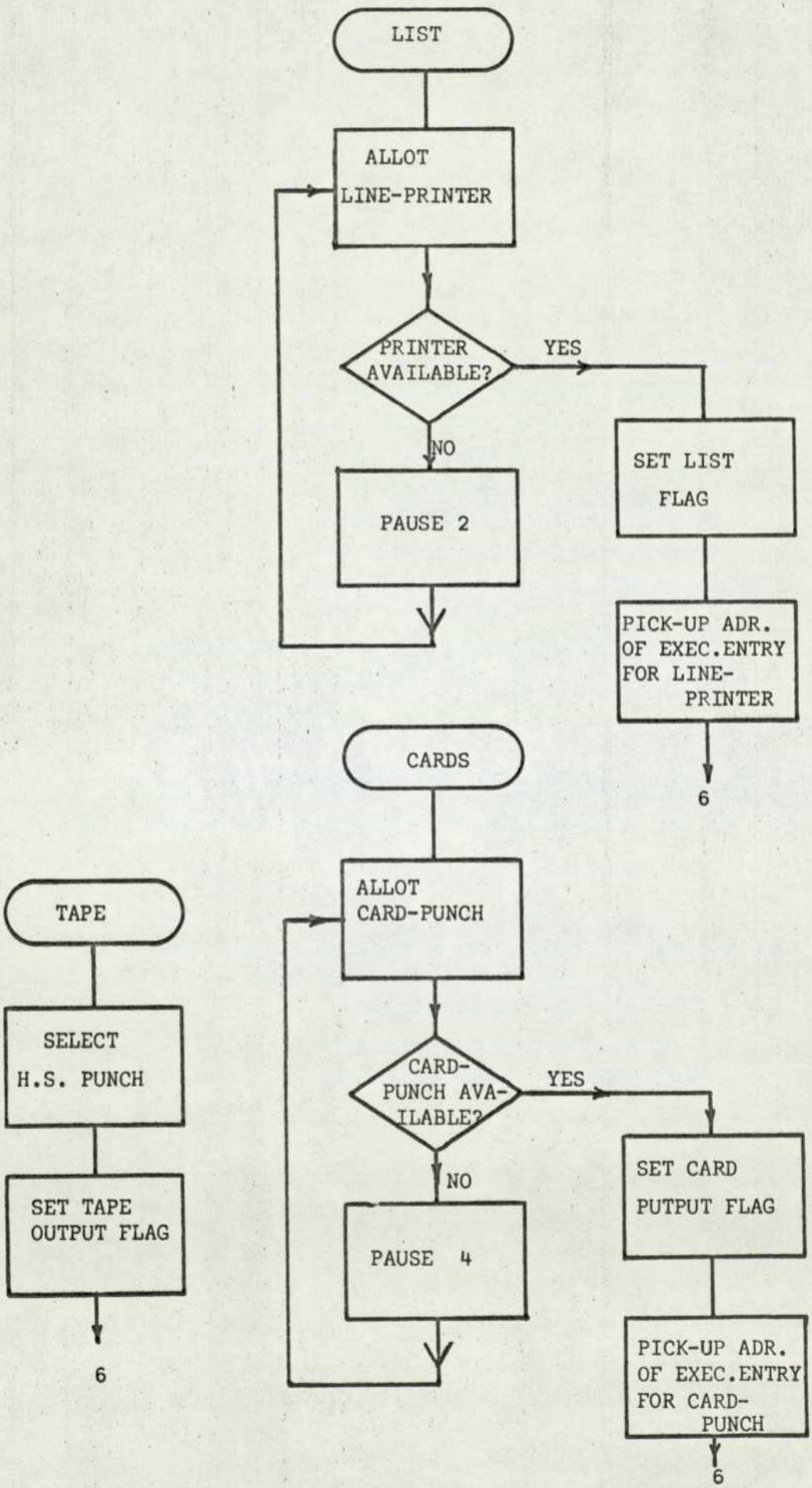
LIST
ALLOT LINE-PRINTER
PRINTER AVAILABLE?
YES
NO
PAUSE 2
SET LIST FLAG
PICK-UP ADR. OF EXEC.ENTRY FOR LINE-PRINTER
6
CARDS
ALLOT CARD-PUNCH
CARD-PUNCH AVAILABLE?
YES
NO
PAUSE 4
SET CARD PUTPUT FLAG
PICK-UP ADR. OF EXEC.ENTRY FOR CARD-PUNCH
6
TAPE
SELECT H.S. PUNCH
SET TAPE OUTPUT FLAG
6

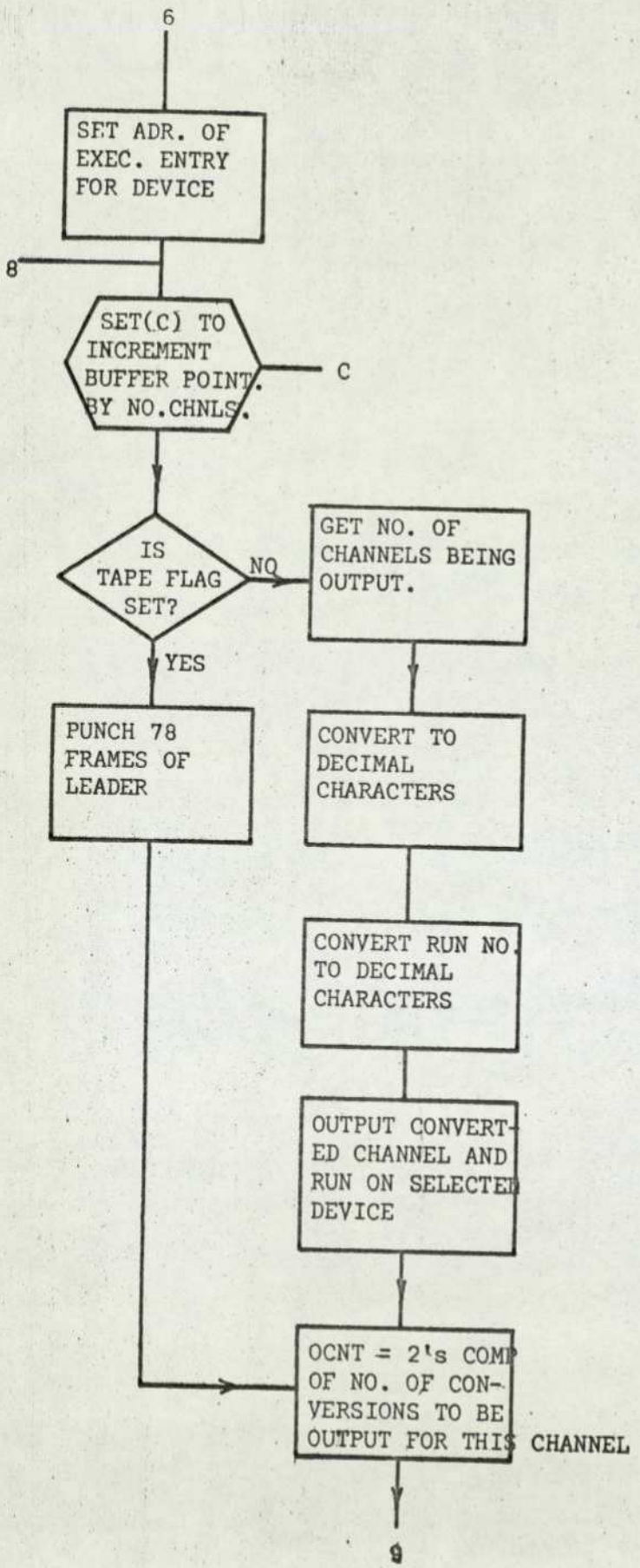
6
SET ADR. OF EXEC. ENTRY FOR DEVICE
8
SET(C) TO INCREMENT BUFFER POINT. BY NO.CHNLS.
C
IS TAPE FLAG SET?
NO
YES
GET NO. OF CHANNELS BEING OUTPUT.
PUNCH 78 FRAMES OF LEADER
CONVERT TO DECIMAL CHARACTERS
CONVERT RUN NO. TO DECIMAL CHARACTERS
OUTPUT CONVERTED CHANNEL AND RUN ON SELECTED DEVICE
OCNT = 2's COMP OF NO. OF CONVERSIONS TO BE OUTPUT FOR THIS CHANNEL
9

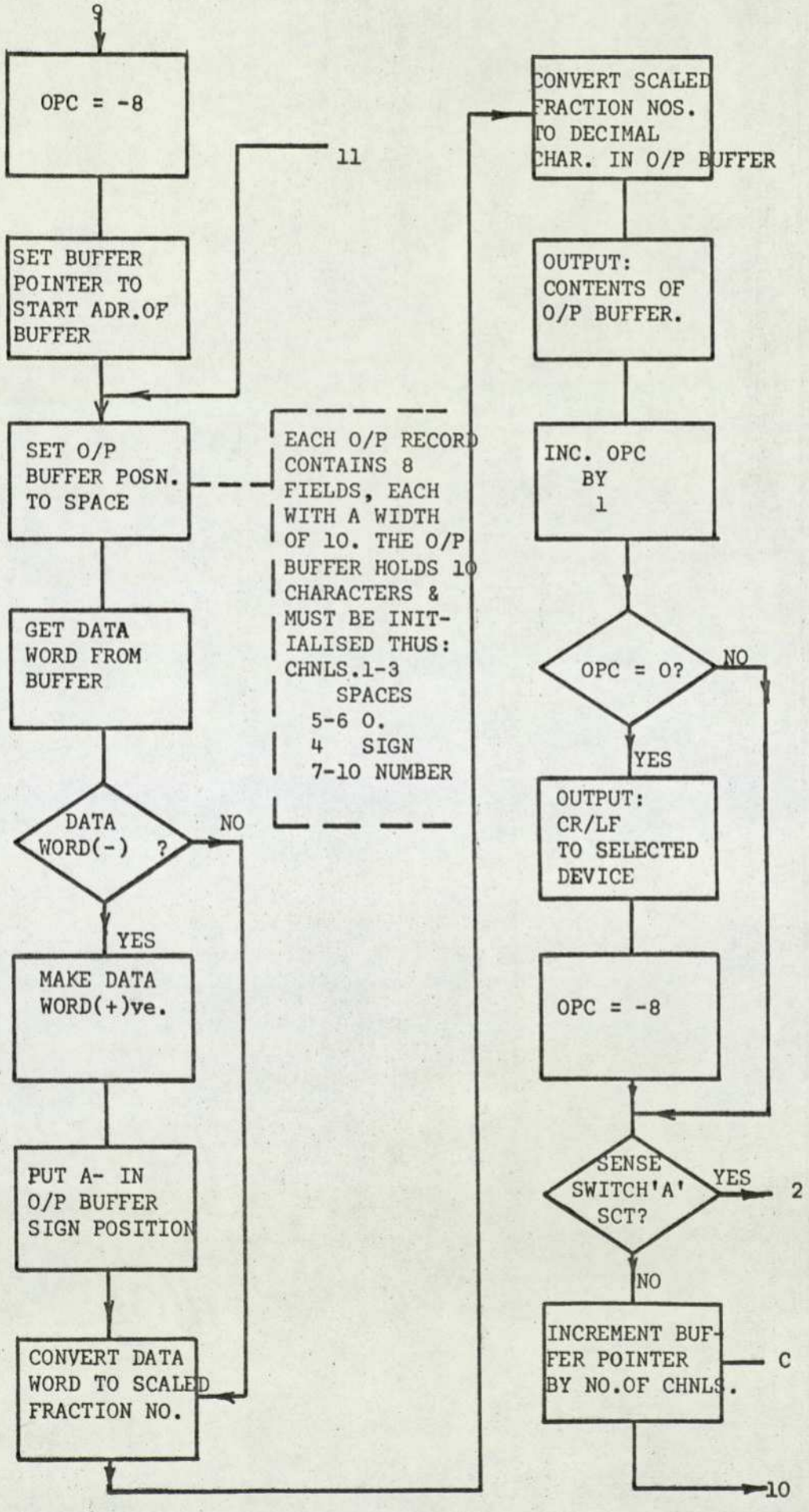
9
OPC = -8
11
SET BUFFER POINTER TO START ADR.OF BUFFER
SET O/P BUFFER POSN. TO SPACE
EACH O/P RECORD CONTAINS 8 FIELDS, EACH WITH A WIDTH OF 10. THE O/P BUFFER HOLDS 10 CHARACTERS & MUST BE INIT-IALISED THUS:
CHNLS.1-3 SPACES
5-6 0.
4 SIGN
7-10 NUMBER
GET DATA WORD FROM BUFFER
DATA WORD(-) ?
NO
YES
MAKE DATA WORD(+)ve.
PUT A- IN O/P BUFFER SIGN POSITION
CONVERT DATA WORD TO SCALED FRACTION NO.
CONVERT SCALED FRACTION NOS. TO DECIMAL CHAR. IN O/P BUFFER
OUTPUT: CONTENTS OF O/P BUFFER.
INC. OPC BY 1
OPC = 0?
NO
YES
OUTPUT: CR/LF TO SELECTED DEVICE
OPC = -8
SENSE SWITCH'A' SET?
YES
2
NO
INCREMENT BUF-FER POINTER BY NO.OF CHNLS.
C
10

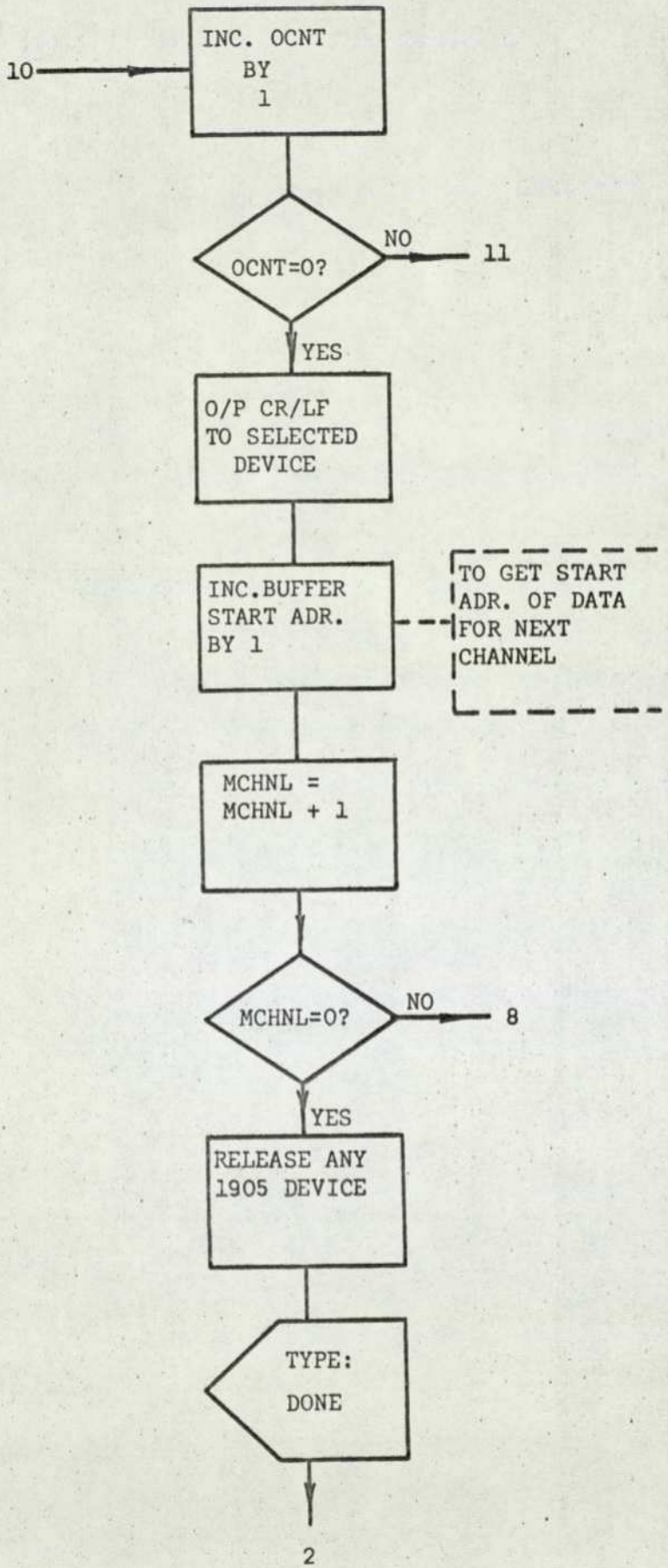
10
INC. OCNT BY 1
OCNT=0?
NO
11
YES
O/P CR/LF TO SELECTED DEVICE
INC.BUFFER START ADR. BY 1
TO GET START ADR. OF DATA FOR NEXT CHANNEL
MCHNL = MCHNL + 1
MCHNL=0?
NO
8
YES
RELEASE ANY 1905 DEVICE
TYPE:
DONE
2

APPENDIX 3.B.

SUMMARY OF PROCEDURE FOR ANALOGUE TO DIGITAL CONVERSION OF SIGNALS

1. Processing of Signals prior to Conversion

A. Decide on the total number, N_T, of digitised data required per channel. The upper limit of N_T is set by the buffer capacity of the EAI 680 and by the available record length.

Assume that for minimising the digital statistical errors (Section III.3.ii.e), this output has to be divided into q groups with N data points per group. Thus

$$N_T = N \cdot q$$

B. Establish a sampling rate, f_s, according to Eqn 3.4.

If the resultant bandwidth

$$\delta n = f_s / N$$

is not sufficiently low/high for subsequent analysis, alter the playback ratio, r (= playback/record speed $\gtrless 1$), of the tape recorder so that an apparent bandwidth

$$\delta n' = r \cdot \delta n$$

is obtained.

The true bandwidth of analysis of the signal is then,

$$\delta n = \frac{1}{r} \cdot \frac{f_s}{N}$$

C. Filter the signals using a low-pass filter according to Eqn 3.6. If the playback ratio, $r \neq 1$, alter the filter settings according to Eqn 3.9. If the signal requires it, use a high-pass filter (Section II.2.ii.a).

D. Amplify the signals so that their maximum peak-to-peak voltage value occupies as much of the quantification range ($\pm$ 10v) of the EAI 680 as possible.

E. Feed the resulting signals into the track/store amplifiers of the EAI 680 after procedure (2.D.viii) given below.

2. Setting up the Hybrid System

A. Display Oscilloscope

(i) Switch on.

(ii) Press selector I.

(iii) Press input 0.

Note: Steps (ii) and (iii) should be repeated for every additional signal which is needed to be displayed on the screen. That is to say, press selector II, input 1; selector III, input 2; etc

(iv) Set sweep time.

(v) Press parallax buttons (actually a vertical shift) until the signal traces appear on the screen.

B. Monitor Oscilloscope

(i) Switch on by turning scale illumination knob clockwise.

(ii) Press pushbutton D.

(iii) Press COMPTR. SYC.

(iv) Set time base according to the sampling frequency (1 m sec for f_s = 500 Hz).

(v) COUPLING setting - A.C. fast.

(vi) SOURCE setting - INT.

(vii) MODE setting - NORM.

(viii) Vertical amplitude: Trace 1 - Displays tracking/store
Set to A.C.
Range - 5v. div^{-1}
Mode - NORM

Trace 2 - Displays timing pulses
Set to A.C.
Range - 5v. div^{-1}
Mode - NORM

C. EAI 680 Analogue Computer

(i) Patch PANEL according to the logic patching shown in Fig. 3.1.

(ii) Engage PANEL.

(iii) MODE CONTROL setting - R.

DIGITAL setting - 10^6.

(iv) Set BCD counters to the value $\frac{10^4}{f_s} - 1$ to obtain sampling frequency.

(v) Depress sense switch '0' for BCD counter to operate when the 640 has subsequent control over it.

(vi) Set potentiometers (P10 and P11) for ramp test.

Press SP.

Press P10 - GO - 9999 - GO.

Press P11 - GO - 1000 - GO.

(vii) Press P/C.

(viii) Set integrating timer at 010 - 200 - 000 to control integrating time for ramp test.

(ix) Set TIME SCALE to N - SEC.

(x) Press A10 - GO.

(xi) When PP pushbutton is pressed, the continuous generation of a ramp voltage from -0.9999 to +0.9999 can be observed on the 680 console display.

(xii) End ramp test by activating PC switch on 680 console.

(xiii) Set time scale to N - MS for subsequent tracing of signals on display oscilloscope.

D. EAI 640 Digital Computer

(i) Call the multichannel A/D conversion routine, ADCN (Appendix 3.1). This can be done by forced loading into the hybrid loader the program written in paper

tape. The program has to be recompiled for every new entry into the system but this can be avoided by having the program on the permanent file of the 1905 in a compiled form. For both methods the relevant instruction manuals should be read.

(ii) To run program, type '1000G' on the teletype of the 640. This is the starting location of the loaded routine.

(iii) Output on the teletype will then be 'NØ ØF CØNVERSIØNS'. The required number of digitisations per channel, 'N_T', should then be entered on the teletype.

(iv) Output on the teletype will be 'ADC CHANNEL'. The number of the first ADC channel to be scanned, P , should then be entered on the teletype. For the present, the three channels to be used are $P = 3$, 4 , 5.

(v) Output on teletype will be 'NØ ØF CHNLS'. The number of channels which require sampling, starting with 'P', should then be entered on the teletype.

(vi) The teletype will reply with a ← ← , and will await a directive.

(vii) The sampling can be tested as follows:

(a) Patch the outputs from the RAMP GENERATOR into the required ADC channels.

(b) Type 'T'.

(c) The track/store trace and the sampling trace will appear on the monitor oscilloscope. Adjust monostables 00 and 10 on the 680 for the smallest possible interval which gives a clear display on the screen. This display will indicate whether the sampling frequency is fast enough (Section III.2.ii.b).

(d) The display oscilloscope will show the sampled test ramp. Adjustment of the scope setting may be necessary at this stage to obtain a good display.

(e) To end TEST MODE, depress sense switch, 1, on the 680 console. Then cancel switch, 1, by depressing the sense switch to the right of it.

(viii) Remove the RAMP GENERATOR inputs from the Track/Store amplifiers and replace them with the signals requiring conversion.

(ix) The following directives can now be typed as one-character directives followed by a carriage return. (If no carriage return is typed a request for a new directive is issued).

R - (RUN - puts program into run mode: does specified number of A/D conversions and stores results).

S - (START - goes back again to start of prpgram if parameters such as N_T, P or number of channels have to be altered).

L - (LIST - lists results on line-printer).

C - (CARDS - punches results on 1905 card punch).

P - (PAPER TAPE - punches results on paper tape on 680 high-speed punch).

D - (DISC - Produces output on 1905 disc store)
When D is typed, the teletype gives a console message, AD, which requests a two-digit (octal) file number. This number must then be typed.

(x) When the last process has been completed the console produces the output 'DONE'.

The following points should be noted:

1. If output is on to disc, care must be taken that a disc is loaded in a 1905 peripheral unit and is available to the user.

2. Signals will appear on the monitor scope only when the program is in the RUN mode. If the signals need to be looked at without any conversion taking place, then typing 'T' will put the program into the TEST mode and the signals will be displayed. Care must be taken that, before any further directive is typed on the teletype of the 640, the program is taken out of the test mode (procedure 2.D.(vii) e).

APPENDIX 4.A. DESIGN OF COWDREY'S VELOCITY-PROFILE SIMULATION GRIDS

The basic method is as proposed by Cowdrey

modification in the analysis to take into account an extra parameter, ie the depth of the boundary-layer required. This consideration is important because of the extent of immersion of the model in the boundary-layer

The method consists of placing rods of diameter, d, across the wind-tunnel mouth at various heights, y, above the tunnel floor.

Cowdrey showed that

$$P - p = \tfrac{1}{2} \rho_a (u^2 - U^2) + \tfrac{1}{2} \rho_a u^2 K = \text{constant}$$

ie $$\frac{P - p}{\frac{1}{2} \rho_a U^2} = \left(\frac{u}{U}\right) (1 + K) - 1 = K_1$$

or $$\left(\frac{u}{U}\right)^2 = \frac{1 + K_1}{1 + K}$$

where P = static pressure upstream of the region of influence of the grid.

p = static pressure downstream of the grid.

U = velocity of air upstream of the region of influence of the grid.

u = local velocity in the profile at height z.

K_1 = overall pressure drop

K = local pressure drop.

If the height of the wind-tunnel is δ and the height of the boundary-layer is δ_1 then for a given power-law profile

$$u / z^{\alpha} = \text{constant}$$

so that $$u / U = (z / \delta_1)^{1/n}$$

where $n=1/\alpha$.

By the continuity equation,

$$U.\delta = \int_{z=0}^{\delta_1} u(z).dz + U.(\delta - \delta_1)$$

$$\text{i.e.} \quad \frac{u}{U} = \frac{n+1}{n}\left(\frac{z}{\delta}\right)^{1/n}$$

Cowdrey also showed that, $K = \dfrac{d/l}{(1 - d/l)^2}$

$$\therefore \frac{z}{\delta} = \frac{n}{n+1}\left[\frac{1+K_1}{1 + \dfrac{d/l}{(1-d/l)^2}}\right]^{n/2}$$

According to Cowdrey, separation can occur at the walls of the wind-tunnel if the rods are close together. If they are far apart, however, the wakes of the individual rods will persist downstream to give regions of low velocity in the wind profile. l is the spacing of the axes of the rods.

He also indicated that the larger values of K_1 (within the limits of practical consideration) gave a higher intensity of turbulence.

Computation of the heights of the rods:

When suitable values of 'n' and 'K_1' have been selected, the heights of the axes of the rods can be determined by a step-by-step procedure involving an iteration scheme (Programme GRID, Appendix B).

An initial value for $z(= 10^{-30})$ to approximate zero is given and with an accuracy determining factor, ϵ $(= 10^{-16})$ in the iteration process, the scheme outlined next is followed to determine the heights of the axes of the rods above the wind-tunnel floor.

Let z — Height above the 'ground level'

l — Spacing of the axes of the rods

h — Height of the rod centre line above 'ground level'

ϵ — Accuracy determining factor in the iteration process.

Suffices, T — temporary value.

$'$ — number of daches indicates the point in the iteration loop.

ROD

(1) $Z_T(1) \xrightarrow{=10^{-30}} l(1) \longrightarrow l(1)/2.0 \longrightarrow z(1) = z(1) \longrightarrow h(1) = z(1) + l(1)/2.0$

(2) $Z_T'(2) \longrightarrow l'(2) \longrightarrow l'(2)/2.0 \longrightarrow z'(2) = Z_T'(2) \longrightarrow \cdots$

If $z'(2) - Z_T'(2) > \epsilon$, $Z_T''(2) = z'(2) \longrightarrow l''(2) \longrightarrow$ continue

If $z'(2) - Z_T'(2) \leq \epsilon$, $h(2) = z'(2) + \frac{l'(2)}{2.0}$

(i) $Z_T'(i) \longrightarrow l'(i) \longrightarrow \frac{l'(i)}{2.0} \longrightarrow z'(i) = Z_T'(i)$

If $z'(i) - Z_T'(i) > \epsilon$, $Z_T''(i) = z'(i) \longrightarrow l''(i) \longrightarrow$ continue

If $z'(i) - Z_T'(i) \leq \epsilon$, $h(i) = z'(i) + \frac{l'(i)}{2.0}$

where $Z_T'(i) = h(i-1) + \frac{l(i-1)}{2}$ for $i = 2, 3, \ldots, n$.

APPENDIX 5.A.

CALCULATIONS FOR MODELLING INERTIA VALUES

The mass-inertia equation for a thin-walled cylinder of length , h, outside cross-sectional dimension, D, and wall thickness, t, is of the following form:

For a square-section cylinder $$I = \rho_{al}\, 4t(D-t)h\left[\frac{h^2}{3} + \frac{D^2+(D-2t)^2}{12}\right]$$

For a circular-section cylinder, $$I = \rho_{al}\, \pi.\, t(D-t).h\left[\frac{h^2}{3} + \frac{D^2+(D-2t)^2}{16}\right]$$

where the density, ρ_{al}, of aluminium is 2.768×10^3 kg m^{-3}

To calculate I for the square-section cylinder, a program INER (Appendix B) was written. With fixed parameters, h, and ρ_{al}, starting values of D' and t' were used. By incrementing t', corresponding D' and I' values were calculated. When $I' = I$, the correct combination of D and t was obtained.

APPENDIX 5.B.

DESIGN CALCULATIONS FOR TORSION BARS

Consider a torsion bar of length, l, breadth, b, and thickness, $t (< b)$, constructed as shown below.

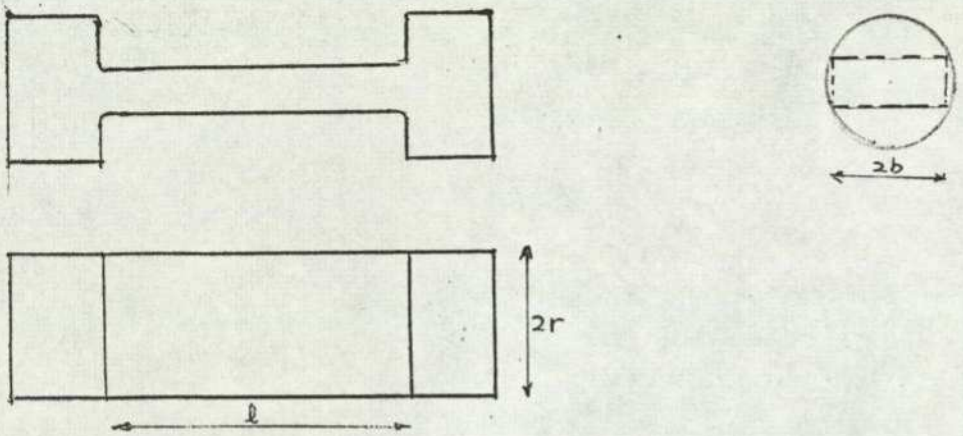

It is assumed that the effective portion of the torsion-bar is the central flat portion. Let the torsion bar be under a torque, T, applied at the two ends and along its longitudinal axis.

If θ is the resulting angle of twist, then it can be shown [86] that,

$$\theta = \frac{Tl}{GJ}$$

where J and G are the torsional stiffness and modulus of rigidity of the bar.

For a rectangular, prismatic bar, Gaylord and Gaylord [87] give the formula,

$$J = \frac{bt^3}{3}\left[1 - 0.63\left(\frac{t}{b}\right) + 0.052\left(\frac{t}{b}\right)^2\right]$$

To obtain a natural frequency of oscillation for the model, the stiffness k of Eqn 5.7.

ie $$n = \frac{1}{2\pi}\left(\frac{k}{I}\right)^{1/2}$$

can be replaced by, $k = T/\theta = G.J/l$

The value of the required natural frequency, n_o, of the model is taken to be known. Neglecting the inertia of the damping system, the inertia, I, of the model can be used as a first approximation. k and thus J can be calculated.

It can also be shown that,

$$b^2 = 4\left(r^2 - \frac{t^2}{4}\right)$$

Given a constant r and a varying b and using PROGRAMME TORS (Appendix B), table of corresponding values for b and J can be obtained giving the appropriate values.

APPENDIX 5.C. STRAIN-GAUGE

Consider the double pair of torque shear-gauges bonded to the surface on the flat portions of the torsion bars.

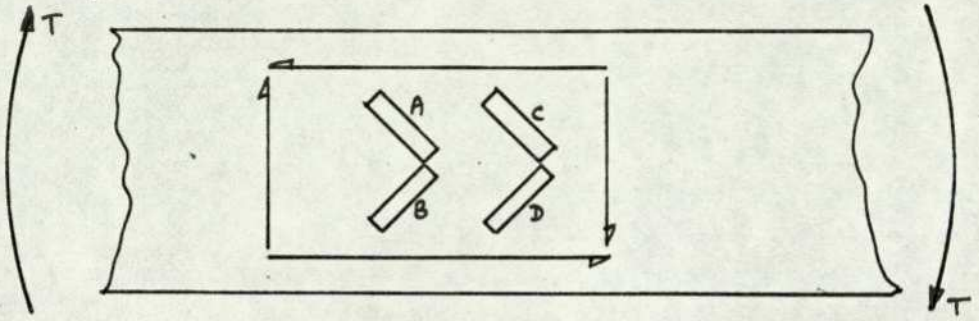

Gauges A and C will suffer tensile strain, $\epsilon = \frac{\gamma}{2} + \epsilon_T$

Gauges B and C " " " " , $\epsilon = -\frac{\gamma}{2} + \epsilon_T$

where γ = shear strain and ϵ_T = thermal strain

Bridge wiring:

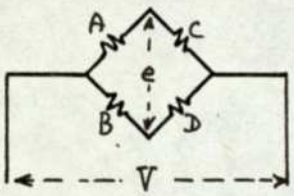

V = bridge voltage supply (usually, 5 volts)

e = bridge output signal (volts)

g = gauge factor of gauges (usually 2.0)

$$e = \frac{V.g}{4}\left[\epsilon_A - \epsilon_D + \epsilon_C - \epsilon_B\right]$$

$$e = \frac{V.g}{4}\left[\frac{\gamma}{2} - \left(-\frac{\gamma}{2}\right) + \frac{\gamma}{2} - \left(-\frac{\gamma}{2}\right)\right]$$

$$= \frac{V.g}{2} \cdot \gamma$$

With the above arrangement of the shear-gauges, temperature compensation is obtained. In addition, a signal level, four times higher than that for a single gauge, or twice that for a pair of gauges is obtained.

APPENDIX 5.D. ELECTROMAGNETIC DAMPING

The equation of motion for a single degree-of-freedom system freely vibrating is

$$m\ddot{x} + c\dot{x} + kx = 0$$

or $$\ddot{x} + 2\xi\omega\dot{x} + \omega^2 x = 0$$

where $\xi = \frac{c}{2\sqrt{mk}} = \frac{c}{c_c} = \frac{c\omega}{2k} = \frac{c}{2m\omega}$ where c_c is the 'critical' damping.

For a damped system, $n_d = n_0(1-\xi^2)^{1/2}$ where $n_0 = \omega/(2\pi)$

Damping that is strictly proportional to velocity is of comparatively rare occurrence. The type of damping that diverges least from proportionality to velocity is 'electromagnetic damping' [88].

The principle of electro-magnetic damping is based on the use of a coil capable of movement within a stationery and uniform magnetic field. A current is induced in the short-circuited conductor which is proportional to the velocity of the movement. Consequently, an electro-magnetic force, proportional to velocity is exerted on the conductor in a direction opposite to its movement.

Van Santen [88] has shown that, if a coil of volume, V, and specific resistivity, ϱ, moves in a magnetic field of strength, B, then the damping constant

$$c \propto B^2 V/\varrho$$

To ensure a high value of c, and hence ξ, the volume of the coil must be as great as possible and ϱ as low as possible with the number of turns of wire being of no consequence. The best thing to use, therefore, is a solid copper bush.

In the experiment, the damping coil consisted of a copper plate (Section V.3.), free to move in a plane between two pairs of electro-magnet poles. The thickness of the copper plate was defined by the gap between the pole faces. The gaps had to be large enough to encompass the movement of the plate between them while being small enough to ensure a high enough value for the flux density, B . The dependence of B on gap separation is shown below.

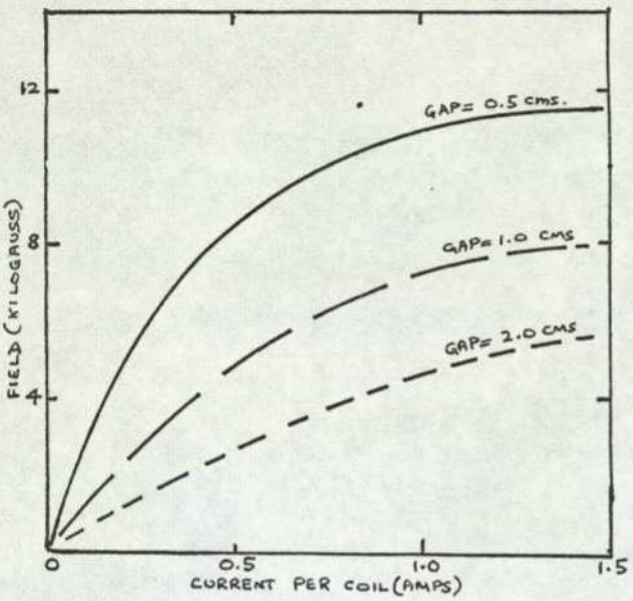

PERFORMANCE CURVES (MANUFACTURER'S SPECIFICATIONS)
FOR TYPE C , NEWPORT INSTRUMENTS 1.5" ELECTRO-MAGNETS

APPENDIX 6.A.

MEAN WIND CHARACTERISTICS FROM VELOCITY PROFILES

The power exponent α was obtained using Eqn 4.17 from which

$$\ln\left[\frac{\bar{U}(z)}{\bar{U}_{ref}}\right] = \alpha \cdot \ln\left[\frac{z}{\delta} \cdot \frac{\delta}{z_{ref}}\right] \qquad (1)$$

Therefore, plotting $\ln[\bar{u}(z)/\bar{U}_{ref}]$ vs $\ln[z/\delta]$ gives as its gradient the exponent, α.

Using the Prandtl equation (Eqn 4.1) and re-writing for completeness

$$\bar{U}(z) = \frac{u_*}{k} \ln\left(\frac{z+z_0}{z_0}\right)$$

then if $z >> z_0$ we have

$$\bar{U}(z) = \frac{u_*}{k} \ln\left(z/z_0\right) \qquad (2)$$

Eqn 2 can be written as

$$\frac{\bar{u}(z)}{\bar{U}_{ref}} = \frac{u_*}{k\,\bar{U}_{ref}}\left[\ln\left(\frac{z}{\delta}\right) - \ln\left(\frac{z_0}{\delta}\right)\right]$$

By plotting $\bar{U}(z/\bar{U}_{ref}$ vs $\ln(z/\delta)$, the friction velocity, u_*, and the roughness length, z_0, can be evaluated directly.

Then the surface drag coefficient

$$C_{D_0} = 2\left(\frac{u_*}{\bar{U}_{ref}}\right)^2$$

and the macro-viscosity

$$N = u_* \cdot z_0$$

are obtained.

APPENDIX 7.A. DETERMINING DAMPING PARAMETERS.

The equation of motion for a single-degree-of-freedom system vibrating freely is given in Appendix 5.D as

$$\ddot{x} + 2\xi\omega\dot{x} + \omega^2 x = 0 \qquad \text{--------(1)}$$

The logarithimic decrement, δ , is related to the critical damping factor, ξ by

$$\delta = \frac{2\pi\xi}{(1-\xi^2)^{1/2}}$$

$$\simeq 2\pi\xi \qquad \text{for } \xi < 0.2$$

The solution to Eqn 1 is [86] .

$$x = e^{-\xi\omega t}\left[x_0 \cdot \cos\left(\omega\sqrt{1-\xi^2}\,t\right) + \frac{\dot{x}_0 + \xi\omega x_0}{\omega\sqrt{1-\xi^2}} \cdot \sin\left(\omega\sqrt{1-\xi^2}\,t\right)\right] \qquad \text{----(2)}$$

The envelope of maximum amplitudes then has the form

$$x = x_0 \cdot e^{-\xi\omega t} \qquad \text{-----(3)}$$

This curve can therefore be used to express the rapidity of the decay of the damped oscillations.

The damping parameter, ξ , can be evaluated from its response in the three different domains using the following methods.

Method (1) - From Amplitude Trace (in still-air conditions)

The structure is given a sudden impulse (in this case, the model is tapped sharply) and the vibrations allowed to decay. A trace of the decaying amplitudes can be taken and the damping parameter estimated using any of the following techniques.

(a) Ratio of maximas

Let a peak of height x_1 occur at time t_1 on the trace. After p complete cycles, the time would be t_{p+1} and the height of this peak would be x_{p+1}.

Using Eqn 3 it can be shown that

$$\xi = \frac{1}{2\pi} \cdot \frac{1}{p} \cdot \ln\left(\frac{x_1}{x_{p+1}}\right)$$

(b) Relaxation Time

Another technique is to measure the time taken for the amplitude of the maximum amplitude envelope to decay to e^{-1} (=0.368) of its original value.

This time is called the 'relaxation time' or 'modulus of decay' and is given by

$$t_r = 1 \Big/ (\xi\omega)$$

such that $x_r = x_0 \cdot e^{-1}$

Hence $\xi = 1 \Big/ (2\pi n_0 . t_r)$

(c) Area Ratio

If the peaks of the trace are ill-defined, because of either harmonics or noise, it is very difficult to obtain a good estimate of the damping using the two above mentioned techniques. To solve this, a method proposed by Russell [89] was used.

Consider the diagram below :

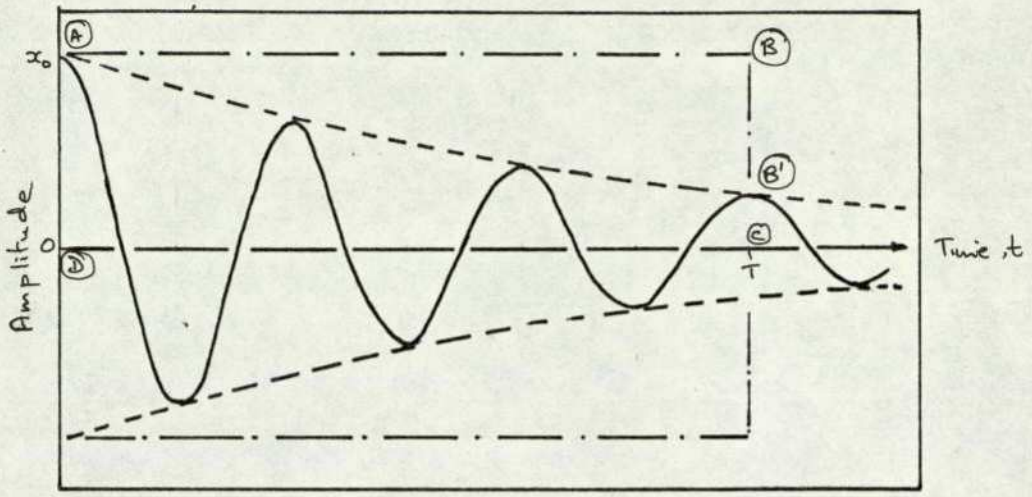

A curve AB is drawn by eye to envelope the peaks.

The area AB CD is measured with a planimeter.

If area AB CD = a'

and ABCD = a

then it can be shown that

$$\frac{a'}{a} = \frac{1 - e^{-\xi\omega t}}{\xi\omega}$$

Since $$a' = \int_0^T x(t)\, dt = \frac{x_0}{\xi\omega}\left\{1 - e^{-\xi\omega T}\right\}$$

From a table of a'/a vs $\xi\omega T$, the value of $\xi\omega T$ for a particular a'/a can be read off. As T and ω are known, ξ can be calculated.

Method (2) -From Auto-Correlation Plots

It has been shown [90, 91] that the auto-correlation function of the response of a single-degree-of-freedom system to band-limited white noise takes the form of an exponentially decaying periodic function, similar to Eqn 2.

Similarly, the curve representing the envelope of the maximum amplitudes in the auto-correlation plots has the form

$$R_x'(\tau) = \text{constant} \times \exp(-\xi\omega\tau)$$

from which damping parameter ξ can be evaluated using the methods (1) (a), (b) and (c), described above.

Method (3) — From auto-power spectral density plots

Damping ratio ξ can be deduced from the power spectral density plots using the so-called Q (Quality) - factor.

If a single-degree-of-freedom structure is excited by white noise, the displacement has a peak in the power spectrum at the resonant frequency, n_o.

The Q-factor indicates the sharpness of the resonance and is defined as

$$Q = \frac{n_o}{n_2 - n_1}$$

where n_2 and n_1 are the frequencies at which the power supplied

$P = \frac{1}{2}$ x maximum power

The frequency difference

$$\delta n_Q = n_2 - n_1$$

is often called the half-power point bandwidth.

It can be shown [88] that,

$$Q = \pi/\delta$$

or $$\xi = \frac{1}{2Q}$$

To estimate ξ correctly, it is necessary that the forcing wind must be turbulent and not smooth. This is because the turbulent wind can be approximated to a white-noise source.

For low-damped structures, the auto-correlation plot is best for estimating ξ while for highly damped structures, the power spectral density plot is better. This is because, with low damping, the response spectra is narrow band. Since ξ is estimated from the half-power band-

width, any variation in measuring a small bandwidth involves a proportionate error in ξ . However, this is no problem on the time-domain plot as data compressed on the frequency axis is expanded on the time axis.

APPENDIX A: EQUIPMENT USED

1. Bruel and Kjaer, Naerum, Denmark:

   Type 1612 band-pass (1/3 and 1/1 octave) filter set.

   Type 2603 Microphone amplifier

2. Bryans Ltd, Mitcham, Surrey, England:

   Bryans XY (Type 20170)

3. DISA Elektronik A/S. Techno House, Bristol, England:

   Type 55 B01 - Sweep-drive unit

   Type 55 D10 - Lineariser

   Type 55 D26 - Signal conditioner

   Type 55 D30 - Digital voltmeter

   Type 55 D31 - Digital voltmeter

   Type 55 D35 - RMS voltmeter

   Type 55 D70 - Correlator

   Type 55 D75 - Time-delay unit

   Type 55 D90 - Calibration tunnel

   Type 55 M01 - Main anemometer unit

   Type 55 M10 - CTA standard bridge

4. Memorex, Hounslow, Middx, England:

   MEMOREX magnetic tapes

5. Newport Instruments Ltd, Newport Pagnell, Bucks, England:

   Type C Electro-magnets

   Type VR3 DC supply

6. Sangamo Electric Co., Farnborough, Hants, England:

   Sangamo West Type 3500 magnetic tape recorder

7. S.E. Laboratories (Engineering) Ltd, Feltham, Middx, England:

   Type S.E. 429 carrier amplifier system

8. Tinsley Telecon, South Norwood, London:

   Type TK9/50/P/C torque strain guages

9. The Wayne-Kerr Laboratories Ltd, Surrey:
   Type B731 A Vibration meter.

10. S.E. Laboratories (Engineering) Ltd, Feltham, England:
    Type 3006 UV Recorder.

APPENDIX B: DIGITAL COMPUTER PROGRAMS

Note: Some of the SUBROUTINES are given in Anderson and Nettleton [40], and can be found in the wallet at the back on microfiche. These are,

FOURIER
HARMON
MODCPOWER
NEWPOWER
CROSSPOWER
HANNING
NEWHANN

```
      MASTER EARL
      DIMENSION S1(514),F1(514),C(514),S(64),A(514)
      DIMENSION STRN(514) PSIGMA(230)
      DIMENSION PR(105),XX(105)TPROB(105)
      DIMENSION HEAD(10),HEAD1(10)
      DIMENSION  IA(2)
      DATA IA(1)/8HHYB63101/
C     ORDER OF INPUTS:----
C        NBATCH
C     IFILT= (FILTERED) OR 0(UNFILTERED).
C        NGP  M  N
C        T
C        NP  NC
C     FR FP
C        HEAD
C        DO 50  II=1,NBATCH
C          HEAD1
C          DO 12  J=1,2
C            DO 9  I=1,NGP
C              READ (S1(L),L=1,N)
C              CONTINUE
C .
C12           CONTINUE
C50         CONTINE
      READ(1,1) NBATCH
      READ(1,1) IFILT
      FORMAT(10I0)
      READ(1,1) NGP,M,N
    2 FORMAT(100F0.0)
46    FORMAT(8F10.4)
47    FORMAT(10A8)
      READ(1,2) T
      READ(1,1) NP,NC
      READ (1,2)  FR,FP
      GP=NGP
      AN=N
      RATIO=FP/FR
      DELTAN=T/(AN*RATIO)
COMMENT -FREQUENCY IN HZ. AT K TH POINT IS (K-1)*T/N
C          WHERE T IS THE SAMPLING PERIOD IN SECONDS.
      IZ=N+2
      IZS=N/8
      READ(1,47)  HEAD
      WRITE(2,48) HEAD
48    FORMAT( H1,10A8)
      READ(1,501) IA(2)
501   FORMAT(A4)
      CALL FILE (5,IA(1),0,0)
      DO 50  IJ=1,NBATCH
      READ(1,47)  HEAD1
      WRITE(2,48)  HEAD1
      DO 3 K=1,NP
      AK=K
3     STRN(K)=(AK-1.0)*DELTAN
      DO 4 K=1,N
      A(K)=0.
    4 C(K)=0.
      READ (1,502) ICOUNT,IRUN,ICHANNEL1,ICHANNEL2
```

```
502   FORMAT(4I0)
      ICHANNEL=ICHANNEL1
      KK=1
509   CONTINUE
      DO 6 K=1,105
    6 PR(K)=0.
      SB=0.0
      SD=0.0
      AL3=0.0
      AL4=0.0
      CALL SORT(IRUN,ICHANNEL,ICOUNT)
      DO 9 I=1,NGP
      READ(5,46) (S1(L),L=1,N)
      CALL PROB(S1,N,SBAR,SIGMA,TPROB,XX,ALPH3,ALPH4)
      PSIGMA(KK,I)=SIGMA
      SB=SB+SBAR
      SD=SD+SIGMA
      AL3=AL3+ALPH3
      AL4=AL4+ALPH4
      DO 8 K= ,105
    8 PR(K)=PR(K)+TPROB(K)
      CALL FOURIER(S1,S,M,IFERR,IZ1,IZS)
    9 WRITE (6) (S1(K),K=1,N)
      SB=SB/GP
      SD=SD/GP
      AL3=AL3/GP
      AL4=AL4/GP
      WRITE(2,52) SB,SD,AL3,AL4
52    FORMAT( HO,6HMEAN= ,E9.3,2X,7HSIGMA= ,E9.3,2X,6HSKEW= E9.32 XO
     1     1OHKURTOSIS= ,E9.3)
      DO  0 K=1,105
   10 PR(K)=PR(K)/GP
      WRITE(2,11)
   11 FORMAT(1HO,7H SIGMA ,3X,4HPROB,//)
      NPR=105
      CALL PLOT(PR,XX,NPR)
      ICHANNEL=ICHANNEL2
      KK=KK+
      IF (KK.EQ.3) GO TO 12
      GO TO 509
   12 CONTINUE
      REWIND 6
COMMENT - COMPUTE THE POWER SPECTRA OF EACH
C         SUBRECORD OF THE FIRST ENSEMBLE.
      DO 13 I= ,NGP
      READ (6)(S1(K),K=1,N)
      CALL NEWPOWER(S1,N,IZ1)
      VARIANCE=PSIGMA( ,I)**2
      DO 120 L= ,N,2
120   S1(L)=S1(L)/VARIANCE
COMMENT - SUM THE ABOVE AND STORE THE AVERAGE
C         POWER SPECTRA IN ARRAY A.
      DO 13 K= ,N,2
   13 A(K)=A(K)+S1(K)
      DO 14 K=1,N,2
14    A(K)=2.0*A(K)/(DELTAN*GP)
      CALL NEWHANN(A,N,IZ1,1,IFILT)
```

```
      AA=A(1)
      J=1
      WRITE(2,15)J
   15 FORMAT( H1,10X,3HJ= ,I210X,14HPOWER SPECTRUM)
      DO 16 K=1,NP
   16 A(K)=A(K)*STRN(K)
      WRITE(2,17)
17    FORMAT( H0,8HFREQ(HZ),2X,15HNON. DIM. POWER,//)
      CALL PLOT(A,STRN,NP)
      CALL THOC(A,STRN,NP,DELTAN)
      A(1)=AA
      DO 18 K=2,NP
   18 A(K)=A(K)/STRN(K)
COMMENT - REPEAT THE ABOVE FOR THE  SECOND
C         ENSEMBLE AND STORE AVERAGE IN ARRAY C
      DO 19 I=1,NGP
      READ (6) (F1(K),K= ,N)
      CALL NEWPOWER(F1,N,IZ1)
      VARIANCE=PSIGMA(2,I)**2
      DO 180 L=1,N,2
 180  F1(L)=F1(L)/VARIANCE
      DO 19 K=1,N,2
   19 C(K)=C(K)+F1(K)
      DO 20 K=1,N,2
20    C(K)=2.0*C(K)/(DELTAN*GP)
      CALL NEWHANN(C,N,IZ1,1,IFILT)
      CC=C(1)
      J=2
      WRITE(2,15) J
      DO 21 K=1,NP
   21 C(K)=C(K)*STRN(K)
      WRITE(2,17)
      CALL PLOT(C,STRN,NP)
      CALL THOC(C,STRN,NP,DELTAN)
      C( )=CC
      DO 22 K=2,NP
   22 C(K)=C(K)/STRN(K)
COMMENT -     PROGRAM DESCRIPTION SEGMENT HAS DIVIDED
C         STORAGE LOCATIONS ON DISC IN BLOCKS OF N.
C         STORE AVERAGE POWER SPECTRA IN REAL FORM
C         OF 1ST ENSEMBLE IN BLOCK  (2*NGP)+1
      WRITE (6) (A(K),K=1,N)
      REWIND 6
      DO 23 K=1,N
   23 A(K)=0.
COMMENT - COMPUTE CROSS POWER SPECTRA FROM APPROPRIATE
C         PAIRS OF SUBRECORDS READ FROM DISC AND SUMMED
      DO 29 I=1,NGP
      READ (6) (S1(K),K=1,N)
      IF(NGP-1)24,26,24
   24 DO 25 II=1,NGP-1
   25 READ(6)
   26 READ (6) (F1(K),K=1,N)
      CALL CROSSPOWER(S1,F1,N,IZ1)
      VARIANCE=PSIGMA(1,I)*PSIGMA(2,I)
      DO 260 L=1,N
260   S1(L)=S1(L)/VARIANCE
```

```
      DO 27 K=1,N
   27 A(K)=A(K)+S1(K)
      IF(I. EQ. NGP) GO TO 29
      REWIND 6
      DO 28 II=1,I
   28 READ(6)
   29 CONTINUE
      DO 30 K=1,N
30    A(K)=2.00*A(K)/(DELTAN*GP)
      DO 310 I=1,N
  310 S1(I)=A(I)
COMMENT - STORE AVERAGE CROSS POWER IN COMPLEX
C          FORM IN BLOCK (2*NGP)*2
      READ(6)
      WRITE(6) (A(K),K=1,N)
COMMENT - COMPUTE MODULUS OF ABOVE AND STORE IN ARRAY A
      CALL MODCPOWER(A,N,IZ1)
      AAA=A(1)
      WRITE(2,31)
   31 FORMAT(1H1,50X,19HAVERAGE CROSS POWER)
      DO 32 K=1,NP
   32 A(K)=A(K)*STRN(K)
      WRITE(2,17)
      CALL PLOT(A,STRN,NP)
      CALL THOC(A,STRN,NP,DELTAN)
      WRITE(2,49)
49    FORMAT(1H1,50X,11HPHASE ANGLE)
      CALL PHASE(S1,N,IZ1)
      CALL PLOT(S1,STRN,NP)
      A(1)=AAA
      DO 33 K=2,NP
   33 A(K)=A(K)/STRN(K)
      REWIND 6
COMMENT - READ-BACK BLOCK (2*NGP)+1 AND STORE IN ARRAY S1
      DO 34 II=1,2*NGP
   34 READ (6)
      READ (6) (S1(K),K=1,N)
COMMENT - COMPUTE TRANSFER FUNCTION AND STORE IN ARRAY F1
      AMAX=0.0
      DO 35 K=1,N/2
   35 IF(S1(K).GT.AMAX) AMAX=S1(K)
      AMAX=AMAX/100.0
      DO 102 K=1,N/2
      IF(S1(K).LT.AMAX) GO TO 100
      F1(K)=A(K)/S1(K)
      GO TO 102
  100 F1(K)=0.0
  102 CONTINUE
      WRITE(2,36)
   36 FORMAT( H1,50X,17HTRANSFER FUNCTION)
      WRITE(2,37)
   37 FORMAT( H0,8HFREQ(HZ),2X,12HMOD TRANSFER,//)
      CALL PLOT(F1,STRN,NP)
COMMENT - COMPUTE COHERENCE FUNCTION AND STORE IN ARRAY A
      AMAX=0.0
      DO 38 K=1,N/2
   38 IF(C(K).GT.AMAX) AMAX=C(K)
      AMAX=AMAX/10.0
      DO 103 K=1,N/2
```

```
      IF(C(K).LT.AMAX) GO TO 101
      A(K)=F1(K)*A(K)/C(K)
      GO TO 103
  101 A(K)=0.0
  103 CONTINUE
      WRITE(2,39)
   39 FORMAT(1H1,50X,9HCOHERENCE)
      WRITE(2,40)
   40 FORMAT( H0,8HFREQ(HZ),2X,9HCOHERENCE,//)
      CALL PLOT(A,STRN,NP)
      K=0
      IF(NC)45,45,41
COMMENT - READ-BACK BLOCK (2*NGP)+2 AND STORE IN ARRAY F1
   41 READ (6) (F1(K),K=1,N)
COMMENT - COMPUTE AUTOCORRELATION FUNCTIONS OF 1ST AND 2ND,
C          ENSEMBLES AND CROSS CORRELATION (ARRAYS S1,C,F1)
      DO 42 K=1,N/2
      F1(K)=F1(K)*DELTAN
      S1(K)=S1(K)*DELTAN
42    C(K)=C(K)*DELTAN
      IFILT=0
      CALL NEWHANN(S1,N,IZ1,2,IFILT)
      CALL NEWHANN(C,N,IZ1,2,IFILT)
      CALL HARMON(S1,S,M-1,1,IFFER,IZ1,IZS)
      CALL HARMON(C,S,M-1,1,IFERR,IZ1,IZS)
      CALL HARMON(F1,S,M-1,1,IFERR,IZ1,IZS)
      CALL NEWHANN(S1,N,IZ1,1,IFILT)
      CALL NEWHANN(C,N,IZ1,1,IFILT)
      CALL NEWHANN(F1,N,IZ1,1,IFILT)
      DO 431 K=1,NC
      AK=FLOAT(K)
      STRN(K)=(2.0*(AK-1.0))/T
431   STRN(K)=STRN(K)*RATIO
      J=1
      WRITE(2,43) J
   43 FORMAT(1H1,50X,17HAUTO CORRELATION ,I1)
      NC=NC/2.0
      WRITE(2,51)
51    FORMAT(1H0,10HTIME(SECS),//)
      CALL PLOT(S1,STRN,NC)
      J=2
      WRITE(2,43)J
      WRITE(2,51)
      CALL PLOT (C,STRN,NC)
      NC=NC*2.0
      WRITE(2,44)
   44 FORMAT(1H1,50X,17HCROSS CORRELATION)
      WRITE(2,51)
      CALL PLOT(F1,STRN,NC)
      REWIND 6
50    CONTINUE
   45 STOP
      END
```

```
      SUBROUTINE PHASE(X,N,IX)
      DIMENSION X(IX)
      PI=4.0*ATAN(1.0)
      DEG=180.0/PI
      AMAX=0.0
      DO 5  I=1,N,2
      I1=I+1
5     IF(ABS(X(I1)).GT.AMAX)  AMAX=X(I1)
      DO 1  I=1,N,2
      I1=I+1
      IF(ABS(X(I1)).LT.(AMAX/100.0)) GO TO 6
      IF(ABS(X(I)).LT.(X(I1)/100.0)) GO TO 7
      THETA=ABS(ATAN(X(I1)/X(I)))*DEG
      IF(X(I).GT.0.0.AND.X(I1).GT.0.0) GO TO 8
      IF(X(I).LT.0.0.AND.X(I1).GT.0.0) GO TO 9
      IF(X(I).GT.0.0.AND.X(I1).LT.0.0) GO TO 10
      IF(X(I).LT.0.0.AND.X(I1).LT.0.0) GO TO 11
8     X(I)=THETA
      GO TO 1
9     X(I)=180.0-THETA
      GO TO 1
10    X(I)=-THETA
      GO TO 1
11    X(I)=-180.0+ THETA
      GO TO 1
6     X(I)=0.0
      GO TO 1
7     IF (X(I)/X(I1)) 2,2,3
2     X(I)=-90.00
      GO TO 1
3     X(I)=90.0
1     CONTINUE
      DO 4  I=1,N/2
4     X(I)=X(2*I-1)
      RETURN
      END
```

```
      SUBROUTINE PROB(X,NXBAR,SIGMA,Y,XX,ALPH3,ALPH4)
      DIMENSION X(N),IPROB(52),JPROB(52),II(1)
      DIMENSION Y(105),XX(105)
      AN=FLOAT(N)
      XBAR=0.
      XN=X(N)
      DO 1 I=1,N
      XBAR=XBAR+X(I)
    1 CONTINUE
      XBAR=XBAR/AN
      DO 2 I=1,N
      X(I)=X(I)-XBAR
    2 CONTINUE
      VAR=0.
      AMU3=0.0
      AMU4=0.0
      DO 3 I=1,N
      VAR=VAR+(X(I)*X(I))
      AMU3=AMU3+(X(I)*(X(I)*X(I)))
      AMU4=AMU4+((X(I)*X(I))*(X(I)*X(I)))
    3 CONTINUE
      VAR=VAR/(AN-.0)
      SIGMA=SQRT(VAR)
      ALPH3=AMU3/(SIGMA**3.0)
      ALPH4=AMU4/(SIGMA**4.0)
      ALPH3=ALPH3/AN
      ALPH4=ALPH4/AN
      RSIGMA=5.0*SIGMA
      DO 4 I=1,52
      IPROB(I)=0
      JPROB(I)=0
    4 CONTINUE
      II(1)=0
      DO 6 I=1,N
      X1=X(I)
      X2=(X1/RSIGMA)*50.0
      IF (NINT(X2))  10,20,30
   30 IX2=INT(X2)+
      IF(IX2.GT.51) IX2=52
      IPROB(IX2)=IPROB(IX2)+1
      GO TO 5
   20 II(1)=II(1)+
      GO TO 5
   10 X2=ABS(X2)
      JX2=INT(X2)+
      IF(JX2.GT.51)  JX2=52
      JPROB(JX2)=JPROB(JX2)+1
      GO TO 5
    5 CONTINUE
    6 CONTINUE
      DO 7 I=1,52
      Y(I)=FLOAT(JPROB(53-I))
      XX(I)=-(FLOAT(53-I))/10.0
    7 CONTINUE
      Y(53)=FLOAT(II(1))
      XX(53)=0.0
      DO 8 I=54,105
```

```
      Y(I)=FLOAT(IPROB(I-53))
      XX(I)=(FLOAT(I-53))/10.0
    8 CONTINUE
      WRITE(2,12)
12    FORMAT(1HO,3X,4HXBAR,6X,5HSIGMA,5X,4HSKEW,3X,8HKURTOSIS)
      WRITE (2,9) XBAR,SIGMA,ALPH3,ALPH4,XN
9     FORMAT(2X,E9.3,2X,E9.3,2X,E9.3,2X,E9.3,2X,E10.4)
      DO 11 I=1,105
      Y(I)=Y(I)/(AN*0.1)
11    CONTINUE
      RETURN
      END
```

```
      SUBROUTINE PLOT(Y,F,NPTS)
      DIMENSION IGRAPH(91),F(NPTS),Y(NPTS)
      REAL MAXE,MINE
      DATA IP/4H+   /,IS/4H    /,IDOT/4H.   /
      DO 1 K=1,91
    1 IGRAPH(K)=IS
      MAXE=0.
      MINE=0.
      DO 2 K=1,NPTS
      IF(MAXE.LT.Y(K)) MAXE=Y(K)
    2 IF(MINE.GT.Y(K)) MINE=Y(K)
      IF(ABS(MAXE).LE.0.1E-10.AND.ABS(MINE).LE.0.1E-10) GO TO 10
      IF(MAXE.GT.0.AND.MINE.EQ.0) GO TO 3
      IF(MAXE.EQ.0.AND.MINE.LT.0) GO TO 5
      IF(MAXE.GT.0.AND.MINE.LT.0) GO TO 7
    3 SCALE=90./MAXE
      IGRAPH(1)=IDOT
      DO 4 K=1,NPTS
      ISCALE=INT(SCALE*Y(K))+ 1
      IGRAPH(ISCALE)=IP
      WRITE(2,9) F(K),Y(K),IGRAPH
      IGRAPH(ISCALE)=IS
    4 IGRAPH(1)=IDOT
      IGRAPH(1)=IS
      GO TO 10
    5 SCALE=90./MINE
      IGRAPH(91)=IDOT
      DO 6 K=1,NPTS
      ISCALE=INT(SCALE*Y(K))+1
      IGRAPH(ISCALE)=IP
      WRITE(2,9) F(K),Y(K),IGRAPH
      IGRAPH(ISCALE)=IS
    6 IGRAPH(91)=IDOT
      IGRAPH(91)=IS
      GO TO 10
    7 SCALE=90./(MAXE-MINE)
      NZERO=INT(-SCALE*MINE)+1
      IGRAPH(NZERO)=IDOT
      DO 8 K=1,NPTS
      ISCALE=INT(SCALE*(Y(K)-MINE))+1
      IGRAPH(ISCALE)=IP
      WRITE(2,9) F(K),Y(K),IGRAPH
      IGRPH(ISCALE)=IS
    8 IGRAPH(NZERO)=IDOT
      IGRAPH(NZERO)=IS
   10 CONTINUE
    9 FORMAT(2X,F8.3,E13.4,6X,91A1)
      RETURN
      END
```

```
      SUBROUTINE THOC (E,F,NP,DELTAF)
      DIMENSION E(NP),F(NP)
      DIMENSION  E1(260),E2(260),FREQ(260)
      REAL LBF
      K=0
      IF(0.1.LE.DELTAF.AND.DELTAF.LT.1.0) GO TO 11
      IF(1.0.LE.DELTAF.AND.DELTAF.LT.10.0) GO TO 12
      IF(10.0.LE.DELTAF.AND.DELTAF.LT.100.0) GO TO 13
11    ALPHA=-1.0
      GO TO 14
12    ALPHA=0.0
      GO TO 14
13    ALPHA=1.0
      GO TO 14
16    ALPHA=ALPHA+ .0
14    BETA=0.0
15    BETA=BETA+0.025
      IF (BETA-1.0)  17,17,16
17    IF(ALPHA) 18,19,20
18    TOC=EXP10(BETA)/EXP10(ABS(ALPHA))
      GO TO 21
19    TOC=EXP10(BETA)
      GO TO 21
20    TOC=EXP10(BETA)*EXP10(ALPHA)
21    K=K+1
      FREQ(K)=TOC
      IF (FREQ(K)-F(NP)) 22,100,100
22    LBF=0.885*FREQ(K)
      UBF=1.115*FREQ(K)
23    SUM=0.0
      DO 24 I=2,NP
      IF(LBF.LE.F(I).AND.F(I).LE.UBF)  GO TO 28
      GO TO 24
28    IF (I.EQ.1) GO TO 27
      E1(I)=(E(I)*DELTAF)/F(I)
      GO TO 29
27    E1(1)=0.0
29    SUM=SUM+E1(I)
24    CONTINUE
      E2(K)=SUM/0.057
      GO TO 15
100   WRITE (2,25)
25    FORMAT(1H1,19H1/3 OCTAVE ANALYSIS,5X,
     * 26HENERGY*FREQ. VS. FREQUENCY)
      WRITE (2,26)
26    FORMAT ( H0,8HFREQ(HZ),15HNON. DIM. POWER,//)
      CALL PLOT(E2,FREQ,K)
      RETURN
      END
```

```
      SUBROUTINE SORT(IRUN,ICHANNEL,ICOUNT)
      IC=1
  504 READ(5,2,END=10) ITEST
    2 FORMAT(A4)
      L=4
      CALL COMP(L,ITEST,1,4HCHAN,1)
      IF(L-4) 504,3,504
    3 BACKSPACE 5
      READ(5,503) ICH,IR
  503 FORMAT(8X,I4,6X,I4,/)
      IF (IR.EQ.IRUN) GO TO 505
      GO TO 504
505   IF (IC.EQ.ICOUNT) GO TO 506
      IC=IC+1
      GO TO 504
506   IF (ICH.EQ.ICHANNEL) GO TO 507
      IC=ICOUNT
      GO TO 504
507   WRITE (2,508)  IRUN,ICOUNT,ICHANNEL
508   FORMAT(1H1,6HIRUN= ,I4,2X,8HICOUNT= ,I4,2X,9HCHANNEL= ,I4,2X,
     *24HPROBABILITY DISTRIBUTION)
      GO TO 4
   10 STOP
    4 RETURN
      END
```

```
      MASTER GRID
      DIMENSION K1(10),YTEMP(50,10),LTEMP(50,10)
      DIMENSION L(50,10),Y(50,10),H(50,10)
C     THIS PROGRAM CALCULATES THE SPACING OF THE RODS NECESSARY TO
C     PRODUCE A VELOCITY PROFILE ACCORDING TO THE METHOD OF COWDREY.
C     THE COUNTER VLAUE OF NJ IS SET AT 10, BUT THIS CAN BE EXTENDED
C     TO LIMITS CONSTRAINED IN THE PRINT-OUT. IF IT IS NECESSARY TO
C     INCREASE THE VALUE OF NJ, DIMENSION STATEMENTS AND FORMAT
C     STATEMENTS, (22), (25) AND (10) MUST BE CHANGED.
C     K1 -- OVERALL PRESSURE DROP COEFFICIENT OF THE GRID
C     DEL -- HEIGHT OF WIND-TUNNEL
C     D -- DIAMETER OF THE RODS
C     N -- POWER EXPONENT
C     H(MM) IS THE SPACING OF THE C/L OF THE RODS FROM THE TUNNEL FLOOR.
      REAL DEL,D,N,EPS,K1,YTEMP, LTEMP,L,Y,H
      REAL  KK , Y1,Y2,L1,L2
      INTEGER  NJ,NI
      EPS=0.1 E-16
      READ(1,10)   DEL,D,N
10    FORMAT(10F0.0)
      READ(1,11)  NI
11    FORMAT(I0)
      READ(1,11)  NJ
      READ(1,10)  (K1(J),J=1,NJ)
      DO 200 J=1,NJ
      YTEMP(1,J)=0.1 E-30
      Y1=YTEMP(1,J)
      KK=K1(J)
      CALL CALC(DEL,D,N,KK,Y1,L1)
      L(1,J)=L1 /2.0
      Y(1,J)=YTEMP(1,J)
      H(1,J)= Y(1,J)+L(1,J)
      I=2
131   YTEMP(I,J)=H(I-1,J)+L(I-1,J)
121   Y2=YTEMP(I,J)
      CALL CALC(DEL,D,N,KK,Y2,L2)
      L(I,J)=L2 /2.0
      Y(I,J)=H(I-1,J)+L(I,J)
      IF((Y(I,J)-YTEMP(I,J))-EPS) 110,110,120
120   YTEMP(I,J)=Y(I,J)
      GO TO 121
110   H(I,J)=Y(I,J) +L(I,J)
      IF(H(I,J).GT.DEL) GO TO 200
      IF(I-NI)  100,200,200
100   I=I+1
      GOTO 131
200   CONTINUE
      WRITE(2,21)  DEL,D,N,EPS
21    FORMAT(1H1,5X,9HDEL(IN)= ,F5.2,9HDIA(IN)= ,F5.3,5X,
     1  10HEXPONENT= ,F3.1,5X,9HEPS(IN)= ,F8.5,//)
      WRITE(2,22)  (K1(J),J=1,NJ)
22    FORMAT(5X,3HROD,1X,10(3HK1=,F4.2,1X),//)
      WRITE(2,25)  (I,(H(I,J),J=1,NJ),I=1,NI)
25    FORMAT((5X,I3,1X,10(F7.3,1X)))
      STOP
      END
```

```
      SUBROUTINE CALC(DEL,D,AN,AK,Y,AL)
C     THIS PROGRAM CALCULATED EQN 3 FROM COWDREY, NPL.AERO.NOTE 1055
1     AK1=1.0+AK
2     AN1=AN+1.0
3     AN2=AN/AN1
4     AN3=(AN2)**2.0
5     BETA=Y/DEL
6     BETA1=BETA**(2.0/AN)
7     BETA2=1.0/BETA1
8     ALAM1=((AN3*AK1)*BETA2)-1.0
81    ALAM=1.0/ABS(ALAM1)
9     ALAM2=ALAM**2.0
10    ALAM3=4.0*ALAM
11    ALAM4=ALAM2+ALAM3
12    ALAM5=SQRT(ALAM4)
13    ALAM6=2.0+ALAM
14    ALAM7=ALAM6-ALAM5
15    ALAM8=2.0*D
16    AL=ALAM8/ABS(ALAM7)
      RETURN
      END
```

```
      MASTER INER
C     AM- MASS OF MODEL(LB)
C     AI- INERTIA OF MODEL[LB(IN**2)]
C     AL- LENGTH OF MODEL (IN)
C     A-- LENTH OF THE SIDES OF THE CROSS-SECTION OF THE SQUARE
C         TUBE.
 TUBE.
C     T--THICKNESS OF THE WALLS OF THE MODEL (IN.)
C     ROW-- DENSITY OF THE MATERUAL OF THE MODEL[LB/(IN**0)]
C     AT--LENGTH OF SIDES OF INNER SQUARE.
      READ(1,10)  AO,AL,ROW
10    FORMAT(100F0.0)
      READ(1,20)  N
20    FORMAT(I0)
      WRITE(2,50)  AL,ROW
50    FORMAT(1H1,5X,7HT(IN)= ,F5.2,5X,19HROW(LB/(IN**3.0))= ,
     |    F5.2,//)
      WRITE(2,511)
511   FORMAT(5X,3HO/L,8X,1HT,8X,2HAT,8X,2HAM,8X,2HAI,//)
      DT=0.001
      T=0.128
      AT=AO-(2.0*T)
      DO 100  I=1,N
      T=T-DT
      A=AT+2.0*T
      A1=A-T
      A2=T*A1
      A3=AL*A2
      AM=4.0*(ROW*A3)
      B1=(AL**2.0)/3.0
      B2=(A**4.0)
      B4=AT*4.0
      B5=(B2-B4)/12.0
      B6=AT**2.0
      B7=B5/B6
      B8=B1+B7
      AI=AM*B8
      WRITE(2,51)  A,T,AT,AM,AI
51    FORMAT(3X,F5.3,5X,F5.3,5X,F5.3,5X,F5.3,5X,F7.3)
100   CONTINUE
      STOP
      END
      FINISH
```

```
      MASTER TORS
      REAL  K1,K11,K2,K22,K3,K33,K4,K
      REAL L
      REAL  I,D,IC,KR
C          THIS PROGRAM ANALYSIS THE DESIGN OF TORSION BA2S
C       FOR TALL MODEL
C     ANALYSIS IN SUPPLYUNG THE STIFFNESSES REQUIRED.
C          THE MODULUS OF RIGIDITY,G[LB./(IN**2)],
C     AND THE LENGTH OF THE ROD,L
C     [IN] ARE THEN READ IN.
C          THE MOMENT OF INERTIA I[LB.(IN**2)] AND A REPRESENTATIVE
C       LENGTH, D[IN]
C        OF THE MODEL ARE THE N NEXT READ IN.
C          IF THE TORSION BAR HAS A WIDTH B[IN] AND THICKNESS T[IN],
C             THEN THE
C     STIFNESS ,STI[LB.FT./RAD] IS GIVEN BY:
C                 STI=(K*G)/(L*12.0) ,
C     WHERE K=[(B*(T**3))/3.0]*[1.0-0.63(T/B)+0.052((T/B)**2)]
C          TORSIONAL SPRING CONSTANT, KR=STI
C          INERTIA IC[SLUG(FT**2)]= I/(32.2*144.0)
C          NATURAL UNDAMPED FREQUENCY F[HZ] OF THE STRUCTURE IS GIVE
C       BY:    F=[1/(2*PI)]*[SQRT(KR/IC)]
C          CRITCAL WIND SPEED VCR(FT/SEC) OF THE MODEL IS GIVEN BY:
C                      VCR=7.0*F*D
C          R IS THE END-RADIUS OF THE  FIXING END OF THE TORSION BARS
      READ(1,10)  R
      READ( ,10)  G,L
10    FORMAT(2F0.0)
      READ(1,10)  I,D
      WRITE(2,5)
5     FORMAT(1H1,10H**********)
      WRITE(2,3)  G,L
3     FORMAT(5X,14HG(LB.FT**-2)= ,E8.2,5X,7HL(IN)= ,F5.2,//)
      WRITE(2,4)  I,D
4     FORMAT(5X,35HINERTIA OF MODEL I,(LB.(IN)**2.0)= ,F7.2,
     1  5X,5H*****,5X,29HLENGTH SCALE OF MODEL,D(IN)= ,F5.2)
      WRITE(2,1)
1     FORMAT(1H0,4X,5HB(IN),4X,5HT(IN),5X,12HK(IN**4/RAD),
     *  4X,14HSTI(FT.LB/RAD),4X,8HFREQ(HZ),4X,11HVCR(FT/SEC),//)
      T=0.115
      DO 100 J= ,400
      T=T+0.001
      T2=(T**2.0)/4.0
      B2=(R**2.0) - T2
      B=2.0*(SQRT(B2))
      K1= B*(T**3.0)
      K11= K1/3.0
      K2= T/B
      K22= 0.63 * K2
      K3= K2**2.0
      K33= 0.052 *K3
      K4= 1.0-K22+K33
      K=K11*K4
      STI= (K*G)/(L*12.0)
      KR=STI
      IC=I/(32.2*144.0)
```

```
      PI=22.0/7.0
      BETA=SQRT(KR/IC)
      FREQ=BETA/(2.0*PI)
      VCR=5.0*(FREQ*(D/12.0))
      WRITE(2,2)  B,T,K,STI,FREQ,VCR
2     FORMAT(5X,F4.3,5X,F5.3,5X,E11.4,5X,E12.4,5X,F6.2,5X,F6.2)
100   CONTINUE
      STOP
      END
      FINISH
```

```
      SUBROUTINE WEIBULL(R,N,IR)
      DIMENSION R(N)
      DIMENSION PRR(110), XX(110)
      IF(IR.EQ.0) GOTO 10
      AN=FLOAT(N)
      DO 50  I=1,N
50    R(I)=ABS(R(I))
      CALL PROB(R,N,RBAR,SIGR,PRR,XX)
      DO 48  I=1,N
48    R(I)=(R(I)+RBAR)/SIGR
      WRITE(2,52)
52    FORMAT(1H0,5H  RM ,5H RM1 ,5H  P1 ,5H  P2 )
      RM=0.0
      DR=0.25
      DO 49  J3=1,20
      RM=RM+DR
      P1=0.0
      DO 51  I=1,N
51    IF(R(I).GT.RM)  P1=P1+1.0
      P1=P1/AN
      IF(P1.EQ.0.0)  P1=1.0E-30
      P2=-ALOG(P1)
      P2=ALOG(P2)
      RM1=ALOG(RM)
49    WRITE(2,53) RM,RM1,P1,P2
53    FORMAT(1X,F5.2,1X,F6.3,1X,E9.2,1X,F6.3)
10    RETURN
      END
```

```
      SUBROUTINE VECTOR(X,Y,R,T,N)
      DIMENSION X(N),Y(N),R(N),T(N)
      AN=FLOAT(N)
      DEG=(180.0*7.0)/22.0
      AMAX=0.0
      AMAY=0.0
      DO 6 I=1,N
      IF(ABS(X(I)).GT.AMAX) AMAX=ABS(X(I))
6     IF(ABS(Y(I)).GT.AMAY) AMAY=ABS(Y(I))
      DO 13 I=1,N
      IF(ABS(X(I)).LT.(AMAX/100.0)) GOTO 7
      IF(ABS(Y(I)).LT.(AMAY/100.0)) GOTO 8
      TMOD=ABS(X(I)/Y(I))
      THETA=(ATAN(TMOD))*DEG
      IF(Y(I).GT.0.0.AND.X(I).GT.0.0) GOTO 9
      IF(Y(I).LT.0.0.AND.X(I).GT.0.0) GOTO 10
      IF(Y(I).GT.0.0.AND.X(I).LT.0.0) GOTO 11
      IF(Y(I).LT.0.0.AND.X(I).LT.0.0) GOTO 12
9     T(I)=THETA
      GOTO 13
10    T(I)=180.0-THETA
      GOTO 13
11    T(I)=-THETA
      GOTO 13
12    T(I)=-180.0+THETA
      GOTO 13
7     IF(Y(I).GT.0.0) T(I)=0.0
      IF(Y(I).LT.0.0) T(I)=180.0
      GOTO 13
8     IF(X(I).GT.0.0) T(I)=90.0
      IF(X(I).LT.0.0) T(I)=-90.0
13    CONTINUE
      DO 16 I=1,N
16    R(I)=SQRT(X(I)*X(I)+Y(I)*Y(I))
      RETURN
      END
```

```
      SUBROUTINE JTPROB(X,Y,N,IXY)
      DIMENSION X(N),Y(N)
      IF(IXY.EQ.0) GOTO 10
      AN=FLOAT(N)
      WRITE (2,461)
461   FORMAT(1H0,5H  X1 ,6H     X2,7H      Y1,7H      Y2,7H      P1)
      X1=-4.0
      X2=-3.5
      DO 42  J1=1,16
      Y1=-4.0
      Y2=-3.5
      DO 43  J2=1,16
      P1=0.0
      DO 44 I=1,N
      IF(X1.LT.X(I).AND.X(I).LE.X2) GOTO 45
      GOTO 44
45    IF(Y1.LT.Y(I).AND.Y(I).LE.Y2) P1=P1+1.0
44    CONTINUE
      P1=P1/AN
      WRITE(2,46)X1,X2,Y1,Y2,P1
46    FORMAT(1H ,F5.2,2X,F5.2,2X,F5.2,2X,F5.2,2X,E10.3)
      Y1=Y1+0.5
      Y2=Y2+0.5
43    CONTINUE
      X1=X1+0.5
      X2=X2+0.5
42    CONTINUE
10    RETURN
      END
```

REFERENCES

1 Baker, B.(1884) The Forth bridge Engineering 38 p.213.

2 Stanton, T. E.(1925) Report on the measurement of the pressure of the wind on structures (Proc. Inst. Civil Engrs 219 p.125.

3 Dryden, H.L. and Hill, G. C.(1933) Wind pressure on a model of the Empire State Building J. Res. Nat. Bur. Stand. 10.

4 Rathbun, J. C.(1940) Wind forces on a tall building Trans Amer Soc Civil Engrs 105 pp.1–41.

5 —— (1966) Report of the Committee of Inquiry into Collapse of Cooling Towers at Ferrybridge, Monday, Nov 1965 Central Electricity Generating Board, London.

6 Page, J.K.(1968) Field investigation of wind failures in the Sheffield gales of 1962 Symp. on Wind Effects on Buildings and Structures (Paper No.12) Loughborough Univ. of Technology, England.

7 Walker, G.R.(1975) Report on Cyclone Tracy Dept of Housing and Construction, Australia.

8 Osipovich, A.A.(1963) Effects of 1962 Columbus Day storm Trans. IEEE (Paper CP–63–1221).

9 Menzies, J. B.(1971) Wind Damage to Buildings in the United Kingdom 1962–1969 (CP 35/71) Building Res. Station, England.

10 —— (1975) Appendix 2 – Survey of full-scale investigations J. Ind. Aerodynamics 1 (No.2) pp.126–137.

11 Lee, B.E.(1974) The wind-induced vibration of a pair of model stacks Proc. Inst. Civil Engrs 57 pp.99–111.

12 Scruton, C.(1967) Aerodynamics of structures International Research Seminar on Wind Effects on Buildings and Structures (Paper No.4) Univ. of Toronto, Canada.

13 Newberry, C. W. and Eaton, K. J.(1974) Wind Loading Handbook HMSO London.

14 Farquaharson, F. B., Smith, F. C. and Vincent, G. S.(1949–1954) Aerodynamic Stability of Suspension Bridges with Special Reference to the Tacoma Narrows Bridge (Bulletin No.116, Parts I–V) Univ. of Washington Engineering Experiment Station, USA.

15 Davenport, A.G.(1961) A Statistical Approach to the Wind Loading of the Tall Mast and Suspension Bridge (Ph.D. Thesis) Dept of Civil Engineering, Univ. of Bristol, England.

16 Liepmann, H.W.(1952) On the application of statistical concepts to the buffeting problem J. Aeronautical Sciences 19 (No.12) pp.793–800.

17 Davenport, A.G.(1964) The buffeting of large superficial structures by atmospheric turbulence Annals, New York Academy of Science pp.135-159.

18 Johns, D.J. and Allwood, R.J.(1968) Wind induced ovalling oscillations of circular shell structures such as chimneys Symp on Wind Effects on Buildings and Structures (Paper No.28) Loughborough Univ of Technology, England.

19 Parkinson, G.V.(1963) Aeroelastic galloping in one degree of freedom Symp. on Wind Effects on Buildings and Structures (Paper No.23) Nat. Physical Lab., England.

20 Parkinson, G.V.(1971) Wind-induced instability of structures Phil.Trans.Roy.Soc.A269 pp.395-409.

21 Smith, J.D.(1962) An Experimental Study of the Aeroelastic Instability of Rectangular Cylinders (MA.Sc.Thesis) Dept of Mechanical Engineering, Univ. of British Colombia, Canada.

22 Wooton, L.R., Warner, M.H., Sainsbury, R.N. and Cooper, D.H.(1972) Oscillations of Piles in Marine Structures - A Description of the Full-Scale Experiments at Immingham. (Tech.Note 40) Construction Industry Res. and Info.Assoc., England.

23 Johns, D.J.(1969) Wind excited behaviour of cylindrical structures - its relevance to aerospace design AGARD Conference on the Aerodynamics of Atmospheric Shear Flows (Paper No.25) NATO.

24 Scruton, C.(1963) On the wind-excited oscillations of stacks, towers and masts Symposium on Wind Effects on Buildings and Structures (Paper No.16) Nat.Physical Lab., England.

25 Ferguson, N. and Parkinson, G.V.(1967) Surface and wake flow phenomena of the vortex-excited oscillation of a circular cylinder ASME Vibration Conference (Paper No.67-Vibr-31) Boston, USA.

26 Parkinson, G.V. and Modi V.J.(1967) Some research on wind effects on bluff two-dimensional bodies Int. Res.Seminar on Wind Effects on Buildings and Structures (Paper No.18) Univ. of Toronto, Canada.

27 Scruton, C. and Flint, A.R.(1964) Wind-excited oscillations of structures Proc.Inst.Civil Engrs 27 pp.673-702.

28 Baines, W.D.(1963) Effects of velocity distribution on wind loads and flow patterns on buildings Symp. on Wind Effects on Buildings and Structures (Paper No.6) Nat.Physical Lab., England.

29 Bearman, P.W.(1968) Some effects of turbulence on the flow around bluff bodies Symp.on Wind Effects on Buildings and Structures (Paper No.11) Loughborough Univ. of Technology, England.

30 Davenport, A.G. and Isyumov, N. (1967) The application of the boundary layer wind tunnel to the prediction of wind loading Int. Res. Seminar on Wind Effects on Buildings and Structures (Paper No. 7) Univ. of Toronto, Canada.

31 Whitbread, R.E. and Scruton, C. (1965) An Investigation of the Aerodynamic Stability of a Model of the Proposed Tower Blocks for the World Trade Centre, New York (Aero. Rep. 1156) Nat. Physical Lab England.

32 Vickery, B.J. (1966) Fluctuating lift and drag on a long cylinder of square cross-section in a smooth and in a turbulent stream J. Fluid Mech 25 (Part 3) pp. 481-494.

33 Whitbread, R.E. (1968) On the introduction of turbulence into wind-tunnel investigations for the determination of wind-induced amplitudes of oscillation Symp. on Wind Effects on Buildings and Structures (Paper No. 32) Loughborough Univ. of Technology, England.

34 Bendat, J. S. and Piersol, A.G. (1971) Random Data: Analysis and Measurement Procedures Wiley-Interscience, London.

35 Bradshaw, P. (1971) An Introduction to Turbulence and its Measurement Pergamon Press, Oxford.

36 Hassan, U. and Perera, E. (1974) Digital Analysis of Analogue Data From Wind Tunnel Experiments (Aero. Memo. 74/4) Dept of Aeronautics, The City University, London.

37 Burford, R.L. (1968) Statistics: A Computer Approach Charles E Merrill Publ. Co., Columbus, Ohio, USA.

38 Otnes, R.K. and Enochson, L. (1972) Digital Time Series Analysis Wiley-Interscience, London.

39 Blake, C.C. and Leighton, C.C. (1970) Linking two alien digital computers via a British Standard Interface The Computer Bulletin 14 (No. 4).

40 Anderson, J. S. and Nettleton, T. (1971) Digital Spectral and Correlation Analysis (Res. Memo. No. ML 31) Dept of Mech. Eng., The City University, London.

41 Anderson, J. S. and Nettleton, T. (1971) Digital spectral analysis in acoustics and vibrations Seventh Int. Conf. on Acoustics, Budapest.

42 Cooley, J.W. and Tukey, J.W. (1965) An algorithm for the machine calculation of complex Fourier series Mathematics of Computation 19 (No. 90) pp. 297-301.

43 Beauchamp, K.G. (1973) Signal Processing - Using Analog and Digital Techniques George Allen and Unwin Ltd, London.

44 Roberts, J.B. and Surry, D. (1972) Some Experiences with 'On-Line' Spectral Analysis Using a Small Digital Computer (CP No. 1225) Aeronautical Res. Council, England.

45 Villasenor, A.J. (1968) Digital Spectral Analysis (NASA TN D-4510), Nat. Aeronautics and Space Admin. Washington.

46 Jensen, M. and Franck, N. (1963) Model-Scale Tests in Turbulent Wind The Danish Technical Press, Copenhagen.

47 Tennekes, H. and Lumley, J.L. (1972) A First Course in Turbulence MIT Press, USA.

48 Van der Hoven, I. (1957) Power spectrum of horizontal wind speed in the frequency range from 0.0007 to 900 cycles per hour J. Meteorology 14 p. 160.

49 Davenport, A.G. (1961) The spectrum of horizontal gustiness near the ground in high wind Quart. J. Roy. Met. Soc. 87 pp. 194-211.

50 Davenport, A.G. (1967) The dependence of wind loads on meteorological parameters Int. Res. Seminar on Wind Effects on Buildings and Structures (Paper No. 2) Univ. of Toronto, Canada.

51 Sutton, O.G. (1953) Micrometeorology McGraw-Hill Book Co., London.

52 Calder, K.L. (1949) Eddy diffusion and evaporation in flow.... Quart. J. Mech. Applied Math. 2 pp. 153-176.

53 Schlichting, H. (1968) Boundary-Layer Theory (6th edn) McGraw-Hill Book Co., London.

54 Davenport, A.G. (1963) The relationship of wind structure to wind loading Symp on Wind Effects on Buildings and Structures (Paper No. 2) Nat. Physical Lab., England.

55 Leutheusser, H. (1965) Pressure Distribution on a Cube at Various Degrees of Boundary-Layer Immersion (UT Mech E TP 6502) Dept of Mech. Eng., Univ. of Toronto, Canada.

56 Davenport, A.G. (1971) On the statistical prediction of structural performance in the wind environment (ASCE National Structural Eng. Meeting Baltimore, Maryland.

57 Hinze, J.O. (1959) Turbulence McGraw-Hill Book Co., London.

58 Pasquill, F. (1961) The statistics of turbulence in the lower part of the atmosphere Symp. on Atmospheric Turbulence and its Relation to Aircraft Roy Aircraft Est., Farnborough, England.

59 Harris, R.I. (1968) On the Spectrum and Auto-Correlation Function of Gustiness in High Winds (Rep. No. TR 5273) Electrical Res. Assoc., England.

60 Armitt, J. (1976) Measurement of length scales Minutes of the 49th Industrial Fluid Mech. Res. Meeting Nat. Physical Lab., England.

61 Kaimal, J. C., Wyngaard, J. C., Izumi, Y. and Coté, O. R. (1972) Spectral characteristics of surface-layer turbulence Quart. J. Roy. Met. Soc. 98 pp. 563-589.

62 Cook, N. J. (1971) The Effect of Turbulence Scale on the Flow Around High Rise Building Models (Ph. D. Thesis) Dept of Aero. Eng Univ. of Bristol, England.

63 Harris, R. I. (1970) The nature of the wind Seminar on the Modern Design of Wind-Sensitive Structures (Paper 3) Construction Ind. Res. and Info. Assoc., London.

64 Panofsky, H. A., Cramer, H. E. and Rao, V. R. K. The relation between Eulerian time and space spectra Quart. J. Roy. Met. Soc. 84 pp. 270-273.

65 Counihan, J. (1973) Simulation of an adiabatic urban boundary layer in a wind tunnel Atmospheric Environment 7 pp. 673-689.

66 Cowdrey, C. F. (1967) A Simple Method for the Design of Wind-Tunnel Velocity-Profile Grids (Aero. Note 1055) Nat. Physical Lab., England.

67 Cockrell, D. J. and Lee, B. E. (1966) Production of shear profiles in a wind-tunnel by cylindrical rods placed normal to the stream J. Roy. Aero. Soc. p. 724.

68 Elder, J. W. (1959) Steady flow through non-uniform gauzes of arbitrary shapes J. Fluid Mech. 1 (Part 3) p. 355.

69 Counihan, J. (1972) The structure and the wind tunnel simulation of rural and urban adiabatic boundary layers Symp. on External Flows Univ. of Bristol, England.

70 Lawson, T. V. (1968) Methods of producing velocity profiles in wind-tunnels Atmospheric Environment 2 (No. 1) pp. 73-76.

71 Baines, W. D. and Peterson, E. G. (1949) An Investigation of Flow through Screens Rep. to the Office of Naval Res. by Iowa Inst. of Hydraulics.

72 Whitbread, R. E. (1972) The use of scale models for the determination of wind effects on buildings and structures Course on Wind Effects on Buildings and Structures Von Karman Inst. for Fluid Dynamics, Belgium.

73 Sachs, P. (1972) Wind Forces in Engineering Pergamon Press, Oxford.

74 Walshe, D. E. J. (1972) Wind-Excited Oscillations of Structures HMSO, London.

75 Whitbread, R.E.(1963) Model simulation of wind effects on structures, Symp. on Wind Effects on Buildings and Structures (Paper No. 21) Nat. Physical Lab., England.

76 Wooton, L.R.(1968) The Oscillations of Model Circular Stacks due to Vortex Shedding at Reynolds Numbers from 10^5 to 3.10^6 (Aero. Rep. 1267) Nat. Physical Lab., England.

77 Strzelecki, A.(1970) Tlumienic w polu magnetycznym drgan wirujacej pily tarczowej (Damping vibration of circular saws by magnetic field) Folia Forestalia Polonica Z 9 (Series B) pp. 29-56.

78 Shellard, H.S.(1963) The estimation of design wind speeds Symp on Wind Effects on Buildings and Structures (Paper No. 1) Nat. Physical Lab., England.

79 Melbourne, W.H.(1975) Probability distributions of response of BHP house to wind action and model comparisons J. of Ind. Aerodynamics 1 pp. 167-175.

80 Melbourne, W.H.(1975) Cross-wind response of structures to wind action 4th Int. Conf. on Wind Effects on Buildings and Structures Heathrow, England.

81 Whitbread, R.E.(1975) The measurement of non-steady wind forces on small-scale building models 4th Int. Conf. on Wind Effects on Buildings and Structures Heathrow, England.

82 Mercer, C.A.(1973) Further note on digital estimation of correlation functions J. Sound and Vibrations 31 (Part 3) pp. 384-387.

83 Davenport, A.G.(1967) The treatment of wind loading on tall buildings. Symp. on Tall Buildings with Particular Reference to Shear Wall Structures Dept of Civil Eng., Univ. of Southampton, England.

84 Siddall, R.G. and Davies, T.W.(1969) The interpretation of anemometer responses in highly turbulent flows Symp. on Heat and Mass Transfer in Flow with Separated Regions and Measurement Techniques Herceg-Novi, Yugoslavia.

85 Davies, T.W. and Patrick, M.A.(1972) A simplified method of improving the accuracy of hot-wire anemometry DISA Conference Leicester, England.

86 Vernon, J.B.(1967) Linear Vibration Theory John Wiley and Sons Inc., London.

87 Gaylord and Gaylord (1968) Structural Engineering Handbook McGraw-Hill Book Co., London.

88 Van Santen, G.W.(1953) Mechanical Vibration Philips Technical Library, Netherlands.

89 Russel, J.B.(1973) Private Communication, Dept of Aeronautics, The City University, London.

Russel, J.B.(1976) Determination of the damping of a system using a planimeter Aeronautical J. 80 (No.782) pp.82–84.

90 Skingle, C.W.(1966) A Method for Analysing the Response of a Resonant System to a Rapid Frequency Sweep Input (Tech.Rep. 66379) Roy.Aircraft Est., Farnborough, England.

91 Jeary, A.P. and Winney, P.E.(1972) Determination of structural damping of a large multi-flue chimney from the response to wind excitation Inst.Civil Engrs (Tech.Note.No.65) pp.569–577.